

SUBCOOLED FLOW BOILING AND CONDENSATION

by

OBIDA M. ZEITOUN
B.Sc., M.Sc.

A Thesis
Submitted to the School of Graduate Studies
in Partial Fulfilment of the Requirements
for the

Doctor of Philosophy Degree

McMASTER UNIVERSITY

1994

© Obida Zeitoun, 1994

**SUBCOOLED FLOW BOILING
AND
CONDENSATION**

To My Kind Parents, Wife, Son and Daughter

DOCTOR OF PHILOSOPHY

McMASTER UNIVERSITY

(Mechanical Engineering)

Hamilton, Ontario

TITLE: SUBCOOLED FLOW BOILING AND CONDENSATION

AUTHOR: Obida M. Zeitoun
B.Sc. & M.Sc. (Alexandria University - EGYPT)

SUPERVISOR: Dr. M. Shoukri

NUMBER OF PAGES: xvii, 263

ABSTRACT

Fundamental problems in two different flow regimes; subcooled water-steam bubbly condensing flow and subcooled flow boiling, in vertical conduits under low pressure and mass flux conditions, were investigated.

For subcooled water-steam condensing bubbly flow, experiments were carried out to obtain a data base for the axial distribution of area-averaged void fraction, interfacial area concentration, interfacial condensation heat transfer and bubble relative velocity. The interfacial area concentration was obtained by measuring the distributions of bubble volume and surface area, using high speed photography and digital image processing techniques, as well as the area-averaged void fraction, using a single beam gamma densitometer, at various axial locations. The interfacial heat transfer coefficient was obtained by monitoring the rate of change of the volume of individual bubbles as a function of local conditions. The data was used to develop new correlations for interfacial area concentration and interfacial condensation heat transfer coefficients. The applicability of the proposed correlations, as closure equations in existing two-fluid model based computer codes, was checked by including them in a two-fluid model to predict the axial void fraction profiles. The prediction of the current two-fluid model was compared with the measured

axial void fraction profiles as well as available data from literature with good agreement.

For subcooled flow boiling, experimental data on the axial profile of void fraction, wall superheat and liquid subcooling along the test section were generated for various levels of mass flux, heat flux and inlet subcooling. The high speed photographic results confirmed the fact that the bubble parallel, or normal, detachment from the heating surface is not the reason of the NVG phenomenon. The digital image processing technique was used to measure the bubble size distributions as function of the local conditions. A correlation for the mean bubble diameter as a function of the mass flux, heat flux and local subcooling was obtained. Physical mechanisms causing the NVG phenomenon were investigated using the high speed photographic results. A net vapour generation model was proposed. The proposed model was based on the balance between the vapour generation and condensation rates at this point. A two-fluid model for the axial void fraction profile in subcooled boiling flow was introduced. A heat flux division model was proposed. The proposed two-fluid model was reasonably capable of predicting the axial void fraction profiles in subcooled flow boiling, without the need for prior identification of the location of the NVG point.

ACKNOWLEDGEMENT

The author would like to express his great thanks to all those who have supported this endeavour with their patience and love.

Sincere thanks are due to my thesis supervisor Prof. M. Shoukri for his guidance and unlimited support which have been invaluable during the course of this work.

The fruitful discussions and support of my supervising committee, Prof. R. L. Judd and Dr. V. Chatoorgoon are greatly appreciated.

The financial support provided by Atomic Energy of Canada Limited and the Canadian International Development Agency is gratefully appreciated .

Last, but not the least, the author would like to express his deep gratitude towards his parents and wife for their encouragement, support and love.

TABLE OF CONTENTS

ABSTRACT	iii
ACKNOWLEDGEMENT	v
TABLE OF CONTENTS	vi
NOMENCLATURE	ix
Lists of Tables	xiii
List of Figures	xiv
CHAPTER 1: INTRODUCTION	1
CHAPTER 2: LITERATURE REVIEW	11
2.1 Onset of Nucleate Boiling Models	12
2.2 Net Vapour Generation Models	13
2.2.1 Thermal-Hydrodynamically Based Models	14
2.2.2 Bubble Detachment Models	18
2.2.3 Bubble Ejection Models	19
2.2.4 Evaluation of previous Models of NVG point	20
2.3 Void Fraction Profile Models	22
2.3.1 Profile Fit Models	23
2.3.2 Mechanistic Models	25
2.3.2.1 Wall Heat Flux Division	26
2.3.2.2 Vapour Condensation Rate	29
2.3.3.3 Vapour Phase Velocity	30
2.3.2.4 Bubble Size and Interfacial Area Concentration	30
2.3.3 Concluding Remarks	31

CHAPTER 3: EXPERIMENTAL FACILITIES AND PROCEDURE	40
3.1 Test Loop	40
3.2 Test Section	41
3.3 Measurements and Instrumentation	42
3.3.1 Temperature	43
3.3.2 Void Fraction	44
3.3.3 High Speed Photography	45
3.3.4 Digital Image processing	47
3.4 Experimental Procedure	48
3.5 Test Conditions and Measurement Sample	49
CHAPTER 4: INTERFACIAL PHENOMENA AND VOID FRACTION IN SUBCOOLED WATER-STEAM BUBBLY CONDENSING FLOW . . .	67
4.1 Interfacial Area Concentration	68
4.1.1 Introduction	68
4.1.2 Results and Data Reduction	71
4.1.3 Discussion of the Results	74
4.1.4 Evaluation of Existing Correlations	76
4.1.5 Proposed Correlations	80
4.2 Bubble Relative Velocity	83
4.3 Interfacial Heat Transfer Coefficient in Subcooled Water- Steam Bubbly Condensing Flow	85
4.3.1 Introduction	85
4.3.2 Experimental Results and Data Reduction	90
4.3.3 Analysis of the Results	92
4.4 Void Fraction Profile in Condensing Subcooled Water-Steam bubbly flow	96
4.4.1 Experimental Results	96
4.4.2 Two-Fluid Void Fraction Profile Model	97
4.4.2.1 Two-Fluid Model Formulation	97
4.4.2.2 Closure Relationships	104
4.4.2.3 Solution Procedure and Results	107
4.4.2.4 Results and Discussion	108
4.5 Concluding Remarks	110
CHAPTER 5: BUBBLE BEHAVIOUR AND SIZE, NET VAPOUR GENERATION MECHANISM AND VOID FRACTION PROFILE IN SUBCOOLED FLOW BOILING	137
5.1 Experimental Results	140
5.1.1 Void Fraction Profile and NVG Point	140
5.1.2 Liquid Subcooling Profiles	143
5.1.3 Heating Surface Temperature	144
5.2 Bubble Behaviour in Subcooled Flow Boiling	147
5.2.1 Background	147

5.2.2 Visual Observations	151
5.3 Bubble Size in Subcooled Flow Boiling	156
5.3.1 Background	156
5.3.2 Mean Bubble Diameter Measurements	159
5.3.3 Data analysis	160
5.3.4 Proposed Correlation	163
5.4 Net Vapour Generation Model	164
5.4.1 Introductory Remarks	164
5.4.2 Formulation	166
5.4.3 Comparison between proposed NVG Model and Experimental Data	169
5.4.4 Effect of mass and Applied Heat Fluxes on NVG Point	169
5.5 Two-Fluid Void Fraction Profile Model	171
5.5.1 Two-Fluid Model Formulation	171
5.5.2 Closure Relationships	173
5.5.3 Solution and Results	179
5.6 Closing Remarks	184
CHAPTER 6: CONCLUSIONS AND RECOMMENDATIONS	238
6.1 Conclusions	238
6.2 Recommendations	242
REFERENCES	244
APPENDIX A: Heat Balance across Test Section	255
APPENDIX B: Uncertainty Analysis	258

NOMENCLATURE

a	Liquid thermal diffusivity	m^2/s
a_b	Bubble surface area	m^2
A_b	Mean bubble surface area	m^2
A	Cross sectional area of channel	m^2
a_i	Interfacial area concentration	m^2/m^3
Bo	Boiling number, $q/G h_{fg}$	
C_l	Coefficient in Equation (5.33)	
C_p	Liquid specific heat	J/kg K
C_s	Coefficient in Equation (5.29)	
C_v	Condensation term	W/m
D_b	Bubble diameter	m
D_{bo}	Initial bubble diameter, at $\tau = 0$	m
D_h	Hydraulic diameter of channel	m
d_s	Sauter bubble diameter, $6 v_b/a_b$	m
D_s	Mean Sauter bubble diameter, $6 V_b/A_b$	m
$(dP/dz)_f$	Gradient of frictional pressure drop	Pa/m
$(dP/dz)_t$	Gradient of total pressure drop	Pa/m
E_o	Eotvas number, $\Delta g D_h/v$	
Fo	Fourier number, $a \tau/D_b^2$	
Fo_o	Fourier number based on initial bubble diameter, $a \tau/D_{bo}^2$	
g	Gravitational acceleration	m/s^2
G	Mass flux	$\text{kg/m}^2 \text{ s}$
G_v	Generation term	W/m
h_a	Heat transfer coefficient in the slightly subcooled	

	region, Ahmad (1970)	W/m ² K
h_c	Condensation coefficient	W/m ² K
h_d	Liquid enthalpy at NVG point	J/kg
h_f	Liquid enthalpy at saturation condition	J/kg
h_{fg}	Latent heat	J/kg
h_g	Vapour enthalpy at saturation	J/kg
h_{HN}	Heat transfer coefficient at NVG point, Hancox and Nicoll (1971)	W/m ² K
h_{in}	Inlet liquid enthalpy.	
h_l	Liquid enthalpy	J/kg
h_{sp}	Single-phase convective heat transfer coefficient	W/m ² K
Ja	Jakob number based on liquid subcooling, $\rho_l C_p (T_s - T_l) / \rho_g h_{fg}$	
Ja_w	Jakob number based on the superheat at the heating surface, $\rho_l C_p (T_w - T_s) / \rho_g h_{fg}$	
J	Superficial velocity	m/s
J_l	Liquid superficial velocity	m/s
J_g	Vapour superficial velocity	m/s
k	Liquid thermal conductivity	W/m K
k_a	Condensation coefficient, Ahmad (1970)	
k_c	Condensation coefficient, Rouhani and Axelsson (1970)	
m	Mass flow rate	kg/s
n_b	Number of measured bubbles at a certain axial location	
N_b	Number of bubble per cubic meter	bubble/m ³
Nu_c	Condensation Nusselt number, $h_c D_b / k$ or $h_c D_s / k$	
NVG	Net vapour generation point	
ONB	Onset of nucleate boiling point	
OSV	Onset of significant void point	
P	Pressure	Pa
Pe	Liquid Peclet number, $Re Pr$	
Pe_b	Bubble Peclet number, $Re_b Pr$	
P_h	Heater perimeter	m
Pr	Liquid Prandtl number	
q	Applied heat flux	W/m ²
q_l	Liquid component of wall heat flux	W/m ²

q_p	Pumping component of wall heat flux	W/m^2
q_v	Vapour component of wall heat flux	W/m^2
R_b	Bubble radius	m
Re	Flow Reynolds number, $G D_h/\mu$	
Re_b	Bubble Reynolds number, $\rho_l U_b D_b/\mu$	
Re_{bo}	Bubble Reynolds number based on initial bubble diameter, $\rho_l U_b D_{bo}/\mu$	
R_g	Universal gas constant	J/kg K
S	Slip ratio between vapour velocity and liquid velocity.	
T_d	Liquid temperature at NVG point	$^{\circ}C$
T_{in}	Inlet liquid temperature	$^{\circ}C$
T_l	Liquid temperature	$^{\circ}C$
T_s	Saturation temperature	$^{\circ}C$
T_w	Heating surface temperature	$^{\circ}C$
U^*	Bubble dimensionless velocity	
U_b	Bubble relative velocity	m/s
u_g	Vapour velocity	m/s
U_g	Area-averaged vapour velocity	m/s
U_{gj}	Drift vapour velocity	m/s
u_l	Local liquid velocity	m/s
U_l	Area-averaged liquid velocity	m/s
v_b	Bubble volume	m^3
V_b	Average bubble volume	m^3
v_l	Specific volume of liquid	m^3/kg
v_{fg}	$v_g - v_l$	m^3/kg
v_g	Specific volume of saturated vapour	m^3/kg
\dot{V}_l	Liquid volumetric flow rate	m^3/s
We	Bubble Weber number, $D_s \rho_l U_b^2/\sigma$	
x	True quality	
x_d	Thermodynamic quality at NVG	
x_{th}	Thermodynamic quality	
z	Axial location in z-direction	m

Greek Symbols:

α	Area-averaged void fraction.	
α_c	Void fraction at the end of highly subcooled region	
α_w	Void fraction at heating surface	
β	Volumetric void fraction	
β	D_b/D_o	
ϵ	Pumping factor	
ϵ_a	Statistical error of gamma processing system	
Γ_o	Evaporation rate per unit length of channel	kg/m s
μ	Liquid viscosity	Pa s
μ_g	Vapour viscosity	Pa s
ν_l	Liquid kinematic viscosity	m ² /s
ρ_f	Saturated liquid density	kg/m ³
ρ_g	Saturated vapour density	kg/m ³
ρ_l	Liquid density	kg/m ³
σ	Surface tension	N/m
ϕ	Experimental factor.	
λ	Empirical coefficient	
$\theta_{in/un}$	Subcooling at unheated section entry	°C
θ_l	Subcooling temperature	°C
θ_o	Static contact angle of the bubble	
$\Delta\rho$	$\rho_l - \rho_g$	kg/m ³
λ_s	Ratio between Weber and Reynolds numbers, $v_f^2 \rho_f / D_h \sigma$	
τ_{bo}	Shear stress at bubble layer edge	N/m ²
τ_w	Wall shear stress	N/m ²
τ	Time	s

Subscripts:

l	Liquid
g	Vapour
o	Initial condition, at time equals zero
s	Saturation

List of Tables

	Page
2.1 Experimental investigations of high pressure flow	32
2.2 Experimental investigations of low pressure flow	33
2.3 Onset of nucleate boiling models	34
2.4 Net vapour generation models	35
2.5 Profile fit models	36
2.6 Heat division mechanisms	37
2.7 Vapour Condensation models	38
2.8 Vapour Velocity models	39
3.1 Test conditions for set number 1	52
3.2 Test conditions for set number 2	53
3.3 Test conditions for set number 3	54
4.1 Interfacial area correlations and models	111
4.2 Bubble condensation models	112
5.1 Different proposed heat flux division mechanisms	186
B.1 Uncertainty in measured quantities	260
B.2 Uncertainty for quantities computed in condensing region	261
B.3 Uncertainty for quantities computed in boiling region	262

List of Figures

		Page
1.1	Diagram of SLOWPOKE energy system	9
1.2a	Subcooled flow boiling regions	10
1.2b	Subcooled flow boiling and condensation regions	10
3.1	Test loop	55
3.2	Test section	56
3.3	Subcooling measurements along test section	57
3.4	Sliding thermocouples	57
3.5	Gamma densitometer signal processing system	58
3.6	Gamma densitometer static calibration	59
3.7	Components of the high speed photography system	60
3.8	Digital image processing system	61
3.9	Typical void fraction profiles along the heated and unheated regions	62
3.10	Typical liquid subcooling along test section	63
3.11	Typical inner heating surface temperature along heating section	64
3.12	Typical photograph shot in the condensing region	65
3.13b	A photograph for the annular gap in boiling region	66
3.13b	A photograph for the heating surface in boiling region	66
4.1	Typical bubble photographs in the condensing region	114
4.2	Void fraction distribution along condensing flow	115
4.3	Bubble size and surface area measurement	116
4.4	Typical frequency distribution of measured Sauter bubble diameter	116
4.5	Measured mean Sauter bubble diameter versus void fraction	117
4.6	Relation between interfacial area and void fraction	118
4.7	Comparison between measured interfacial area and previous correlations	119
4.8	Comparison between measured interfacial area and previous correlations	119
4.9	Comparison between measured interfacial area and previous correlations	120
4.10	Comparison between measured interfacial area and previous correlations	120

4.11	Comparison between measured interfacial area and Kocamustafaogullari's model	121
4.12	Comparison between proposed correlation and present data	121
4.13	Comparison between the calculated and measured mean Sauter bubble diameter	122
4.14	Bubble relative velocity	122
4.15	Samples of condensing bubbles	123
4.16	Typical condensing bubbles	124
4.17	Comparison between present data of bubble condensation Nusselt number and existing models	124
4.18	Comparison between present data and proposed correlation	125
4.19	Comparison between the present model of bubble history and previous models	126
4.20a	Void fraction Distribution along unheated region	127
4.20b	Void fraction Distribution along unheated region	128
4.20c	Void fraction Distribution along unheated region	129
4.21a	Void fraction Distribution along unheated region	130
4.21b	Void fraction Distribution along unheated region	131
4.22	Effects of distribution parameter on void fraction profile . .	132
4.23a	Effect of mass flux on void fraction and subcooling profiles	133
4.23b	Effect of inlet void fraction on void fraction and subcooling profiles	133
4.23c	Effect of inlet subcooling on void fraction and subcooling profiles	133
4.24	Comparison between present model and existing data . . .	134
4.25	Comparison between present model and existing data . . .	135
4.26	Comparison between present model and existing data . . .	136
5.1a	Void fraction distribution along heating section	187
5.1b	Void fraction distribution along heating section	188
5.1c	Void fraction distribution along heating section	189
5.1d	Void fraction distribution along heating section	190
5.1e	Void fraction distribution along heating section	191
5.2a	Void fraction distribution along heating section	192
5.2b	Void fraction distribution along heating section	193
5.2c	Void fraction distribution along heating section	194
5.3a	NVG point location	195
5.3b	NVG point location	195
5.4	Subcooling at NVG versus applied heat flux	196
5.5a	Comparison between experimental data and existing NVG models	197
5.5b	Comparison between experimental data and existing NVG models	197
5.5c	Comparison between experimental data and existing	

	NVG models	198
5.5d	Comparison between experimental data and existing NVG models	198
5.5e	Comparison between experimental data and NVG model of Yang and Weisman (1991)	199
5.5f	Comparison between experimental data and NVG model of Levy (1967)	199
5.5g	Comparison between experimental data NVG model of Sekoguchi et al. (1974)	200
5.5h	Comparison between experimental data and NVG model of Rogers et al. (1987)	200
5.5i	Comparison between experimental data and NVG model of Serizawa (1979)	201
5.6	Liquid subcooling along test section	201
5.7	Inner wall superheat along heating section	202
5.8	Inner wall superheat along heating section	203
5.9	Comparison between measured wall superheat and Shah's model (1983)	204
5.10	Bubble growth-collapse cycle before, near and after the NVG point for run No. B1	205
5.11	Bubble growth-collapse cycle before, near and after the NVG point for run No. B2	206
5.12	Bubble growth-collapse cycle before, near and after the NVG point for run No. B4	207
5.13	Bubble growth-collapse cycle before, near and after the NVG point for run No. B8	208
5.14	Bubble behaviour along subcooled flow boiling regions for run No. B3	209
5.15	Bubble behaviour along subcooled flow boiling regions for run No. B4	210
5.16	Bubble behaviour along subcooled flow boiling regions for run No. B8	211
5.17	Bubble behaviour along subcooled flow boiling regions for run No. B9	212
5.18	Bubble size measurement	213
5.19	Typical histogram of bubble occurrence frequency versus individual Sauter bubble diameter	213
5.20a	Measured mean Sauter bubble diameter along heating section	214
5.20b	Measured mean Sauter bubble diameter along heating section	215
5.21a	Relation between bubble size and void fraction along heating section	216
5.21b	Relation between bubble size and void	

	fraction along heating section	217
5.22	Effect of mass flux on bubble size	218
5.23	Effect of applied heat flux on bubble size	219
5.24a	Comparison between measured mean Sauter bubble diameter and existing models of maximum and detachment bubble diameter	220
5.24b	Comparison between measured mean Sauter bubble diameter and existing models of maximum and detachment bubble diameter	221
5.25	Comparison between proposed correlation and measured mean Sauter bubble diameter	222
5.26a	Comparison between proposed correlation and measured mean Sauter bubble diameter	223
5.26b	Comparison between proposed correlation and measured mean Sauter bubble diameter	224
5.27	Speculated vapour generation and condensation function	225
5.28	Comparison between the proposed NVG model and experimental data	226
5.29a	Effect of heat flux on the subcooling at the NVG point	227
5.29b	Effect of mass flux on the subcooling at the NVG point	227
5.30	Effect of imposing the NVG point on the predicted void fraction profile	228
5.31	Effect of various bubble condensation models on the predicted void fraction profile	229
5.32	Effect of various bubble condensation models on the predicted void fraction profile	234
5.33	Effect of various bubble condensation models on the predicted void fraction profile	235
5.34	Effect of various bubble condensation models on the predicted void fraction profile	236
5.35	Effect of various bubble condensation models on the predicted void fraction profile	237
A.1	Heat balance across test section	257
B.1	Uncertainty in the NVG point location	263

CHAPTER 1

INTRODUCTION

The importance of two-phase flow studies has increased significantly in the last five decades with the fast development of nuclear power reactors. This has led to an enormous number of investigations, especially in the high pressure flow, typical of power reactors. Meanwhile, the development of small reactors, like SLOWPOKE and MAPLE, still requires detailed investigation of low pressure flow boiling. These reactors, which are designed by Atomic Energy of Canada Limited are mainly used for scientific research and radioactive isotope production, and they can be used as an economical heating source for large buildings. One SLOWPOKE can heat 150,000 square meters. These types of reactors are characterized by an open-chimney in pool design and operate near atmospheric pressure. A schematic diagram for SLOWPOKE is shown in Figure 1.1, Snell et al. (1992). The primary flow is driven by natural convection, which removes the nuclear heat generated from the fuel elements. The heated water rises by natural convection to the top of chimney where it flows through a heat exchanger and transfers its energy to a separate water circuit. The single

phase coolant (water) which circulates along the fuel elements perform two tasks. The coolant transfers the fission energy from the nuclear fuel elements and provides the neutron moderation necessary to sustain the fission process. Under normal conditions, heat transfer is by single phase convection. Under some abnormal conditions, the heat flux level can be high enough that subcooled boiling may be encountered in the reactor core. The vapour generated in the core may subsequently be condensed downstream in the chimney. Knowledge of the detailed void fraction distribution is important for many reasons. The void fraction distribution affects the pressure drop, heat transfer rates in the reactor core and flow stability. It also affects the characteristics of neutron moderation and, consequently, the reactor power. The SLOWPOKE has a negative reactivity safety system, as the temperature of water rises, the degree of reactivity of the uranium fuel naturally decreases, which means that the amount of heat released by the fuel decreases. The control system needs only to respond slowly to maintain the temperature of the pool water at an appropriate level. Fast acting shutdown systems associated with large power reactors, are not required. Because of their inherent safety characteristics, SLOWPOKES will be licensed for up to 24 hours of unattended, remotely-monitored operation.

When a subcooled liquid enters a heated channel, the temperature distribution adjacent to the hot surface may result in local boiling at the surface while the bulk of the flow is still subcooled. This leads to a case of thermal

non-equilibrium. Bubbles nucleate on the heating surface and condense as they leave the heating surface and move through the subcooled bulk. The net amount of vapour generation is determined by the difference between the generation rate at the heating surface and the condensation rate in the bulk.

As shown in Figure 1.2a, subcooled boiling starts after the heating wall temperature exceeds the saturation temperature enough to cause nucleation at point (A), which is called the onset of nucleate boiling (ONB). The subcooled boiling continues downstream from point (A) but the void fraction cannot grow significantly because of the high level of liquid subcooling. At point (B), the void fraction starts to increase sharply. This point is called the net vapour generation (NVG) or the onset of significant void (OSV). The subcooled boiling continues after the NVG point until it reaches the saturated, bulk, boiling at point (C), where the mean bulk enthalpy of the flow equals the enthalpy of the saturated liquid. The mechanism of subcooled boiling continues until the minimum enthalpy of the liquid phase across the flow area reaches the saturation condition at point (D). The subcooled boiling region can be divided into two regions. The highly subcooled region, which is upstream of point (B), has low void fraction, almost constant (2-9 %) and the slightly subcooled region, which is downstream of point (B), has significant void fraction. The NVG point is the transition boundary between these two regions. This point is of great importance. The accurate prediction of the void fraction profile in the slightly subcooled region, using available models, depends on the accurate prediction

of the NVG location. If the heating stops at a certain point, e.g. point F in Figure 1.2b, the bubbles generated by boiling in the region from A to F will condense and consequently the void fraction will decrease as shown in Figure 1.2b. This situation will be similar to what may happen in the chimney of the SLOWPOKE if voids are generated along the fuel elements.

Among the various mathematical formulations of two phase flow used to simulate the flow in the reactor, the two-fluid model is considered the most accurate. In this type of formulation, the two phases are described separately in terms of averaged phasic mass, momentum and energy equations. Moreover, the interaction between the two phases is modelled by interfacial transfer terms to account for interfacial mass, momentum and energy transport. Modelling these terms requires accurate knowledge of the interfacial area concentration, bubble size, interfacial heat transfer coefficient and bubble relative velocity. Consequently, relationships for these parameters are needed as parts of the constitutive equations for closure. In the subcooled flow boiling region, besides the above parameters, the following problems have to be addressed in order to accurately predict the void fraction profiles:

- 1- Point of the onset of nucleate boiling (ONB).
- 2- Point of the net vapour generation (NVG).
- 3- Division mechanisms of the applied heat flux at the heating surface.

The objective of the current research program is to develop advanced models for subcooled flow boiling pertinent to the operation and the safety

analysis of small nuclear reactors, e.g., SLOWPOKE and MAPLE. The results of the proposed research are to be incorporated into computer codes used for safety and stability analyses of these reactors, to enhance the accuracy of their predictions. The accurate prediction of the thermal hydraulic behaviour of small reactors will lead to improvements in the safety margins and the allowable operating limits resulting in improved system efficiency and safety. The results will also be of a fundamental nature and will be applicable to other heat exchange equipment.

A review of the literature on subcooled flow boiling with particular emphasis on the net vapour generation phenomenon and the void fraction profile models indicates that:

- a- There is a lack of agreement on the basic mechanisms associated with the net vapour generation phenomenon.
- b- Most of the previous studies, especially the modelling, are related to high pressure flows.
- c- There is a lack of knowledge of the interfacial phenomena in subcooled boiling and condensing flows.

This research program was designed to achieve the following:

- 1- Perform detailed experiments on low pressure and low mass flux subcooled flow boiling in vertical channels in order to generate an accurate database pertinent to void fraction distribution, bubble size, interfacial area concentration and bubble condensation rate.

- 2- Investigate interfacial area concentration in subcooled water-steam bubbly condensing flow.
- 3- Investigate the interfacial heat transfer coefficient in subcooled water-steam bubbly condensing flow.
- 4- Investigate bubble size in subcooled flow boiling.
- 5- Identify the physical mechanisms causing the net vapour generation phenomenon.
- 6- Use this data base to develop accurate models for the NVG point and the axial void fraction profile.

To achieve the above goals, an experimental facility was developed to separately study vapour generation and condensation. The test section consisted of two regions associated with a heated and an unheated sections. The vapour which was generated in the heated section condensed in the downstream unheated section. The measurements included:

- 1- Area-averaged void fraction profiles along both the heated and the unheated sections obtained with a gamma densitometer.
- 2- Subcooled liquid temperature along both the heated and the unheated sections.
- 3- Heating surface temperature along the heater.
- 4- General conditions: inlet and outlet temperatures, inlet pressure, water flow rate, voltage drop across the heater and current through the heater.
- 5- High speed video camera information for boiling and condensing processes

along both the heated and unheated sections respectively.

A digital image processing technique was used to analyze the images recorded by the high speed video system (frame by frame) to study: bubble size, bubble condensation rate and bubble velocity in the condensing region and the mechanism of the NVG phenomenon and bubble size in the subcooled boiling region.

The present thesis contains six chapters including the current chapter. Critical reviews of the literature on the onset of nucleate boiling, the net vapour generation phenomenon and the axial void fraction profile models in subcooled flow boiling are presented in chapter 2. Descriptions of the experimental facilities, procedures and some raw results are presented in chapter 3. Detailed investigation of the interfacial area concentration, interfacial heat transfer coefficient and bubble velocity in subcooled water-steam condensing bubbly flow are included in chapter 4. The experimental findings in this flow regime were incorporated in a steady-state two-fluid model for closure to predict the axial void fraction profile and this analysis is also included in Chapter 4. Chapter 5 focuses on the subcooled flow boiling. In this chapter, bubble size, bubble behaviour and net vapour generation phenomenon were investigated, a model for the NVG point was presented and a two-fluid model for the void fraction profile in the subcooled flow boiling region is proposed.

It was found convenient to start by investigating the condensing region rather than the subcooled boiling region for the following reasons; the simplicity

of the condensation with respect to the subcooled boiling and an understanding the condensation in the subcooled water-steam bubbly flow may be helpful in understanding the subcooled flow boiling where evaporation and condensation take place simultaneously. The conclusions of the present study and the recommendations are presented in chapter 6.

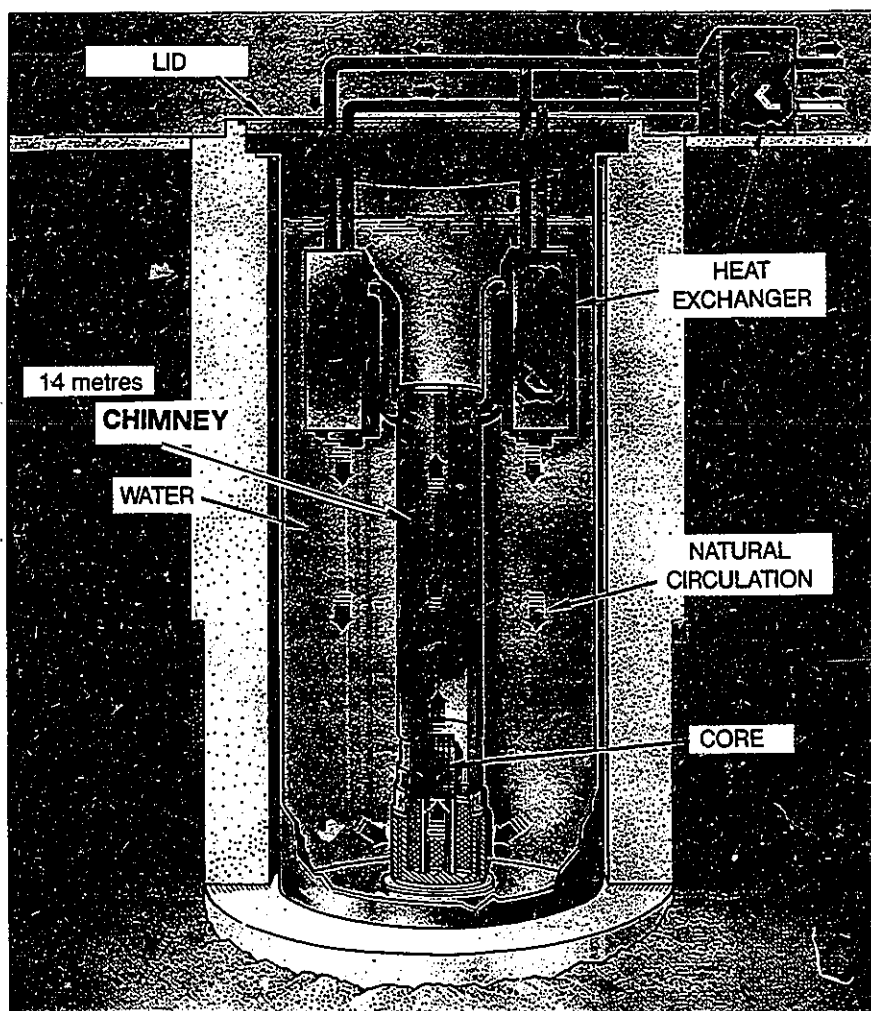


Figure 1.1 Diagram of a SLOWPOKE energy system

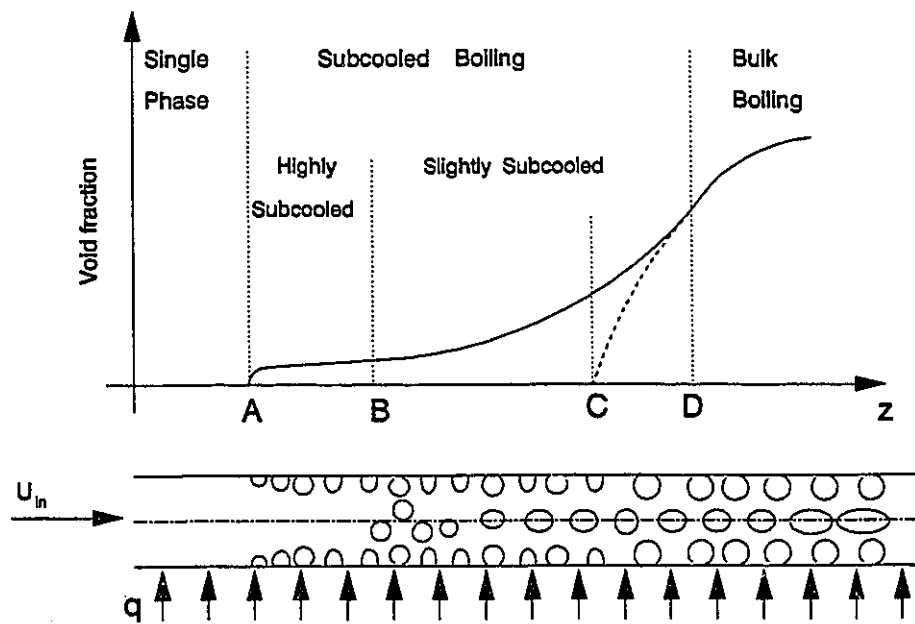


Figure 1.2a Subcooled flow boiling regions

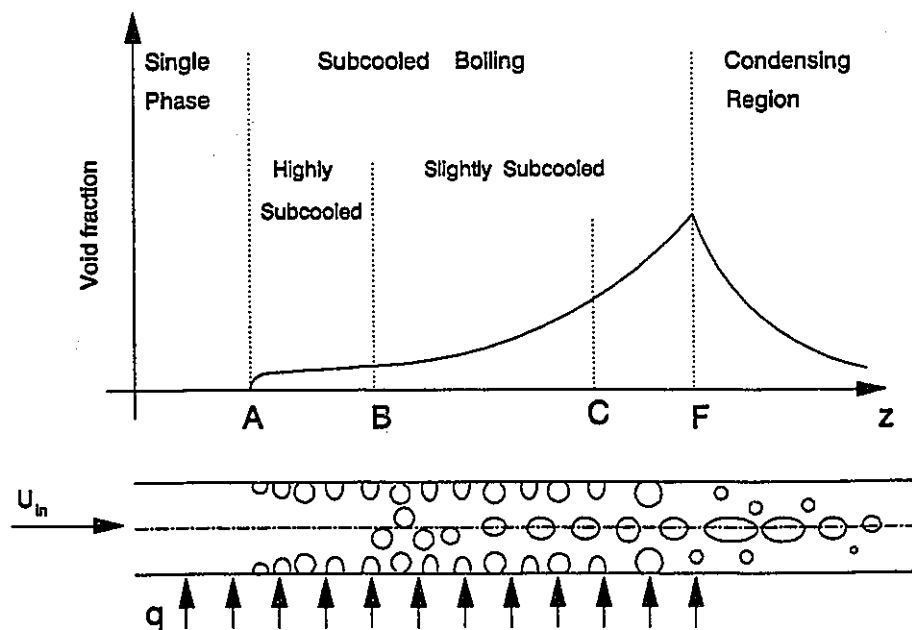


Figure 1.2b Subcooled flow boiling and condensation regions

CHAPTER 2

LITERATURE REVIEW

One of the most important thermal non-equilibrium two phase flow processes is that of forced convective subcooled flow boiling. Due to the importance of this subject, it has been extensively investigated by many researchers. Moreover, a number of reviews on the subject were published, Dix (1970), Bucher and Normann (1976), Mayinger and Bucher (1977), Lahey and Moody (1977), Collier (1972), and Katto (1986). As discussed earlier, the subcooled boiling region is divided into two regions, highly subcooled and slightly subcooled regions, according to Griffith et. al (1958). The highly subcooled region starts at the ONB point and continues to the NVG point. The void fraction is very low in this region because of the high subcooling. The slightly subcooled region starts at the NVG point and continues into the saturated boiling region. The following review focuses on three aspects of subcooled flow boiling; the onset of nucleate boiling point, the net vapour generation point and axial void fraction profile models.

The development of power reactors has led to many extensive ex-

perimental investigations in high pressure conditions. The experimental studies undertaken at high pressure are listed in Table 2.1. The test section geometry, the pressure range and the working medium of these investigation are also listed in this table. Recently, the development of small low pressure reactors, like the SLOWPOKE and MAPLE reactors, increased the interest in understanding low pressure subcooled flow boiling. The experimental investigations of low pressure flow are listed in Table 2.2. The cross sectional area, the pressure range and the working medium are listed in this table too.

2.1 Onset of Nucleate Boiling Models

In analyzing the thermal-hydraulic characteristics of subcooled flow boiling in a heated channel, the location of the onset of nucleate boiling (ONB) is an essential parameter. No boiling can occur while the temperature of the heating surface is still below the saturation temperature. Available models for the prediction of ONB are listed in Table 2.3. In the first attempt to predict the ONB point, McAdams, et al., as reported by Bergles and Rohsenow (1964), considered the intersection between the forced convection heat transfer curve of single phase flow and the fully developed boiling curve. The experimental investigations showed that the onset of nucleation occurred at a lower wall temperature than that estimated by this method. For pool boiling, Hsu (1962) postulated that the bubble nucleus would only grow if the lowest temperature

of the liquid at the bubble tip was greater than the vapour temperature inside the bubble, as calculated from mechanical equilibrium across the vapour-liquid interface. By assuming that the temperature profile was linear near the heating surface, Bergles and Rohsenow (1964) implemented Hsu's idea (1962) graphically. They determined the wall superheat at ONB point by means of the empirical relationship listed in Table 2.3. Davis and Anderson (1966) followed Hsu's idea and obtained the analytical relationships listed in Table 2.3.

Ünal (1977) divided the heat flux at the ONB point into nucleate boiling and single phase convection components. The subcooling at ONB was calculated by means of the empirical relationship in Table 2.3.

Serizawa (1979) estimated the condition at ONB from a heat balance applied at the vapour-liquid interface, in which he considered two thermal resistances in series, one for the liquid film beneath the bubble and the other for the vapour-liquid interface. The subcooling at the ONB point is predicted by the empirical relationship listed in Table 2.3, where h_c is the interfacial heat transfer coefficient (the condensation coefficient at the bubble surface). The heating surface superheat at the ONB point can be calculated from the fully developed forced convection relationship of single phase flow.

2.2 Net Vapour Generation Models

NVG is the point at which the void fraction starts to increase

significantly, i.e. it is the transition boundary between the two regions of subcooled boiling, the highly subcooled and the slightly subcooled regions. The models of NVG are categorized into three groups. The models of the first group are thermal-hydrodynamically controlled. The models of this group depend on correlating the heat transfer rate at the NVG point. In the second group, the NVG point is considered the point of the first bubble departure from the heating surface. The third group of models considers the ejection of bubbles from the wall bubbly layer into the subcooled bulk flow to be the point of NVG.

Recently, Lee et al. (1992) published a comparison study between predictions of various NVG models and experimental data undertaken at low pressure in the literature. The comparison showed the inability of available models to accurately predict the conditions at the NVG point. However, they reported that the models of Saha and Zuber (1974) and Levey (1967) were the best models to fit the experimental data.

2.2.1 Thermal-Hydrodynamically Based Models

The models of Griffith et al. (1958), Ahmad (1970), Hancox and Nicoll (1971), Saha and Zuber (1974), Ünal (1975) and Yang and Weisman (1991) fall into this category. Despite differences in the description of the physical phenomenon occurring at the NVG point, all these models depend on modelling the heat transfer rate at this point. Available models of the NVG point are listed

in Table 2.4.

Griffith and et al. (1958) were the first to introduce the concept of the two regions of subcooled flow boiling, highly subcooled boiling associated with low void fraction and slightly subcooled boiling accompanied by significant void fraction. They defined the transition between the two regions by the location at which the heating surface is fully covered with a layer of attached bubbles. They also assumed that at the NVG point, vapour condensation and generation were equal. The total wall heat flux was used to generate the vapour and the sensible heat transfer to the subcooled liquid was totally provided by the condensation of the vapour bubbles. The subcooling at the NVG point was estimated from the relationship listed in Table 2.4. The idea of a surface fully covered by a layer of attached bubbles was not confirmed by the high speed photography results of the present study and Dix (1970).

Ahmad (1970) determined the NVG point location by correlating the heat transfer coefficient at the transition between the two subcooled flow boiling regions. The heat transfer coefficient increased from the single phase value at the ONB point to a higher value at the NVG point, see Table 2.4. The subcooling at the NVG point was estimated by assuming that the total wall heat flux was transferred to the liquid up to the end of the highly subcooled region and the heating surface temperature was equal to the saturation temperature.

Hancox and Nicoll (1971) presented a model based upon the assumption

that the existence of attached bubbles in the highly subcooled region increases the effective conductivity in the near wall region. Therefore, the heat flux that can be transferred to the liquid core is greater than the specified wall heat flux, and hence the vapour formation is suppressed. As the fluid advances downstream, the liquid subcooling is reduced, resulting in reducing the potential heat flux because the temperature gradient is no longer sufficient to remove the applied heat flux and consequently vapour generation must begin. The heat transfer coefficient at the NVG point was calculated by employing logarithmic velocity and temperature profiles and turbulent Prandtl number of unity in the liquid core. A relationship for the heat transfer coefficient and the subcooling at the NVG point are presented in Table 2.4.

Saha and Zuber (1974) reported that the point of NVG is thermally as well as hydrodynamically controlled. They postulated that this point is not necessarily the point of bubble departure. They reasoned that at the NVG point certain thermal and hydrodynamical conditions must be satisfied. Saha and Zuber (1974) argued that the point of NVG was only dependent on local thermal conditions which determine the rates of vapour generation at the heating surface and condensation in the bulk of the flow. Based on data from the literature, they introduced the empirical model listed in Table 2.4. Two distinct regions were found, thermally and hydrodynamically based on the Peclet ($G D_h C_p / k$) number as shown in the table. For Peclet number less than 70,000, the NVG point was thermally controlled, while for the Peclet number

higher than 70,000, this phenomenon was found to be totally hydrodynamically controlled.

Based on high speed photography, Ünal (1975) concluded that the bubble detachment was not related to the NVG point. He reported detached bubbles in the flow bulk before this point. Ünal (1975) considered that the subcooled boiling was the transition between the single phase forced convection and the fully developed boiling regimes. Consequently, the heat flux in the subcooled region was affected by both regimes, forced convection and fully developed boiling. Considering that the effect of the forced convection will vanish at the beginning of the fully developed boiling and assuming that the NVG point was the boundary between the subcooled boiling and the fully developed boiling, he obtained the empirical relationship for liquid subcooling at the NVG point listed in Table 2.4.

While Yang and Weisman (1991) accepted the fact that bubble departure is the cause of the sudden increase in void fraction at the NVG point, they introduced the following model based on the heat balance at the edge of the bubbly layer. The flow was considered to be divided into two layers, a bubbly layer adjacent to the heating surface and a subcooled liquid core. They assumed that the total wall heat flux was transferred through the bubbly layer to the liquid core. The subcooling at the NVG point was estimated by assuming that the void fraction would not grow significantly until the enthalpy of the fluid entering the core from the bubbly layer was above the saturation

condition. They estimated the condition at the NVG from the model listed in Table 2.4.

2.2.2 Bubble Detachment Models

Bowring (1962) was the first to introduce the idea of predicting the NVG point by modelling the point of bubble departure from the heating surface. Many models were later developed based on the same idea such as the models of Levy (1967), Staub (1968), Rogers et al. (1987), Rogers and Li (1992) and Lee and Bankoff (1992). In these models, the flow was considered to be divided into two regions. The first is the highly subcooled region where the bubbles remain attached to the heating wall, grow and condense on it. The void fraction starts to increase significantly, in the second region, when the bubbles start to detach from the heating surface giving the chance for new bubbles to nucleate.

Levy (1967) used a balance between buoyancy, surface tension and wall shear forces in the flow direction to predict the bubble diameter at departure. In order for the bubble to leave the surface, Levy (1967) suggested that the temperature at the tip of the bubble, which was still attached to the surface, should reach saturation temperature. Therefore, he used the temperature profile of the fully developed turbulent single phase flow to determine the degree of subcooling at which the bubble would leave the surface. The subcooling at the NVG point was calculated as presented in Table 2.4, where C is an empirical

constant and τ_w is the shear stress at the heating surface.

Rogers et al. (1987) incorporated the effect of bubble contact angles based on the findings of Winterton (1984) in calculating bubble size at the NVG point. They included the drag force, rather than the wall shear force, in their force balance. Later, Rogers and Li (1992) modified this model by including surface roughness (due to bubbling). They also extended it to flows at high pressure. Rogers et al. (1987) reported that for low mass flux, the subcooling at the NVG point increased as the mass flux increased. Apparently, this concept can be accepted only if the bubble departure is the cause of the NVG phenomenon. The subcooling at the NVG was calculated as presented in Table 2.4, where F_R is an empirical factor to allow for rough surface effects, θ_0 is the equilibrium contact angle, C_s is an empirical correction factor for the surface tension force and C_1 , C_2 and C_3 are functions of the equilibrium contact angle.

2.2.3 Bubble Ejection Models

Based on visual observations and high speed photography, Dix (1970) introduced the idea of modelling the NVG as the point of bubble ejection from the bubbly layer adjacent to the heated wall. When bubbles grow on a heating surface, they reach a certain diameter determined by thermo-hydraulic force balance at which they detach from the surface and move downstream. Under high subcooling conditions, they tend to remain close to the wall forming a

bubbly layer due to thermocapillarity action (Serizawa, 1979). When the bubbly layer thickness reaches a certain critical size the bubbles are no longer stable in the bubbly layer and they are ejected into the subcooled core. Dix (1970) determined the condition of the NVG point based on this idea by the relationship listed in Table 2.4. Serizawa (1979) formulated an analytical based model by assuming that the point of bubble ejection was the inflection point of the axial void fraction profile. This profile was calculated as a function of active nucleation site density and frequency along the heating surface. The condensation effect was ignored. The conditions of NVG predicted by Serizawa (1979) are listed in Table 2.4.

2.2.4 Evaluation of the Previous Models for the NVG Point

It is clear that there is significant disagreement amongst various researchers regarding the physical mechanisms causing the rapid increase of the void fraction at the NVG point. Recent data obtained for low pressure subcooled flow boiling by Rogers et al. (1987), Donevski and Shoukri (1989), Dimmick and Selander (1990) and Bibeau and Salcudean (1990) has shown that the low void fraction region, preceding the NVG point, in low pressure flow tends to be longer than for high pressure flow and is characterized by almost uniform void fraction in the range of 2% to 9%. Bibeau and Salcudean (1990) measured the void fraction profile in subcooled flow boiling for upward and

downward flows. The interesting point of their results was that the NVG point occurred at higher subcoolings in the case of downward flow. This is contrary to the bubble detachment models because bubbles are expected to detach earlier in upward flow. For downward flow, bubble relative and absolute velocity are lower than that in the upward flow because the drag force acts against the buoyant force. Lower absolute bubble velocity is a direct cause of high void fraction and consequently the chance for the NVG phenomenon to occur at higher subcooling is better. Lower bubble relative velocity can lead to lower condensation rates and early coalescence which can also cause the NVG point to occur at higher subcooling.

The models of bubble detachment presented by Levy (1967), Staub (1968), Rogers et al. (1987), Rogers and Li (1992) and Lee and Bankoff (1992) incorporated a force balance in the flow direction to estimate bubble size at departure. The high speed film studies of Dix (1970), Michel and Bartsch (1983), Bibeau (1993), the present work and the visual observation of Jain et al. (1980) showed that bubbles eject in a direction normal to the flow. This means that a force balance should be considered in the lateral direction also.

The mechanisms of bubble detachment and ejection were not the cause of the NVG. This fact was confirmed by the results of high speed photography of the present work and Bibeau (1993). Also, Jain et al (1980) reported that the ONB point coincided with the point of bubble ejection from the heating surface.

2.3 Void Fraction Profile Models

Many studies have been carried out to predict the axial void fraction profile in forced convection subcooled flow boiling. In most of these studies, the subcooled boiling was divided into two regions. The first is the highly subcooled zone, in which the bubbles remain small and attach to the surface. It is, therefore, called the wall voidage region. In high pressure flow, this region is characterized by negligible void fraction. The second region is distinguished by significant increase in the void fraction.

The available models can be divided into two categories: profile fit models and mechanistic models. The profile fit models are fully empirical, while the mechanistic models satisfy some conservation laws and they use some empirical relations to close the problem. The second category of models tends to be based on one of two approaches as exemplified by the mixture flow model, particularly the drift flux model as developed by Zuber and Findlay (1965), or the two-fluid model. The mechanistic models can also be called generation-condensation models since they tend to account for both vapour generation and condensation simultaneously.

In a new approach, Lai and Farouk (1992) included turbulence effects in a two-dimensional two-fluid model. The $k-\epsilon$ method was used to model the turbulence. Changes in the radial direction were considered by solving conservation equations in the radial direction. Recently, Bibeau (1993)

introduced a bubble accounting model in which the void fraction was calculated by accounting for the bubble frequency and active nucleation density as introduced earlier by Serizawa (1979). In calculating the void fraction, Bibeau (1993) used the mean bubble size at the heating wall and ignored the convection effects, i.e, he considered only the void generated at the heating surface. Apparently this assumption may be valid only for the highly subcooled region.

2.3.1 Profile Fit Models

In this group of models, the void fraction profile is obtained by empirical correlations. Most of these models depend on the drift flux model of Zuber-Findlay (1965) where the relationship between the void fraction and the true flow quality was obtained from:

$$\alpha = \frac{x}{\rho_g} \left[C_o \left(\frac{x}{\rho_g} + \frac{1-x}{\rho_l} \right) + \frac{U_{gj}}{G} \right]^{-1} \quad (2.1)$$

and the vapour drift velocity was calculated from:

$$U_{gj} = C_{zf} \left[\frac{\sigma g (\rho_l - \rho_g)}{\rho_l^2} \right]^{1/4} \quad (2.2)$$

where C_o and C_{zf} are empirical constants.

In this group of models, the thermodynamic equilibrium quality profile along the boiling flow passage was calculated using a simple energy balance. The true flow quality, in terms of the thermodynamic quality, was obtained using empirical relationships. The axial void fraction profile was then calculated using Equations (2.1) and (2.2). The profile fit models are also listed in Table 2.5. The models used to predict the vapour phase velocity are also listed in this table.

The works of Zuber, Staub and Bijwaard (1966), and Kroeger and Zuber (1968) were finally revised by Saha and Zuber (1974). They assumed that the relation between the mass quality and the thermodynamic equilibrium quality could be predicted as follows:

$$x = \frac{x_{th} - x_d \exp\left(\frac{x_{th}}{x_d} - 1\right)}{1 - x_d \exp\left(\frac{x_{th}}{x_d} - 1\right)} \quad (2.3)$$

where x_{th} is thermodynamic quality, and x_d is thermodynamic quality at the NVG point. The above expression satisfies the following boundary conditions: at the NVG point, where $x_{th} = x_d$, the net amount of vapour generated is very small i.e. $x = 0$, and at the transition from subcooled boiling into bulk boiling ($x_{th} \gg x_d$) x approaches x_{th} . The void fraction profile was predicted from the drift flux model of Zuber-Findlay (1965) as given in Equation 2.1.

Dimmick and Selander (1990) introduced an empirical generation-conden-

sation profile model. The condensation term was modelled by:

$$\frac{da}{dz}|_c = -\lambda_s U_l a^{2/3} \quad (2.4)$$

where U_l is the liquid velocity and λ_s is an empirical coefficient. The evaporation rate was estimated by suppressing the evaporation rate of the bulk boiling as shown in the following equation:

$$\frac{da}{dz}|_g = \frac{4 q}{D_h h_{fg} \rho_g} f(T_s - T_l) \quad (2.5)$$

where $f(T_s - T_l)$ is a decreasing function which approaches unity at the beginning of the bulk boiling region. This function was expressed by:

$$f(T_s - T_l) = \exp\left(C_o \frac{x_{th}}{\sqrt{-x_d}}\right) \quad (2.6)$$

and C_o is an empirical constant. The net axial void fraction profile was determined from the difference between the vapour generation and the condensation rates.

2.3.2 Mechanistic Models

The conservation equations, the continuity and energy equations of the

two phases were solved simultaneously along the heated channel to calculate the flow quality or the void fraction directly. When the models were solved for the flow quality, the void fraction was calculated from the relation between the void fraction and the flow quality, mainly drift flux model of Zuber and Findlay (1965) and Equations (2.1) and (2.2) were used.

In evaluating various void profile models, special attention was given to the treatment of:

- a- Wall heat flux division.
- b- Vapour condensation rate.
- c- Vapour relative velocity.
- d- Bubble size and interfacial area concentration.

2.3.2.1 Wall Heat Flux Division

The heat removed from the surface is typically divided between the vapour and liquid phases. The first part is used to generate the vapour while the second is used to heat the subcooled liquid. The mechanisms involving the division of the wall heat flux in the slightly subcooled region are listed in Table 2.6. In an early attempt, Griffith et al. (1958) considered only the vapour component i.e. the total applied heat flux was used in evaporation while the liquid was heated only due to vapour condensation. Recently, Lai and Farouk (1992) considered only the liquid component, i.e the total wall heat flux is

absorbed by the liquid while evaporation occurs within the liquid superheated layer. Bowring (1962) assumed the liquid component to consist of single phase forced convection and pumping (agitation) components. The latter is caused by convection due to bubble nucleation and departing cycles. The single phase component was calculated based on the heat transfer coefficient of the single phase which was predicted by the Dittus-Boetler Correlation:

$$h_{sp} = 0.023 Re^{0.8} Pr^{0.4} k / D_h \quad (2.7)$$

where Re is the flow Reynolds number based on total mass flux G . The wall temperature was assumed to equal the saturation temperature. The major mechanism of energy transfer was, as assumed by Bowring (1962), the pumping action of departing bubbles as suggested by Forster and Greif (1959). The ratio between the pumping and the vapour components which is called the pumping factor ϵ , was empirically correlated. Bowring (1962) introduced the following relationship for the pumping factor:

$$\begin{aligned} \epsilon &= 3.2 \left[\frac{\rho_l C_p \theta_l}{\rho_g h_{fg}} \right] & \text{for } 1 \leq P \leq 9.5 \text{ atm} \\ &= 1.3 & \text{for } 9.5 \leq P \leq 50 \text{ atm} \end{aligned} \quad (2.8)$$

Rouhani and Axelsson (1970) neglected the single phase component based on the assumption that the heater surface was fully covered by bubbles and considered only the pumping component. Ahmad (1970) and Chatoorgoon

(1992) combined both of the liquid components of convection and pumping into one component. Ahmad (1970) used the heat transfer coefficient correlated at the NVG point to predict the liquid component. Chatoorgoon (1992) used an empirical expression for the fractional power that goes directly into vapour generation. This expression, which is exponential function of local subcooling, is based on the NVG point location, which Chatoorgoon et al. (1993) believed that extended the range of applicability to different geometries without the need for returning to the empirical model. Larsen and Tong (1969) and Hancox and Nicoll (1971) assumed the liquid component to be equal to the heat transfer at the edge of the bubble layer. Maroti (1977) assumed the vapour component to equal the energy stored in the superheated layer where the superheated layer thickness was estimated from the conduction equation at the heating surface. Lahey (1978) followed the division mechanism of Bowring (1962) and Dix (1970) but the single phase component was calculated from an expression which is linear with respect to local subcooling. Sekoguchi et al. (1980) estimated the vapour component from the deviation between the fully developed turbulent radial temperature profile for single phase and the measured radial temperature profile for flow boiling near the heating surface. Michel and Bartsch (1983) used a statistical method to estimate the vapour and the liquid components. High speed photography was used to observe the growing and the collapsing bubbles separately.

2.3.2. Vapour Condensation Rate

The high level of applied heat flux causes local boiling at the heating surface while the bulk is still subcooled. This leads to a thermal non-equilibrium process. The bubbles condense while they grow and leave the heating surface and move through the subcooled bulk. The net amount of vapour generation is determined by the difference between the vapour generation and vapour condensation rates. The condensation rate at the vapour-liquid interface is controlled by the temperature difference between the two phases, the interfacial area, the relative velocity between the two phases, and the interfacial condensation heat transfer coefficient. Many empirical models were developed to predict the vapour condensation rate in the subcooled flow boiling. These models are listed in Table 2.7, where q_c is the heat transfer rate due to condensation per unit length of the heating channel. All these models incorporated the interfacial area in the condensation coefficient except the models of Maroti (1977) and Chatoorgoon (1992). It should be mentioned that all these models employed empirical relationships for the vapour condensation rate to fit the axial void fraction profile while, Dix (1970), Lahey (1978) and Chatoorgoon (1992) used empirical relationships for bubble condensation coefficient to model the vapour condensation rate. Lai and Farouk (1992) considered the interfacial heat transfer coefficient on both the liquid and vapour sides. On the vapour side, the interfacial heat transfer coefficient was

approximated with a high value (10000 W/m^2) to drive the vapour to quickly reach the equilibrium state. However, this value of the vapour side heat transfer coefficient seems to be unreasonably high.

2.3.2.3 Vapour Phase Velocity

The vapour phase velocity, in subcooled flow boiling, is governed by the forces acting on the bubbles; buoyancy, drag, weight, inertia and surface tension. Many models were developed in order to predict the vapour phase velocity. There are three approaches. Wallis (1974) developed a model for the bubble terminal velocity in infinite medium, Zuber and Findlay (1965) and Dix (1970) developed models for the vapour drift velocity and many models were developed for the slip ratio, the ratio between the vapour and liquid velocities by Ahmad (1970) and Smith (1969-70). The models used to predict vapour velocity in the subcooled flow boiling are listed in Table 2.8.

2.3.2.4 Bubble Size and Interfacial Area Concentration

Due to the lack of experimental data, effects of bubble size and interfacial area concentration were neglected by many investigators who worked on modelling the axial void fraction profile in subcooled flow boiling. A

few who considered these parameters were Maroti (1977), Chatoorgoon (1992) and Lai and Farouk (1992). Maroti (1977) used Fritz's relationship to calculate bubble diameter. This relationship is independent of the effects of heat flux, mass flux, subcooling and void fraction. Chatoorgoon (1992) in his analysis found that a 2.5 mm bubble diameter was appropriate in the flow boiling region. Lai and Farouk (1992) used a bubble diameter of 10 mm in their numerical analysis of subcooled flow boiling. This value is thought to be very high for the subcooled flow boiling region.

2.3.3 Concluding Remarks

- All the models reviewed above were developed for high pressure flow, typical of power reactors, except the models of Chatoorgoon (1992) and Dimmick and Selander (1990) which were developed for low pressure flow. The models developed for high pressure flow do not predict the void fraction profile of low pressure flow accurately as reported by Evangelisti and Lupoli (1969).
- Despite the extensive effort to model the void fraction profile, there are significant disagreements concerning modelling wall heat flux division, vapour condensation rate and vapour velocity.
- There is a significant lack of experimental information concerning bubble size and interfacial area concentration in subcooled flow boiling.

Table 2.1 Experimental Investigations of High Pressure Flow:

Authors	Cross-Section	Pressure Range	Working Medium
Griffith et al. (1958)	Rectangular	500- 1500 psi	Water
Bowring (1962)	Tube, Annulus & Rectangular	1- 140 atm	Water
Thom et al. (1965-66)	Tube	750- 1500 psi	Water
Rouhani and Axelsson (1970)	Annulus	19- 50 bar	Water
Staub and Walmet (1970)	Tube & Rectangular	8- 69 bar 1.2- 3.3 bar	Water R22
Martin (1970)	Rectangular	80- 140 kg/cm ²	Water
Dix (1972)	Annulus	3.16- 8.48 bar	R114
Sekoguchi et al. (1974)	Tube	2.2-15.69 bar	Water
Jain et al. (1980)	Annulus	3.5- 41 bar	R113
Sekoguchi et al. (1980)	Tube	1- 140.6 ata	Water
Stangl and Mayinger (1990)	Annulus	12-25 bar	CCL ₂ F ₂

Table 2.2 Experimental Investigations of Low Pressure Flow:

Authors	Cross-Section	Pressure Range	Working Medium
Fristenberg and Neal (1960)	Tube	Atmospheric	Water
Evangelisti and Lupoli (1969)	Annulus	Atmospheric	Water
Staub and Walmet (1970)	Tube & Rectangular	1- 3 bar	Water
Sekoguchi et al (1974)	Tube	1.27- 1.96 bar	Water
Maitra and Subba Raju (1975)	Annulus	Atmospheric	Water
Edelman and Elias (1981)	Tube	Atmospheric	Water
Michel and Bartsch (1983)	Annulus	Atmospheric	Water
Rogers et al (1987)	Annulus	1.55 bar	Water
Dimmick and Selander (1990)	Tube	1.65 bar	Water
Toda and Hori (1989)	Tube	Atmospheric	Water
Donevski and Shoukri (1989)	Annulus	1- 2 bar	Water
Bibeau and Salcudean (1990)	Annulus	1.55 bar	Water
Bibeau (1993)	Annulus	1-3 bar	water

Table 2.3 Onset of Nucleate Boiling Models

Author	Condition at ONB
Bergles & Rohsenow (1964)	$q = 1120 \rho^{1.1166} (1.8 (T_w - T_s)_{ONB})^{2.16/P^{0.074}}$
Davis & Anderson (1966)	$q = \frac{k \rho_g h_{fg} (T_w - T_s)_{ONB}^2}{8 \sigma T_s}$
Ünal (1977)	$(T_s - T_l)_{ONB} = 0.665 \frac{q}{h_{sp}}$
Serizawa (1979)	$\frac{q}{G C_p (T_s - T_l)} = 0.0142 \left(\frac{\rho_g}{\rho_l} \right)^{0.1} \left[\frac{h_c D_h}{k} \frac{\sigma T_s (v_g - v_l) k}{h_{fg} q D_h^2} \right]^{0.29}$

Table 2.4 Net Vapour Generation Models

Author	Condition at NVG point
<u>- Thermal-Hydrodynamic based models:</u>	
Griffith et al. (1958)	$q = 5 h_{sp} (T_s - T_d)$
Ahmad (1970)	$h_s D_h / k = 2.44 (G D_h / \mu)^{0.5} (C_p \mu / k)^{1/3} (h_{in} / h_f)^{1/3} (h_{ig} / h_f)^{1/3}$ $q = h_s (T_s - T_d)$
Hancox & Nicoll (1971)	$h_{HN} = 0.4 Re^{0.662} Pr k / D_h$ $q = h_{HN} (T_s - T_d)$
Saha & Zuber (1974)	$q D_h / k (T_s - T_d) = 455$ for $Pe \leq 70000$ $q D_h / G C_p (T_s - T_d) = 0.0065$ for $Pe > 70000$
Ünal (1975)	$h_{sp} (T_s - T_d) / q = 0.24$ for $U_l \geq 0.45$ $= 0.11$ for $U_l \leq 0.45$
Yang & Weisman (1991)	$h_f - h_d = \frac{\sqrt{2} \pi q / G}{0.79 Re^{-0.1} (D_b / D_h)^{0.6}}$
<u>- Bubble detachment models:</u>	
Bowring (1962)	$T_s - T_d = q (14 + 0.1 P) / U_l$ units in: °C, W/cm ² , atm and cm/s
Levy (1967)	$T_s - T_d = q / h_{sp} - T_b^* q / (\rho_f C_p \sqrt{T_w} \bar{\rho}_l)$ where: $Y_b^* = C(\sigma D_h \rho_l)^{1/2} / \mu$ $T_b^* = Pr Y_b^*$ $Y_b^* \leq 5$ $= 5 [Pr + \ln(1 + Pr(Y_b^* / 5 - 1))]$ $5 \leq Y_b^* \leq 30$ $= 5 [Pr + \ln(1 + 5 Pr) + 0.5 \ln(Y_b^* / 30)]$ $Y_b^* \geq 30$
Rogers et al. (1987)	$T_s - T_d = q / (F_R h_{sp}) - T_b^* q / (\rho_f C_p \sqrt{T_w} \bar{\rho}_l)$ where: T_b^* calculated as in Levy (1967) at $Y_b^* = r_{bd} \rho_l \sqrt{T_w} \bar{\rho}_l (1 + \cos \theta_o) / \mu$ $r_{bd} = 0.75 C_2 C_d u_r^2 / (\pi C_1 g) \left[1 + \frac{8 \pi^2 C_1 C_3 C_s g \sigma}{3 C_2^2 C_d^2 \rho_l u_r^4} \right]^{1/2} - 1$ u_r is liquid velocity calculate at $Y_b^* / 2$ from turbulent universal velocity profile
<u>- Bubble ejection models:</u>	
Dix (1970)	$T_s - T_d = 0.00135 q Re^{1/2} / h_{sp}$
Serizawa (1979)	$T_s - T_d = (3 K_1 (T_s - T_l)_{ONB} + 1 + n \sqrt{D^*}) / (6 K_1)$ where K_1 , n and D^* are empirical functions of G , q , D_h and fluid properties

Table 2.5 Profile Fit Models:

Authors	Vapour Phase Velocity
Thom et al (1965)	$S = 10$
Saha and Zuber (1974)	Drift Flux Model, Zuber-Findlay (1965)
Levy (1967)	Drift Flux Model, Zuber-Findlay (1965)
Yamazaki and Yamaguchi (1976)	$k_y = (U_g - U_l)/J_g$ where: $k_y = 1$ for $E_o \lambda \geq 2 \cdot 10^{-6}$ $k_y = 0.57$ for $E_o \lambda < 2 \cdot 10^{-6}$ where E_o is Eotvas number and $\lambda = We/Re$
Dimmick and Selander (1990)	$S = 1$

Table 2.6 Heat Flux Division Models:

Authors:	Wall Heat Flux Division Mechanisms
Griffith et al. (1958)	$q_v = q$
Bowring (1962)	$q_l = q_{sp} + q_p = h_{sp} \theta_l + \epsilon q_v$ $\epsilon = 3.2 \rho_l C_p \theta_l / (\rho_g h_{fg}) \quad \text{for } 1 \leq P \leq 9.5 \text{ atm}$ $\epsilon = 1.3 \quad \text{for } 9.5 \leq P \leq 50 \text{ atm}$
Rouhani and Axelsson (1970)	$q_l = q_p = \epsilon q_v = \frac{\rho_l C_p \theta_l}{\rho_g h_{fg}} q_v$
Larsen and Tong (1969)	$q_l = \rho_l C_p \tau_{be} / (\rho_l Pr_l) (T_s - T_c) / (u_c - u_{be})$ <p>where τ_{be} and u_{be} are shear stress and liquid velocity at bubbly layer edge and u_c and T_c are liquid velocity and Temperature at tube center line</p>
Ahmad (1970)	$q_l = q_{sp} = h_a \theta_l$ <p>h_a is defined in Table 2.4</p>
Dix (1970)	as Bowring (1962)
Hancox and Nicoll (1971)	$q_l = h_{HN} \theta_l$ <p>h_{HN} is defined in Table 2.4</p>
Maroti (1977)	$q_v = q (T_w - T_s)^2 / (T_w - T_l)^2$
Lahey (1978)	$q_l = q_{sp} + q_p = q (h_f - h_l) / (h_f - h_d) + \epsilon q_v$ $\epsilon = \rho_l C_p \theta_l / (\rho_g h_{fg})$
Sekoguchi et al. (1980)	q_v was calculated from the deviation between temperature profile of fully developed single phase turbulent flow and measured values.
Michel and Bartsch (1983)	Statistical method was used to count the growing and collapsing bubbles.
Chatoorgoon (1992)	$q_v = q (1 - \exp(-A_{ch} (h_l - h_d) / (h_l - h_f))) + q_{v_{avg}}$ <p>where A_{ch} is an empirical constant</p>
Lai and Farouk (1992)	$q_l = q$

Table 2.7 Vapour Condensation Models:

Authors:	Condensation Rate:
Griffith et al. (1958)	$q_c = 5 h_{sp} P_h \theta_l$
Bowring (1962)	$q_c = 0$
Rouhani and Axelsson (1970)	$q_c = k_c \theta_l$ $k_c = 30 (k/Pr) (\rho_g/\rho_l)^2 (A \alpha)^{2/3} Re (h_{fg} \Delta \rho \sigma/q \mu)$ <i>where k_c in $W/m \text{ } ^\circ C$</i>
Larsen and Tong (1969)	$q_c = 0$
Ahmad (1970)	$q_c = k_s h_{fg} \sqrt{z} \theta_l \quad Btu/ft \text{ } hr$ $k_s = 2.79 C B_k r_{bd} P_h q^2 / \sqrt{GS}$ <i>where: C is an empirical constant</i> $B_k = 71 \text{ } lb^{3/2} / ft^{5/2} \text{ } hr^{3/2} \text{ } ^\circ f$
Dix (1970)	$q_c = k_v \alpha^{1.15} \theta_l \quad Btu/hr \text{ } ft$ $k_v = 17800 \text{ } Btu/hr \text{ } ft^\circ f \quad \text{for low flow rates}$ $k_v = 7750 \text{ } Btu/hr \text{ } ft^\circ f \quad \text{for high flow rates}$
Hancox and Nicoll (1971)	$q_c = 0$
Maroti (1977)	$q_c = q (3 \alpha A/R_b) (T_s - T_l)^2 / ((T_w - T_l)^2 - (T_w - T_s)^2)$ $R_b = 0.4 (\sigma/g (\rho_l - \rho_g))^{1/2}$
Lahey (1978)	$q_c = 0.075 h_{fg} A \alpha \theta_l / v_{fg}$
Sekoguchi et al. (1980)	$q_c = 0$
Michel and Bartsch (1983)	Statistical method
Chatoorgoon (1992)	$h_c = 0.37 Re_b^{0.6} Pr^{1/3} k/D_b \quad \text{Akiyama (1973)}$ $q_c = 6 h_c \theta_l \alpha A/D_b$

Table 2.8 Vapour Velocity Models:

Authors:	Vapour Velocity or Slip Ratio Models
Griffith et al. (1958)	$S = 1$
Bowring (1962)	S was obtained experimentally
Rouhani and Axelsson (1970)	Zuber and Findlay (1965)
Larsen and Tong (1969)	$S = 1$
Ahmad (1970)	$S = (\rho_l / \rho_g)^{0.206} Re^{-0.016}$
Dix (1970)	$U_g = C_o J + U_{gi}$ $C_o = \beta \left(1 + (1/\beta - 1)^b \right) \quad \text{where} \quad b = (\rho_g / \rho_l)^{0.1}$
Hancox and Nicoll (1971)	$S = 1$
Maroti (1977)	from Zuber and Findlay (1965)
Lahey (1978)	from Dix (1970)
	from Smith's (1969-70):
Sekoguchi et al. (1980)	$S = K_1 + (1 - K_1) \left[\frac{1 + K_1 (1/\alpha - 1)}{\rho_g / \rho_l + K_1 (1/\alpha - 1)} \right]^{1/2}$
	where k_1 is the ratio between liquid flow rate in the bubble layer to total liquid flow rate.
Michel and Bartsch (1983)	$S = 1.3$
	from Wallis (1974):
	$U_b = (1 - \alpha) U_\infty$
	where:
Chatoorgoon (1992)	$U_\infty = U^* (\rho_l^2 / (\mu g (\rho_l - \rho_g)))^{-1/3}$ $U^* = r^* / 3 \quad r^* < 1.5$ $U^* = r^{*1/2} \quad r^* > 1.5$ $r^* = R_b (\rho_l g (\rho_l - \rho_g) / \mu^2)^{1/3}$

CHAPTER 3

EXPERIMENTAL FACILITIES AND PROCEDURE

3.1 Test Loop

A schematic of the test loop is presented in Figure 3.1. The low pressure circulating loop consists mainly of a 20 litre holding tank, in which the water temperature is controlled by an immersed electric heater and an immersed cooling coil, a circulating pump, a preheater and the test section. Degassed distilled water from the holding tank is pumped through a rotameter and a preheater to the bottom of the vertically mounted annular test section. The test section contains a heated section, where vapour bubbles are formed, followed by an unheated section, where the vapour bubbles are condensed. The single-phase water at the test section outlet is pumped back to the holding tank where its temperature is regulated using the cooling coil and tank heater. The power of the tank heater and preheater could be regulated using Variacs (20 kVA). The system pressure and flow rate were controlled by two valves, located downstream of the test section and the circulating pump.

3.2 Test Section

The test section is a vertical concentric annular test section. The inner tube consists of three sections, as shown in Figure 3.2. The middle section of the inner tube is a 12.7 mm outside diameter by 30.6 cm long, thin-walled stainless-steel tube (0.25 mm thickness) which is electrically heated. This heated section is preceded and followed by 34 cm long, by 50 cm long, thick-walled copper tubes (0.7 mm thickness) respectively. The entire inner tube assembly was connected to a 55 kW DC power supply. Up to 600 amp was applied. Accordingly, heat was generated uniformly in the middle section of the inner tube. The outer tube is a 25.4 mm inner diameter plexiglass tube that permits visual observation. The flow that enters the annulus develops through the first unheated section of the annular test section. Voids, which are generated in the heated section, collapse in the unheated section that follows it. This arrangement was found to be convenient for examining both vapour generation and condensation separately. In the unheated section, down stream of the heated section, bubble condensation was a primary factor in controlling the void fraction, while in the heated section, both bubble generation and condensation existed simultaneously. By means of the arrangement described herein, it was possible to study bubble size and condensation in the unheated region and bubble behaviour, the mechanism of net vapour generation and bubble size in the subcooled flow boiling region. A square cross section

plexiglass shield was put around the outer tube and filled with water during the photography to reduce light reflection and refraction. It was found that by using the filled square cross section shield that test section lighting improved significantly. Reducing the light refraction leads to the appearance of bubbles of the right size compared to the reference, which is another major advantage. Any small change in the inlet temperature to the tested region, due to transfer of heat to the water in the shield, was compensated for by readjusting the preheater.

3.3 Measurements and Instrumentation

The measurements carried out during the present experiments included measurements of the test section inlet and exit fluid temperatures, the subcooling temperature distribution along both the heated and unheated regions, the flow rate, the pressure at the test section inlet as well as the area-averaged axial void fraction distribution along the test section. High speed photography and image processing techniques were used to obtain and analyze visual data concerning the local bubble size in the boiling and condensing regions. The flow rate was measured using a calibrated rotameter, which had an estimated error of $\pm 2\%$. The range of the rotameter is 0.04-0.24 litre/s. The maximum expected mass flux in the loop was $523 \text{ kg/m}^2 \text{ s}$ for single phase flow (water). The inlet pressure to the test section was measured using a

Bourdon gauge with 0.1 psi resolution. The heat flux was calculated from the measured electric current through the heater and the voltage drop across it. The calibration of the voltmeter showed that the uncertainty in the voltage drop measurements was within $\pm 1\%$. The resolution of the measurements is 10 ampere for the current and 0.5 for the voltage drop. Uncertainties in the measurements are reported in Appendix B.

3.3.1 Temperature

The test section inlet and exit temperature, as well as the preheater inlet temperature, were measured using calibrated platinum resistance temperature detectors. The subcooling along the test section was measured using 32 gauge calibrated J type thermocouples. The resolution of the temperature measurements was 0.1 °C. Both of the platinum resistance detectors and the thermocouples were calibrated at 0 and 100 °C within ± 0.2 °C. The locations of these thermocouples are shown in Figure 3.3. The temperature of the inner heating surface was measured using a spring-loaded sliding thermocouple. The design and assembly of it is shown in Figure 3.4. This arrangement was found useful for measuring the inner heating surface temperature along the heater. These measurements were conducted at 2 cm intervals along the heating section. A heat balance was conducted across the test section to examine the accuracy of the heat flux calculation. The results showed that the heat flux

calculated from the heat balance across the test section was less than 5% lower than the value calculated from measuring the electrical current and voltage drop across the heater. The details of this heat balance calculations are found in Appendix A.

3.3.2 Void Fraction

A single beam gamma densitometer was used for void fraction measurements. It consisted of a 75 mCi Cobalt-57 sealed line source and a cubic NaI (TI) scintillator. The densitometer was operated in the count mode. The design of this system was reported in Ballyk (1986). The main components of the system are shown in Figure 3.5. The main signal processing components were similar to those reported by Chan and Banerjee (1981). The gamma beam from the line source was collimated as a thin beam wide enough to cover the entire cross section for area-averaged measurements. The gamma source and the scintillator were mounted on a vertical traversing table to obtain the axial void fraction distributions.

For the present gamma densitometer design, the sensitivity to water content was about 20%. The sensitivity to water content is defined by:

$$S_I = \frac{N_1 - N_0}{(N_1 + N_0)/2} \quad (3.1)$$

where N_1 and N_0 are the counts for the empty and liquid filled test section respectively. The statistical error, defined by:

$$\varepsilon = \frac{1}{S_i \sqrt{N}} \quad (3.2)$$

was reduced by counting for a relatively long time. The corresponding statistical error was estimated to be in the range 1-2%. For counts N_e corresponding to a void fraction α , the void fraction was calculated from:

$$\alpha = \frac{\ln(N_e/N_0)}{\ln(N_1/N_0)} \quad (3.3)$$

The system was statically calibrated. The static calibration tests showed that, for the range $0.02 < \alpha < 0.3$, the errors were in the range of $\pm 4\%$ of the actual void fraction, as shown in Figure 3.6. The static calibration was conducted by means of a test section similar to the actual test section which included an inner metallic tube, 25.4 mm ID plexiglass tube and a square plexiglass shield. The liquid phase was simulated by a lucite plug, in which the voids were generated by drilling holes into the plug.

3.3.3 High Speed Photography

A high speed video system, Kodak Ektapro EM Motion Analyzer, which

can run up to 1000 frame/s and has 200x190 pixel resolution was used to visualize the flow. In the condensing region, the bubbles were visualized in two orthogonal directions simultaneously. Three prism mirrors enabled the same camera to obtain two orthogonal images. This procedure was used because of the large bubble size and their deviation from the spherical shape in this region. The high speed photography system components and their arrangement are shown in Figure 3.7a. The metal inner tube was used as a reference for calibrating the screen in this arrangement. In the boiling region, two methods were used to visualize bubbles. In the first, the camera was focused on the annular gap between the heater and outer plexiglass tube to investigate bubble detachment and lift off from the heating surface. In the second method, the camera was focused on the heater surface in order to investigate bubble interaction. The camera and the light setting are shown in Figure 3.7b. A one millimetre tube reference was put in the field of the view to calibrate the monitor screen in the first method. In the second method, the heater itself was used as the reference. Two light sources were used. A fibreoptic illuminator (150 W) with two branches, each having a lens to focus the light, was used to illuminate the test section from the back. A video light (150 W) was used to illuminate the test section from the side or front. Sand blasted glass plates were used as light filters between the back light sources and the object. The camera, the mirrors and the light were mounted on the vertical traversing table to visualize the flow at various locations along the test section. The high speed

video camera was equipped with a Macro-Takumar 1:4/50 mm lens. By these arrangements, it was possible to focus on area of 25×28 mm and 14×12 mm for condensing and boiling section respectively. The recorded frames in the memory of the high speed processor (the capacity of the processor is 400 frames) were recorded on a video tape. About 800 frames were stored for each axial location.

3.3.5 Digital Image Processing

The stored images on the video tape were transmitted, using a VCR, to a frame grabber installed in a host personal computer. The frame grabber was a Data Translation DT-2803 single board microprocessor-based system providing 6-bit digitization of the RS-170 monochrome signal. The resolution of the frame grabber is 240×256 pixel. The frame grabber output was displayed on a video monitor. A Logitech Logimouse was interfaced with the computer to facilitate the fast and accurate curser movement needed to identify the required coordinates. The main components of the system are shown in Figure 3.8. A bubble tracking and measuring system, which was developed by Mosher (1989), was modified to measure the size of various bubbles in the two images. The scale used in the heated and unheated region were usually 0.08 and 0.15 mm/pixel respectively. Considering that the curser movement resolution is 3 times finer than the grabber resolution, the length measurement from the

monitor screen should be accurate within ± 0.04 mm for the boiling region and ± 0.1 mm for the condensing region.

3.4 Experimental Procedure

The following steps were carried out in collecting the data:

- 1- The loop was filled with distilled water. The distilled water was changed regularly every week during the period in which the data were collected. The water was degassed by heating it for about two hours.
- 2- Zero and hundred percent void fractions were calibrated at one or two centimetre steps along the test section. For zero void fraction, the counts N_0 was obtained for the test section filled with water while for hundred percent void fraction, the counts N_1 was obtained for the empty test section.
- 3- The pump was turned on and the mass flux was set to the desired value.
- 4- The heating was started, the heat flux was adjusted and the inlet subcooling was established by regulating the preheater and cooling water.
- 5- The system was allowed to operate for one to two hours to reach steady state.
- 6- After reaching the steady state, the measurements were started and the mass flux, current, voltage drop, inlet pressure and water temperature were checked about four times during the test.
- 7- The area-averaged void fraction along the test section was measured, it was

measured at one or two centimetre intervals along the test section.

8- The heating surface temperature was measured at two centimetre interval along the heater.

9- The square shield was filled with water. Any small change in the inlet temperature to the tested region due to the transfer of heat was compensated for by readjusting the preheater. Then the lights and high speed video camera were turned on and visual information was collected at various locations along the test section.

3.5 Test Conditions and Measurement Sample

Three sets of experiments were conducted. The first set included 19 tests. The conditions investigated in this set are presented in Table 3.1. These experiments were carried out to generate data including void fraction profiles along both the heated and unheated regions. In this set of tests, the measurements were conducted in both the heated and unheated regions. The measurements included void fraction and subcooling profiles along both the boiling and condensing region and heating surface temperature along the heater. Samples of the measured values are shown in Figure 3.9-3.11. The objective of this set of tests was to generate experimental data in both of the subcooled flow boiling and the condensing regions. More discussions of these results are presented in Chapters 4 and 5.

The second set of experiments was carried out in the unheated region i.e, the subcooled water-steam condensing flow region downstream of the heater. The conditions of these tests are shown in Table 3.2. Besides measuring axial void fraction profiles in this region, the high speed video camera was used to visualize the condensing flow from two orthogonal directions. A typical bubble photograph is shown in Figure 3.12. The right half of the shown frame was focused on the inner copper tube which was considered as the reference. In the left half of the frame, the annular gap is shown. Also, information on the speed of the camera, exposure time, frame numbers and identification number of the shot are also shown on the photograph. The objectives of this experiment set were the investigation of interfacial phenomena in subcooled water-steam condensing bubbly flow. The analysis of these results are presented in Chapter 4.

The third set of experiments was carried out in the subcooled flow boiling region. The condition of these tests are listed in Table 3.3. Axial void fraction, water subcooling, and heating surface temperature profiles were measured along the heated section. The high speed video camera was used to visualize the flow. These tests were conducted to examine the bubble size, bubble behaviour and physical mechanisms of the net vapour generation phenomenon. Figures 3.13a and 3.13b show typical photographs in the boiling region. As mentioned earlier, two procedures were followed to collect the visual information in the boiling region. The photograph shown in Figure 3.13a was

used to investigate how the bubble nucleates, slides and moves out from the heated surface. In this photograph, the heater edge is shown at the right side of the frame while the transparent tube wall and the one millimetre tube reference are shown at the left. The photograph shown in Figure 3.13b was used to investigate bubble interference along the heating section, before and after the net vapour generation point. It was also used to measure the mean bubble size. As shown in the figure, the camera was focused on the heater surface and the heater itself was considered the reference to calibrate the screen of the monitor. Detailed analysis of these results will follow in Chapter 5.

Table 3.1 Test Conditions for Set Number 1

[illegible]

Table 3.2 Test Conditions of Set Number 2

Run No.	G kg/m ² s	q kW/m ²	P bar	Ts °C	θ_{in} °C	θ_3 °C	θ_4 °C	θ_{out} °C	Inlet void fraction
C1	205.5	372.8	1.096	102.5	16.2	4.8	4.42	3.5	0.3
C2	327.4	523.6	1.35	108.4	17.2	7.5	7.3	6.1	0.3
C3	205.5	366.3	1.096	102.5	18.2	6.3	6.1	5.7	0.25
C4	327.4	521.2	1.28	107	19.8	9.8	8.9	8.7	0.18
C5	413.9	622.4	1.618	113.9	19.3	10.7	9.3	10	0.32
C6	492.39	725	1.7	115.4	23.4	13.4	13.2	13.2	0.28
C7	506.24	1039.4	1.8	117.1	32.85	18.8	18.7	18.1	0.38
C8	139.03	251.8	1.03	100.6	14.6	2.6	2.4	2.5	0.28

θ_{in} : Water subcooling at the inlet to the test section

θ_3 : Water subcooling at the inlet to the unheated section (end of heating section)

θ_4 : Water subcooling at 10 cm in the unheated section (measured from the end of the heating section)

θ_{out} : Water subcooling the outlet of the test section

Table 3.3 Test Conditions for Set Number 3

Run No.	q kW/m ²	G kg/m ² s	P bar	T _s °C	θ_{in} °C	θ_1 °C	θ_2 °C	θ_3 °C	θ_4 °C	θ_{out} °C	T _{wa} °C
B1	286.68	156.15	1.37	108.9	14.9	15.3	10.3	3.1	2.1	2.1	133.4
B2	286.5	258.16	1.22	105.5	11.6	11.9	8.2	4.3	3.6	3.6	130.6
B3	487.88	252.78	1.17	103.1	16.6	16.8	10.5	4.7	2.8	2.6	131.2
B4	478.44	152.5	1.19	104.7	24.7	25	14.1	4.3	2.8	2.7	132.5
B5	503.0	264.34	1.5	111.6	16.8	17.5	11.5	5.7	4.9	4.7	137.3
B6	496.5	151.4	1.56	112.5	21.7	22.5	11.8	1.2	0.8	0.8	139.3
B7	705.5	411.7	1.5	111.6	22.5	23.3	18.1	13.1	12.3	10.3	138.6
B8	596.0	263.8	1.2	104.8	20.1	21.1	13.8	6.5	5.0	4.3	133.1
B9	593.2	152.6	1.22	105	31.1	31.2	21.7	4.6	3.1	1.8	133.5
B10	603.24	403.0	1.68	115	19.1	19	14.0	11.3	10.7	9.1	141.3

where:

θ_{in} water subcooling at the test section inlet.

θ_1 water subcooling at the heating section inlet.

θ_2 water subcooling at the middle of the heating section.

θ_3 water subcooling at the end of the heating section.

θ_4 water subcooling at 10 cm (measured from the end of the heating section) in the unheated section.

θ_{out} water subcooling at the test section outlet.

T_{wa} Average inner heating surface temperature (along heating section)

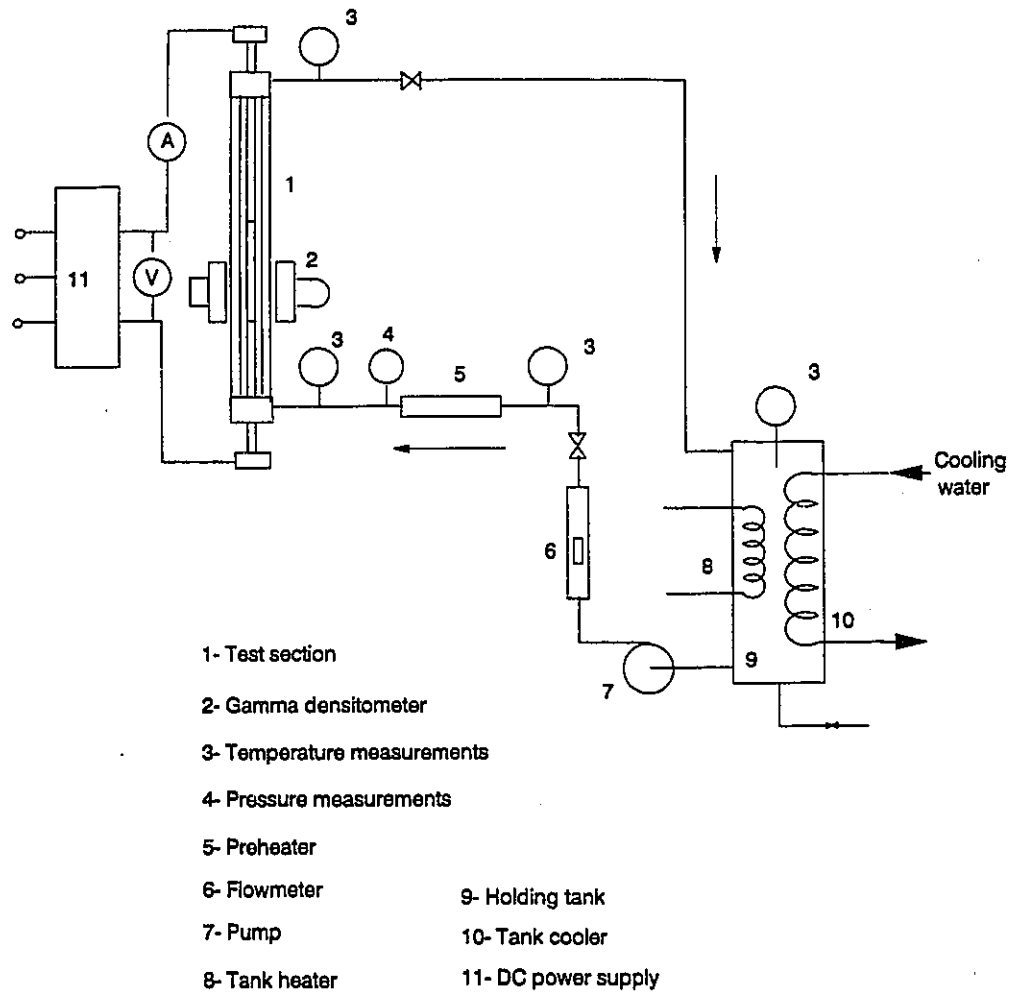


Figure 3.1 Test loop

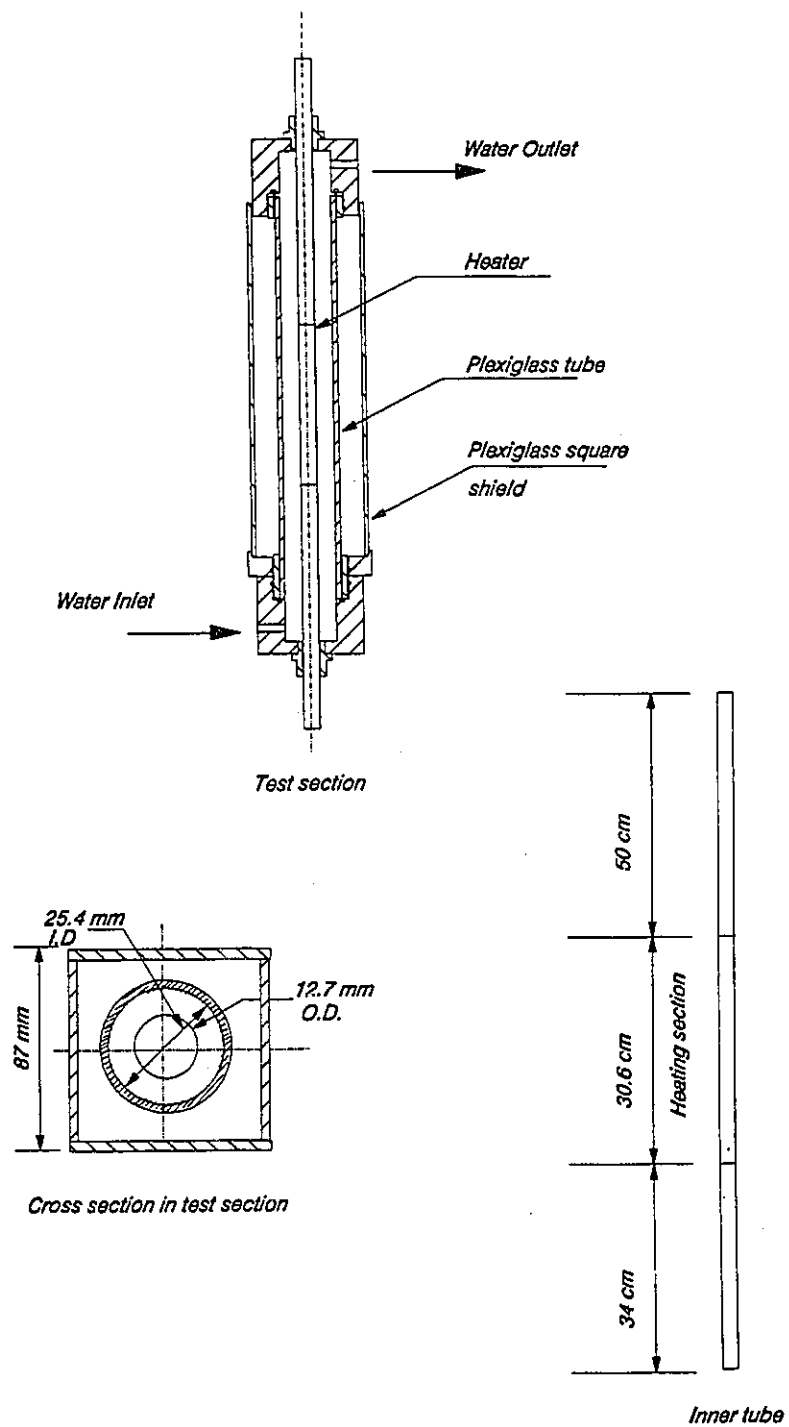


Figure 3.2 Test section

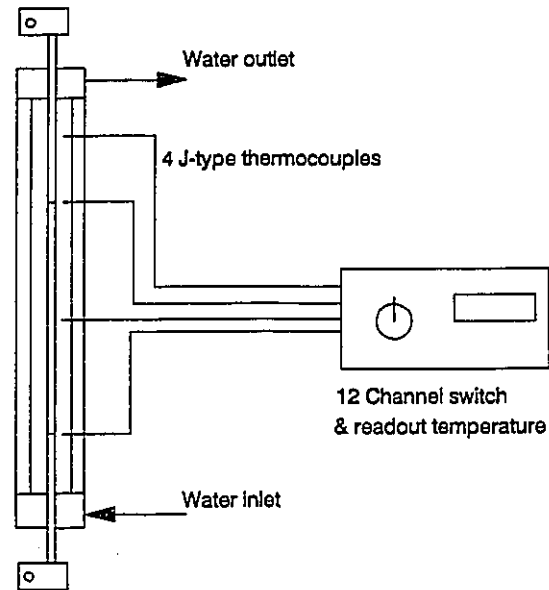


Figure 3.3 Subcooling measurements along test section

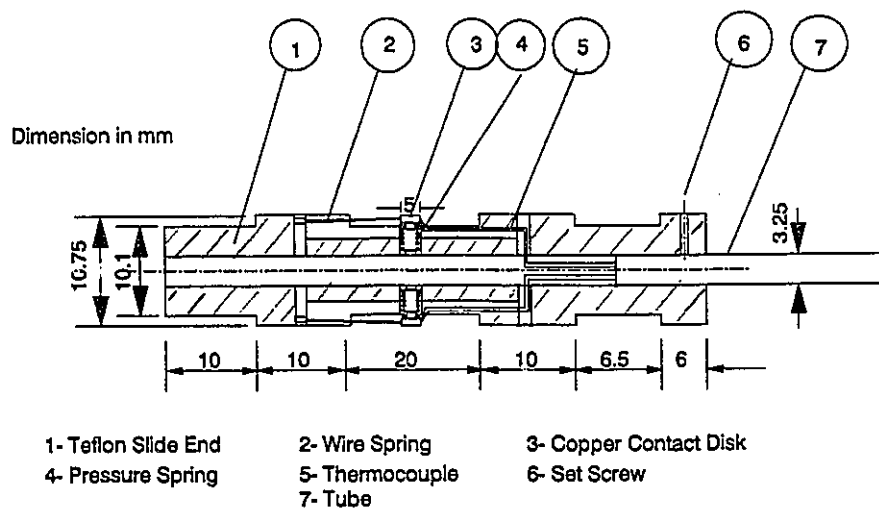


Figure 3.4 Sliding thermocouples

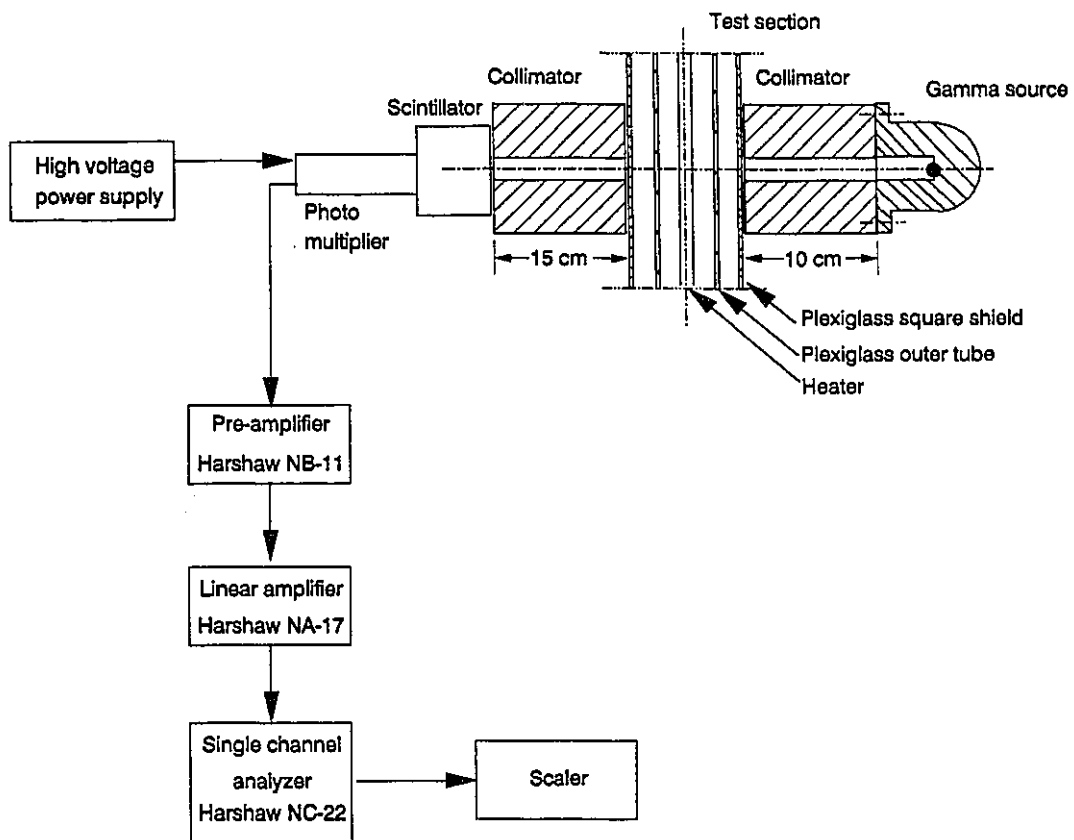


Figure 3.5 Gamma densitometer signal processing system

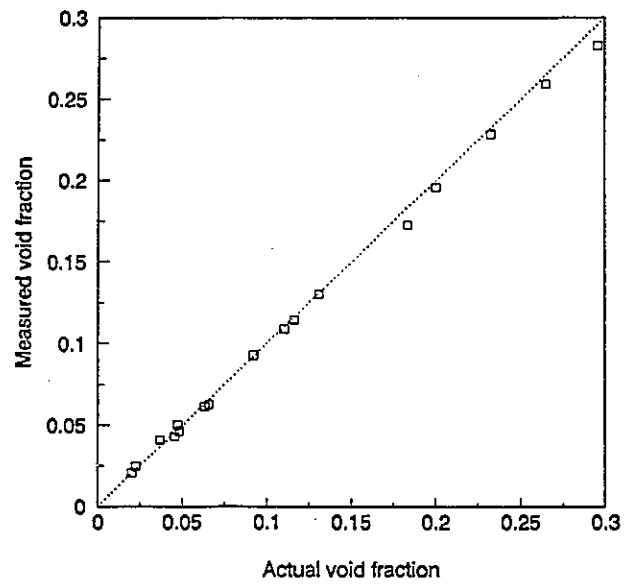
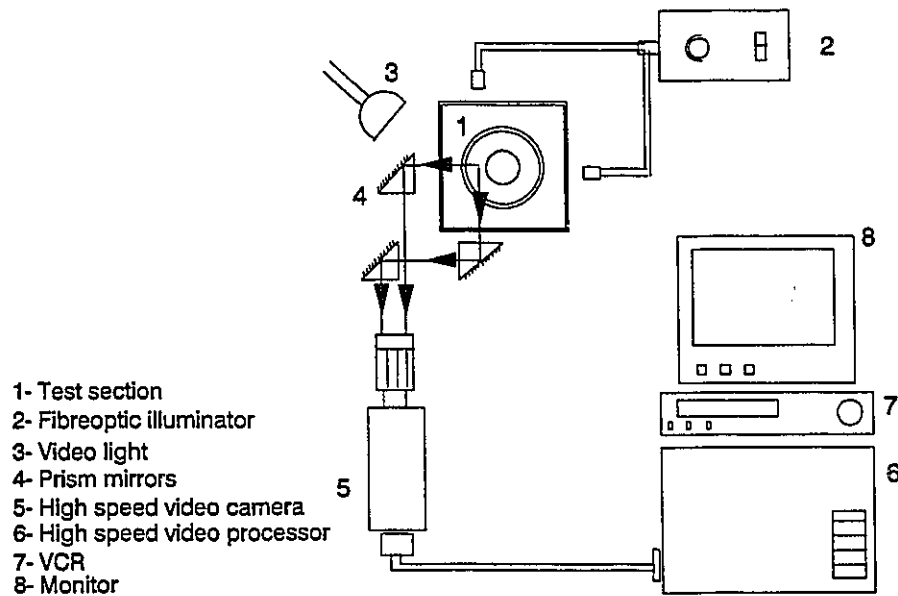
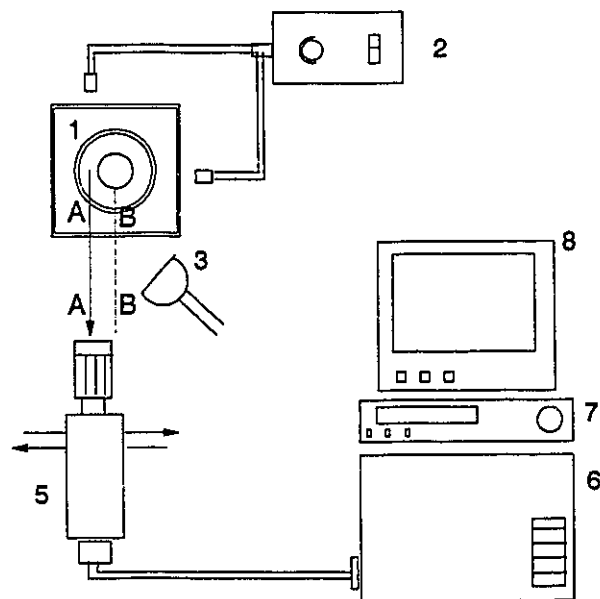


Figure 3.6 Gamma densitometer static calibration



a- The setting used in to visualize the bubbles in the condensing region



b- The setting used to visualize the bubbles in the boiling region

Figure 3.7 Components of the high speed photography system

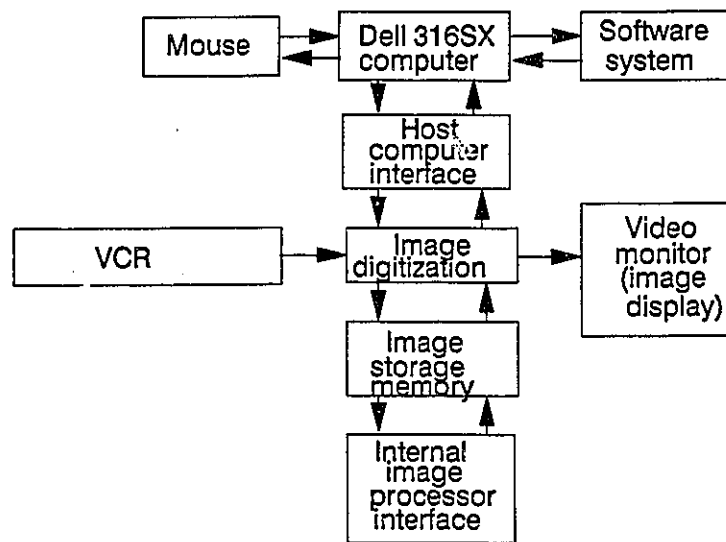


Figure 3.8 Digital image processing system

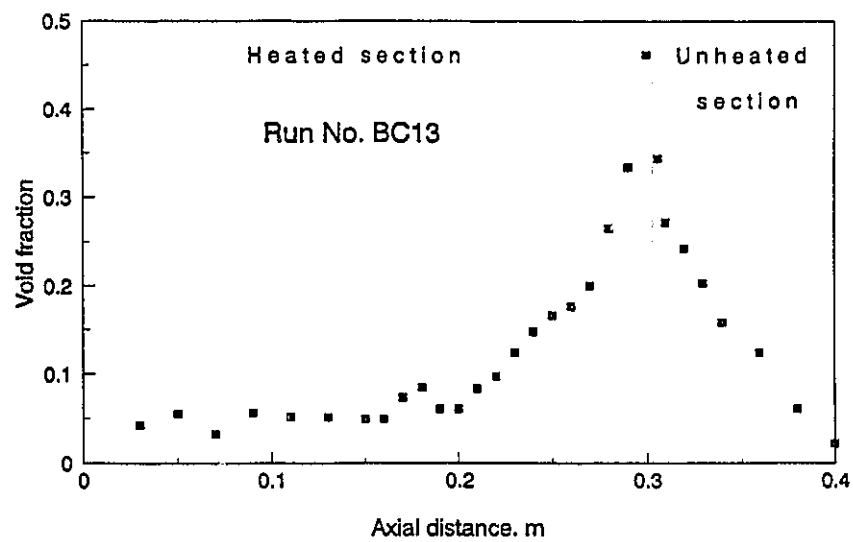
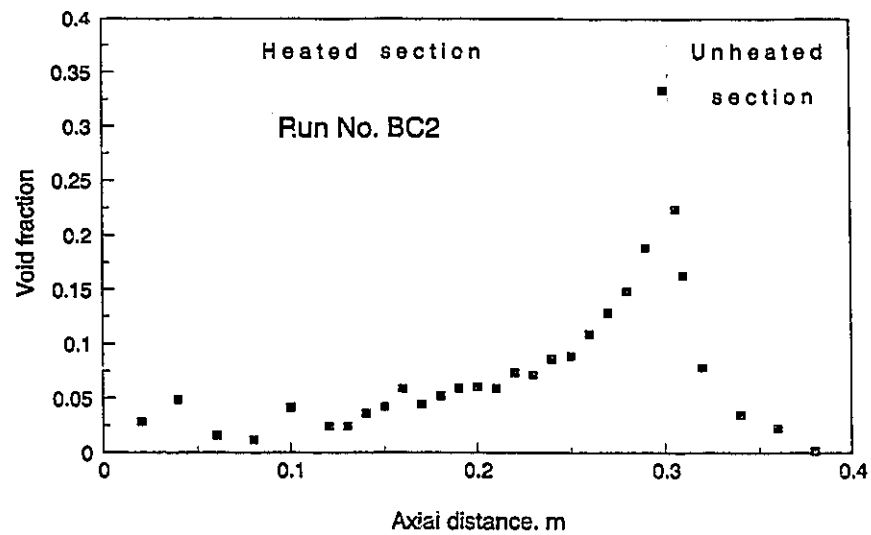


Figure 3.9 Typical void fraction profiles along the heated and unheated regions

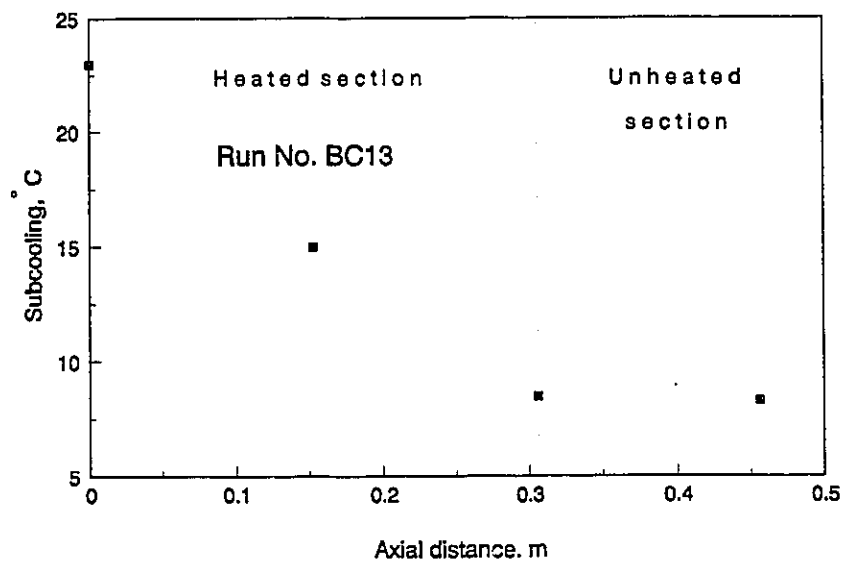
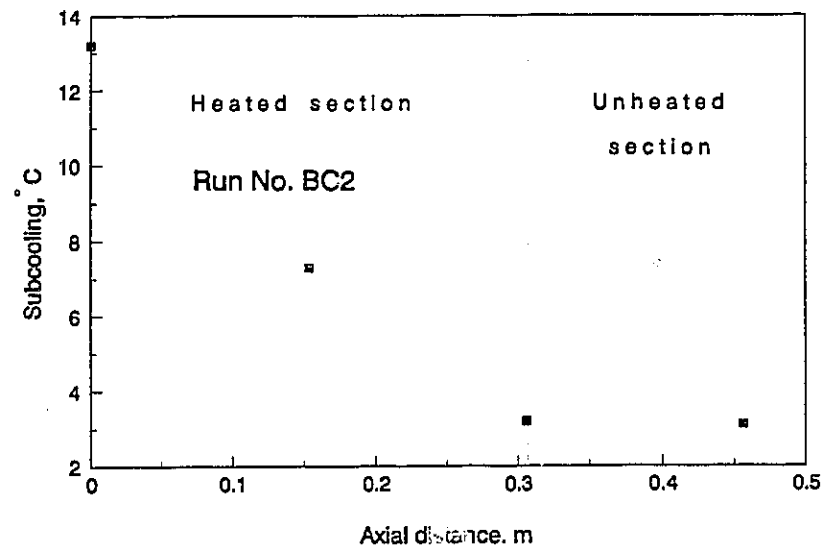
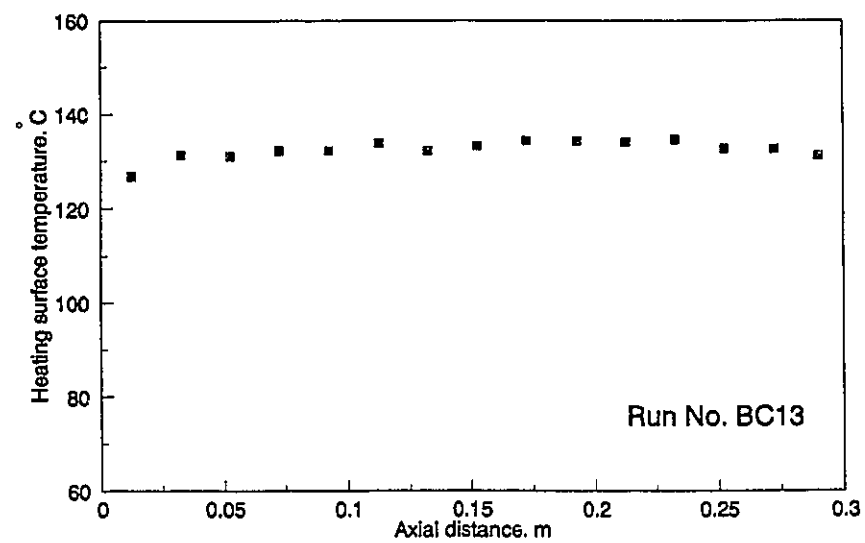
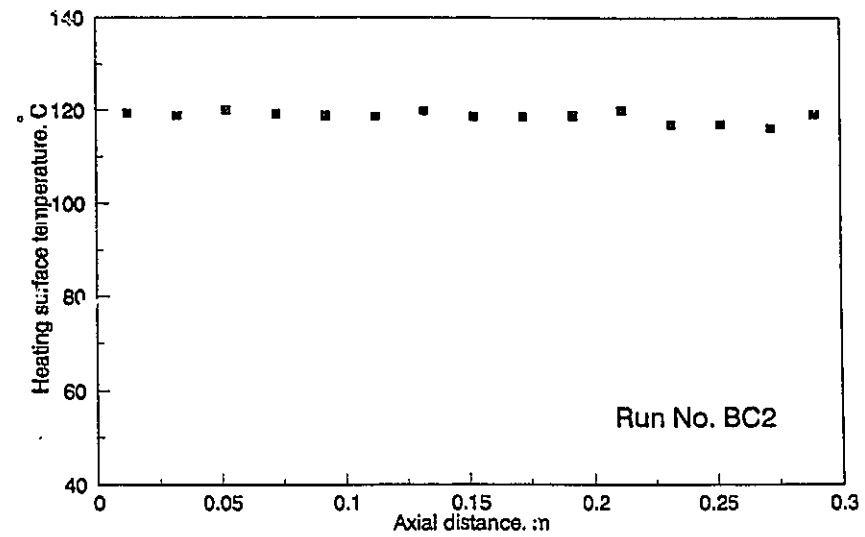


Figure 3.10 Typical liquid subcooling along test section



**Figure 3.11 Typical inner heating surface temperature profiles
along heating section**

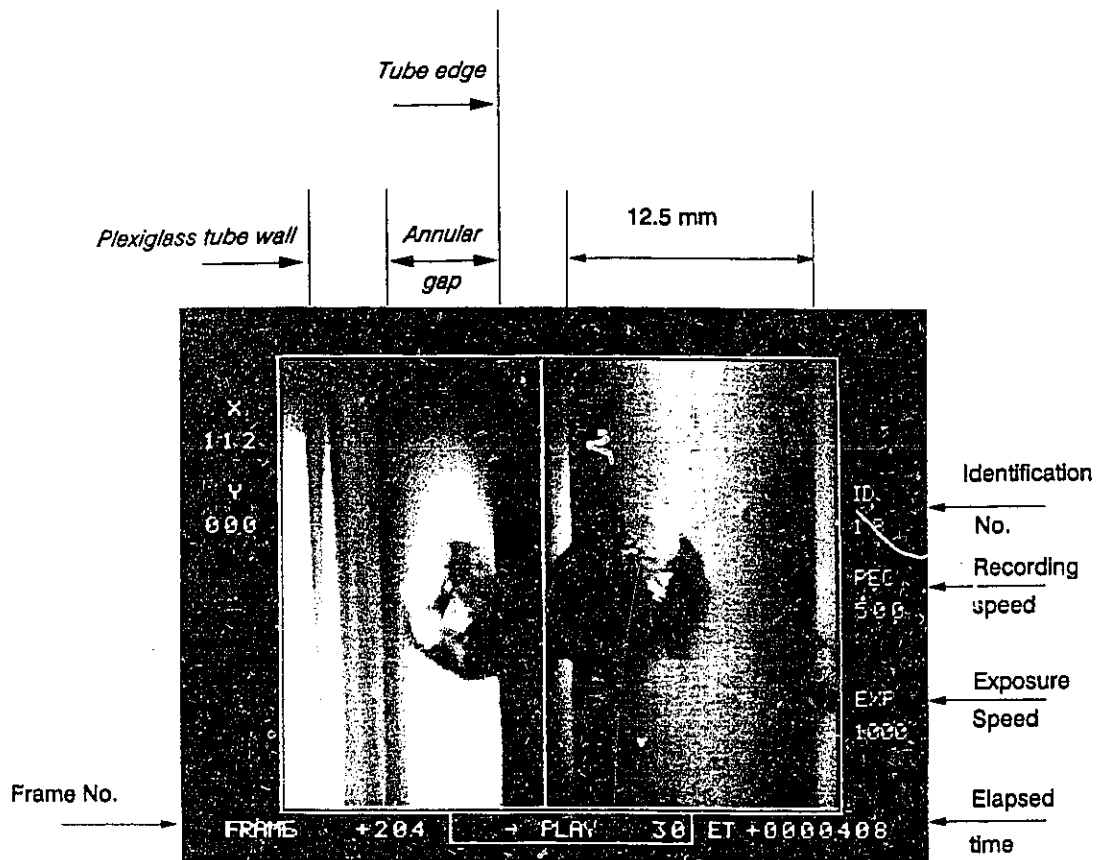


Figure 3.12 A typical photograph shot in the condensing region

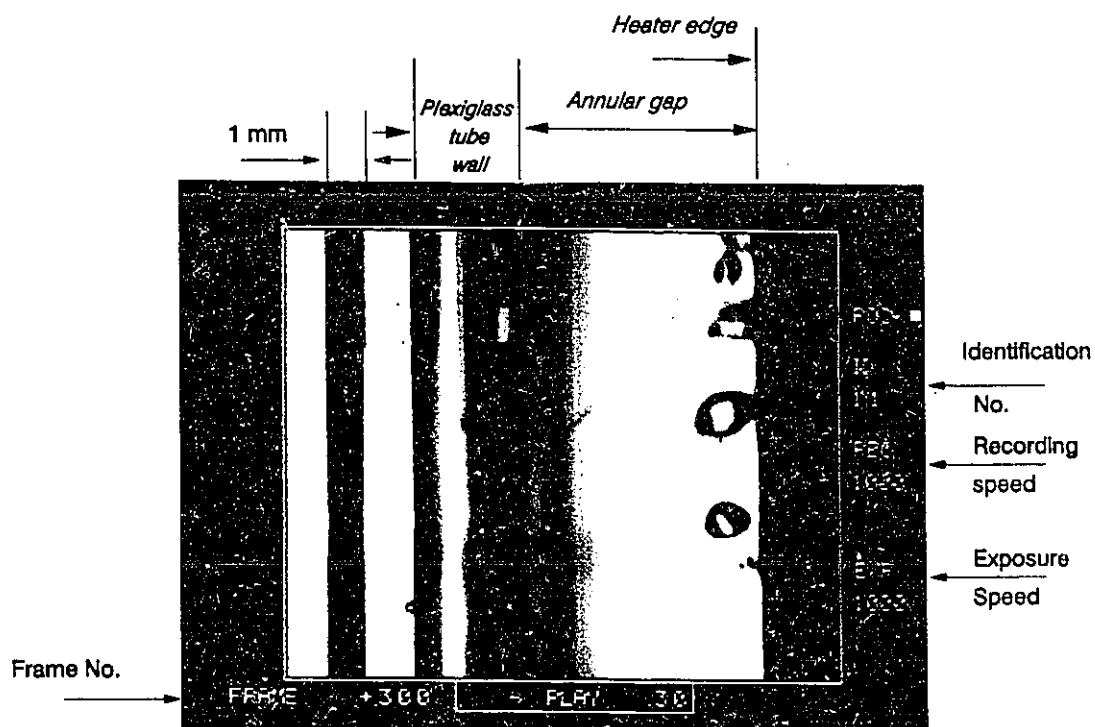


Figure 3.13a A photograph for the annular gap in boiling region

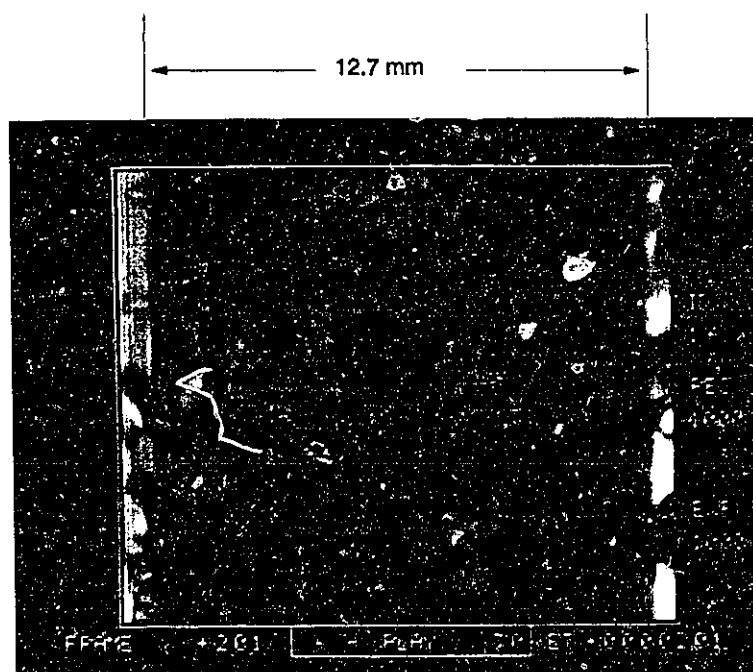


Figure 3.13b A photograph for the heating surface in boiling region

CHAPTER 4

INTERFACIAL PHENOMENA AND VOID FRACTION IN SUBCOOLED WATER-STEAM BUBBLY CONDENSING FLOW

Among the various mathematical formulations of two phase flow, the two-fluid model is considered the most accurate. In this formulation, the two phases are described separately in terms of averaged phase mass, momentum and energy equations. Moreover, the interactions between the two phases are modelled by interfacial transfer terms to account for interfacial mass, momentum and energy transport. Modelling of the interfacial phenomena requires accurate knowledge of a number of important parameters; particularly the interfacial area concentration, interfacial heat transfer coefficients and bubble rise velocity. In the work reported herein, experimental results are reported on interfacial area concentration, interfacial heat transfer coefficient and bubble rise velocity in subcooled water-steam flow in a vertical annulus. The findings of this investigation were incorporated in a steady state two-fluid model for closure to predict the axial void fraction profile in subcooled water-steam condensing bubbly flows.

4.1 Interfacial Area Concentration

4.1.1 Introduction

The interfacial area concentration is an essential parameter in determining the total rate of interfacial mass, momentum and energy transport. Available data, and accordingly existing correlations, are limited to adiabatic gas-liquid flows and were found to be inadequate in predicting the interfacial area concentration in diabatic steam-water flows under low pressure as shown by Chatoorgoon (1992) and Chatoorgoon et al. (1992).

At present, several methods are available for measuring the interfacial area concentration, such as photography, light attenuation, ultrasonic attenuation, resistivity probes and chemical absorption. However, these methods have different limitations. Although, the chemical absorption method can be used to measure the volume-averaged interfacial area concentration in various flow regimes, it is not appropriate for boiling and condensing steam-water flows because of the chemical additives used in this method. The photographic and light attenuation techniques are only applicable in bubbly and slug flow regimes. They can be used to measure local and area-averaged interfacial area concentrations. However, they require a transparent test section to visualize the flow. The main advantage of the photographic methods over other methods is that they provide direct visual measurement of bubble shapes and sizes. The disadvantage of the photographic method is the enormous effort

required to analyze the images. The main advantage of the ultrasonic attenuation method is its applicability to flows inside metallic pipes. However, it is limited to low void fraction bubbly flow. The electroresistivity probe technique is only used to measure local interfacial area in bubbly flows. Studies comparing various interfacial area measuring techniques were published by Landau et al. (1977) and Sridhar and Potter (1978). An extensive review of experimental studies on interfacial area concentration for various flow regimes was published by Ishii and Mishima (1980).

Several correlations for interfacial area concentration were reported in the literature. These correlations are presented in Table 4.1. All the correlations presented were developed on the basis of adiabatic gas-liquid flow data. Moreover, except that of Kocamustafaogullari et al. (1992), they were based on observations in two-phase flow in vertical conduits.

The common approach in correlating interfacial area concentration data followed the earlier work of Banerjee et al. (1970) and Jepsen (1970) who considered the interfacial area, and interfacial mass transfer, to be dependent on the level of energy dissipation in the fluid. Accordingly, the interfacial area concentration was correlated in terms of frictional pressure drop as well as a measure of the flow velocity. Following this idea, Kasturi and Stepanek (1974), Shilimkan and Stepanek (1978), Tomida et al. (1978) and DeJesus and Kawaji (1990) correlated the interfacial area concentration in terms of frictional or total pressure drop as shown in Table 4.1. The correlations mentioned above were

based on the measurement of interfacial area concentration in co-current upward gas-liquid flow using the chemical absorption method. The data were mostly in the slug and annular flow regimes, except for that of DeJesus and Kawaji (1990) which covered a wider range of flow regimes from bubbly to annular flow. A few investigators, including Akita and Yoshida (1974), Fukuma et al. (1987) and Tabei et al. (1989), correlated the interfacial area concentration in terms of void fraction. These correlations are applicable for the bubbly flow regime and they were developed from data obtained by different measuring techniques. The correlation of Akita and Yoshida (1974) was developed from data obtained using the photographic method for flow in a vertical bubble column. The correlation of Fukuma et al. (1987) was based on the measurements of Yasunishi et al. (1986), which was obtained by a double sensor probe in a slurry bubble column. Recently, Kocamustafaogullari et al. (1992) introduced a mathematical model for bubble diameter and interfacial area concentration. The maximum bubble size was estimated based on a critical Weber number above which the bubbles are no longer stable. The interfacial area concentration was calculated using the mean bubble size and the void fraction, based on the drift flux model. The model gave good agreement with their data for bubbly flow measured by the double sensor probe in horizontal pipes.

Based on the above review, it is clear that all available interfacial area correlations are based on adiabatic gas-liquid data. Their applicability to boiling

and/or condensing flows needs to be evaluated. Moreover, preliminary work reported by Shoukri et al. (1991), has shown that under the same condition of mass flux, void fraction and subcooling, the average bubble size, and consequently the interfacial area concentration, is dependent on whether vapour generation or condensation is taking place.

The main purpose of this section was to obtain and correlate new data on interfacial area concentration in condensing subcooled water-steam co-current upward flow and to compare these data with existing correlations.

4.1.2 Results and Data Reduction

Tests were carried out at different mass flow rates and various levels of subcooling. The test conditions are listed in Table 3.2. The subcoolings at the end of the heating section and 10 centimetre in the down stream direction, and the inlet void fraction to the unheated region are also listed in Table 3.2. The void fraction measurement and the flow photography were conducted at one centimetre intervals along the condensing region of the test section. Typical sample photographs are shown in Figure 4.1. Liquid subcooling in the condensation region was measured at various locations along ^{the} test section. The measured void fraction distributions along the condensing section are shown in Figure 4.2. This figure confirms what was expected, in that the rate of void collapse increases as the subcooling increases, the subcooling values are listed

in Table 3.2.

In measuring the volume and surface area of individual bubbles, the bubbles were divided into two categories; small nearly spherical bubbles and large elongated bubbles as shown in Figures 4.1a and 4.1b respectively. The volume and the surface area of small bubbles were calculated by measuring two diameters in each view. The measured diameters were the maximum diameter and that perpendicular to the maximum diameter as shown schematically in Figure 4.3a. The cross sectional area was assumed to be an ellipse and the two measured diameters were considered the maximum and the minimum diameters. The bubble volume and surface area were calculated by rotating this cross section around the maximum diameter. This was done for each view and the bubble volume and surface area were considered the average of the two views. For these nearly spherical small bubbles, the ratio d_{\max}/d_{\min} was typically less than 1.5 and the mean diameter less than 4 mm. For the elongated bubbles, e.g. Figure 4.b, the surface area and volume of the individual bubbles were estimated by cutting each bubble into six slices as shown in Figure 4.3b. The upper and the bottom sections of each bubble were considered domes. The inner sections were considered parts of conical bodies where the two bases were assumed ellipses. The two measured diameters at a given horizontal level, obtained from the two views, were considered the maximum and the minimum diameters of the elliptical base.

At each axial location, a total of about 200 bubbles were analyzed. The

bubble volume v_b and surface area a_b were calculated as discussed above. For each bubble, the Sauter bubble diameter, $d_s = 6 v_b / a_b$, was calculated. A typical histogram representing the individual Sauter bubble diameter versus its frequency of occurrence is shown in Figure 4.4. This procedure was repeated more than sixty times at various axial locations of the tested region for experimental tests listed in table 3.2.

To calculate the interfacial area concentration at each axial location, the average bubble surface area and volume at each location were calculated as follows:

$$A_b = \frac{1}{n_b} \sum_{j=1}^{n_b} a_{b,j} \quad (4.1)$$

$$V_b = \frac{1}{n_b} \sum_{j=1}^{n_b} v_{b,j} \quad (4.2)$$

By assuming that the bubble density per cubic meter is N_b , the local void fraction and interfacial area concentration are:

$$\alpha = N_b V_b \quad (4.3)$$

$$a_i = N_b A_b \quad (4.4)$$

The mean Sauter bubble diameter at any given axial location was defined by:

$$D_s = \frac{6.0 V_b}{A_b} \quad (4.5)$$

The mean Sauter bubble diameter was found to increase as the void fraction is increased. The rate of increase of bubble diameter was higher at low void fraction as shown in Figure 4.5.

The interfacial area concentration at various axial locations can be estimated from Equations (4.3, 4.4 and 4.5):

$$\begin{aligned} a_i &= \alpha \frac{A_b}{V_b} \\ &= \frac{6.0 \alpha}{D_s} \end{aligned} \quad (4.6)$$

It should be noted that estimating the interfacial area concentration using Equation 4.6 is based on the measured average bubble volume and interfacial area, i.e. independent of whether the bubbles are spherical or not.

4.1.3 Discussion of the Results

The measured interfacial area concentration versus the void fraction are shown in Figure 4.6 for different values of mass and inlet void fraction and inlet

subcooling. For each experimental run, the data points represent the local void fraction and local interfacial area concentration measured at various elevations along the test section. It is clear from Figure 4.6 that the interfacial area concentration is a strong, which may not be unique, function of void fraction. Closer examination of the data has shown that the interfacial area is also a function of mass flux, as this will be discussed later.

Since the bubble size is one of the parameters controlling the interfacial area concentration, it is important to report visual observations related to bubble break-up and/or coalescence. The present work focused on the condensation region, i.e. the adiabatic wall section. Accordingly, the void fraction decreases systematically along the region of interest as shown in Figure 4.2. Near the transition region between the heated and unheated sections, the vapour bubbles formed upstream by surface boiling, tended to coalesce forming larger bubbles. Downstream of this short entrance region, the bubble remained stable and no bubble break-up or coalescence was encountered. The size of each bubble decreased while advancing along the test section until it collapsed completely due to condensation in the subcooled liquid. It is known, in most practical applications, that the stability of bubbles, or droplets, is governed by the Weber number, which is the ratio of the fluid inertia to surface tension forces. Bubble break-up occurs when this ratio exceeds a critical value at which the local turbulent fluctuations in the liquid determine the break-up characteristics, and consequently the bubble size. In the

present work, the maximum mass flux was limited to 500 kg/m² s and accordingly the steam bubbles observed appeared to be stable.

Another factor that affects the interfacial parameters in bubbly flow is the bubble generation mechanism and its initial size (Kocamustafaogullari et al., 1992). In the present case, the vapour bubbles were generated by surface boiling upstream of the unheated section. The present data showed no clear effect of the rate of bubble generation.

4.1.4 Evaluation of Existing Correlations

The present interfacial area data were compared with the existing correlations given in Table 4.1. Comparisons are shown in Figures 4.7-4.11. To compare the present data with some of the correlations given in Table 4.1, prior calculation of the pressure drop was required. Pressure drop calculations have shown that the effect of the acceleration term was rather negligible, and accordingly the total pressure gradient was calculated from:

$$\left(\frac{dP}{dz}\right)_t = g [\alpha \rho_g + (1 - \alpha) \rho_l] + \left(\frac{dP}{dZ}\right)_f \quad (4.7)$$

where the first term on the right hand side represents the gravitational pressure gradient and the second term represents the frictional pressure gradient. The measured void fraction profiles were used for calculating the gravitational component. In calculating the frictional component, a number of models were

used, which gave similar results. The results shown in Figures 4.7, 4.10 and 4.11, however, were based on calculating the frictional pressure drop from Chisholm's model (1973), as this was developed for two-phase flow with phase change. While this model was developed for evaporating flow which permits phase change, it is also applicable for condensing flow.

The relative bubble velocity, required for calculating the frictional component in Chisholm's model, was calculated from the drift flux model of Zuber and Findlay (1965):

$$U_b = \frac{1.53}{1 - \alpha} \left[\frac{g \sigma (\rho_l - \rho_g)}{\rho_l^2} \right]^{1/4} \quad (4.8)$$

As shown in Figures 4.7-4.11, the present data fall within the range predicted by the majority of these correlations, but in general they do not satisfactorily fit the data. It is interesting to note that in comparing the present data with the correlations of Kasturi and Stepanek (1974), as well as Shilimkan and Stepanek (1978), Figure 4.7, the data falls into five distinct groups corresponding to the mass fluxes used. This was true irrespective of the frictional pressure drop correlation used, suggesting that the present data shows other hydrodynamic effects that are not accounted for in the two correlations tested in Figure 4.7. Also these correlations are not consistent at very low void fraction. For example, for single phase flow, i.e., zero void fraction and consequently zero interfacial area, these correlations give zero

frictional pressure drop.

The correlation of Akita and Yoshida (1974), which was developed for bubbly flow in square conduits using the photographic method, underpredicted the present data by about 30% as shown in Figure 4.8. This difference can be attributed to the difference in the observed bubble size. While the authors measured void fractions up to 14%, the observed bubbles were up to 14 mm diameter for air-water adiabatic flow. The maximum effective bubble size observed in the present work was in the order of 7mm. The predictions of the correlation of Fukuma et al. (1987), which was developed for slurry bubble columns, was much lower than the measured values as shown in Figure 4.8. The presence of solid particles in their experiments could be responsible for this observed trend. In general, the correlation of Tabei et al. (1989) predicts the present data better than the others, perhaps because it was mainly developed for bubbly flow and was based on more extensive data obtained from various sources.

The effect of Weber number on the predictions of the interfacial area models used in the two-phase numerical codes, TRAC-P1A and MINI-TRAC as reported in Kelly and Kazimi (1981) and Hori and Toda (1991) respectively, are shown in Figure 4.9. A Weber number of a value of 50 was used in TRAC-P1A, which was developed for high mass flux ($G > 2700 \text{ kg/m}^2\text{s}$). A lower value of Weber number of 7.5 was used in the MINI-TRAC code. As shown, the use of the lower value of the critical Weber number improves the agreement

drastically. Figure 4.10 shows that the correlation of Tomida et al. (1978) overpredicts the present data while the correlation of Dejesus and Kawaji (1990) underpredicts the same data. It should be mentioned that these two correlations as well as the correlations of Kasturi and Stepanek (1974) and Shilimkan and Stepanek (1978) were developed for similar flow configurations, i.e. co-current upward air-water flows in vertical tubes. The chemical absorption method was used to measure the interfacial area concentration in these experiments. However, there are noticeable discrepancies among these data sets. Dejesus and Kawaji (1990) reported that the data of Tomida et al. (1978) was 10 times higher than theirs. Ishii and Mishima (1980) attributed the scatter among various experiments to the sensitivity of the interfacial area to various experimental conditions such as the inlet conditions and the existence of surface contamination. One can add the effect of chemical additives on the physical properties of the fluids and consequently on the bubble or droplet dispersion characteristics.

The model of Kocamustafaogullari et al. (1992) was developed for bubbly flow in horizontal tubes. The interfacial area concentration was correlated in terms of the total pressure drop as well as other parameters. Poor agreement was obtained between this model and the present data. This is not surprising since in the present case the main pressure drop component is the gravitational component. Accepting the dependence of the interfacial area concentration on energy dissipation, the use of the frictional pressure drop

instead of the total pressure drop is justified. Using the frictional component in the model improved the level of agreement significantly. Figure 4.11 shows the comparison between the present data and the model when the frictional pressure drop was used. It is shown that the model's predictions are still not in good agreement with the present data.

In general, the lack of agreement between the present data and the predictions of the available correlations can be attributed to differences in flow regimes and the fact that the present data was obtained for single component subcooled condensing two-phase flow while the published correlations were developed for adiabatic two-component flow.

4.1.5 Proposed Correlations

In the present work, a unique set of data on interfacial area concentration in subcooled water-steam upward flow in vertical conduits was obtained. The data covered test conditions that were not examined before. The present data set was comprised of the interfacial area concentration a_i as a function of the area-averaged void fraction α , local subcooling and mass flux.

To correlate the data, a simple dimensional analysis was performed. The interfacial area concentration was assumed to be a function of the above parameters, the thermophysical properties of the fluids and the hydraulic diameter of the channel. Attempts were made to correlate the data in terms of

the resulting dimensionless groups using standard regression analysis. The best correlation was found to be of the form;

$$\frac{a_i}{\sqrt{g \Delta \rho / \sigma}} = 2.91 \frac{a^{0.688}}{Re_i^{0.092}} \quad (4.9)$$

where the characteristic length used in the Reynolds number is the inverse of the interfacial area concentration. The correlation coefficient was 97.3%. An explicit equation for the interfacial area concentration can be deduced from Equation (4.9) in the form:

$$a_i = 3.24 a^{0.757} \left(\frac{g \Delta \rho}{\sigma} \right)^{0.55} \left(\frac{\mu}{G} \right)^{0.1} \quad (4.10)$$

The experimental data are compared with the predictions of the proposed equation in Figure 4.12 where 95% of the data lies within $\pm 10\%$ of the predicted values.

It is interesting to note that the proposed correlation is in a dimensionless form and has the correct limit in void fraction, i.e. the interfacial area concentration vanishes at zero void fraction. Equation (4.10) shows that there is no dependency of interfacial area concentration on the local subcooling and a rather weak dependency on the mass flux. It is also interesting to note that for completely spherical bubbles, Equations (4.3) and (4.4) would lead to the interfacial area concentration a_i being proportional to $a^{2/3}$. Equation (4.10) shows a_i to be proportional to $a^{0.757}$, which reflects the fact that the observed

bubbles were not completely spherical.

Although Equations (4.9) and (4.10) represent the best correlation obtained using the present data, the strong dependence of the interfacial area concentration on the void fraction, shown in Figure 4.6, provided a strong incentive to correlate the interfacial area in terms of void fraction only. In this case, the data can be correlated in the simple form:

$$a_i = 556.4 \alpha^{0.74} \quad (4.11)$$

where a_i has units of (m^2/m^3) . For Equation (4.11), the correlation coefficient is 96% and 90% of the data lies within $\pm 20\%$ of the predicted values. Equation (4.11) is superimposed on the data in Figure 4.6.

The mean Sauter bubble diameter can be calculated using the relation between it, void fraction, and interfacial area concentration. Substituting from Equation (4.10) into Equation (4.6), the mean Sauter bubble diameter can be calculated from:

$$D_s = 1.85 \alpha^{0.243} \left(\frac{\sigma}{g \Delta \rho} \right)^{0.55} \left(\frac{G}{\mu} \right)^{0.1} \quad (4.12)$$

The predictions of Equation (4.12) are compared with the mean Sauter bubble diameter measured in the present work as shown in Figure 4.13.

4.2 Bubble Relative Velocity

The high speed photographic data were also used to obtain the relative bubble velocity. The absolute bubble velocity was determined by measuring the displacement of each bubble during a known time period. The displacement was measured by marking the upper and lower points of each bubble from the time of its appearance in the field of view until it disappeared. This procedure was carried out for 1400 bubbles, twenty bubbles at each axial location. The average absolute bubble velocity at each axial location was obtained by averaging the measured individual absolute bubble velocities. The mean bubble relative velocity was calculated from the difference between the mean absolute bubble velocity and the mean liquid velocity at the same axial location. The mean liquid phase velocity was determined by solving the continuity equation using the known flow rate and the measured area-averaged void fraction at the same location.

The present data for the measured mean relative bubble velocity versus the measured void fraction is shown in Figure 4.14 together with predictions of the available correlations. It is shown that, within the range of the present test conditions, the mean bubble relative velocity is in the range of $0.2 < U_b < 0.4$ m/s. Zuber and Findlay (1965) recommended the following relationship for bubble rise velocity,

$$U_b = \frac{C_z}{1 - \sigma} \left[\frac{g \sigma (\rho_l - \rho_g)}{\rho_l^2} \right]^{1/4} \quad (4.13)$$

This correlation was found to be generally capable of predicting the present data when the constant C_z is taken to be 1.53 as recommended by Zuber and Findlay (1965) for churn-turbulent bubbly flow.

4.3 Interfacial Heat Transfer Coefficient in Subcooled Water-Steam Bubbly Condensing Flow

4.3.1. Introduction

Vapour bubble condensation is an important physical phenomenon which is encountered in liquid-vapour two-phase flow when the liquid temperature is below saturation, i.e. subcooled liquid. The rate of vapour bubble condensation plays a major role in the stability of flows in which subcooled boiling and/or condensation occur.

Bubble collapse during condensation can be either inertia or heat transfer controlled. For high liquid subcooling, bubbles collapse rapidly satisfying the so called Rayleigh solution (1917) for the collapse of a spherical cavity in an infinite liquid in which the process is controlled by the inertia of the surrounding liquid. On the other hand, if the subcooling is relatively low, the bubble collapse period will be longer and the process will be controlled by the heat transfer at the interface. Chen and Mayinger (1992) showed that for a single bubble, the condensation is completely controlled by interfacial heat transfer for Jakob numbers $Ja < 80$, while for $Ja > 100$ the process is completely inertia controlled. The present work focuses on the heat transfer controlled bubble condensation in a typical liquid-vapour bubbly flow.

Most of the available studies on heat transfer controlled bubble condensation were conducted for simple cases such as heat diffusion from a

stagnant bubble and convection around a single bubble moving in an irrotational flow field. These studies were typically carried out to obtain the bubble history during condensation, i.e. the relation between bubble diameter and time, from which the instantaneous interfacial condensation coefficient can be estimated. When a saturated vapour bubble was encountered in contact with a subcooled liquid, the energy released due to the phase change should be conducted to the liquid phase at the interface. Using a simple energy balance for a condensing bubble, the interfacial heat transfer coefficient can be estimated as follows:

$$h_c = \frac{\rho_g h_{fg} (-dv_b/d\tau)}{a_b (T_s - T_l)} \quad (4.14)$$

For a spherical bubble, the interfacial condensation coefficient is:

$$h_c = \frac{\rho_g h_{fg}}{2 (T_s - T_l)} (-dD_b/d\tau) \quad (4.15)$$

Available models and correlations for bubble history and instantaneous condensation Nusselt number are listed in Table 4.2.

For nearly stagnant bubbles, condensation is governed by heat diffusion at the interface. Convective effects at the interface become important when the relative motion between the bubble and the liquid is significant. The condensation of stagnant bubbles was investigated experimentally and theoretically by a number of investigators; Zuber (1961), Florschuetz and Chao (1965) and Theofanous et al. (1970). The analysis of Zuber (1961) was based

on the similarity between the well known transient conduction with a moving boundary and heat transfer at a bubble surface. Florschuetz and Chao (1965) included the convection effect due to interfacial movement. They obtained the transient temperature distribution in the liquid boundary layer around the bubble from either Plesset-Zwick's (1952) solution for a growing bubble, or from the solution of transient conduction with a moving boundary. Accordingly, two bubble history models, and consequently two heat transfer coefficients, were obtained as listed in Table 4.2. Florschuetz and Chao's study involved the condensation of a bubble which was suddenly introduced into subcooled liquid and consequently, the condensation Nusselt number would be initially infinite. Theofanous et al. (1970) pursued a two-fluid formulation but did not include the phasic momentum equations in the analysis. However, thermal non-equilibrium at the interface was considered. Okhotsimskii (1988) investigated the effect of Jakob number on bubble collapse. Although his analysis covered the range of high Jakob number, where inertia effects are significant, the liquid momentum was ignored.

Many theoretical investigations were carried out to study the condensation of moving bubbles in a stagnant liquid. The energy equation of the two phases were combined with the hydrodynamic solution of irrotational flow around a solid sphere to solve for the thermal boundary layer around the condensing bubble. This procedure was followed by Ruckenstein (1959) and (1967), Ruckenstein and Constantinescu (1969) and Ruckenstein and Davis

(1971) to estimate the interfacial heat transfer coefficient. Using similar analysis, Wittke and Chao (1967) showed that the rate of condensation increased with increasing bubble velocity and that the effect of bubble motion increased at lower Jakob numbers. Dimić (1977) introduced an analytical solution and investigated the effect of bubble size dependent velocity. Moalem and Sideman (1973) and Akiyama (1973) used standard relationships for modelling the interfacial condensation heat transfer coefficient, to determine the bubble collapse history. The former modified the Nusselt number for potential flow across a sphere by a factor of $(0.5 \text{ Pr}^{-1/6})$ to account for viscous flow effects and the latter used an empirical relationship for forced convection across a solid sphere. Experimental investigations of the condensation of moving bubbles in a stagnant liquid were carried out by Levenspiel (1959), Wittke and Chao (1967), Hewitt and Parker (1968), Isenberg and Sideman (1970), Akiyama (1973), Brucker and Sparrow (1977), Simpson et al. (1986), Chen and Mayinger (1992). Hewitt and Parker (1968) reported that the model of Florschuetz and Chao (1965) for stagnant bubbles underpredicted their experimentally determined bubble condensation rate. They attributed the higher collapse rate in their data to the effect of bubble movement.

As shown in Table 4.2, the various models and correlations appear to disagree on the effect of subcooling, or Jakob number, on the condensation heat transfer coefficient. The models of Levenspiel (1959), Ruckenstein (1959), Akiyama (1973) and Isenberg and Sideman (1970) show that the Nusselt

number is independent of subcooling which is also supported by the high pressure data of Brucker and Sparrow (1977). The effect of subcooling, however, appears in other correlations either explicitly or implicitly through the bubble history relationship of β . While the models of Dimić (1977) and Simpson (1986) show that the Nusselt number is increased with increasing liquid subcooling, the model of Chen and Mayinger (1992) shows an opposite trend. The effect of bubble Reynolds number is strong in models involving moving bubbles. The interfacial condensation Nusselt number varies in proportion to Re_b^n where n is in the range of $0.5 < n < 1.0$.

In the above investigations, single bubbles were mostly considered. Ruckenstein (1959) reported that multi-bubble effects should be included in the Nusselt number correlations through the effect of void fraction. Among the few investigations involving multiple bubbles are those of Abdelmessih et al. (1977) and Mayinger and Bucher (1977) who experimentally investigated the condensation of bubbles in subcooled flow boiling. The data of Abdelmessih et al. (1972) showed that an increase in the mass flux increases the rate of condensation. However, it is not clear whether this effect is caused by the mass flux or the bubble size which tended to become smaller due to the increase in mass flux. The condensation coefficients used in the two-phase numerical codes TRAC-P1A and MINI-TRAC as reported by Kelly and Kazimi (1982) and Hori and Toda (1991) respectively, are also listed in Table 4.2.

Based on the above review, a number of difficulties exist in applying

some of existing correlations, given in Table 4.2, to predict the interfacial heat transfer in subcooled water-steam bubbly flow. The simple models developed for a single bubble in stagnant liquid are certainly not appropriate. Moreover, it is difficult to apply the Nusselt number correlations which contain the initial bubble diameter D_0 or β . In other correlations, e.g. Chen and Mayinger (1992), the initial bubble diameter was even based on the diameter of the nozzle from which the bubbles were introduced.

In the present work, data on interfacial heat transfer between bubbles and subcooled water are obtained for subcooled water-steam bubbly flow. The data is correlated and the proposed correlation was recommended for use as a closure equation for interfacial heat transfer in condensing bubbly flow.

4.3.2 Experimental Results and Data Reduction

Eight tests were carried out at various levels of mass flow rate, input power and subcooling, the same tests which were already discussed with respect to the determination of the interfacial area concentration investigation. The test conditions are listed in Table 3.2. The void fraction measurements and the photography of the flow field were conducted at one centimetre intervals along the condensing region of the test section. The void fraction distributions along the condensing section are shown in Figure 4.2. Representative sample photographs of the condensing bubbles are shown in Figure 4.15.

The bubble size and surface area were measured as discussed in section 4.1.2. The bubble history was then obtained by tracking the volume and surface area through the field of view. This procedure was carried out at time intervals of 1 or 2 ms depending on the framing speed used. Figure 4.16 shows a typical sample of the bubble Sauter diameter versus time. Since the duration of the bubble passage through the field of view was small as compared to the total bubble life, the rate of change of the diameter of each bubble with time appeared constant within the field of view as depicted in Figure 4.16.

Using the two orthogonal views of a given bubble, an algorithm was developed for calculating the bubble surface area a_b and volume v_b . The method used was described in detail in 4.1.2. The interfacial heat transfer rate was estimated by tracking the volume and surface area of individual bubbles through the field of view. For a typical bubble velocity using a framing speed of 500 frame/s, it was possible to obtain 10-12 measurements of v_b and a_b versus time for each condensing bubble. The interfacial heat transfer coefficient was calculated based on the change of bubble volume between each two consecutive measurements using Equation (4.14). The calculated values were averaged to obtain the average heat transfer coefficient for each bubble. The average interfacial heat transfer coefficient at a given axial location h_c was obtained by further averaging the calculated values for about 10-20 individual bubbles at that location. The calculated averaged interfacial heat transfer coefficient at each axial location can, accordingly, be correlated in terms of the

local void fraction, bubble size, subcooling, mass flux etc. The bubble condensation Nusselt number was calculated using the measured local mean Sauter bubble diameter at the same location,

$$Nu_c = \frac{h_c D_s}{k} \quad (4.16)$$

4.3.3 Analysis of the Results

The calculated bubble condensation Nusselt number versus the bubble Reynolds number is shown in Figure 4.17. The bubble Reynolds number was calculated using the measured mean bubble relative velocity and mean Sauter bubble diameter. The actual measured bubble velocities were used, rather than those predicted by existing correlations, to eliminate unnecessary smoothing of the data. As shown in the figure, the bubble condensation Nusselt number increases as the bubble Reynolds number increases. Existing correlations in which the Nusselt number, for a given fluid, is a unique function of the bubble Reynolds number are superimposed on the experimental data in Figure 4.17. In general, no correlation appears to be in good agreement with the present data. However, the data falls within the ranges predicted by these correlations, except for the MINI-TRAC correlation (reported in Hori and Toda, 1991) which overpredicts the data significantly. As shown, the data is overpredicted by Ruckenstein's correlation and generally underpredicted by the model of Isenberg

and Sideman (1970). As mentioned earlier Isenberg and Sideman's model is basically a modification of the irrotational flow model of Ruckenstein (1959) where a correction factor of $1/2 \text{Pr}^{-1/6}$ was used to account for viscous effects. It is also shown in Figure 4.17 that TRAC-P1A (Kelly and Kazimi, 1982) may be capable of predicting the present data at low bubble Reynolds numbers, while the model of Akiyama (1973) predicts the data well at high bubble Reynolds numbers.

A stepwise regression analysis was used to correlate the present data on bubble condensation Nusselt number in terms of the local values of Jakob number, void fraction and bubble Reynolds number. The resulting correlation was in the form:

$$Nu_c = 2.04 Re_b^{0.61} \alpha^{0.328} Ja^{-0.308} \quad (4.17)$$

which is valid for steam-water flow at near atmospheric pressure and for void fraction up to 30%. This correlation predicts the present data within $\pm 20\%$, as shown in Figure 4.18, with a correlation coefficient of 96%.

It is interesting to note that in the above correlation, the power index of the bubble Reynolds number is 0.61, which is in the range of the existing correlations in which it tended to lie within the range of 0.5 to 1.0. The dependence of the Nusselt number on the concentration of the vapour phase α reflects the fluid mixing caused by the multi-bubble effect as suggested by Ruckenstein (1959). The present correlation also includes the effect of Jakob

number, where the Nusselt number increases with decreasing Jakob number. This trend is consistent with the predictions of the Chen and Mayinger correlation as given in Table 4.2.

By assuming that the mean Sauter bubble diameter represents the instantaneous bubble diameter, the bubble history was obtained by integrating Equation (4.15) using Equation (4.17),

$$\beta = \left(1 - 5.67 Re_{bo}^{0.61} \alpha^{0.328} Ja^{0.692} Fo_o\right)^{0.72} \quad (4.18)$$

The predictions of Equation (4.18) are compared with those of other correlations for fixed values of Re_{bo} and α at two values of Jakob number, $Ja = 10$ and 30 . As shown in Figure 4.19, the present correlation as well as the models of Akiyama (1973), Simpson (1986) and Chen and Mayinger (1992) predict a much faster rate of condensation than the two models of Florschuetz and Chao (1965) which were based on pure thermal diffusion. This higher condensation rate is attributed to the effect of forced convection (bubble motion). At the beginning of the condensation process, the models of Florschuetz and Chao (1965) for pure thermal diffusion predict higher condensation rate than the others because of the initial condition used to obtain the transient temperature distribution in the thermal boundary layer around the vapour bubble. The interface, initially at saturation, was assumed to suddenly come in contact with the subcooled liquid at $\tau = 0$, i.e. infinite heat transfer

rate. Zuber's diffusion model (1961) on the other hand (see Table 4.2), assumes that the bubble collapse follows a period of bubble growth in non-uniform temperature field, i.e. $dD_b/d\tau = 0$ at $\tau = 0$, resulting in a zero condensation rate initially. The degree of agreement, or disagreement, between Equation (4.16) and the rest of the available correlations, on the other hand, is clearly dependent on the values of Jakob number and void fraction. It should be noted, however, that the present correlation is the only one that shows a dependence on void fraction.

In recommending Equation (4.17) for calculating the interfacial condensation Nusselt number as a function of the bubble Reynolds number Re_b , it is important to recommend appropriate correlations for bubble relative velocity and bubble diameter. Based on the present data for the measured mean relative bubble velocity, the model of Zuber and Findlay (1965), Equation (4.13), is recommended for calculating bubble relative velocity. The bubble diameter which is required as characteristic length in bubble Reynolds and Nusselt numbers can be calculated from the relation between mean Sauter bubble diameter, void fraction and interfacial area concentration or Equation (4.12) directly.

4.4 Void Fraction Profile in Condensing Subcooled Water-Steam Bubbly Flow

4.4.1 Experimental Results

Detailed experiments were carried out in order to generate accurate data on void fraction and subcooling in the condensing region. The experimental procedure and measurements were described in Chapter 3. Two sets of experiments were carried out in this region. The first set was conducted without flow visualization. Nineteen runs were carried out for various levels of mass flux, input heat flux and subcooling. The run conditions of this set are listed in table 3.1. The area averaged void fraction was measured along the heated and the unheated region. The measured axial void fraction profiles in the unheated region for this set are shown in Figures 4.20a-c. The subcooling was measured at the beginning of the unheated region and 15 cm in the downstream direction. The measured subcooling values are listed in Table 3.1. The test conditions of the second experiment set carried out in this region are listed in Table 3.2. The flow visualization was conducted as well as void fraction measurements in this set. Eight runs were carried out at various levels of mass flux and inlet subcooling. The measured area-averaged void profiles in these tests are shown in Figures 4.21a and 4.21b. The measured liquid subcooling at the end of the heating section and ten centimetre in the downstream direction are listed in Table 3.2.

4.4.2 Two-Fluid Void Fraction Profile Model

Among the various mathematical formulations of two-phase flow, the two-fluid model which treats the two phases separately, can be considered the most accurate formulation, in as much as it attempts to account for more details of the interfacial phenomena. In this type of formulation, as mentioned before, the two phases are described separately in terms of average phasic mass, momentum and energy equations. The interactions at the interface are modelled by interfacial conservation equations of mass, momentum and energy. These equations are called jump conditions. To model the interfacial terms, accurate knowledge of interfacial area concentration, interfacial heat transfer coefficient and bubble rise velocity are required. In the following section, the experimental results obtained on interfacial area concentration, interfacial heat transfer coefficient and bubble rise velocity were introduced into a two-fluid model in order to predict axial void fraction profiles in condensing bubbly flow.

4.4.2.1 Two-Fluid Model Formulation

The one dimensional conservation equations can be obtained by the space and time averaging of the integral transport equations, Todreas and Kazimi (1990). For practical applications, following Ishii and Mishima (1984), the one dimensional two-fluid model can be simplified to:

Phase continuity equation:

$$\frac{\partial}{\partial \tau}(\alpha_k \rho_k) + \frac{\partial}{\partial z}(\alpha_k \rho_k u_k) = \Gamma_k \quad (4.19)$$

Phase momentum equation:

$$\begin{aligned} \frac{\partial}{\partial \tau}(\alpha_k \rho_k u_k) + \frac{\partial}{\partial z}(\alpha_k \rho_k u_k^2) + \alpha_k \frac{\partial P}{\partial z} - \alpha_k \rho_k g \\ = -F_{wk} - F_i - F_{ki} \end{aligned} \quad (4.20)$$

Phase energy equation:

$$\begin{aligned} \frac{\partial}{\partial \tau} \left[\alpha_k \rho_k \left(h_k + \frac{u_k^2}{2} \right) \right] + \frac{\partial}{\partial z} \left[\alpha_k \rho_k u_k \left(h_k + \frac{u_k^2}{2} \right) \right] - \\ \alpha_k \frac{\partial P_k}{\partial \tau} - \alpha_k \rho_k u_k g = q_i + q_{wk} + q_{ki} \end{aligned} \quad (4.21)$$

In the above equations, the subscript k refers to the phase k (k = g for the vapour and k = l for the liquid). The terms on the right-hand side of the above equations represent the interfacial transport terms. Γ_k is the rate of mass transfer into phase k per unit volume, F_{wk} is the wall friction force on phase k per unit volume, F_i is the interfacial force term, F_{ki} is a term representing the exchange of momentum associated with interfacial mass transfer, q_i is the interfacial heat exchange rate, q_{wk} is the wall heat transfer rate and q_{ki} is a term representing the exchange of energy associated with interfacial mass transfer. The interfacial force term F_i is typically made of two terms, a drag force term

and a virtual mass term.

For the present case of steady state subcooled liquid-vapour, or subcooled boiling flow, through a channel, the above equations can be simplified by neglecting terms representing kinetic and potential energy. These terms are expected to be very small compared to the terms which include thermal energy. Also, these equations can be modified by integrating various terms over the cross sectional area to include effects of the nonuniform profiles of the velocity, temperature and void fraction in the radial direction.

Following the above procedure, the steady state mixture continuity equation, obtained by adding the two phasic continuity equations, can be rewritten as:

$$\frac{d}{dz} \int (\rho_l (1 - \alpha) u_l + \rho_g \alpha u_g) dA = 0 \quad (4.22)$$

where α , u_l and u_g are the local radial values of the void fraction, liquid velocity and vapour velocity respectively .

Similarly, the vapour energy equation can be written in the form:

$$\frac{d}{dz} \int (\rho_g h_g \alpha u_g) dA = G_v + A \Gamma_g h_f - C_v \quad (4.23)$$

Similar to Equation (4.21), the right-hand-side of Equation (4.23) represents the net energy added to the vapour phase. However, here it is accounted for

differently. The first term in the right hand side is called the vapour generation term (heat energy rate per unit length). This term includes the fraction of the applied wall heat flux which is responsible for evaporation at the heater surface. The second term represents the energy of the liquid phase convected through the interfacial area. The liquid, which crosses the liquid-vapour interface, was assumed to be saturated. Γ_g is the net interfacial mass flow rate per unit volume of channel, difference between evaporation and condensation, and it can be evaluated from the vapour continuity equation,

$$\frac{d}{dz} \int (\rho_g \dot{u}_g) dA = A \Gamma_g \quad (4.24)$$

C_v is the condensation term (heat transfer per unit time per unit length of channel). This term represents the energy conducted to the liquid phase at the interface due to phase change by condensation in the subcooled liquid. Substituting from Equation (4.24) into Equation (4.23), the latter can be modified to:

$$\frac{d}{dz} \int (\rho_g h_{fg} \dot{u}_g) dA = G_v - C_v \quad (4.25)$$

The steady-state energy equation of the mixture was obtained by combining the energy equations of the two phases, neglecting the transient terms and integrating across the channel area,

$$\frac{d}{dz} \int (\rho_l u_l (1 - \alpha) C_p \hat{T}_l + \rho_g h_g \alpha u_g) dA = q P_h \quad (4.26)$$

where \hat{T}_l is the liquid temperature distribution in the radial direction and q is the applied heat flux at the wall.

The momentum equation of the mixture was obtained by combining the momentum equations of the two phases,

$$-\left(\frac{dP}{dz}\right)_t = \rho_a g + \left(\frac{dP}{dz}\right)_f + \frac{1}{A} \frac{d}{dz} \int (\rho_l (1 - \alpha) u_l^2 + \rho_g \alpha u_g^2) dA \quad (4.27)$$

where the left hand side of the above equation represents the total pressure gradient and the terms on the right hand side represent gravitational, frictional and acceleration pressure gradients respectively and ρ_a is the average density of the two phases along a distance dz . Averaging Equations (4.22), (4.25), (4.26) and (4.27) over the cross sectional area results in the so called area-averaged conservation equations:

$$\frac{d}{dz} [\rho_l (U_l - \overline{u\alpha}) + \rho_g \overline{u\alpha}] = 0 \quad (4.28)$$

$$\frac{d}{dz} \left[\rho_g h_{fg} \overline{u_g \alpha} \right] = \frac{G_v}{A} - \frac{C_v}{A} \quad (4.29)$$

$$\frac{d}{dz} \left[\rho_l C_p (\overline{T_l u_l} - \overline{T_l u_l \alpha}) + \rho_g h_g \overline{u_g \alpha} \right] = \frac{q p_h}{A} \quad (4.30)$$

$$-\left(\frac{dp}{dz}\right)_t = \left(\frac{dP}{dz}\right)_f + \rho_a g + \frac{d}{dz} \left[\rho_l (\overline{u_l^2} - \overline{\alpha u_l^2}) + \rho_g \overline{\alpha u_g^2} \right] \quad (4.31)$$

where the over bar represents the cross sectional area-averaged value. The area-averaged terms in the above four equations can be obtained by averaging the radial distributions over the cross sectional area, i.e.

$$\overline{F} = \frac{1}{A} \int F dA$$

Consider a condensing bubbly flow in the unheated region, i.e. $q = 0$. Consequently, the liquid temperature can be assumed uniform in the radial direction. The relations between the distribution parameters and area-averaged terms in the above equations are:

$$\overline{u_l \alpha} = D_1 U_l \alpha \quad (4.32)$$

$$\overline{u_g \alpha} = D_2 U_g \alpha \quad (4.33)$$

$$\overline{u_l^2} = D_3 U_l^2 \quad (4.34)$$

$$\overline{u_g^2} = D_4 U_g^2 \quad (4.35)$$

$$\overline{u_l^2 \alpha} = D_5 U_l^2 \alpha \quad (4.36)$$

$$\overline{u_g^2 \alpha} = D_6 U_g^2 \alpha \quad (4.37)$$

where U_l , U_g and α are the area-averaged liquid velocity, vapour velocity and void fraction, respectively. D_1 to D_6 are the distribution parameters to be determined from the radial profiles of $u_l \alpha$, $u_g \alpha$, u_l^2 , u_g^2 , $u_l^2 \alpha$ and $u_g^2 \alpha$. Substituting from the above equations into Equations (4.28-4.31), they can be reduced to:

$$\frac{d}{dz} \left[\rho_l U_l (1 - D_1 \alpha) + D_2 \rho_g U_g \alpha \right] = 0 \quad (4.38)$$

$$\frac{d}{dz} \left[D_2 \rho_g h_{fg} U_g \alpha \right] = - \frac{C_v}{A} \quad (4.39)$$

$$\frac{d}{dz} \left[\rho_l C_p U_l T_l (1 - D_1 \alpha) + D_2 \rho_g h_g U_g \alpha \right] = 0 \quad (4.40)$$

$$-\left(\frac{dP}{dz}\right)_t = \left(\frac{dP}{dz}\right)_f + g \rho_a + \frac{d}{dz} \left[\rho_l U_l^2 (D_3 - D_5 \alpha) + D_6 \rho_g U_g^2 \alpha \right] \quad (4.41)$$

where T_l is area-averaged liquid temperature.

4.4.2.2 Closure Relationships

To close the above four equations, which contain five unknowns: U_l , U_g , α , T_l and $(dP/dz)_f$, three expressions for the vapour velocity, the condensation term C_v and the frictional pressure drop are needed. The vapour velocity was obtained from the drift flux model,

$$U_g = J + u_{gj} \quad (4.42)$$

where J and u_{gj} are the local mixture superficial and vapour drift velocity respectively. The local mixture superficial velocity is given by:

$$J = (1 - \alpha) u_l + u_g \alpha \quad (4.43)$$

By eliminating J from the above two equations, the vapour velocity was

obtained;

$$u_g = u_l - \alpha u_l + \alpha u_g + u_{gj} \quad (4.44)$$

Averaging the above equation over the cross sectional area results in:

$$U_g = U_l - \overline{\alpha u_l} + \overline{\alpha u_g} + U_{gj} \quad (4.45)$$

Substituting from Equations (4.32-4.33) into the above equation, the vapour average velocity is reduced to:

$$U_g = \frac{1 - D_1 \alpha}{1 - D_2 \alpha} U_l + \frac{U_{gj}}{1 - D_2 \alpha} \quad (4.46)$$

The mean drift velocity for bubbly turbulent flow was given by, Zuber and Findlay (1965):

$$U_{gj} = 1.53 \left[\frac{\sigma g (\rho_l - \rho_g)}{\rho_l^2} \right]^{1/4} \quad (4.47)$$

Equations (4.46 and 4.47) can be reduced to Equation (4.13) for uniform radial void fraction and velocity distributions.

The condensation term C_v represents the heat transfer from the bubbles to the subcooled liquid per unit length of channel. The condensation term is estimated from:

$$C_v = h_c a_i A (T_s - T_l) \quad (4.48)$$

where a_i is the interfacial area concentration, m^2/m^3 . The interfacial area concentration was calculated from Equation (4.9) which was developed for subcooled liquid-vapour bubbly flow. The interfacial heat transfer coefficient, bubble condensation coefficient in present case, was calculated from Equation (4.17). The bubble diameter, in bubble Reynolds number and condensation Nusselt number was calculated from the relation between bubble interfacial area concentration and void fraction, Equation (4.6).

The frictional pressure drop was estimated as in Chisholm (1973), who modelled the pressure drop for evaporating two phase flow. The frictional pressure drop for two phase flow was modelled by:

$$\frac{\Delta P_{f\,tp}}{\Delta P_{fo}} = 1 + (\Gamma_f^2 - 1) \left[\beta_f x^{\frac{2-n_f}{2}} (1 - x)^{\frac{2-n_f}{2}} + x^{2-n_f} \right] \quad (4.49)$$

where,

$$n_f = 0.25$$

$$\Gamma_f = (\rho_l / \rho_g)^{0.5} (\mu_g / \mu)^{n_f/2}$$

$$\beta_f = (C_f \Gamma_f - 2^{2-n_f} + 2) / (\Gamma_f^2 - 1) \quad (4.50)$$

$$C_f = \sqrt{\rho_l / \rho_g} / K_u + K_u \sqrt{\rho_g / \rho_l}$$

$$K_u = U_g / U_l$$

The frictional pressure drop for the liquid phase was calculated from:

$$\left(\frac{dP}{dz} \right)_{lo} = 2 F \frac{G^2}{\rho_l D_h} \quad (4.51)$$

The friction factor, F , for the turbulent single phase flow was calculated from:

$$F = 0.079 Re^{-0.25} \quad (4.52)$$

4.4.2.3 Solution Procedure

The Runge-Kutta method (Burden et al., 1981) was used to integrate Equations (4.38-4.40) simultaneously. The boundary conditions for these equations were the inlet conditions to the unheated region, which are listed in Table 3.1 and 3.2. The distribution parameters D_1 to D_6 are functions of the radial distributions of velocity and void fraction. These radial distributions of the flow parameter were neither measured in the present work nor reported in the literature. Solving for void fraction, velocity and liquid temperature requires D_1 and D_2 only. If we assume that the pressure gradient is not large enough to cause significant change in the thermophysical properties of the two phases. If we further assume that the radial velocity profiles of the liquid and vapour are similar, D_1 and D_2 are equal.

The distribution parameters, $D = (1/A \alpha U) \int \alpha u \, dA$, equals unity if

either the void fraction or the velocity profile is uniform across the flow channels. Realizing that both the void fraction and flow velocity equal zero at the walls and they will tend to peak somewhere in the channel, it can be shown that D should be greater than unity. The effect of the distribution parameter on the results is shown in Figure 4.22. It was found that the best value to fit the present data was 1.3 which was used in all the following simulations.

4.4.2.4 Results and Discussions

Effects of mass flux, inlet void fraction and inlet subcooling on the calculated void fraction and local subcooling, are shown in Figures 4.23a-c. Figure 4.23a shows the effect of the mass flux. Increasing the mass flux, i.e. increasing the liquid and vapour velocities, tends to decrease the rate of collapse of void fraction along the axial direction. For the same level of void fraction, increasing the mass flux means increasing the vapour content in the flow and consequently the rate of void collapse will be less for higher mass fluxes.

As shown in Figure 4.23b, for given mass flux and inlet subcooling, increasing the inlet level of void fraction tends to increase the interfacial area concentration. Accordingly, the collapse rate of the axial void fraction profile at the entrance will be higher for the higher inlet void fraction.

Figure 4.23c illustrates the effect of the inlet subcooling on the axial void fraction profile. For given values of a mass flux and an inlet void fraction,

increasing the liquid subcooling increases the rate of bubble condensation and consequently increases the rate of void collapse significantly. As shown in the figure, raising the inlet subcooling from 5 to 15 °C condenses the same amount of vapour in 25% of the axial distance.

Comparisons between the prediction of the proposed model and the measured axial void fraction profiles are shown in Figures 4.20-4.21 for experiment sets number 1 and 2 respectively. The test conditions of these runs are listed in Table 3.1 and 3.2. Comparisons between the prediction of present model and axial void fraction data of Donevski and Shoukri (1989), Dimmick and Selander (1990) and Toda and Hori (1989) are shown in Figures 4.24, 4.25 and 4.26 respectively. It should be noted that different techniques were used in measuring these data, the gamma radiation method was used in the first and second references and the photographic method was used in the third reference. It should be also noted that the data of Donevski and Shoukri (1989) were for flow inside an annular channel and the data of Dimmick and Selander (1990) and Toda and Hori (1989) were for flow inside tubes. Although the proposed correlations used in calculating the interfacial area concentration, bubble condensation coefficient and bubble rise velocity were developed for data up to 30% void fraction, they were used in the present comparisons for up to 50% inlet void fraction. The comparisons show reasonable agreement between the current two-fluid model and the experimental data from various sources measured by different techniques.

4.5 Concluding Remarks

New experimental data on interfacial area concentration in one-component subcooled liquid-vapour bubbly flow as a function of void fraction, local subcooling and mass flux were obtained. The present data were compared with available correlations, developed on the basis of adiabatic gas-liquid flows. It was shown that available correlations were unable to predict the data accurately. Based on the present data, a new correlation was proposed. The proposed correlation shows that the interfacial area concentration is a strong function of void fraction, a weak function of mass flux and is independent of local subcooling.

Experimental data on bubble condensation in low pressure cocurrent upward subcooled liquid-vapour bubbly flow were obtained. Digital image processing techniques were used to obtain the rate of bubble condensation in terms of bubble size, local subcooling, void fraction and bubble rise velocity. The data was used to develop a new empirical correlation for the interfacial condensation Nusselt numbers as a function of bubble Reynolds number, void fraction and Jakob number. Since the proposed correlation requires the knowledge of bubble relative velocity, the present data set was also used to recommend appropriate correlations for this purpose. The proposed correlation for interfacial heat transfer coefficient is also compared with those available in the literature which were mostly developed on the basis of condensation of

single bubbles.

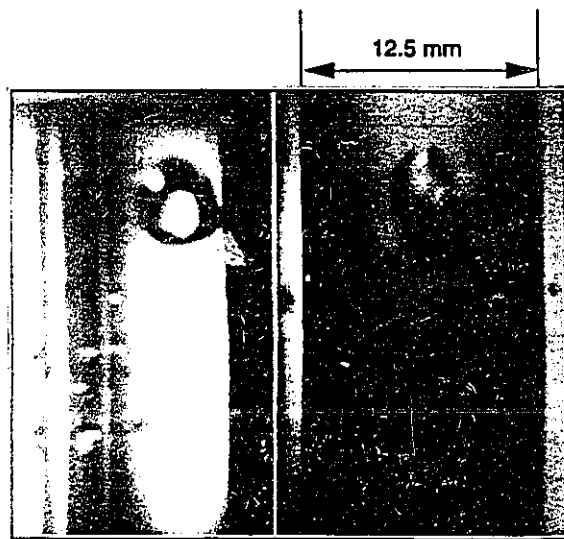
The applicability of the proposed correlations of interfacial area concentration, interfacial heat transfer coefficient and bubble rise velocity was examined by incorporating them in a two-fluid model to the predict axial void fraction profiles in condensing bubbly flows. The comparison between the prediction of the model and present data as well as data from literature shows good agreement.

Table 4.1 Interfacial Area Correlations and Models

Authors	Correlation or Model
Kasturi & Stepanek (1974)	$a_i \dot{V}_i / (1 - \alpha) = 2.26 \times 10^{-5} (dP/dz)_f^{1.07}$
Akita & Yoshida (1974)	$a_i = (g D_h^2 \rho_i / \sigma)^{1/2} (g D_h^3 / v_i^{2/3})^{0.1} \alpha^{1.13} / (3 D_h)$
Shilimkan & Stepanek (1977)	$a_i \dot{V}_i / (1 - \alpha) = 3.16 \times 10^{-5} (dP/dz)_f^{1.31}$
Tomida et al. (1978)	$a_i = 0.22 (dP/dz)_i \alpha$ for $J_g < 8$ m/s
TRAC-P1A as in Kelly & Kazimi (1982)	$a_i = 6 \alpha \rho_i U_b^2 / (We \sigma)$ where $We = 50$
Fukuma et al. (1987)	$a_i = 300 \alpha$
Tabei et al. (1989)	$a_i = 2100 (\alpha)^{1.25} (1 - \alpha)^{0.75}$
DeJesus & Kawaji (1990)	$a_i = 1.535 (dP/dz)_i^{0.12} J_g^{1.2} J_i^{-0.14} (1 - \alpha)^{1.6}$
MINI-TRAC as in Hori & Toda (1991)	$a_i = 6 \alpha \rho_i U_b^2 / (We \sigma)$ where $We = 7.5$
Kocamustafaogullari et al. (1992)	$a_i = 6 \alpha \rho_i^{1/9} (J_i + J_g) (dP/dz)_i^{2/9} / (1.06 \sigma^{1/3} (\alpha (1 - \alpha) D_h^{2/9}))$

Table 4.2 Bubble Condensation Models

Author	Bubble History	Condensation Nusselt Number
Zuber (1961)	$\beta = (\tau/\tau_m)^{1/2} (2 - (\tau/\tau_m)^{1/2})$	-----
Florschuetz & Chao (1965)	a- $\beta^2 + 2/\beta - 3 = 48/\pi Ja^2 Fo_o$ b- $\beta = 1 - (16/\pi Ja^2 Fo_o)^{1/2}$	$Nu_c = 12/\pi Ja \beta^3/(1 - \beta^3)$ $Nu_c = 4/\pi Ja \beta/(1 - \beta)$
Levenspiel (1959)	$\beta = \exp(-3.933 (T_s - T_l) \tau)$	$Nu_c = 1.968 D_b^2 h_{fg} \rho_g/k$
Ruckenstein (1959)	-----	$Nu_c = \sqrt{4/\pi} (Re_b Pr)^{1/2}$
Hewitt & Parker (1968)	$\beta = 1 - (\sqrt{4\pi/3} Ja^2 Fo_o / \beta^2 (1.3 D_b/(T_s - T_l))^{3/2})^{1/2}$	$Nu_c = \frac{4 \pi (1.3 D_b/(T_s - T_l))^{3/2} \beta^{1/2}}{(\beta^{1/4} - \beta^{5/4}) (\beta^{1/4} - 5 \beta^{5/4})}$
Isenberg & Sideman (1970)	$\beta = (1 - 3/\sqrt{\pi} Ja Re_{bo}^{1/2} Pr^{1/3} Fo_o)^{2/3}$	$Nu_c = 1/\sqrt{\pi} Re_b^{1/2} Pr^{1/3}$
Akiyama (1973)	$\beta = (1 - 2.8 + 0.37 Re_{bo}^{0.6} Pr^{1/3} Ja Fo_o)^{1/1.4}$	$Nu_c = 0.37 Re_b^{0.6} Pr^{1/3}$
Dimić (1977)	$\beta = (1 - 6/\sqrt{\pi} Ja Re_{bo} Pr Fo_o)^{2/3}$	$Nu_c = 2/\sqrt{\pi} Re_b Pr \beta^{-1/2}$
TRAC-PIA as in: Kelly & Kazimi (1982)	-----	<i>The maximum of.</i> $Nu_c = 12/\pi Ja$ $Nu_c = 2 + 0.74 Re_b^{1/2}$
Simpson et al. (1986)	$\beta = (1 - 4.35 Ja^{1.1} Pe_{bo}^{0.55} Fo_o^{1.11})^{2/3}$	-----
MINI-TRAC as in Hori & Toda (1991)	-----	$Nu_c = 0.02 Re_b Pr$
Chen & Mavinger (1992)	$\beta = (1 - 0.56 Re_{bo}^{0.7} Pr^{0.5} Ja Fo_o)^{0.9}$	$Nu_c = 0.6 Re_b^{0.6} Pr^{1/2} \beta^{0.4}$ Before detachment $Nu_c = 0.185 Re_b^{0.7} Pr^{1/2} \beta^{0.3}$ After detachment



a- Small bubble



b- Elongated bubble

Figure 4.1 Typical bubble photographs in the condensing region

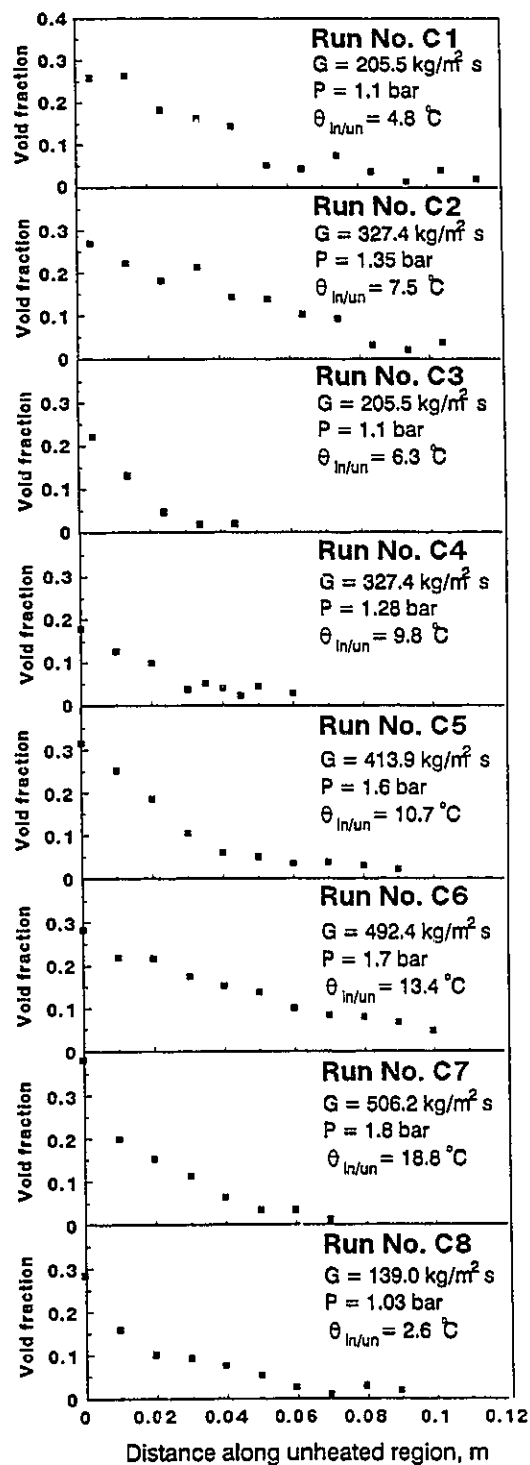
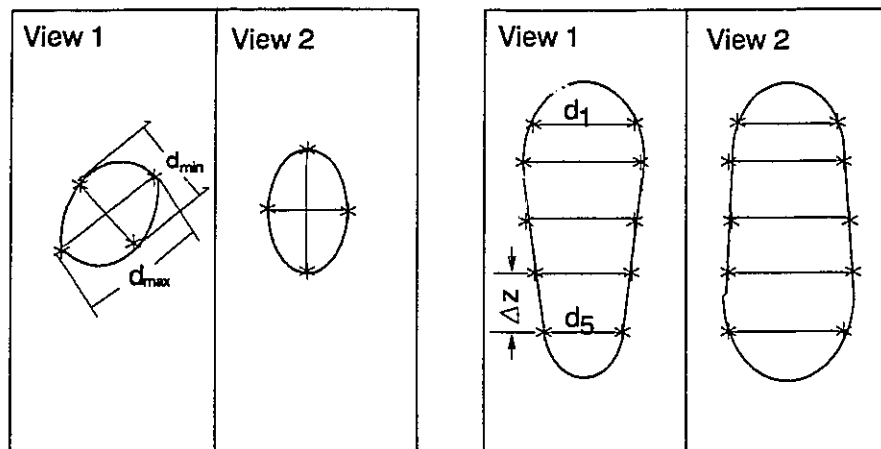
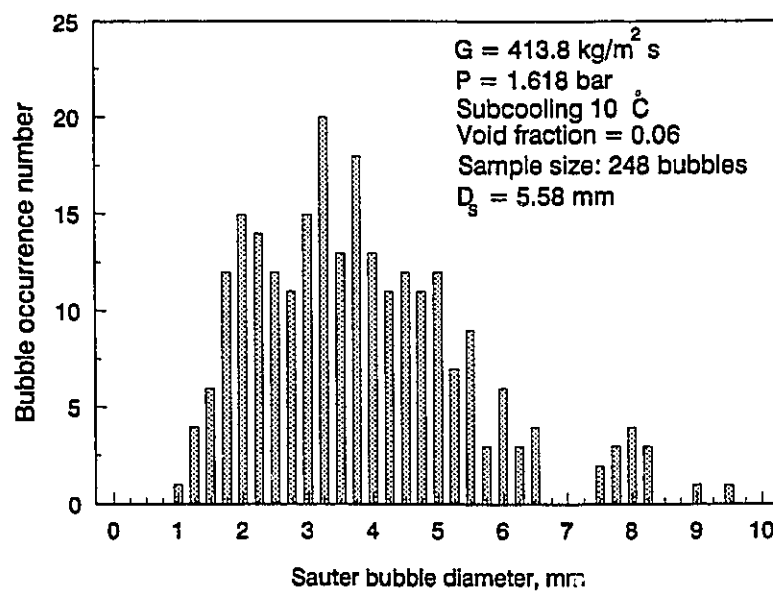


Figure 4.2 Void fraction distribution along condensing flow region



a- Small nearly spherical bubble

b- Elongated bubble

Figure 4.3 Bubble size and surface area measurement**Figure 4.4 Typical frequency distribution of measured Sauter bubble diameter**

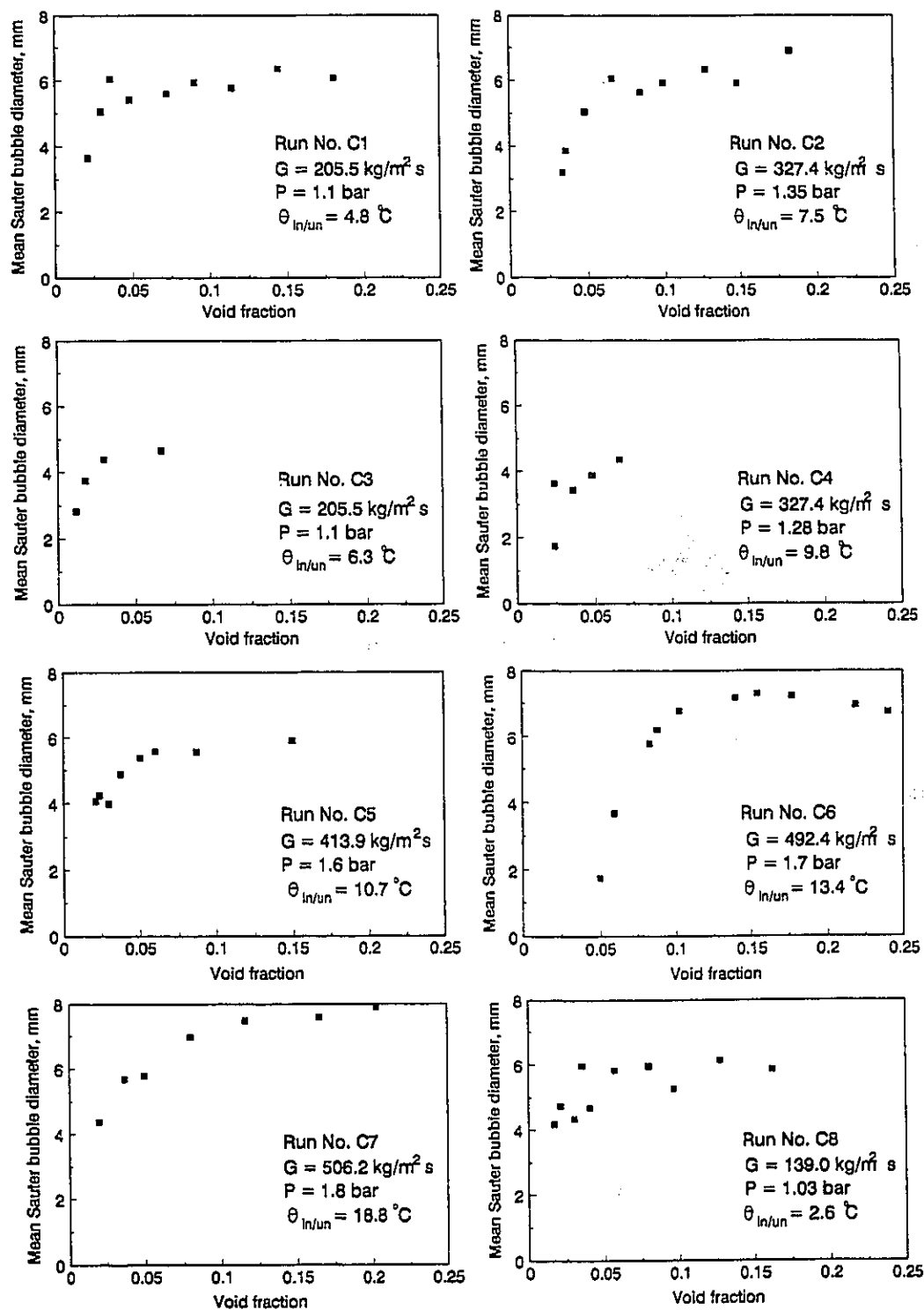


Figure 4.5 Measured mean Sauter bubble diameter versus measured void fraction

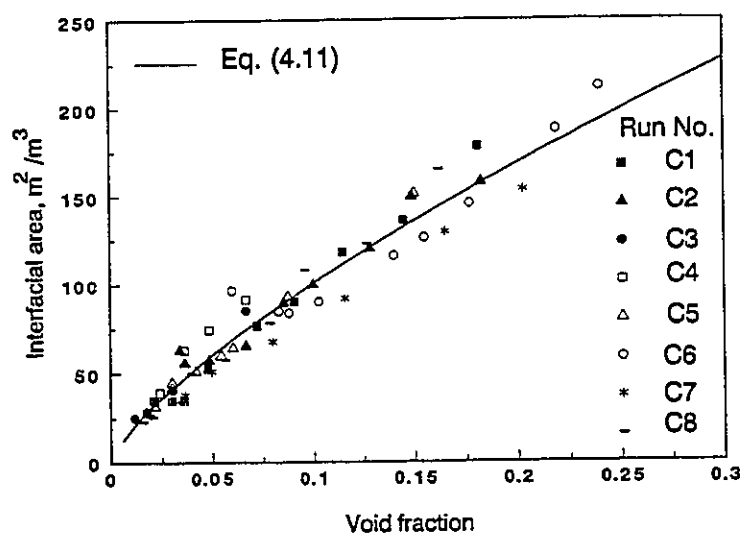


Figure 4.6 Relation between interfacial area concentration and void fraction

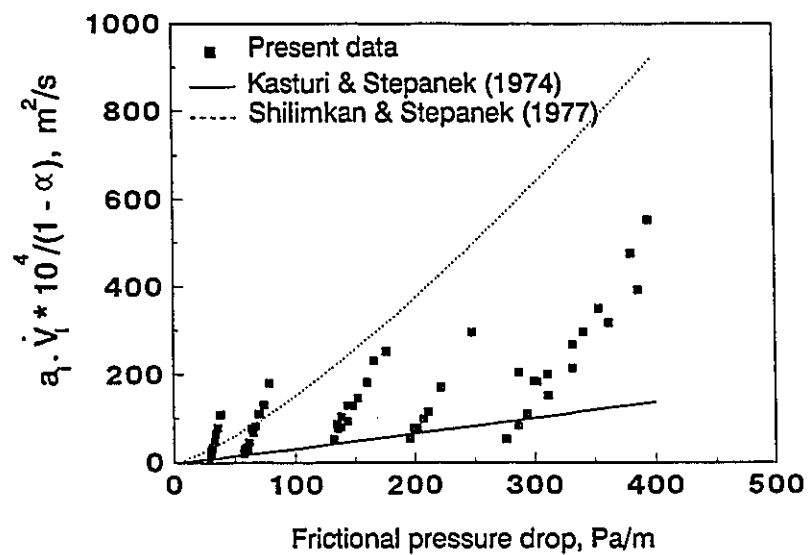


Figure 4.7 Comparison between measured interfacial area and previous correlations

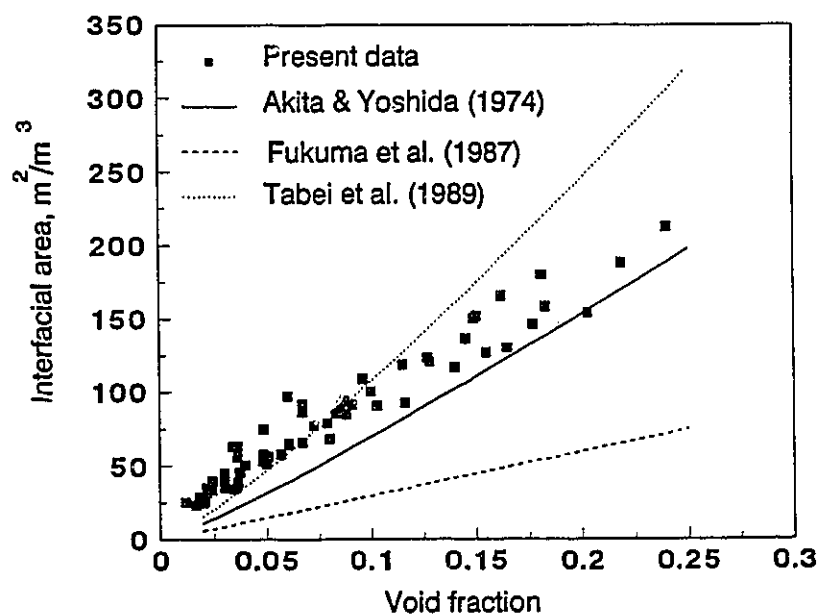


Figure 4.8 Comparison between measured interfacial area and previous correlations

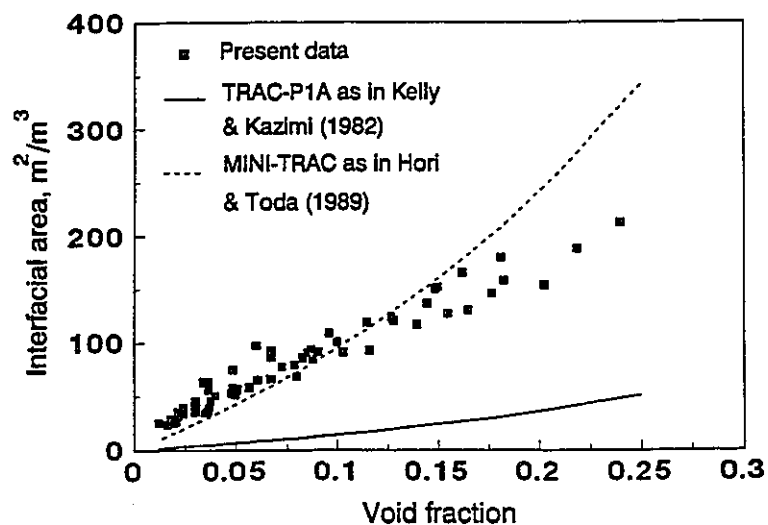


Figure 4.9 Comparison between measured interfacial area and previous correlations

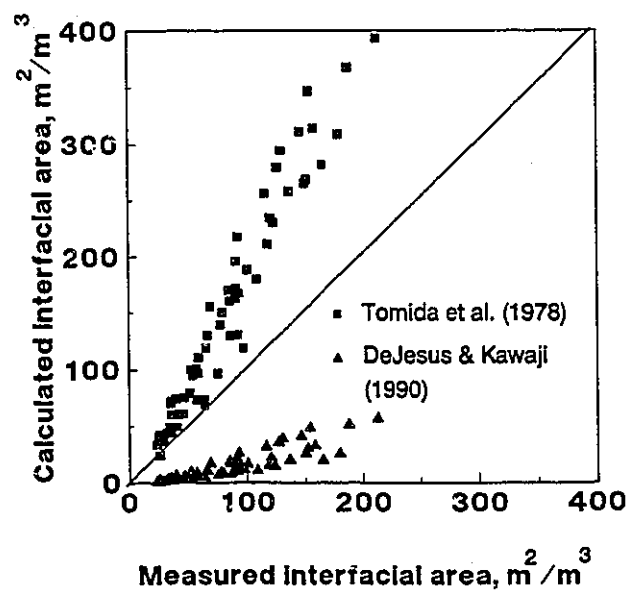


Figure 4.10 Comparison between measured interfacial area and previous correlations

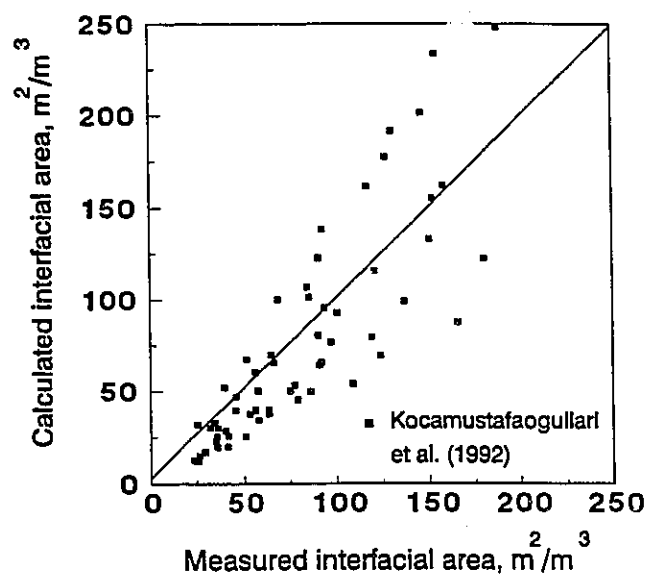


Figure 4.11 Comparison between present data and Kocamustafaogullari's model

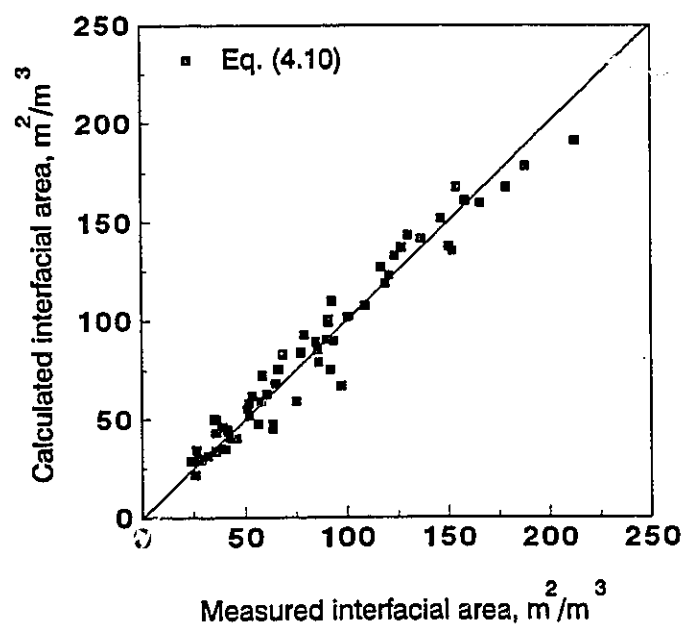


Figure 4.12 Comparison between proposed correlation and present data

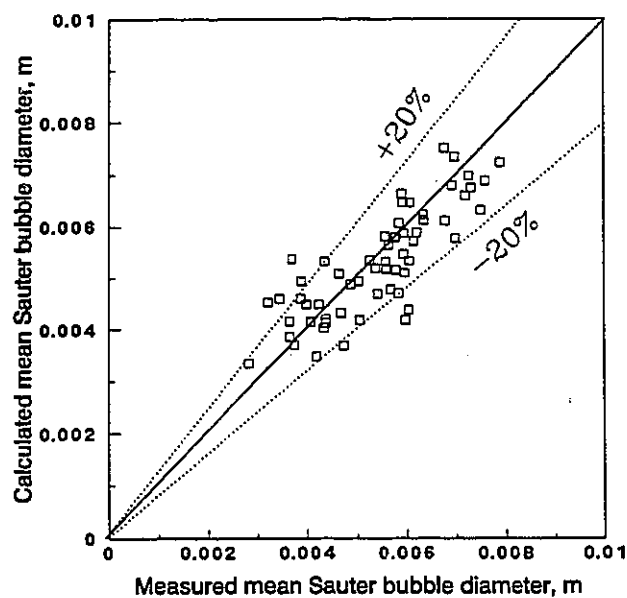


Figure 4.13 Comparison between calculated and measured mean Sauter bubble diameter

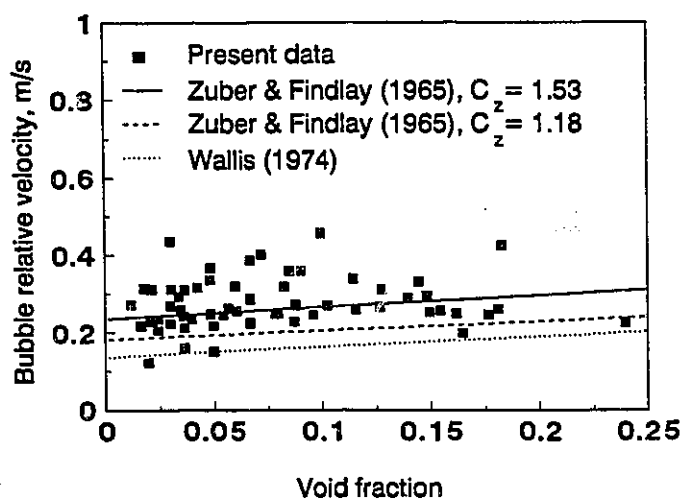


Figure 4.14 Bubble relative velocity

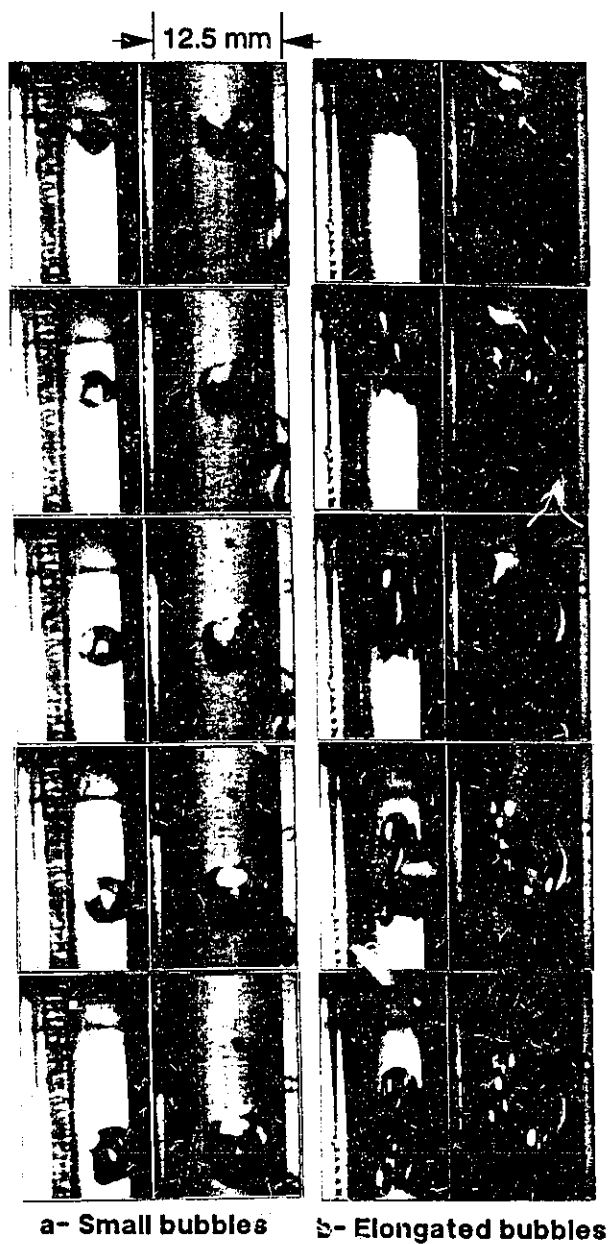


Figure 4.15 Samples of condensing bubbles

(obtained at 500 frame/s and 1 ms exposure time)

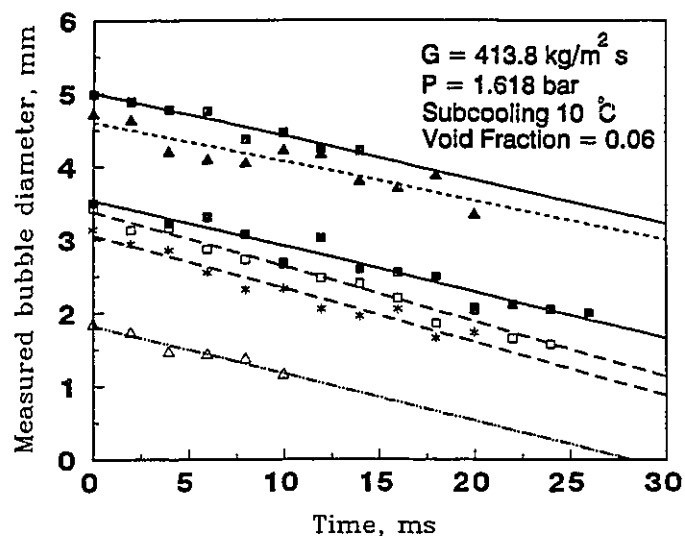


Figure 4.16 Typical condensing bubbles

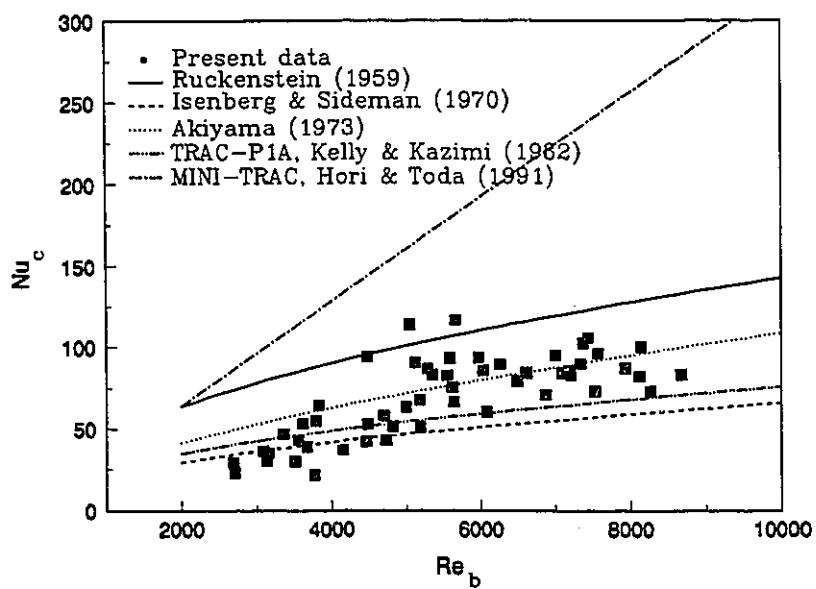


Figure 4.17 Comparison between present data of bubble condensation
Nusselt number and existing models

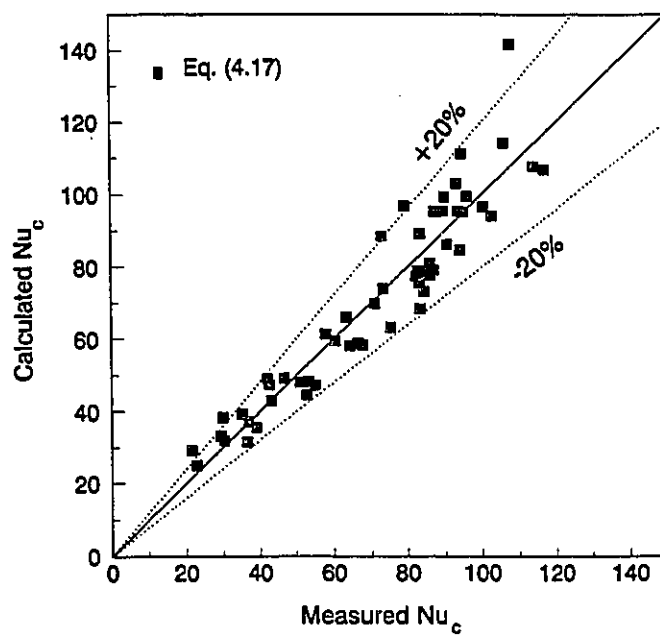


Figure 4.18 Comparison between present data and proposed correlation

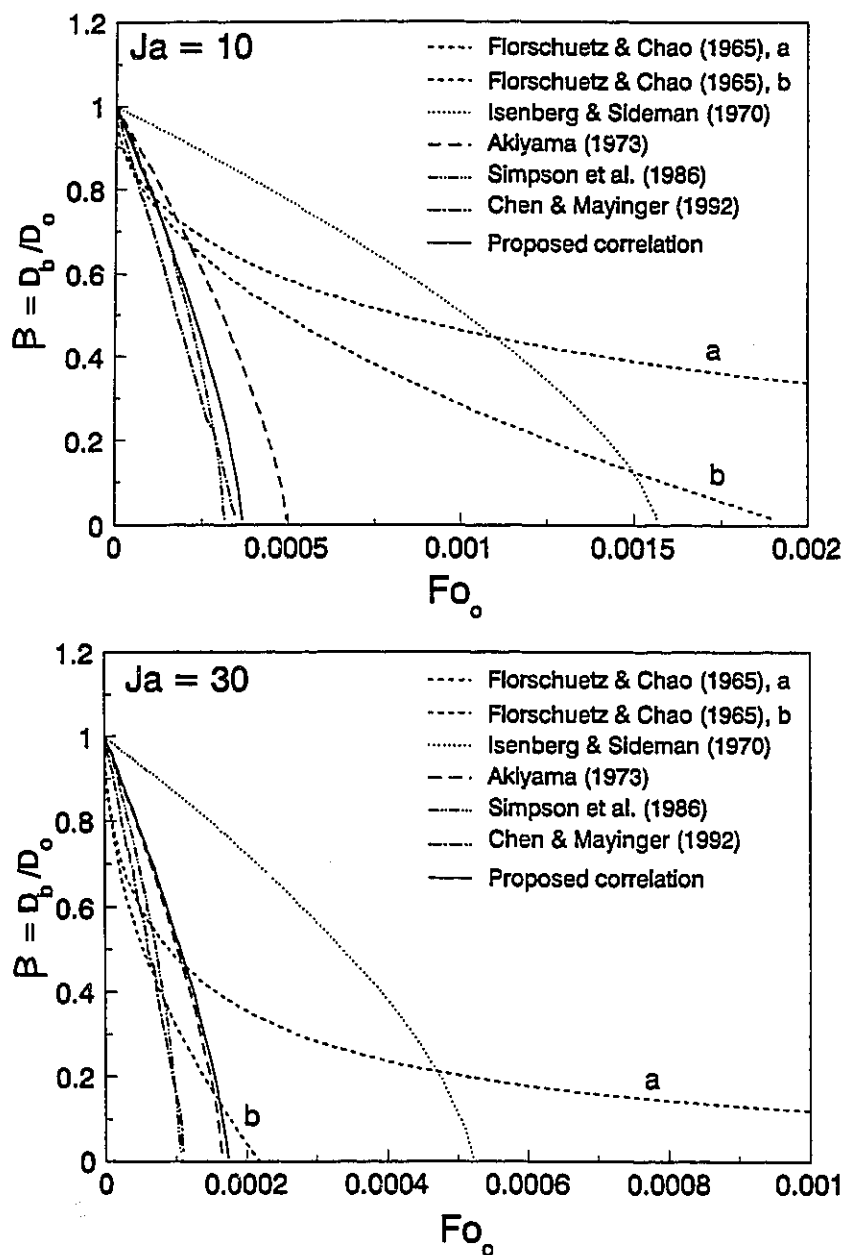


Figure 4.19 Comparison between the present model of bubble history and previous models ($Re_{b0} = 5000$, $Pr = 1.6$, $\alpha = 0.15$)

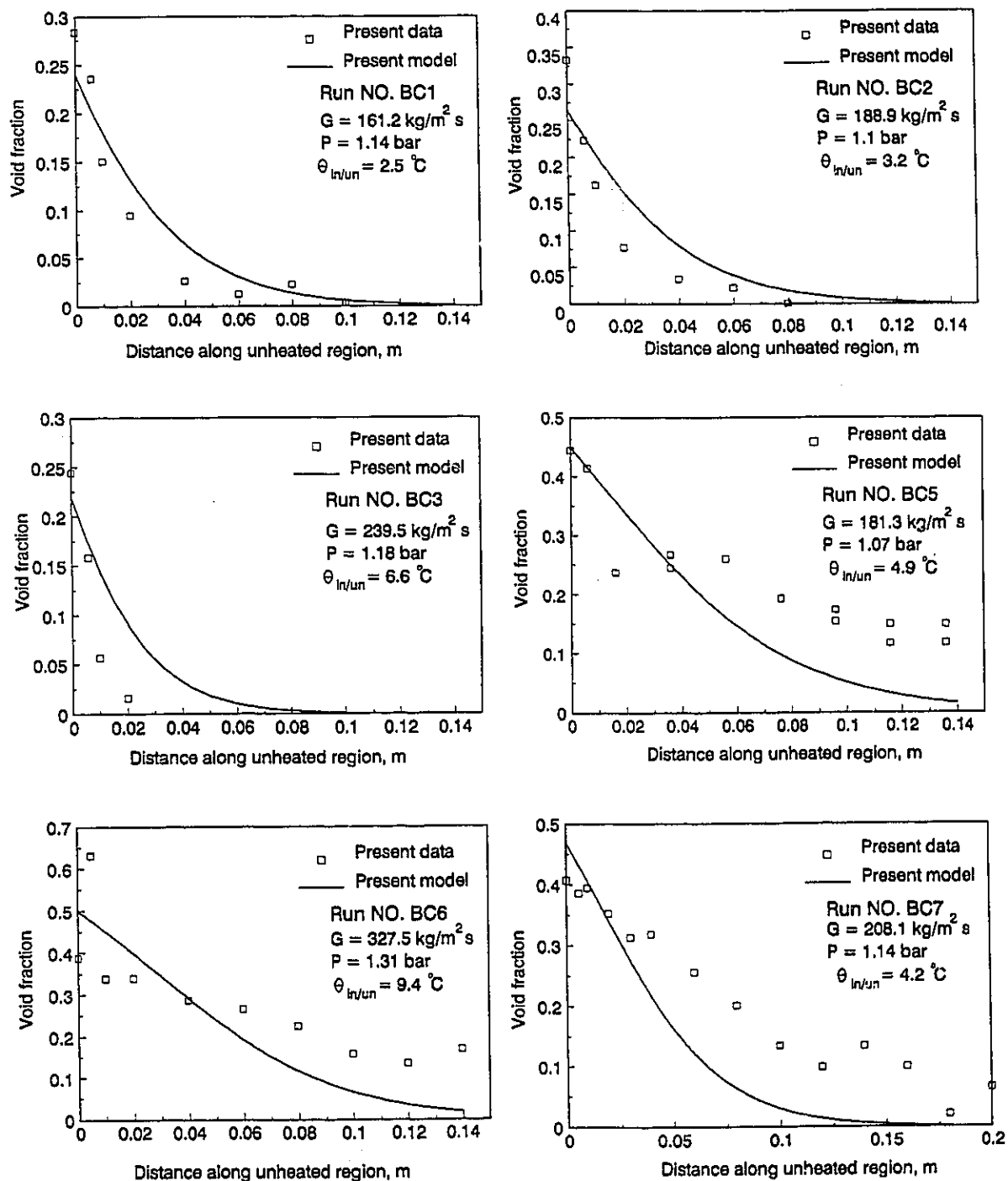


Figure 4.20a Void fraction Distribution along unheated region

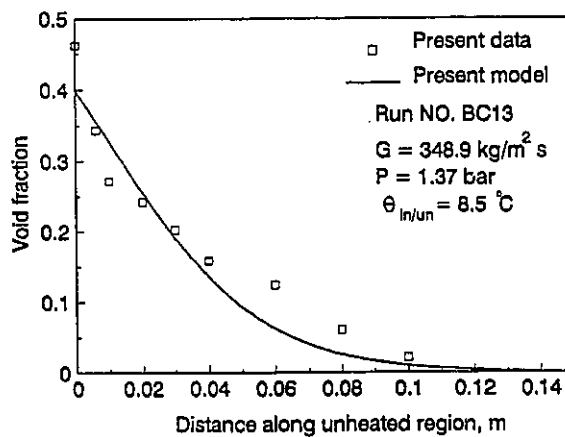
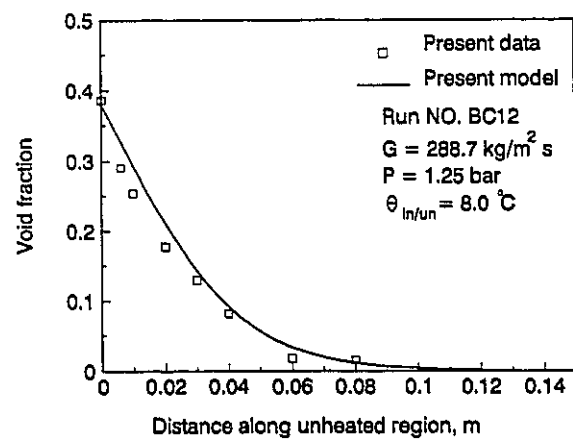
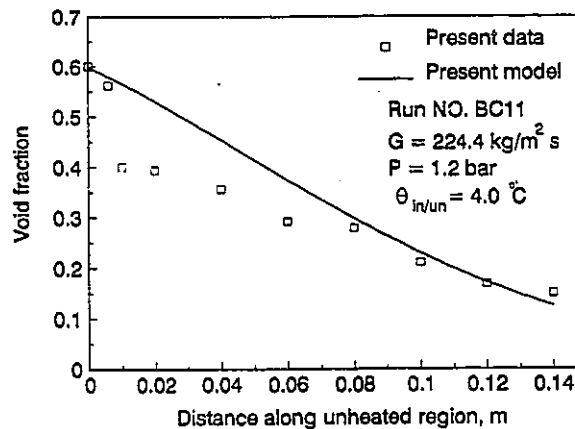
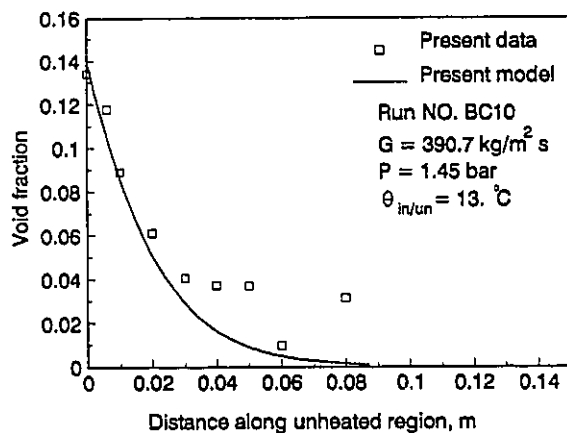
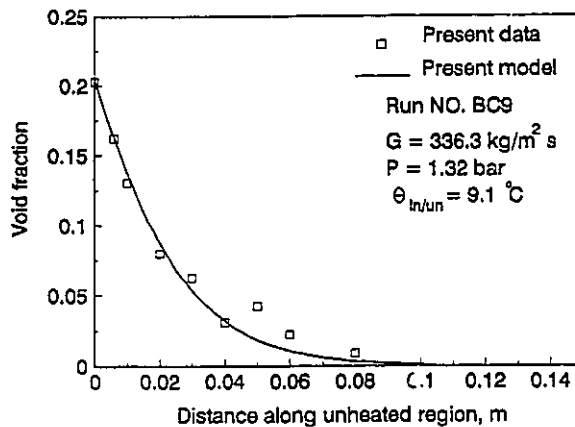
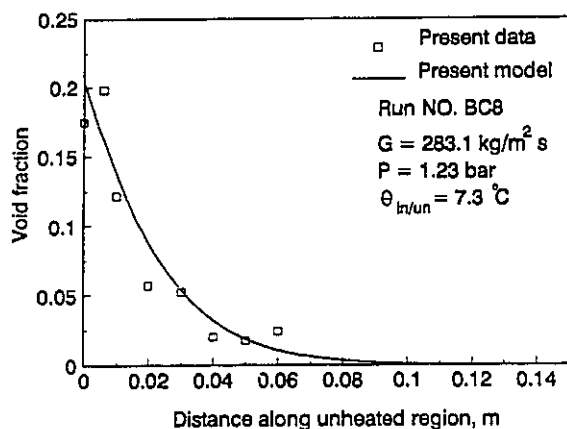


Figure 4.20b Void fraction Distribution along unheated region

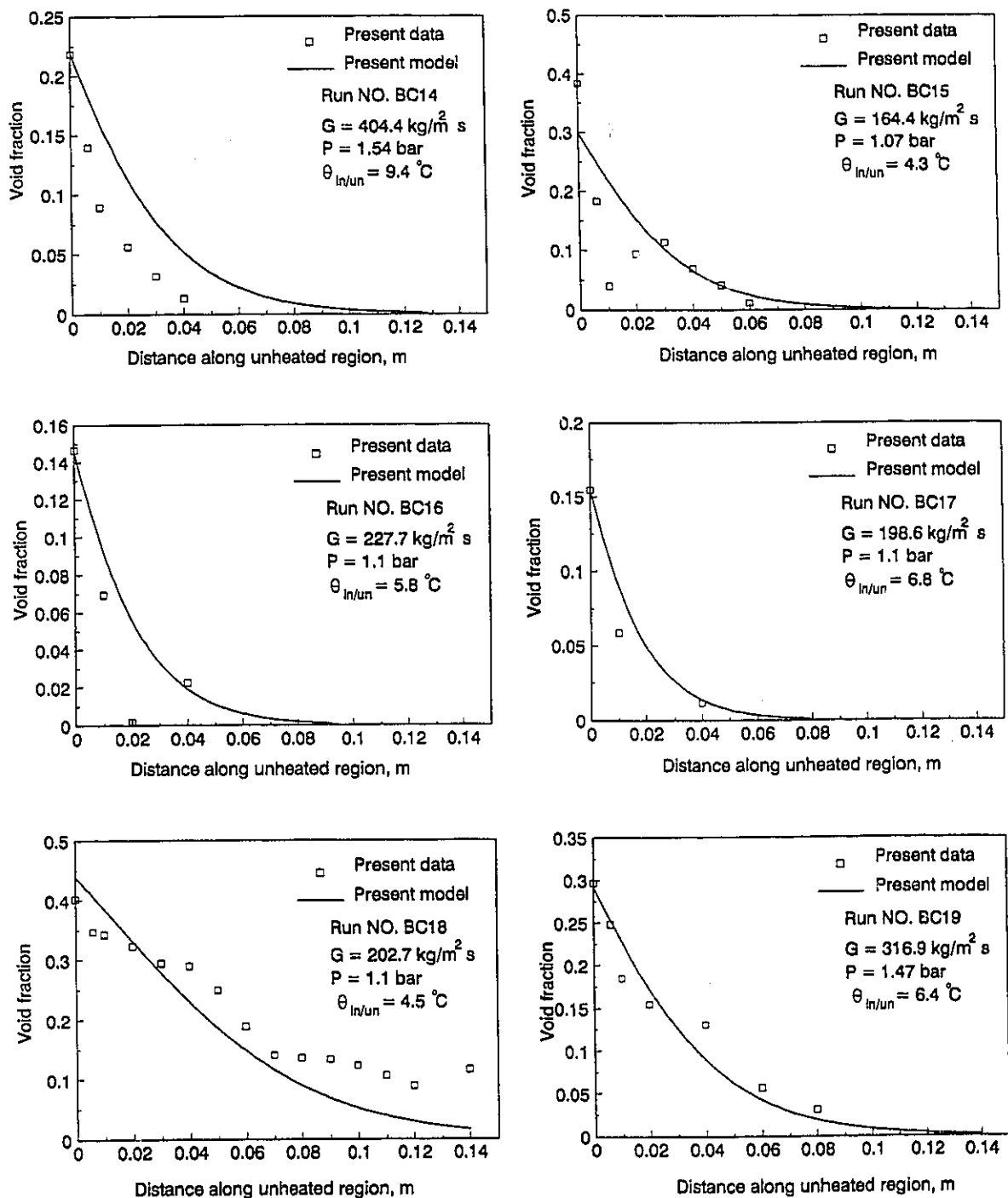


Figure 4.20C Void fraction Distribution along unheated region

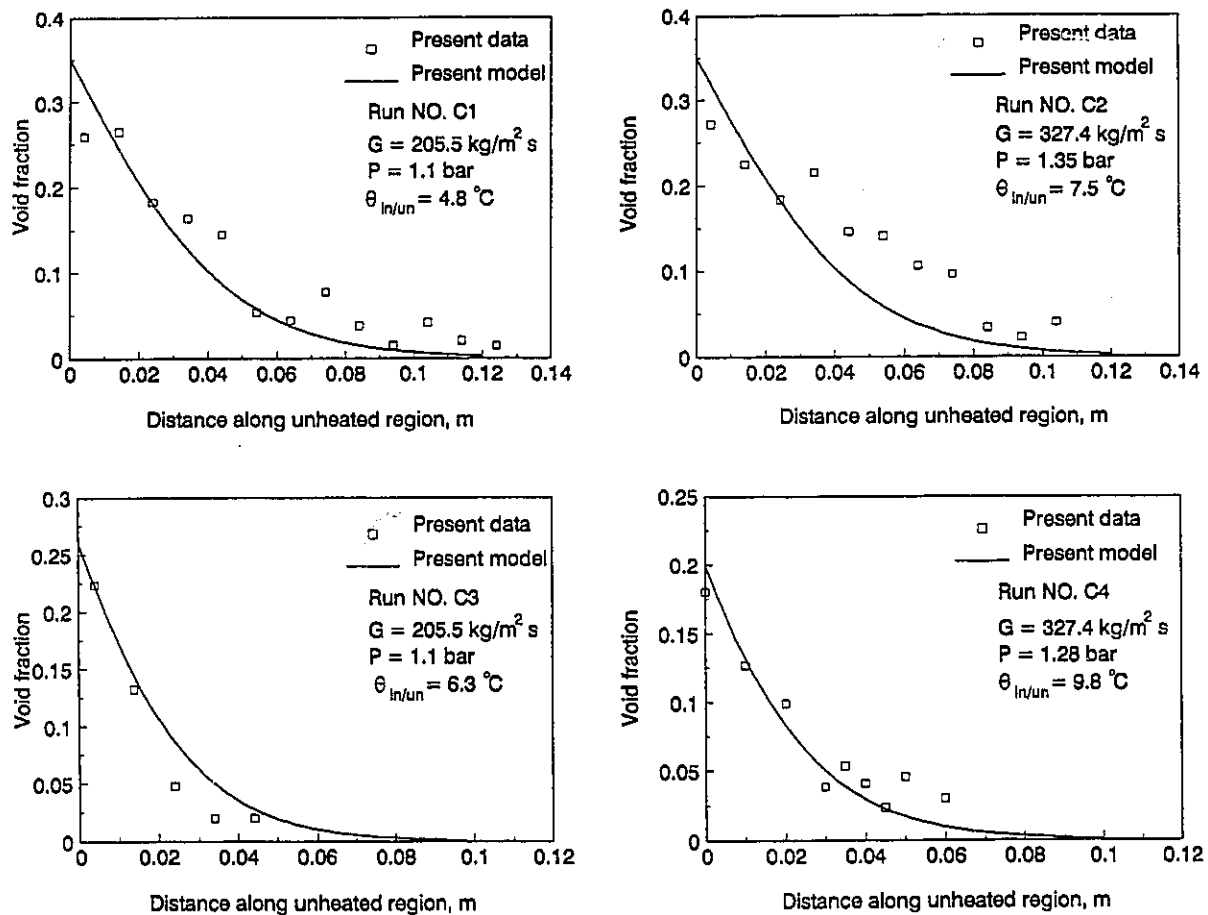


Figure 4.21a Void fraction Distribution along unheated region

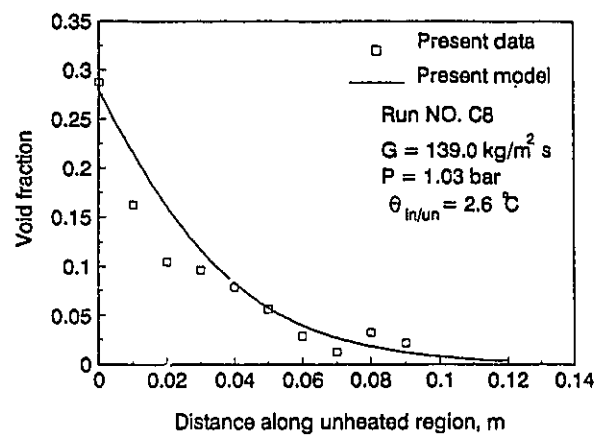
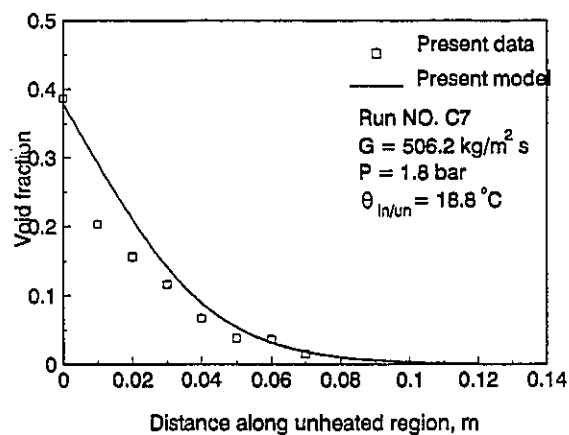
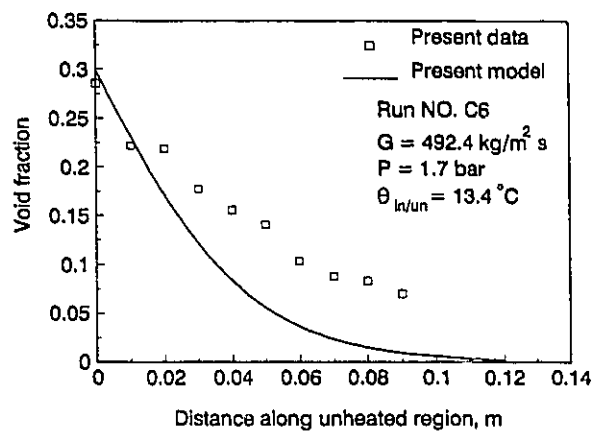
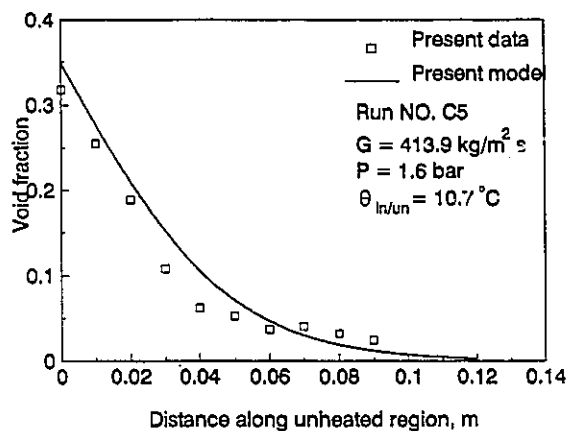


Figure 4.21B Void fraction Distribution along unheated region

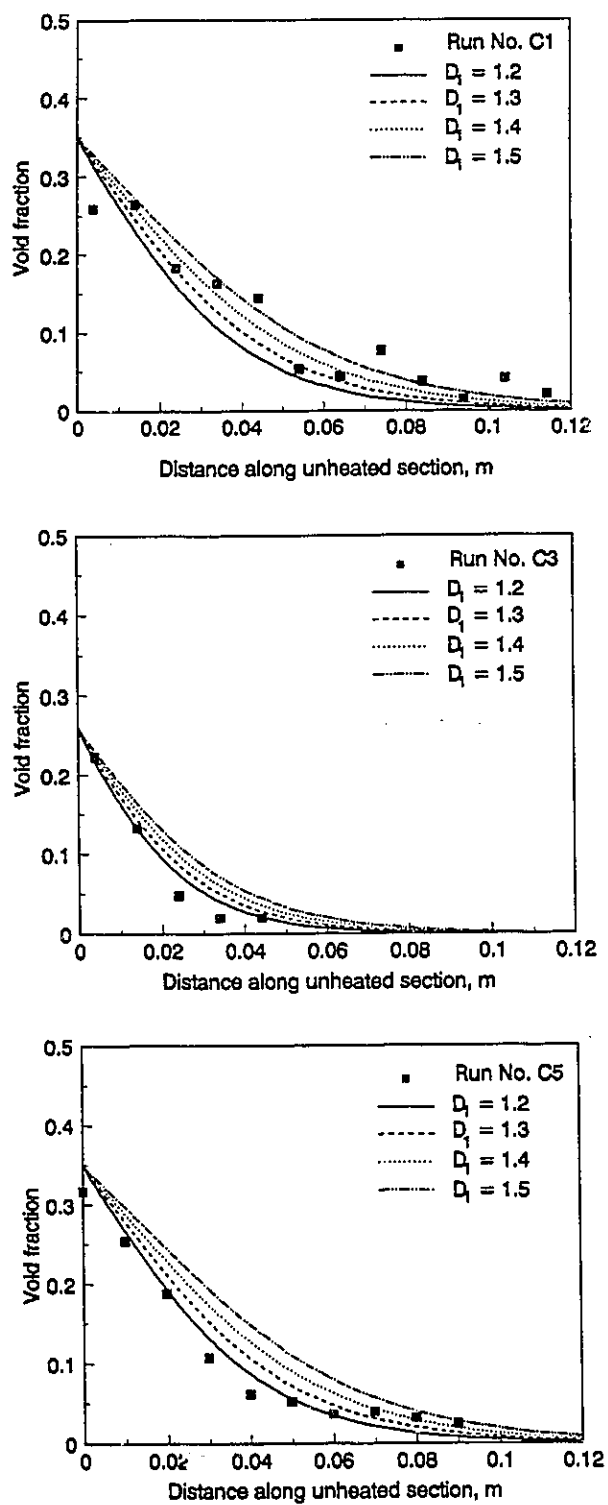


Figure 4.22 Effects of distribution parameters on void fraction profile

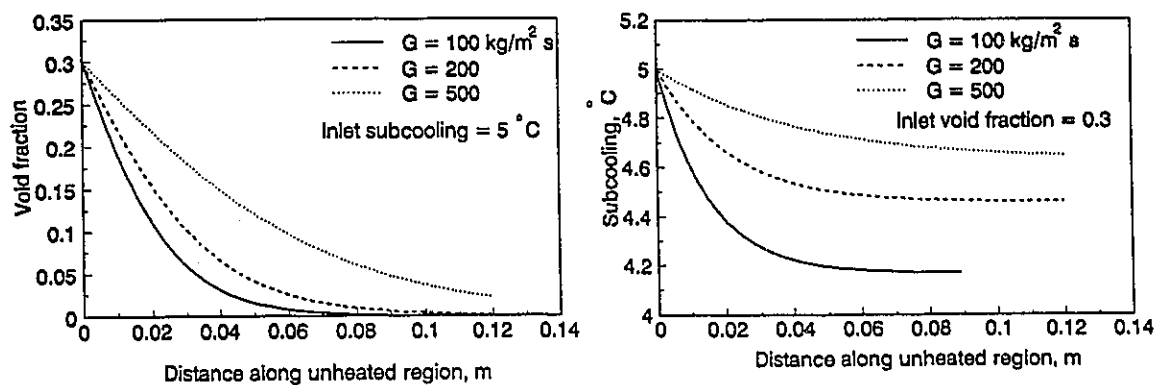


Figure 4.23a Effect of mass flux on void fraction and subcooling profiles

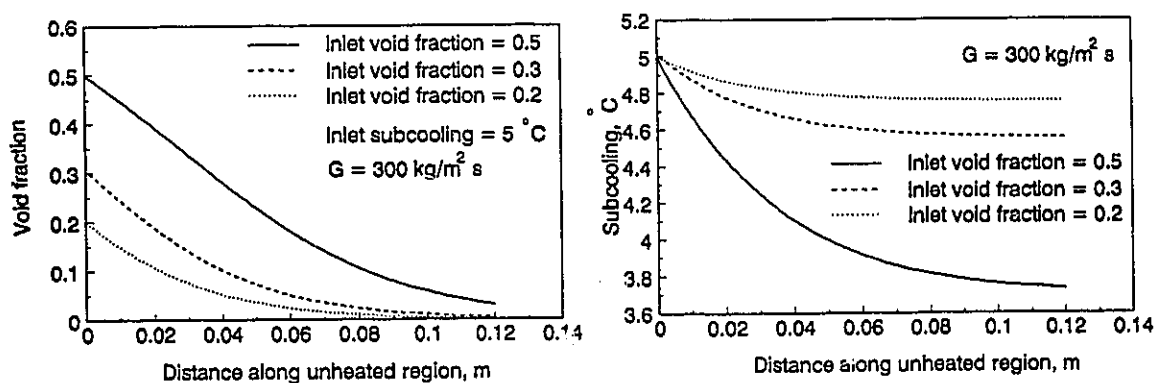


Figure 4.23b Effect of inlet void fraction on void fraction and subcooling profiles

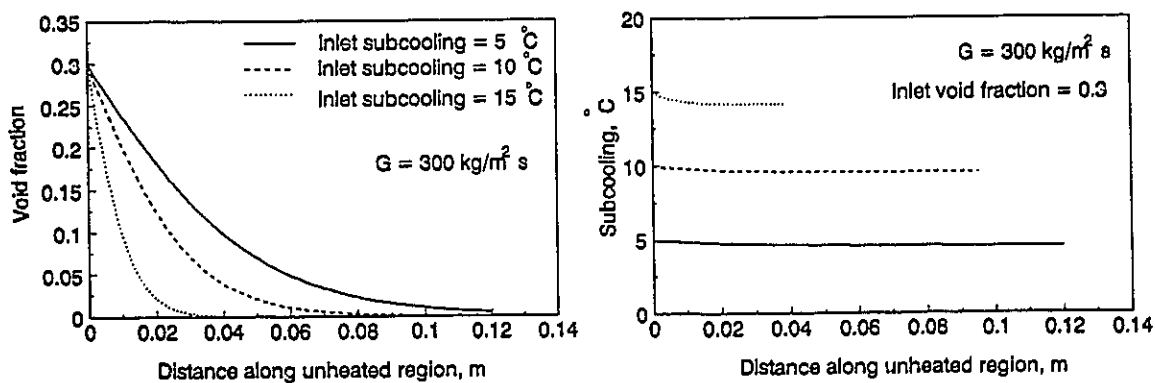


Figure 4.23c Effect of inlet subcooling on void fraction and subcooling profiles

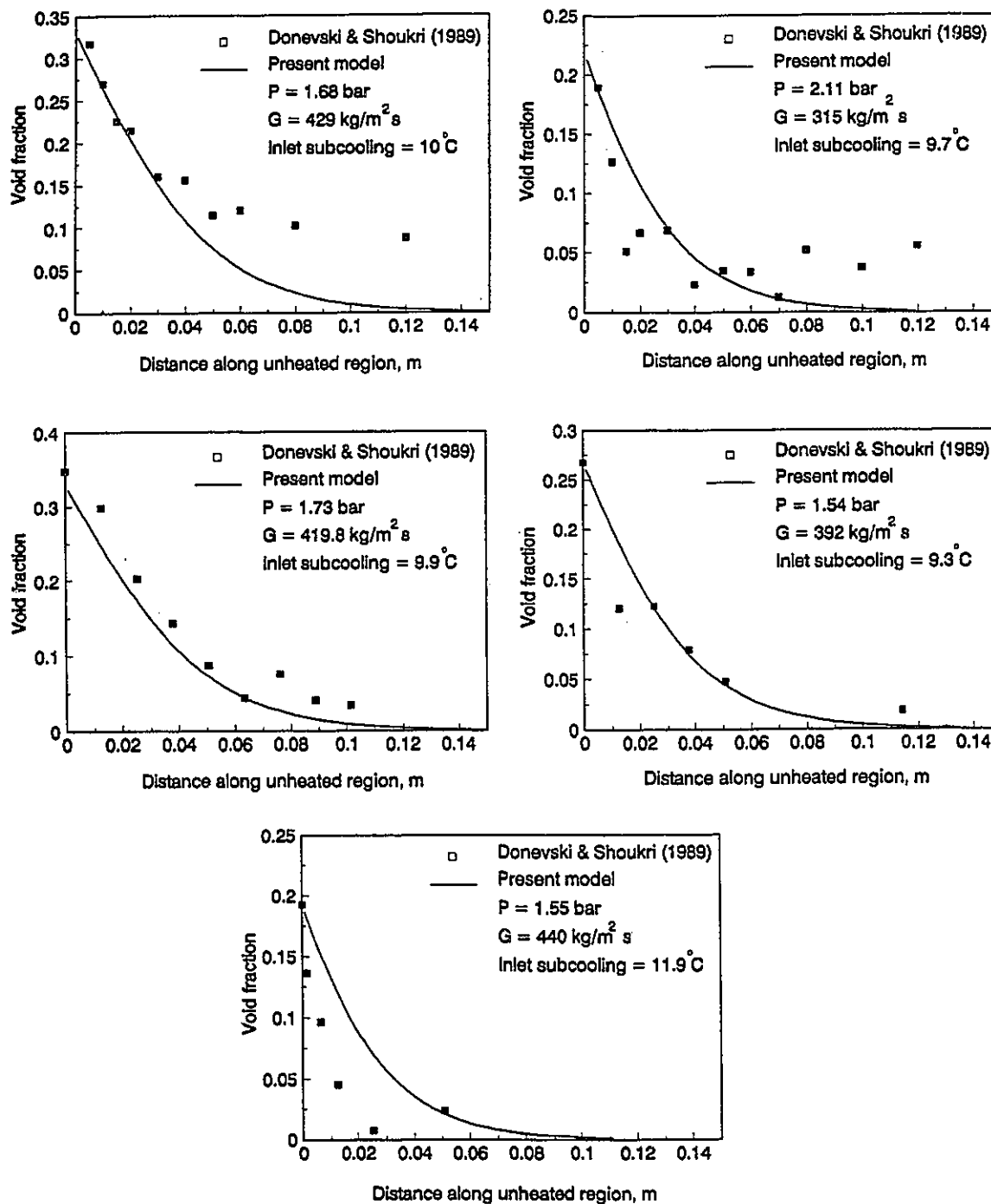


Figure 4.24 Comparison between present model and existing data

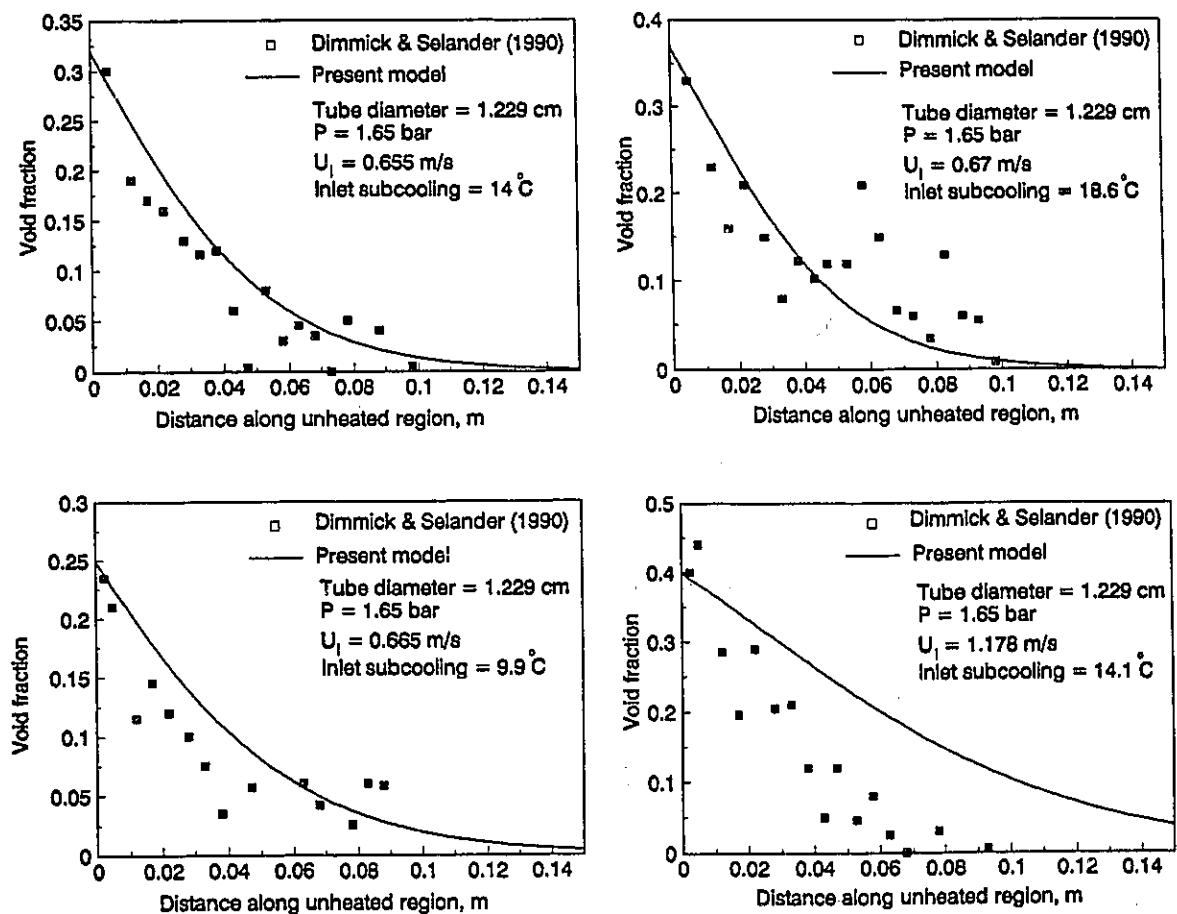


Figure 4.25 Comparison between present model and existing data

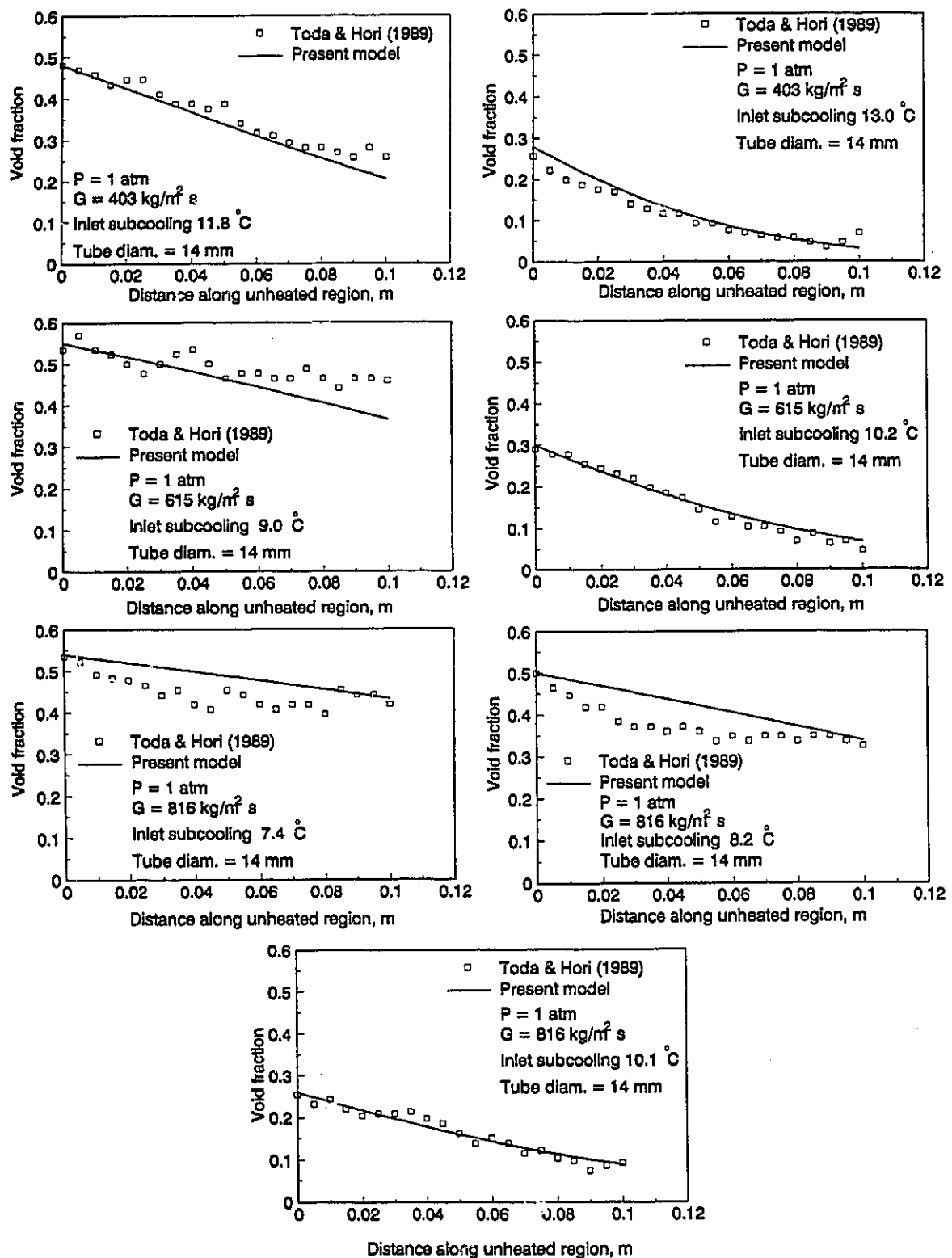


Figure 4.26 Comparison between present model and existing data

CHAPTER 5

BUBBLE BEHAVIOUR AND SIZE, NET VAPOUR GENERATION MECHANISM AND VOID FRACTION PROFILE IN SUBCOOLED FLOW BOILING

The high heat flux, usually required in engineering applications, has led to extensive studies in boiling. The enormous heat flux which can be achieved without using high heating surface temperature is the main advantage of the nucleate boiling regime. However, most studies have been concerned with pool boiling rather than forced convection boiling because of relative simplicity of the former, and in spite of the latter, far greater practical importance. Subcooled flow boiling is encountered in many applications; nuclear reactors, boilers, refrigeration systems and heat exchangers. As discussed in Chapters 1 and 2, *the* subcooled flow boiling region is divided in the literature into two regions, a highly subcooled region, where the void fraction is very low, and a slightly subcooled region, where the void fraction is significant. The transition between these two regions is called the net vapour generation (NVG) or the onset of significant void (OSV) point.

To understand the NVG phenomenon, many investigations have been conducted. In most of these studies, the NVG phenomenon was related directly or indirectly to bubble behaviour. Griffith et al. (1958) related the NVG to the bubble density on the heating surface. The authors specified the point at which the heating surface was fully covered with bubbles to identify the NVG point. Many authors including Bowring (1962), Levy (1967), Staub (1968), Rogers et al. (1987), Rogers and Li (1992) and Lee and Bankoff (1992) related the bubble detachment from the heating surface to occurrences at the NVG point. In another approach, Dix (1970) and Serizawa (1979) attributed the NVG phenomenon to the bubble ejection from the bubbly layer in the vicinity of the heating surface. Generally speaking, these ideas were developed for high pressure flows, typical in power reactors. In this case it was difficult to use high speed photography, because of the absence of a transparent tube which could resist high pressure, to visualize the flow. Despite the importance of what was happening at the NVG point in modelling the axial void fraction profile, insufficient effort was given to measuring detailed void fraction distribution and bubble size or for investigating bubble behaviour in the region near the NVG point, particularly in low pressure flow. Recently, Bibeau (1993), Shoukri et al. (1991), Stangl and Mayinger (1990), Dimmick and Selander (1990), Bibeau et al (1990) reported void fraction measurements in this region under low pressure conditions. They found that the void fraction profile upstream of the NVG point tended to be flat and formed a plateau longer than that associated with the

high pressure case. The Bibeau (1993) high speed photographic results indicated that no bubbles remained attached to the heating surface in this region.

In modelling of the axial void fraction profile in the slightly subcooled region, most existing models tended to require accurate information on the location of the NVG point. As discussed in Chapter 4, the two-fluid model can be considered as the most accurate mathematical formulation of two phase flow. As such, it captures more details at the vapour-liquid interface. However, using this formulation in subcooled flow boiling needs accurate knowledge on the bubble size, interfacial area concentration, bubble velocity and interfacial heat transfer coefficient.

In the present work, detailed experiments were carried out to generate a data base for subcooled flow boiling at low mass flux and low pressure. The measurements included axial void fraction, liquid subcooling and heating surface temperature profiles in subcooled flow boiling. A high speed video system was used to collect visual information to study bubble behaviour before, at, and after the NVG point in order to determine its physical mechanism. A digital image processing technique was used to analyze the high speed visual information and to measure bubble size distributions along the subcooled boiling region.

5.1 Experimental Results

Two sets of experiments were carried out at different levels of mass flux, heat flux and inlet subcooling. The test conditions are listed in Tables 3.1 and 3.3 respectively. In set number one, which includes 19 experimental runs, the void fraction, heating surface temperature and liquid subcooling profiles were measured along the heating section. In set number three which includes 10 experimental runs, a high speed video system was also used to collect visual information along the heating section.

5.1.1 Void Fraction Profiles and NVG Point

The measured void fraction profiles along the subcooled boiling regions are shown in Figures 5.1 and 5.2 for experiment sets numbers one and three respectively. The test conditions of these runs are listed in Table 3.1 and 3.3. The results showed that the void fraction profile was almost flat at the beginning of the heating section, i.e in the high subcooled region. The void fraction was in the 2-9% range. The void fraction started to increase significantly at a certain point defining the location of the NVG point. The region after this point, where the void fraction was significant, was called the slightly subcooled region. The location of the NVG point was defined by fitting the void fraction data in the highly subcooled boiling region with a straight line,

the point at which the profile deviates from the straight-line fit was considered the NVG point as shown schematically in Figure 5.3a. This procedure is applied as shown in Figure 5.3b. Subcooling at the NVG point was calculated from the heat balance between the heating section inlet and the NVG point,

$$T_s - T_d = T_s - T_{in} - \frac{q \rho_h Z_d}{G A C_p} \quad (5.1)$$

where T_d is the liquid temperature at the NVG point, T_{in} is the liquid temperature at the heating section entry, Z_d is the axial location of the NVG point, P_h is the heated perimeter and A is the flow area (the cross sectional area of the channel). This procedure was followed rather than using the measured subcooling profiles for two reasons; 1- the procedure matches that of other investigators, 2- the latent heat gained by evaporation will be very small compared to the sensible heat gained by the liquid phase in the highly subcooled region. The conditions (subcooling) at the NVG point, estimated by this method, are shown in Figure 5.4. In general, the subcooling at the NVG point tends to increase as the applied heat flux increases. As shown in Figure 5.1 and 5.2, the NVG point is not sharply defined and it rather falls in a range not at a point. Uncertainty analysis for the subcooling at the NVG point was reported in Appendix B. It was found that the uncertainty in computing the subcooling at the NVG point was in the range $\pm 5\%$ - $\pm 15\%$.

Comparisons between present data and available data from literature at low pressure and existing NVG models (Table 2.4) are shown in Figures 5.5a-

5.5i. For practical reasons, available data for water at low pressure were used only in the comparisons. It should be noted that the procedure mentioned earlier was used to determine the location of the NVG point for other data from authors who reported void fraction profiles. As shown in Figures 5.5a and 5.5b, the models of Griffith et al. (1958), Dix (1970) and Hancox and Nicoll (1974) underpredict the experimental data except that of Sekoguchi et al. (1974) and Evangelisti and Lupoli (1969). The difference between the last two data sets and the others is that the range of heat flux was low for the last two sets. The prediction of Saha and Zuber's model (1974) fall within the experimental data as shown in Figure 5.5c but the scatter is too high and no clear trend for the $(q D_h/k \Delta T_d)$ parameter versus the flow Peclet number Pe is shown. The model of Ünal (1974) can only represent the high mass flux data as shown in Figure 5.5d. The model of Yang and Weisman (1991) depends on bubble diameter. The bubble diameter was calculated from the proposed correlation, Equation (5.13). The subcooling at the NVG point obtained by trial and error is shown in Figure 5.5e. Levy's model (1967) is capable of predicting the data, except the data of Sekoguchi et al. (1974), within $\pm 40\%$ as shown in Figure 5.5f. In this model, bubble detachment from the heating surface was considered the reason for the NVG phenomenon. This physical mechanism was not confirmed particularly for low pressure flow. In fact, the high speed photography results indicated that bubbles detach from the heating surface before the NVG point. This will be discussed later. The model of Sekoguchi et al. (1974) is only able

to predict their data as shown in Figure 5.5g. Generally, it overpredicts the other data and no clear relation is shown between x_d , the thermodynamic quality at NVG, and the boiling number. The model of Rogers et al. (1987), as shown in Figure 5.5h, predicts most of the experimental data, except the data of Sekoguchi et al. (1974) and Edelman and Elias (1981), within $\pm 40\%$. In this comparison, the bubble static attachment angle θ_0 was assumed 80° as proposed by Rogers et al. (1987). It should also be noted that this model relies on modelling bubble detachment as the cause of the NVG phenomenon, which is incorrect particularly for low pressure flow as previously mentioned. The model of Serizawa (1979) underpredicts the experimental data by about 50% as shown in Figure 5.5i.

Generally, as shown in Figures 5.5a-i, available models of the NVG, developed on the basis of different theories, were incapable of predicting the experimental data at low pressure. The comparison also shows that the data of Sekoguchi (1974) is hardly represented by available NVG models. This may be attributed to the range of their experimental conditions. Edelman and Elias (1981) data has very low subcooling at the NVG point (0.5-5 °C), thus making it difficult to differentiate from saturated boiling .

5.1.2 Liquid Subcooling Profiles

The water subcooling along the heating section was measured by using

three calibrated thermocouples located at its inlet, middle and end. These thermocouples were located in the middle of the annular gap. The measured results are shown in Figure 5.6. The subcooling values are also listed in Tables 3.1 and 3.3 for experimental sets number one and three respectively. Although the temperature was measured only at the mid-distance in the radial direction, it will be very close to the average liquid temperature along the radial direction due to turbulence enhanced by bubble growth-collapse cycles. The temperature gradient is expected to be linear near the heating section entry where most of the applied heat is absorbed by the liquid phase. After the NVG point, where the evaporation is intensified, the rate of increase of liquid phase temperature will be less than that near the entry. However, the change in liquid temperature should be close to linear because the true quality, i.e. actual vapour mass content, of the flow is very small.

5.1.3 Heating Surface Temperature

The inner heating surface temperature was measured by using the sliding thermocouple at two centimetre steps along the heating section. Under the present test conditions, the ONB point occurred near the inlet of the heating section. This was the reason of the approximately uniform wall superheat profiles shown in Figure 5.7 and 5.8. The outer temperature of the heating surface, i.e. the flow boiling side, can be calculated using the conduction heat

transfer theory combined with an inner heat generation. For a very thin cylindrical wall, the temperature difference across the heating wall can be estimated as:

$$T_{wi} - T_w = \frac{q \delta_w}{2 k_s} \quad (5.2)$$

where T_{wi} and T_w is the inner and outer wall temperature respectively, δ_w is the heater thickness and k_s is the thermal conductivity of heater material.

Many empirical correlations developed for subcooled flow boiling coefficient are available in the literature; i.e Shah (1983), Shah (1977), Moles and Shaw (1972), Gungor and Winterton (1986), Hodgson (1968) and Bjorge, Hall and Rohsenow (1982). The model of Shah (1983) was used to predict the heating surface temperature for the test conditions listed in Tables 3.1 and 3.3. For the following conditions:

$$\begin{aligned} Bo &< 0.0003 \\ \frac{T_s - T_l}{T_w - T_s} &< 2 \end{aligned} \quad (5.3)$$

Shah (1983) correlated the heat flux at the heating surface by:

$$q = 230 h_{sp} Bo^{1/2} (T_w - T_s) \quad (5.4)$$

where the single phase heat transfer coefficient, h_{sp} , can be calculated from the Dittus-Boetler correlation, Equation (2.7). It was found from the comparison

between the prediction of the above correlation and the outer heating surface temperature that the constant of the above equation should be multiplied by a factor of 1.187 (i.e. the constant 230 should be modified to 270) in order to reasonably predict the present data. The comparison between Shah's model after this modification and the present data is shown in Figure 5.9. In the comparison the average heating surface temperature along the heater was used. The comparison indicates that Shah's model (1983) is capable of predicting present data within $\pm 20\%$.

5.2 Bubble Behaviour in Subcooled Flow Boiling

5.2.1 Background

It is well accepted that a bubble is generally initiated from a small gas filled cavity or crack on a solid surface, provided that the surrounding fluid is heated to a sufficiently high temperature. The nucleation process for nucleate pool boiling was described in detail by Hsu (1962) and Cole (1979). Many theories have been established to describe the bubble growth process in nucleate pool boiling among which is the microlayer evaporation beneath the growing bubble. In this mechanism, the evaporation rate is controlled by the heat transfer through a very thin liquid film (e.g. $4\text{ }\mu\text{m}$) underneath the bubble base, between it and the heating surface. The microlayer theory is well established; Cooper and Lloyd (1969), Van Stralen et al. (1975) and Zijl et al. (1979). The microlayer thickness was measured by many investigators including, Voutsinos and Judd (1975) and Koffman and Plesset (1983). In another bubble growth mechanism, Mikic and Rohsenow (1969) attributed the bubble high growth rate to the evaporation at the liquid-bubble interface which generated fast temperature fluctuations, associated with bubble nucleation cycle, in the superheated liquid layer surrounding it. Van Stralen (1979) reported temperature fluctuations of the heating surface during nucleate pool boiling. These fluctuations were attributed to the relaxation of the heating surface due to the nucleation process. The mechanism can be explained as

follows; before nucleation commences (i.e. after the last bubble detachment), the wall temperature rises because of the low single phase heat transfer coefficient until a certain point when the nucleation starts and accordingly the wall temperature falls very quickly due to the high evaporation coefficient. As the bubble grows, a microlayer is formed beneath it and the thickness of the microlayer increases as the bubble surface advances. As the bubble growth continues, the microlayer becomes thicker and consequently, the wall temperature starts to rise again until the bubble detaches from the heating surface to start a new cycle.

Bubble dynamics in flow nucleate boiling were examined in a few studies. Among these studies, Koumoutsos et al. (1968) and Zeng et al. (1993) investigated bubble departure in horizontal flow boiling and Gunther (1951), Abdelmessih et al. (1972), Akiyama and Tachibana (1974), Cooper et al. (1983) and Bibeau (1993) reported experimental investigations of bubble dynamics in vertical upward flow boiling. Ünal (1975) and Meister (1979) studied bubble growth and collapse in subcooled flow boiling theoretically. However, they did not include bubble detachment in their studies, i.e. they considered that the bubble grew and collapsed on the heating surface perhaps causing a longer condensation period. In their analysis, the bubble continued to receive heat energy from the heating surface during the total condensation period. A more reasonable description is transfer of heat from the wall to the bubble should stop as soon as the bubble departs from the heating surface in

the normal direction. To clarify this point, consider nucleate pool boiling on a horizontal surface. During the growth process, the forces acting on the bubble determine its size at departure. After detachment, the bubble moves in the vertical direction due to buoyancy. In this type of boiling, the normal detachment marks the end of the evaporation process for subcooled or saturated boiling regimes. The conditions at this point are important parameters in determining bubble growth, waiting times, and, consequently, the bubble frequency.

In the case of flow boiling, there are two types of detachment. As the bubble grows on a heating surface, it reaches a certain size and starts to slide along the heating surface (first type) and the growth continues until it leaves the surface (second type). The first type is called detachment or parallel detachment (Bibeau, 1993). The second type is called bubble ejection (Dix, 1970 and Serizawa, 1979), normal detachment (Bibeau, 1993) or lift off (Zeng et al., 1993). For vertical upward flow, the parallel detachment is very difficult to determine since it begins because of the mirage near the heating surface as reported by Cooper et al. (1983). High speed photographic results reported by Bibeau (1993) showed that parallel detachment occurred very early after nucleation. It also showed that the bubble continued growing while sliding along the heating surface until it reached the maximum size after which the bubble size decreased as the condensation rate exceeded the evaporation. The normal detachment occurred while the bubble condensed along the heating

surface. The bubble collapsed completely as it moved through the subcooled bulk. The normal detachment is the phenomenon which determines the end of the evaporating process in subcooled flow boiling.

Bubbles detach in two directions due to the forces acting on them. Modelling these forces is a very difficult task because of the link between them and the thermal bubble growth-collapse process. Formulation of these forces was investigated for pool boiling by Beer (1973) and Zeng et al. (1993a) and for forced flow boiling along a horizontal surface by and Koumoutsos (1968) and Zeng et al. (1993b). For upward flow boiling, the forces acting in the axial direction are buoyancy, drag, weight, surface tension and inertia of the surrounding liquid. Forces acting in the normal direction are surface tension, excess pressure force, capillary pressure force, drag and the inertia of surrounding liquid. However, the cause of the normal detachment was not agreed upon by various researchers. Serizawa (1979) reported that after parallel detachment the bubble tended to slide along the heating surface due to thermo-capillarity action (surface tension) forming a bubbly layer. The instability of bubbles in this layer is the cause of bubble normal ejection. Contrarily, Bibeau (1993) suggested that the gradient of the surface tension force, due to temperature gradient near the heating surface, was the reason of the normal detachment.

Bubble detachment cannot be studied independently from the bubble growth-collapse process. Many authors used asymptotic bubble growth relation

($D_b = C \tau^{1/2}$) to calculate the inertia forces; Beer (1973) and Zeng et al. (1993a). While their models reasonably predict the bubble diameter at detachment, they are incapable of predicting the actual bubble detachment time. Any investigation of the bubble detachment should be carried out simultaneously with the bubble growth-collapse process.

5.2.2 Visual Observations

In the following, some visual observations derived from high speed photography are presented. For the experimental runs, listed in Table 3.3, the high speed video system was used to visualize the flow at two centimetres increments along the subcooled flow boiling region. In fact, two procedures were followed to obtain the visual information. Firstly, the camera was focused on the annular gap where it was found appropriate to investigate bubble detachment, sliding and ejection. Figures 5.10-5.13 show typical bubble behaviour before, near and after the NVG point for runs B1, B2, B4 and B8, listed in Table 3.3, respectively. In these figures, the heater edge appears at the right side of the image and the wall of the plexiglass tube and the one-millimetre reference tube appear at the left side, as also shown in Figure 3.13a. The measured void fraction profiles for these experimental runs are shown in Figure 5.2. The photographs shown in Figures 5.10-5.13 show the change of bubble size and population upstream of, near, and downstream of the NVG

point. Some individual bubbles are identified to show the bubble cycle as it nucleates, grows and slides along the heating surface, detaches and collapses in the subcooled liquid bulk.

Upstream of the NVG point, the photographs show that after nucleation, the bubbles grow while attached to, or slowly sliding along, the heating surface until they lift off. After detachment, the bubbles condense very rapidly in the subcooled bulk. The photographs confirm that bubbles consistently detach from the heating surface upstream of the NVG point and accordingly, at least under the present test conditions, bubble detachment is not the cause of the NVG phenomenon. Moreover, the concept of a bubbly layer from which a bubble ejected to mark the occurrence of NVG, Dix (1971) and Serizawa (1979), cannot be supported by the present observations. The reason can be attributed to the relatively large bubbles observed under these low pressure flow boiling conditions. The bubbles may be contained in a relatively large envelope along the heating section and this envelope may become thicker due to the decrease in subcooling along the heated section. For high pressure and high mass flow rate, where the bubbles tend to be very small, the bubbly layer may be encountered. This observation is in agreement with recent results of Bibeau (1993).

The effect of the decreasing subcooling along the heated section on the bubble size and period, i.e. growth-collapse time, can be demonstrated in these figures. For example, Figure 5.12 identifies three bubbles at three different

elevations, below, near and after the NVG point. The first at $z = 3$ cm where the void fraction and the subcooling were 3% and 22.6 °C respectively. The second at $z = 13$ cm where the void fraction and subcooling were 3% and 14.8 °C respectively. The third at $z = 23$ cm where the void fraction and subcooling were 6% and 7 °C respectively. Analyzing these photographs shows that the maximum bubble diameter increased; 1.0 mm at $z = 3$ cm, 2.25 mm at $z = 13$ cm and 3.25 mm at $z = 23$ cm and the bubble total growth-collapse time increased; 7, 11 and 22 ms respectively. Of significance here is the trend, rather than the exact values, because of the sensitivity of the nucleation process to nucleation site size and bubble interaction. The effect of the subcooling will be investigated in detail during the analysis of the mean bubble size.

In the second method, used to visualize the bubbles in the subcooled flow boiling region, the high speed video camera was focused on the heater surface itself. This procedure was found convenient to examine bubble population density, bubble interactions and bubble size along the heating surface. Figures 5.14-5.17 show typical bubble behaviour along the test section for runs number B3, B4, B8 and B9 listed in Table 3.3. The measured void fraction and the location of the NVG point of these runs are shown in Figure 5.2. As shown in the photographs, the bubble size increases as the subcooling decreases. The main reason for the size increase along the heating section is the decrease in the condensation at the subcooled water-bubble

interface. In subcooled boiling, the bubble grows on the heating surface under two opposing mechanisms; evaporation at the heating surface and at the superheated liquid-bubble interface and condensation at the subcooled water-vapour interface. The final bubble size and life duration are mainly dependent on the relative importance of these mechanisms. The bubble population density increases also as the subcooling decreases. The increase in the bubble population may be caused by longer bubble life and by the increase of the nucleation site density which were activated as the subcooling was decreased.

Two distinct regions were observed along the heating section, which can be seen in Figures 5.14-5.17. In the region before the NVG point, the bubbles behave as individual bubbles, or discrete bubbles. Bubble interactions or coalescence is not a major mechanism in this region. Bubble coalescence intensifies in the region after the NVG point and is caused by the increase in bubble size, bubble density and bubble growth-collapse period. This is clearly associated with reduction in the relative importance of condensation at the bubble interface due to the decrease in the subcooling. It appears that this behaviour is related to the NVG phenomenon and a detailed discussion of this phenomenon will be presented later. As the bubble coalescence intensifies in the region after the NVG point, bigger bubbles are formed. The increase in bubble size decreases the interfacial area concentration, for a given void fraction value, causing a reduction in the condensation rate per unit volume of channel. Consequently, the relative effect of condensation is reduced and

noticeable increase of void fraction is observed along the channel. Near the end of the heater, the coalescence intensifies significantly and the flow regime changes from bubbly flow to churn flow.

Comparing Figures 5.14, 5.15, 5.16 and 5.17 indicates the effects of the mass and heat fluxes on the bubble size and population along the heating section. For high mass flux, the bubbles tend to be smaller, possibly due to the decrease in the wall superheat caused by the increase in the single phase heat transfer coefficient. The change of the heat flux results in a different trend, i.e. increasing the heat flux tends to increase the bubble size due to the increase in the wall superheat. More details will be presented in the following section.

5.3 Bubble Size in Subcooled Flow Boiling

5.3.1 Background

One of the parameters required to estimate the interfacial transport of mass, momentum and heat energy is the bubble size, or interfacial area concentration. Despite the importance of the bubble size in two-fluid formulation of subcooled flow boiling, no measurement was reported in the literature for mean bubble diameter. Moreover, a few investigators, Gunther (1951), Abdelmessih et al. (1972) and Bibeau (1993), reported measurements for bubble growth-collapse history in subcooled flow boiling. Ünal (1976) and Meister (1978) theoretically investigated the bubble growth-collapse in subcooled flow boiling. Ünal (1976) analyzed the growth and collapse of an attached hemispherical bubble. The bubble grew on the heating surface under the influence of microlayer evaporation beneath the bubble base and the condensation at the curved surface. The condensation at the interface was calculated using Levenspiel's model (1959) of bubble condensation. The detachment effects were excluded from the analysis as it was assumed that the bubble remained attached to the heating surface during the growth-collapse cycle. This will, in fact, cause a longer collapse time due to the continuous evaporation during the total bubble life. Based on this analysis, the following relationship was obtained for the maximum bubble diameter, considered the bubble detachment diameter,

$$D_{\max} = \frac{2.42 \times 10^{-5} P^{0.709} (q - h_{sp} (T_s - T_l))^{1/3} k \gamma_u}{2 C_u^{1/3} \rho_g h_{fg} (\pi a)^{1/2} (b_u \phi_u)^{1/2}} \quad (5.5)$$

where:

$$\begin{aligned} \gamma_u &= \sqrt{k_s \rho_s C_{ps} / k \rho_l C_p} \\ C_u &= \frac{h_{fg} \mu (C_p / 0.013 h_{fg} Pr^{1.7})^3}{(\sigma / g \Delta \rho)^{1/2}} \\ b_u &= (T_s - T_l) / 2 (1 - \rho_g / \rho_l) \\ \phi_u &= (U_l / 0.61)^{0.47} \quad \text{for } U_l > 0.61 \text{ m/s} \\ &\text{or} \\ \phi_u &= 1 \quad \text{for } U_l \leq 0.61 \end{aligned} \quad (5.6)$$

where k_s , ρ_s and C_{ps} are the thermal conductivity, density and specific heat of heater material. The effect of pressure on D_{\max} appears both explicitly and implicitly, through its effect on the thermo-physical properties, in the above equation. The equation correctly predicts a net decrease in the maximum bubble diameter with increasing pressure as reported by a number of investigators, e.g. Bibeau (1993).

For bubble departure diameter, Ünal (1976) recommended the use of Equation (5.5) in flow boiling. However, it should be noted that the high speed photographic results of Bibeau (1993) showed that bubble detachment occurred after reaching the maximum diameter, not at the maximum diameter.

Based on data from literature, Serizawa (1979) introduced the following empirical relationship for bubble detachment diameter D_d ,

$$D_d = \psi_s \exp(-k_1 (T_s - T_l) - k_2 q) \quad (5.7)$$

where k_1 , k_2 and ψ_s are empirical functions of mass flux, heat flux, test section geometry and fluid properties.

Bibeau (1993) reported that Farajisarir (1993) analyzed his high speed photographic results and obtained the following correlation for the maximum bubble diameter,

$$\frac{D_{\max} \sigma}{\rho_l a^2} = 10.02 \times 10^3 Ja_w^{-1.65} \left[\frac{T_w - T_l}{T_w - T_s} \right]^{-1.65} \quad (5.8)$$

where a is the water thermal diffusivity and Ja_w is the Jakob number based on the heating surface superheat. Examination of this correlation showed that the maximum bubble diameter is proportional to $(T_w - T_l)^{-1.65}$. This parameter, in fact, includes the effect of the wall superheat and bulk subcooling. It implicitly assumes that the effect of liquid subcooling and wall superheat can simply be added to form a single parameter.

In formulating a two-fluid model for subcooled flow boiling, there is a need to estimate the mean bubble diameter in subcooled flow boiling. No correlations are available for this purpose. Current models use available correlations, which mostly reflects an estimate of the maximum bubble diameter or the bubble diameter at detachment.

5.3.2 Mean Bubble Diameter Measurements

The high speed video and digital image processing systems, described in Chapter 3, were used to obtain data on bubble size in subcooled flow boiling. Measurements were obtained at two centimetre intervals along the heated section for the ten experimental runs listed in Table 3.3. As mentioned in the previous section, two procedures were used to visualize the bubbles. The visual results of the second procedure, in which the camera was focused on the heater surface, were used in measuring the mean bubble diameter along the subcooled boiling region. The digital image processing technique was used to analyze the high speed photographic images stored on the video tape, frame by frame, to measure the bubble size. The volume, and the surface area of each bubble, was calculated by measuring two diameters. The measured diameters were the maximum diameter and that perpendicular to the maximum diameter, as shown schematically in Figure 5.18. The cross sectional area was assumed to be an ellipse and the two measured diameters were considered the maximum and the minimum dimensions of that ellipse. The bubble volume and surface area were calculated by rotating this cross section around the maximum diameter. It was endeavoured to measure the maximum number of bubbles from each frame.

At each axial location, a total of about 350 bubbles were analyzed. The bubble volume v_b and surface area a_b were calculated as discussed above. For

each bubble, the Sauter bubble diameter, $d_s = 6 v_b / a_b$, was calculated. Typical histograms representing the individual Sauter bubble diameter, versus its frequency of occurrence, are shown in Figure 5.19. The average bubble surface area and volume at each location were calculated as follows:

$$A_b = \frac{1}{n_b} \sum_{j=1}^{n_b} a_{b_j} \quad (5.9)$$

$$V_b = \frac{1}{n_b} \sum_{j=1}^{n_b} v_{b_j} \quad (5.10)$$

where n_b is the number of the measured bubbles. The mean Sauter bubble diameter at any given axial location was defined by:

$$D_s = \frac{6.0 V_b}{A_b} \quad (5.11)$$

The mean bubble size measurements were conducted 136 times under differing conditions (more than 45,000 bubbles were measured).

5.3.3 Data Analysis

The mean Sauter bubble diameter measured along the heated section for different levels of mass flux, heat flux and inlet subcooling, for the test conditions listed in Table 3.3, are shown in Figure 5.20a and 5.20b. The

measured axial void fraction profiles and the heating surface superheats for the same conditions are shown in Figures 5.2 and 5.8 respectively. The subcooling values measured along the heating section are listed in Table 3.3. As shown in Figures 5.20a and 5.20b, the bubble diameter increased gradually in the region upstream of the NVG point due to the decrease in the condensation, caused by the reduction in the subcooling, at subcooled water-bubble interface. The bubble diameter appears to increase at a higher rate in the region downstream of the NVG point. This was caused by two factors; the decrease in the subcooling, and consequently the condensation, and the bubble coalescence.

It is important to note the similarity between the bubble size and the measured void fraction in the region before, and after, the NVG point. To magnify the response of the bubble diameter, D_b^3 was plotted as well as the void fraction along the heating section as shown in Figures 5.21a and 5.21b. The interesting finding, based on these figures, is the strong link between bubble size and void fraction. The parameter D_b^3 and the void fraction have similar trends before and after the NVG point. The rate of increase of both along the heated section appears to increase at the point of NVG.

To examine the effect of mass and heat flux on the bubble size, the measured mean bubble diameter was plotted versus Jakob number (subcooling) for certain experimental runs listed in Table 3.3. The subcooling was calculated from the heat balance as follows:

$$T_s - T_l = T_s - T_{in} - \frac{q P_h z}{A G C_p} \quad (5.12)$$

The effect of the mass flux is shown in Figure 5.22 while the effect of heat flux is shown in Figure 5.23. Increasing the mass flux decreases the bubble size, particularly for high Jakob number region before the NVG point. As the subcooling decreases, i.e. the Jakob number decreases, increasing the mass flux reverses the above trend, i.e. increasing the mass flux tends to increase the bubble size. In this region which is crowded by bubbles, increasing the mass flux increases the bubble absolute velocity. The increase in the bubble absolute velocity increases the coalescence between detached and attached bubbles. Increasing the heat flux, as shown in Figure 5.23, tends to increase the bubble size. This may be caused by the increase in the driving force of the bubble growth process, the wall superheat.

The author is not aware of existing correlations for the mean bubble diameter in the subcooled flow boiling. Sorizawa (1979) presented a correlation for bubble size at detachment, Ünal's (1976) and Farajisari (1993) (as reported in Bibeau, 1993) presented correlations for the maximum bubble diameter, which represents an upper limit for the bubble diameter. The predictions of these correlations are superimposed on the present data in Figures 5.24a and 5.24b. As shown in the figures, the prediction of Ünal's model (1976) of the maximum bubble diameter is lower than the measured mean bubble diameter. However, the trend of the predicted maximum bubble size along the heating

section is qualitatively similar to the measured mean bubble diameter. The maximum bubble size predicted by Farajisarir (1993) (as reported in Bibeau, 1993) is mostly higher the measured mean bubble diameter as one could expect. It should be noted that Farajisarir's correlation for the maximum bubble diameter was based on small bubbles in the range of 2 mm.

5.3.4 Proposed Correlation

Many methods were tried to correlate the present data of the mean bubble diameter. In these analyses, a dimensionless form with correct limits was considered. It was found appropriate to correlate the present data by the following formula:

$$\frac{D_s}{\sqrt{\sigma / g \Delta \rho}} = \frac{0.0683 (\rho_l / \rho_g)^{1.326}}{Re^{0.324} \left[Ja + \frac{149.2 (\rho_l / \rho_g)^{1.326}}{Bo^{0.487} Re^{1.6}} \right]} \quad (5.13)$$

The comparison between the present data and the proposed correlation is shown in Figure 5.25. This correlation has a correlation coefficient of 90% and is capable of predicting the present data within $\pm 15\%$. The comparison between the above correlation and the measured mean bubble diameter along the heating section is shown in Figures 5.26a and 5.26b.

5.4 Net Vapour Generation Model

5.4.1 Introductory Remarks

Examining the measured void fraction profiles in the highly subcooled region of the present study, Bibeau (1993), Dimmick and Selander (1990), Stangl and Mayinger (1990) and Donevski and Shoukri (1989), showed that the void fraction starts from a zero value at the ONB point (or at the beginning of the heating section provided that the inlet condition is appropriate for boiling) and increases, initially with a high gradient, to form a flat plateau with an almost constant void fraction. This flat plateau continues until the NVG point is reached where the void fraction increases significantly, as shown schematically in Figure 5.27. From the above description, it is clear that the NVG point is the inflection point of the void fraction profile as suggested by Serizawa (1979). In subcooled boiling, bubbles grow and collapse under simultaneous evaporation and condensation processes. The high speed photographic results showed, as discussed in 5.2 and 5.3, the NVG point was not initiated by any dramatic change in bubble behaviour or the flow field. The high speed photography confirmed that the bubble detachment, or ejection, is not the mechanism causing the NVG phenomenon. Moreover, it was found that the change in the average bubble diameter is smooth along the heating section. However, the variation of the bubble volume along the heating section was found to be similar to that of the void fraction. This finding indicates a strong

link between bubble size and void fraction. This result should be expected; the void fraction can be calculated easily if information on the bubble density (number of bubbles per unit volume) is available. The bubble density is a complicated parameter and it will be a function of active nucleation site density, bubble frequency, bubble condensation rate and bubble velocity. In the following, the NVG phenomenon will be modelled from a macroscopic point of view to overcome difficulties due to unavailable information.

The void fraction profile described earlier is the result of the competition between the vapour generation at the heating surface and condensation at the subcooled liquid-bubble interface. By examining this profile, one can imagine the profiles of the vapour generation and condensation functions, as shown schematically in Figure 5.27. At the ONB, the void fraction is zero and consequently the interfacial area concentration is zero. Accordingly, the condensation term will be zero and the absence of the condensation component results in the initial high gradient of the void fraction at the ONB point. This high gradient cannot continue because of the high subcooling which suppresses the net void generation due to condensation. This trend will carry on to the NVG point, after which the vapour generation rate will exceed the vapour condensation rate giving the opportunity for significant net vapour formation.

As observed from the high speed photographic results, in the highly subcooled region, discrete bubbles nucleate on the heating surface, slide along it and then eject in a lateral direction and condense completely in the subcooled

bulk. At any instant, there are two types of bubbles, attached and detached. The attached bubbles grow due to vaporization caused by the direct heat transfer from the wall and the heat transfer from the thin superheated liquid layer adjacent to the wall. Condensation occurs at the subcooled liquid-bubble interface if the bubble penetrates the subcooled core while still attached to the heating surface. The detached bubbles are completely influenced by condensing conditions. The analysis of this problem is complicated due to the large number of parameters controlling the evaporation and condensation processes.

5.4.2 Formulation

The vapour generation term, responsible for evaporation, includes that portion of the applied heat flux responsible for evaporation through the microlayer beneath the bubbles as well as the component which causes evaporation at the superheated liquid-bubble interface within the superheated liquid layer, in the vicinity of the heating surface. The last part can be neglected by assuming that the superheated layer is very thin. Based on this assumption, the vapour generation term is only proportional to the applied heat flux and the contact area between the attached bubbles and the heated surface. The vapour generation term or energy rate per channel length, can be estimated as follows:

$$G_v = C_1 q N_{bb} a_c \quad (5.14)$$

where a_c and is the contact area between an attached bubble and the heated surface and N_{ba} is the number of the attached bubbles per unit length of the heating section.

For attached and detached bubbles, the condensation occurs at the subcooled liquid-bubble interface. The condensation term or energy rate per channel length, can be represented by:

$$C_v = C_2 a_b N_{bt} h_c (T_s - T_l) \quad (5.15)$$

where a_b is the bubble surface area, N_{bt} number of bubbles per unit length of the channel and h_c is the interfacial condensation heat transfer coefficient between the bubbles and the subcooled liquid. C_1 and C_2 are proportionality constants which include the uncertainty due to approximation in the above two equations. At the NVG point, the vapour generation term will be equal to the vapour condensation term. Using this idea and substituting from Akiyama's model (1973) for bubble condensation coefficient, see Table 4.2, the condition at the NVG point is reduced to:

$$\frac{q D_s}{(T_s - T_l) k} = \left[\frac{0.37 C_2 N_{bt} a_b}{C_1 N_{bo} a_c} \right] Re_b^{0.6} Pr^{1/3} \quad (5.16)$$

where the bubble Reynolds number was estimated based on the mean bubble diameter and the bubble relative velocity. The mean bubble diameter can be calculated from the correlation proposed in section 5.3.1, Equation (5.13). The bubble relative velocity was calculated based on the drift flux model of Zuber

and Findlay (1965), Equation (4.13). The term inside the square brackets in the above equation is a complicated function of active nucleation site density, bubble frequency and bubble growth-collapse time. However, these parameters will affect both the numerator and the denominator. Accordingly, the net effect of these parameters on the square bracket term will be small. Based on this assumption, the above equation can be approximated to:

$$\frac{q D_s}{(T_s - T_f) k} = C_{oz} Re_b^{0.6} Pr^{1/3} \quad (5.17)$$

The present data was used to calculate the value of the empirical constant C_{oz} and was found to equal unity. The left hand side of Equation (5.17) represents the Nusselt number based on the bubble diameter as the characteristic length. Saha and Zuber (1974) defined the Nusselt number based on the hydraulic diameter of the channel and showed that it is a constant for the thermally controlled region ($Pe < 70,000$), which is the case for the data presented in this work. Saha and Zuber (1974) can be written in the following form:

$$\frac{q D_s}{(T_s - T_f) k} = 455 \left[\frac{D_s}{D_h} \right] \quad (5.18)$$

Comparing Equations (5.17) and (5.18) one can see that the proposed equation includes bubble dynamics effects through the bubble Reynolds number.

5.4.3 Comparison between proposed NVG Model and Experimental Data

The prediction of the proposed model, obtained by solving Equation (5.17) by trial and error, was compared to the experimental data of the present work, and available data from the literature including that of Donevski and Shoukri (1989), Rogers et al. (1987), Evangelisti and Lupoli (1969), Dimmick and Selander (1990) and Bibeau and Salcudean (1990). These data are for water at low pressure (1-2 bar) and in the thermally controlled region, $Pe < 70000$ as defined by Saha and Zuber (1974), with the exception of a point in the data of Dimmick and Selander (1990). The comparison between the experimental, and the predicted subcooling at the NVG point, is shown in Figure 5.28. The comparison shows that the current model can predict the data within $\pm 30\%$. One reason for this wide margin is the uncertainty in determining the exact location of the NVG point. As shown in Figures 5.1 and 5.2, the change at the NVG point is not sharp.

5.4.4 Effect of Mass and Applied Heat Fluxes on NVG point

Effects of various parameters on the prediction of the proposed model are shown in Figures 5.29a and 5.29b. The effect of the applied heat flux on the subcooling at the NVG point is shown in Figure 5.29a. Subcooling at the NVG point increases as the heat flux is increased, i.e. the NVG phenomenon

occurs early. The reason is that the increase in the heat flux, at a given mass flux, increases the bubble formation rate, bubble size, bubble frequency and active nucleation site density. The effect of the mass flux on the subcooling at the NVG point is not significant as shown in Figure 5.29a. In general, the effect of mass flux on the subcooling at the NVG point is clearly less pronounced than that of the heat flux. At high heat flux, the increase in the mass flux delays the NVG phenomenon, i.e. it occurs at lower subcooling. The increase in the mass flux in this region tends to decrease the heated surface superheat and consequently decreases evaporation rate at the heated surface. For low heat and mass fluxes, the increase in the mass flux advances the NVG phenomenon, i.e. it occurs at higher subcooling. This unexpected trend was also reported by Rogers et al. (1987) but was predictable from Levy's model (1967). If this finding is true, then the question is what makes the increase in the mass flux (in the low mass flux region) enhance the boiling. The only way in which the mass flux can help the boiling is by helping the bubble parallel departure and sliding. The sliding of bubbles on the heating surface may enhance the evaporation through the microlayer beneath the bubbles as reported by Tsung-Chang and Bankoff (1990). They reported that the bubble sliding over the heating surface may enhance the evaporation by a factor of at least two.

5.5 Two-Fluid Void Fraction Profile Model

The model presented herein is a mechanistic, two-fluid generation-condensation, model. The main features of the two-fluid model were discussed earlier in the previous chapter (Section 4.3.2). The same procedure used in solving the condensing flow was followed in solving the subcooled flow boiling. The continuity and energy equations of the mixture and vapour phase were integrated simultaneously to obtain the liquid velocity, liquid temperature and void fraction. The momentum equation of the mixture was integrated also to calculate the total pressure drop. Some empirical relationships for applied heat flux division, bubble rise velocity, interfacial heat transfer coefficient and interfacial area concentration were used for closure.

5.5.1 Two-Fluid Model Formulation

The one-dimensional conservation equations, Equations (4.22, 4.25, 4.26 and 4.27) were recalled and were averaged over the cross sectional area.

- The area-averaged mixture continuity equation is:

$$\frac{d}{dz} \left[\rho_l (U_l - \overline{u_g \alpha}) + \rho_g \overline{u_g \alpha} \right] = 0 \quad (5.19)$$

- The area-averaged vapour energy equation is:

$$\frac{d}{dz} \left[\rho_g h_{fg} \overline{u_g \alpha} \right] = \frac{G_v}{A} - \frac{C_v}{A} \quad (5.20)$$

- The area-averaged mixture energy equation is:

$$\frac{d}{dz} \left[\rho_l C_p (\overline{T_l U_l} - \overline{T_l u_l \alpha}) + \rho_g h_g \overline{u_g \alpha} \right] = \frac{q \rho_h}{A} \quad (5.21)$$

- The area-averaged mixture momentum equation is:

$$\left(\frac{dp}{dz} \right)_t = \left(\frac{dP}{dz} \right)_l + \rho_g g + \frac{d}{dz} \left[\rho_l (\overline{u_l^2} - \overline{\alpha u_l^2}) + \rho_g \overline{\alpha u_g^2} \right] \quad (5.22)$$

In Chapter 4, the relationships between the distribution parameters and the area averaged terms in the above equations were discussed. For the subcooled flow boiling, where the temperature is not uniform in the radial direction, the relationships between the area-averaged liquid temperature and area averaged liquid phase velocity and void fraction are:

$$\overline{T_l u_l} = D_7 T_l U_l \quad (5.23)$$

$$\overline{T_l u_l \alpha} = D_8 T_l U_l \alpha \quad (5.24)$$

where \dot{T}_l and T_l are the local and average liquid temperatures. Substituting the area-averaged terms in the conservation equations gives:

$$\frac{d}{dz} \left[\rho_l U_l (1 - D_1 \alpha) + D_2 \rho_g U_g \alpha \right] = 0 \quad (5.25)$$

$$\frac{d}{dz} \left[D_2 \rho_g h_{fg} U_g \alpha \right] = \frac{G_v}{A} - \frac{C_v}{A} \quad (5.26)$$

$$\frac{d}{dz} \left[\rho_l C_p U_l T_l (D_7 - D_8 \alpha) + D_2 \rho_g h_g U_g \alpha \right] = \frac{q \rho_h}{A} \quad (5.27)$$

$$\left(\frac{dP}{dz} \right)_t = \left(\frac{dP}{dz} \right)_l + g \rho_s + \frac{d}{dz} \left[\rho_l U_l^2 (D_3 - D_5 \alpha) + D_6 \rho_g U_g^2 \alpha \right] \quad (5.28)$$

5.5.2 Closure Relationships

According to the vapour generation-condensation concept, there are simultaneous vapour generation and condensation processes. The applied heat flux at the wall is divided into two components. The first goes directly into the liquid by convection and includes single phase convection and pumping effects, while the second component generates voids at the heating surface.

The current problem is complicated because of the large number of unknowns or lack of information on:

- 1- Heat flux division mechanism within both the highly and slightly subcooled regions.
- 2- Interfacial heat transfer coefficient.
- 3- Bubble size and interfacial area concentration.
- 4- Bubble relative velocity.
- 5- Effect of non uniform profiles of velocity, void and temperature in the radial direction.
- 6- Frictional pressure drop component.

To overcome these problems, the following assumptions and approximations were considered:

- 1- The effect of the nonuniform profiles of the velocity, temperature and void fraction in the radial direction was neglected, i.e. D_1 to $D_8 = 1.0$.
- 2- The bubble relative velocity was calculated from the drift flux model of Zuber-Findlay model (1965) as discussed in 4.2.
- 3- The bubble average diameter or average Sauter diameter was calculated from the proposed correlation, Equation (5.13). Consequently, the interfacial area concentration can be calculated from the relationship between the void fraction and bubble diameter; $a_i = 6 \alpha / D_s$. However, the portion of the interfacial area concentration in contact with the subcooled liquid remains unresolved.

- 4- The bubble condensation coefficient can be calculated from the correlation developed for subcooled liquid-vapour flow in Chapter 4, Equation (4.17), or based on Akiyama (1973). According to the above three assumptions, the vapour condensation term can be estimated from:

$$C_v = C_s a_i A h_c (T_s - T_l) \quad (5.29)$$

where the constant C_s is the fraction of the bubbles, or the interfacial area concentration, that is associated with condensation.

- 5- The frictional pressure component can be calculated based on Chisholm (1973) correlation as discussed in 4.3.2.2.

The remaining problem is the applied heat flux division mechanism. Most available models of the heat flux division mechanisms were developed for high pressure flows and, specifically for the slightly subcooled region, while the void fraction in the highly subcooled region was neglected. Recent void fraction measurements, for low pressure flows in the current work and in the literature, indicated that the void fraction in the highly subcooled region was significant and in the range of 2-9%. In the following, the objective is simulating the subcooled flow boiling in its two regions. As mentioned, the applied heat flux is divided into two components, a component that generates vapour at the heating surface and another component that heats the subcooled liquid:

$$q = q_v + q_l \quad (5.30)$$

The vapour generation term G_v , which is responsible for the void generation, can be estimated from:

$$G_v = P_h q_v \quad (5.31)$$

In the highly subcooled region upstream of the NVG point, the vapour generation term should equal, or slightly exceed, the condensation term, i.e. the following constraint should be satisfied:

$$G_v \geq C_v \quad (5.32)$$

Many scenarios could be proposed for the heat flux division, q_v and q_l , before, and after, the NVG point. The liquid component, q_l , includes the heat transfer due to the single phase forced convection, which is proportional to the temperature difference between the heated surface and the liquid temperature, and the energy transfer due to bubble growth-collapse cycle which is called the pumping action. The liquid component may be put in the form:

$$q_l = C_l h_{sp} (T_w - T_l) + q_p \quad (5.33)$$

where the parameter, C_l , accounts for the portion of the heating surface not covered by bubbles. The pumping component q_p includes effects due to the bubble growth-collapse cycle. The single phase heat transfer coefficient h_{sp} can

be calculated from the Dittus-Boetler correlation, Equation (2.7). The heating surface temperature can be estimated from Shah's model (1983) for subcooled flow boiling. However, in the following analysis, the heating surface temperature based on correcting the measured inner surface temperature will be used. Accordingly, the vapour component of the applied heat flux is:

$$q_v = q - C_f h_{sp} (T_w - T_l) - q_p \quad (5.34)$$

The ratio between the pumping and vapour components is called the pumping factor ϵ as defined by Bowring (1962). In Bowring's definition, the liquid volume pushed away from, and vapour volume generated at, the heating surface were assumed similar. Assuming that the liquid is at saturation condition at the heating surface, Bowring (1962) calculated the pumping factor as follows,

$$\epsilon = \frac{\text{Vapour volume} \times \rho_l C_p (T_s - T_l)}{\text{Vapour volume} \times \rho_g h_{fg}} \quad (5.35)$$

Following this procedure gives a high pumping factor which results in suppressing the vapour generation process. There are two aspects for discussions in Bowring's formulation. The energy pushed away from the heating surface should be based on the volume of the thermal boundary layer pushed by the nucleated bubbles and the average temperature difference across the thermal boundary layer. Using this analysis, the pumping factor can defined by:

$$\epsilon = \frac{\frac{\pi}{4} D_s^2 \delta_{th} \rho_l C_p \left[\frac{T_w + T_l}{2} - T_l \right]}{\frac{\pi}{6} D_s^3 \rho_g h_{fg}} \quad (5.36)$$

or,

$$\epsilon = \frac{3}{4} \frac{\rho_l C_p (T_w - T_l)}{\rho_g h_{fg}} \frac{\delta_{th}}{D_s} \quad (5.37)$$

where the thermal boundary layer thickness δ_{th} can be calculated from the following approximation:

$$\delta_{th} = \frac{k (T_w - T_l)}{q} \quad (5.38)$$

At this stage, the conservation equations, Equations (5.25-5.28), can be solved simultaneously using the closure relationships described above and the appropriate boundary conditions. However, there are two remaining unknown parameters in Equations (5.29) and (5.33), C_s and C_l . The parameter C_l which accounts for the portion of the heating surface not covered by bubbles will be a function of the void fraction at the heating surface which is very difficult to measure. To simplify the problem, this parameter will be assumed unity,

$$C_l = 1.0 \quad (5.39)$$

The portion of interfacial area concentration in contact with the subcooled

liquid, C_s , is expected to change along the heating section. However, no information is available on the variation of this parameter. For simplicity, the parameter C_s is assumed to be constant along the heating section. The value of this parameter at the NVG point can be calculated from the balance between the vapour generation and condensation rates. The average value of parameter C_s calculated at the NVG point determined from Figures 5.1 and 5.2 for the test conditions listed in Table 3.1 and 3.3 was found:

$$C_s = 0.5 \quad (5.40)$$

5.5.3 Solution and Results

The Runge-Kutta method was used to integrate Equations (5.23-5.28) simultaneously along the heating section. Boundary conditions were the heating section inlet conditions, i.e. at $z = 0$:

$$\begin{aligned} U_l &= G/\rho_l \\ T_l &= T_{in} \\ \alpha &= 0.0 \end{aligned} \quad (5.41)$$

The last boundary condition, zero void fraction at the entry, caused mathematical overflow at $z = 0$. To overcome this difficulty, a very small void fraction was used at $z = 0$. Different values were checked, $\alpha = 0.00001$ - 0.001 , and no effect was observed in the results.

In the following, the effect of imposing the NVG model, to calculate C_s ,

on the void fraction profiles, predicted using the proposed heat flux division mechanisms will be investigated. In this analysis, the bubble condensation coefficient was calculated from Akiyama's model (1973). The cases examined are:

Case No. 1:

This case is the simplest case. The heat applied at the heating surface was divided between the liquid and vapour phase. The pumping component was neglected. The liquid component was calculated from the single phase forced convection. For the condensation term, 50% of the interfacial area concentration was assumed in contact with the subcooled liquid. These assumptions are listed in Table 5.1.

Case No. 2:

In this case, the pumping component was calculated from the proposed relationship, Equation (5.37). The portion of the interfacial area concentration, factor C_s , subjected to condensation was calculated at the NVG condition from the balance between the vapour generation and condensation functions. The location of the NVG point was estimated from the measured void fraction profile and these assumptions are summarised in Table 5.1.

Case No. 3:

This case is similar to the above, except that the location of the NVG point was calculated from the proposed model, Equation (5.17) (See Table 5.1 for assumptions of this case).

Case No. 4:

This case is similar to the above case except that parameter C_s was assumed 50% based on the average of the estimated values of this parameter in Case No. 3. The interesting feature of this case is that in calculating the void fraction profile, information on the location of the NVG point is not needed. The assumptions of this case are summarised in Table 5.1.

Void fraction profiles predicted from the developed two-fluid model using the assumptions of these cases are compared to a sample of the measured void fraction profiles as shown in Figure 5.30. As shown in the figure, the void fraction starts from a very low value (0.001) and initially increases rapidly depending on the heat flux division model. The reason for the high void fraction gradient at the beginning is the absence of the vapour condensation function due to the very small value of the interfacial area concentration at $z = 0$. As shown in the comparisons, case no. 1 gives the highest void fraction values. These high values are the results of neglecting the pumping component. Using the experimentally located NVG point to calculate the parameter C_s , case no. 2, gives good predictions for the void fraction profiles. This case is not practical

because it needs prior experimental information on the NVG location which is unavailable during computational simulation. Using the conditions at the NVG point calculated from the proposed NVG model, Equation (5.17), to calculate the parameter C_s , case no. 3, gives reasonable profiles. However, the accuracy of this method depends on the accurate prediction of the NVG model. Note that the uncertainty margin of the available NVG models, including the current model, is in the range of $\pm 30\%$ or higher. Therefore, using any NVG model is not expected to improve the prediction of the void fraction profile as also reported by Chatoorgoon et al. (1992). Using a value of 50% for parameter C_s , case no. 4 gave reasonable agreement between the predicted and measured void fraction profiles. The interesting feature of this case is the independence of the calculated profiles from the NVG location, i.e. it was possible to obtain reasonable void fraction profile without looking for the location of the NVG point. At this point, it can be concluded that an accurate void fraction profile can be obtained, provided that accurate information on the heat flux division and vapour condensation terms, is available, without identifying the NVG point location.

The following analysis was carried out to examine the effect of using various bubble condensation coefficients. This was conducted by using the correlation developed in Chapter 4, Equation 4.17, and Akiyama (1973) to calculate the vapour condensation rate, Equation 5.29. The procedure described in case no. 4 was followed. In this case, the vapour generation rate was

calculated using the proposed heat flux division mechanism, Equations 5.34 and 5.37. Half of the interfacial area concentration was assumed in contact with subcooled liquid, i.e. $C_s = \%50$.

Comparisons between the void fraction profiles predicted from the current two-fluid model and experimental data including data from the literature are shown in Figures 5.31-5.35. It should be mentioned that these data were measured in different channel geometries and for water-steam at low pressure 1-2 bar. As shown in these figures, the current bubble condensation model gives lower condensation rates than that of Akiyama (1973) in the low void fraction region. However, this trend is changed in the high void fraction region since the current model accounts for the void fraction concentration while Akiyama is does not.

The comparison between the prediction of the two-fluid model and present data shows reasonable agreement. Using the interfacial heat transfer correlation developed in subcooled liquid-vapour bubbly flow gave better results than using Akiyama's model. Near the end of the heating section where the bubble coalescence is a major factor, the model gave lower predictions. This was expected since the models used only considered the bubbly regime. Comparisons between the predicted void fraction and data from the literature including Donevski and Shoukri (1989), Dimmick and Selander (1990), Rogers et al. (1987) and Bibeau and Salcudean (1990) are shown in Figures 5.32-5.35. The model reasonably predicted most of these data. However, it

underpredicted one case in the data of Dimmick and Selander (1990) and overpredicted two cases in the data of Bibeau and Salcudean (1990), these two cases showed low void fraction profiles compared to the data of Rogers et al. (1987) which were measured in the same range.

5.6 Closing Remarks

Experimental data on void fraction, wall superheat and liquid subcooling profiles along the subcooled flow boiling region were generated for various levels of mass flux, heat flux and inlet subcooling. A high speed video system was used to visualize the subcooled flow boiling before, at, and after the NVG point. The high speed photographic results confirmed the fact that bubble parallel, or normal detachment, is not the reason for the NVG phenomenon. A digital image processing technique was used to analyze the high speed photographic information, frame by frame, to obtain the bubble size distributions along the subcooled boiling region. A correlation for mean bubble diameter, as function of the mass flux, heat flux and local subcooling, was obtained.

The physical mechanisms of the NVG phenomenon were investigated using the high speed photographic results. A net vapour generation model was proposed. The proposed model was based on the balance between the vapour generation and condensation rates at this point. The predictions of the model

were compared with the current experimental data as well as available data from the literature. The agreement between the proposed model and the experimental data was within $\pm 30\%$.

A two-fluid model for void fraction profile was introduced and various closure relationships were investigated. A modified heat flux division mechanism was proposed by modifying Bowring's pumping factor (1962). Various bubble condensation correlations were examined. It was found that the correlation developed in the subcooled liquid-vapour region is applicable in the subcooled boiling region. The proposed two-fluid model was reasonably capable of predicting the void fraction profiles along the both regions of the subcooled flow boiling. The location of the NVG point is not required in the model.

Table 5.1 Different Proposed Heat Flux Division Models

Case No.	C_l	q_p	ϵ	NVG location	C_s	q_v
1	1.0	0.0	-	not needed	0.5	Eq. (5.34)
2	1.0	$\epsilon \times q_v$	from Eq. (5.37)	from the measured void fraction profile	calculated based on $G_v = C_v$ at NVG point	Eq. (5.34)
3	1.0	$\epsilon \times q_v$	from Eq. (5.37)	from NVG model, Eq. (5.17)	calculated based on $G_v = C_v$ at NVG point	Eq. (5.34)
4	1.0	$\epsilon \times q_v$	from Eq. (5.37)	not needed	0.5	Eq. (5.34)

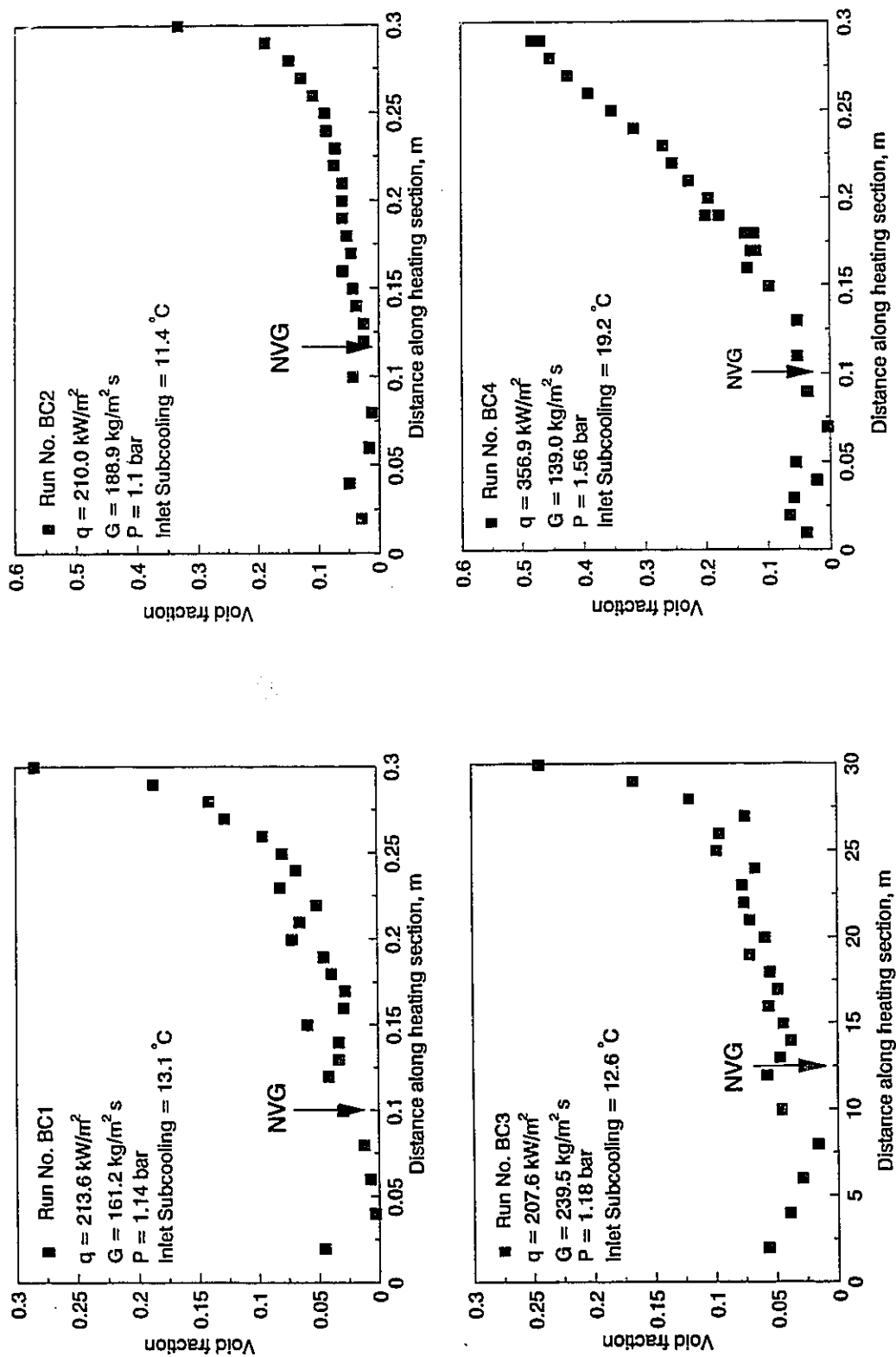


Figure 5.1a Void fraction distribution along the heating section

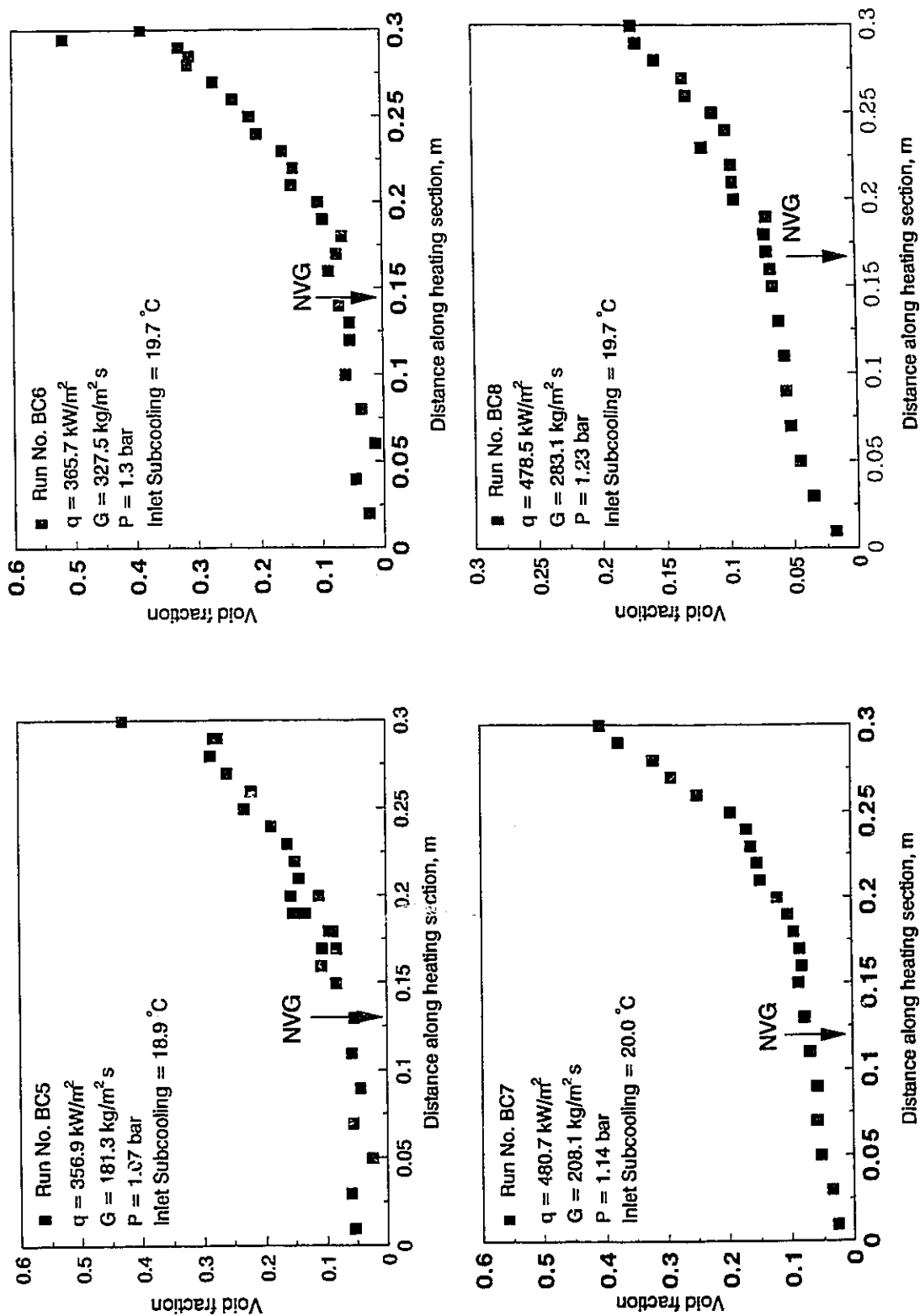


Figure 5.1b Void fraction distribution along heating section

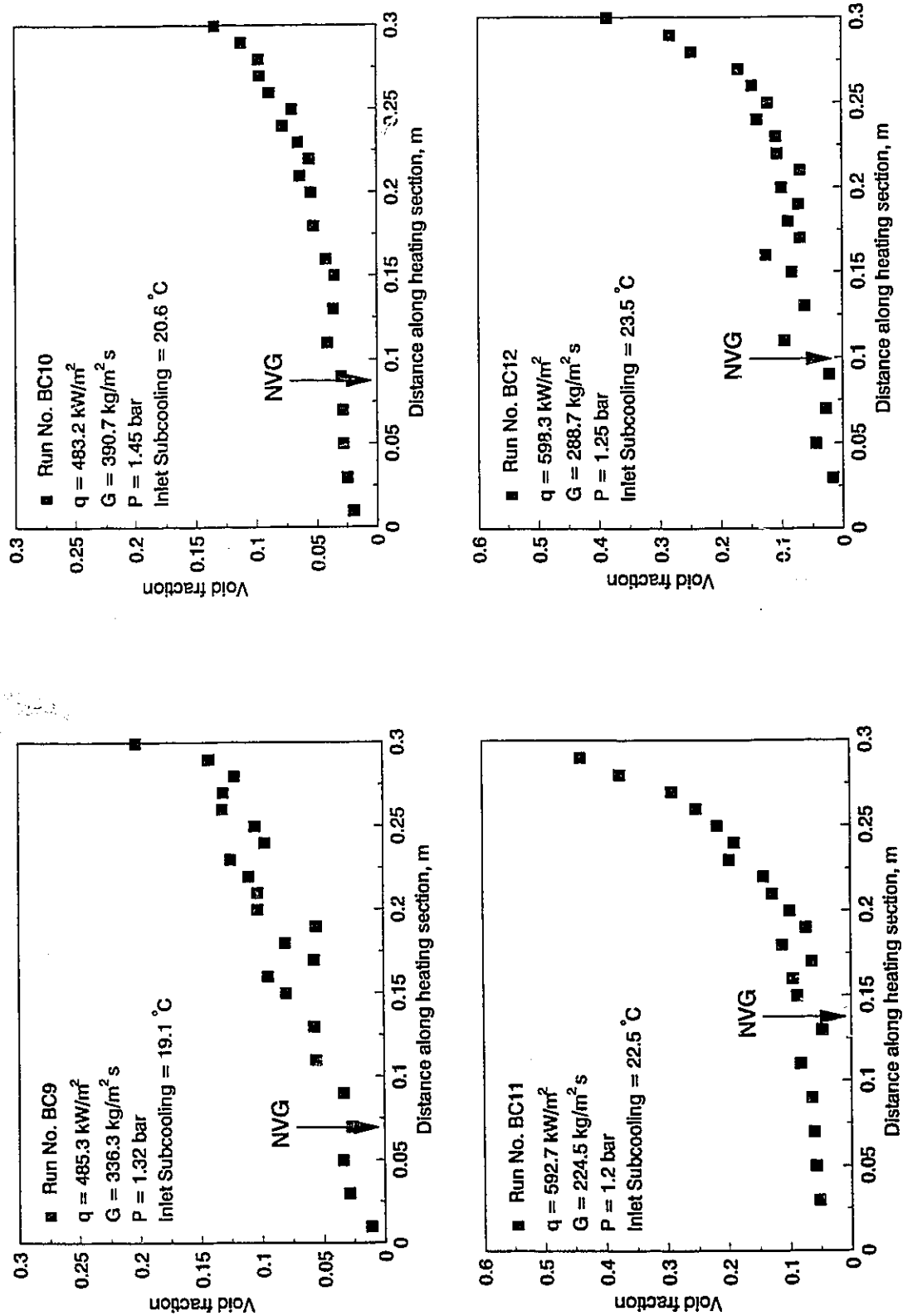


Figure 5.1c Void fraction distribution along the heating section

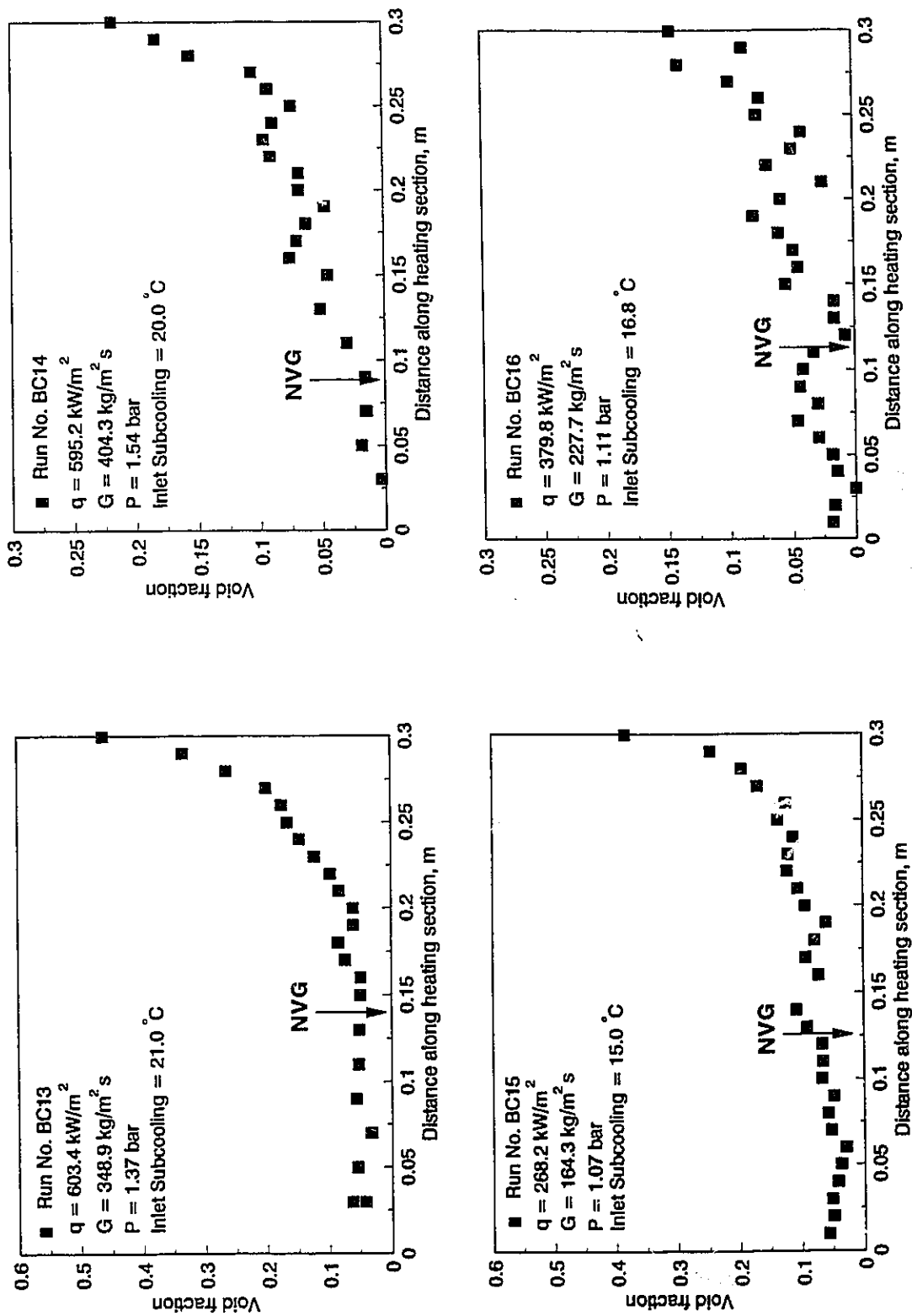


Figure 5.1d Void fraction distribution along the heating section

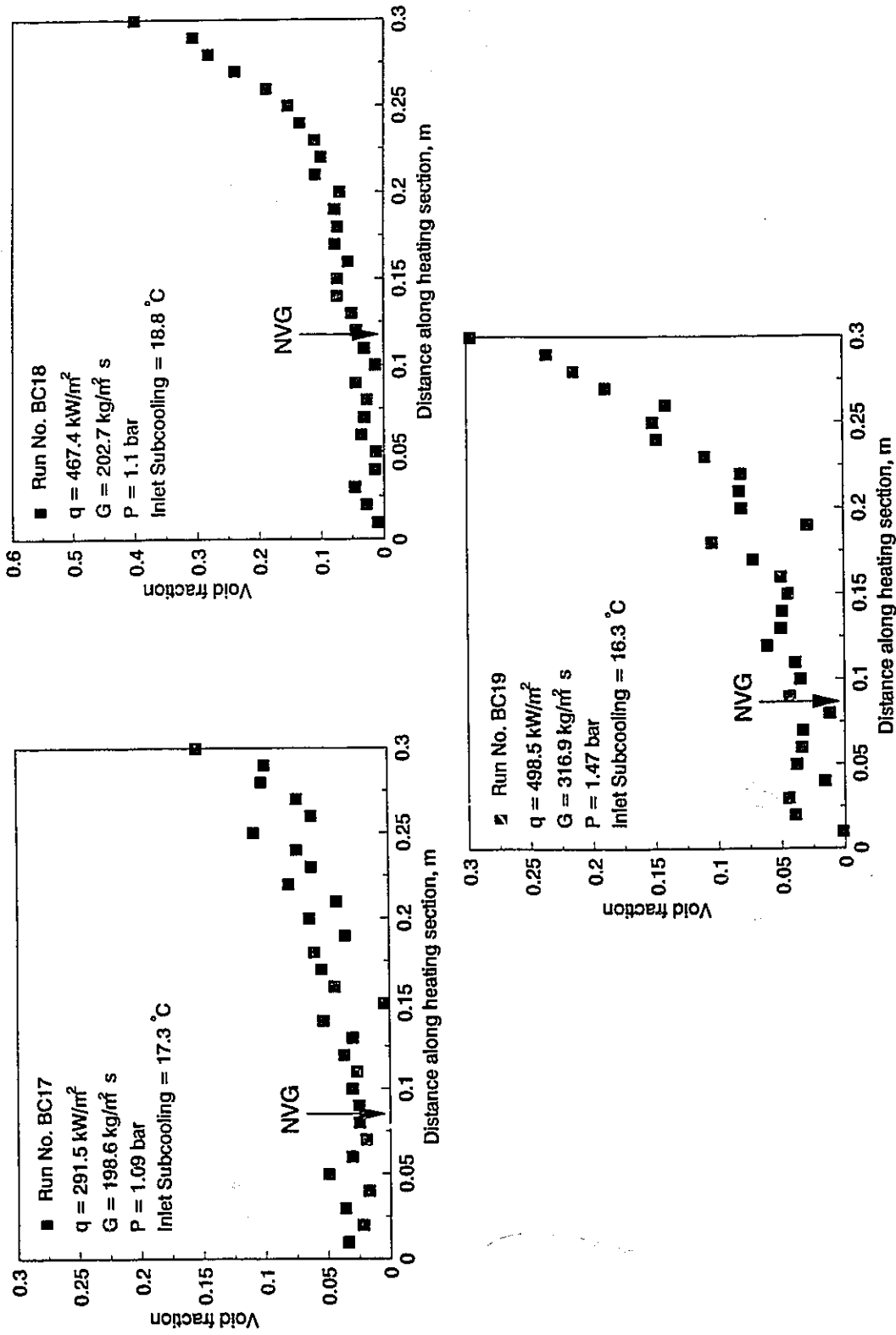


Figure 5.1e Void fraction distribution along the heating section

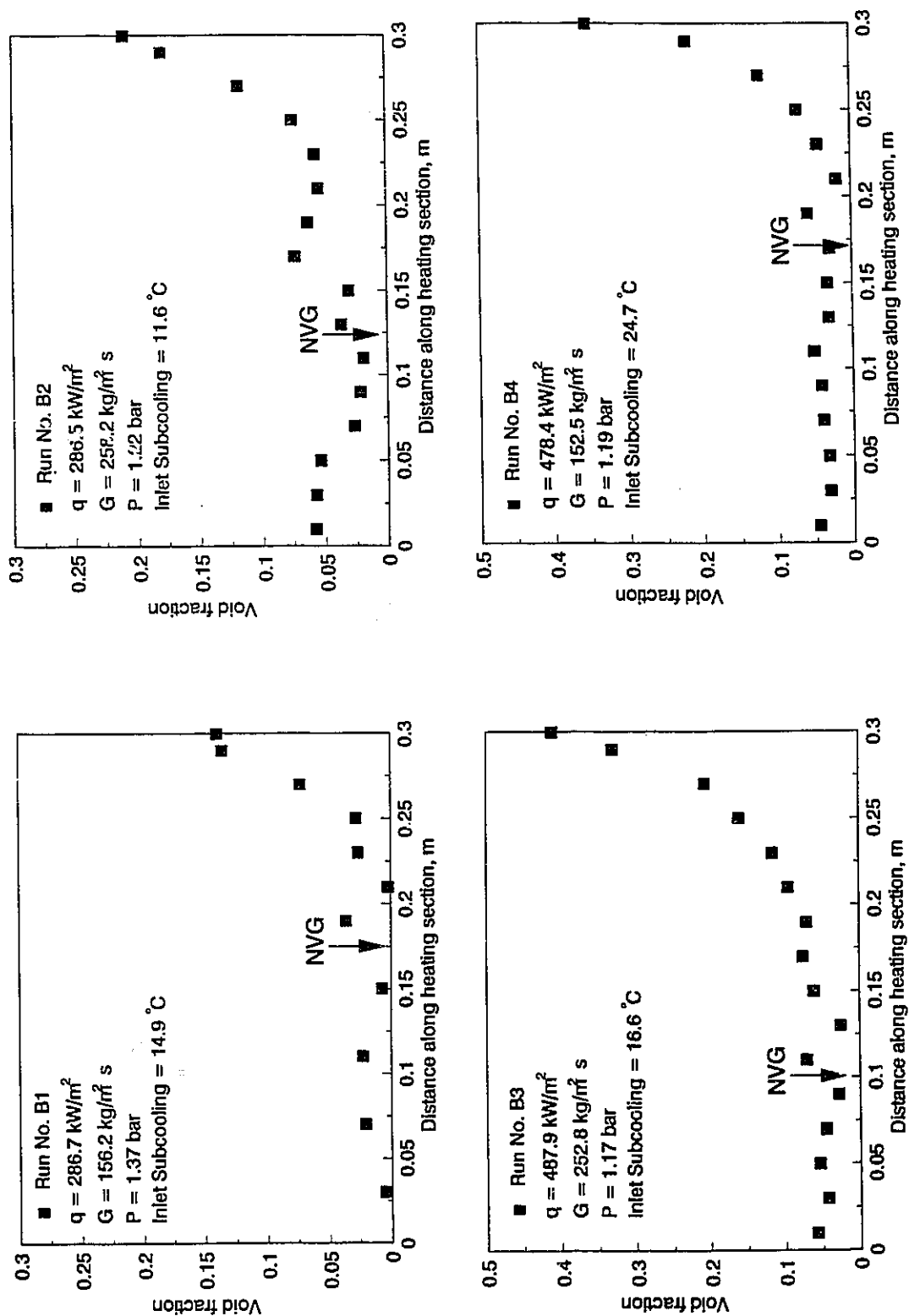


Figure 5.2a Void fraction distribution along the heating section

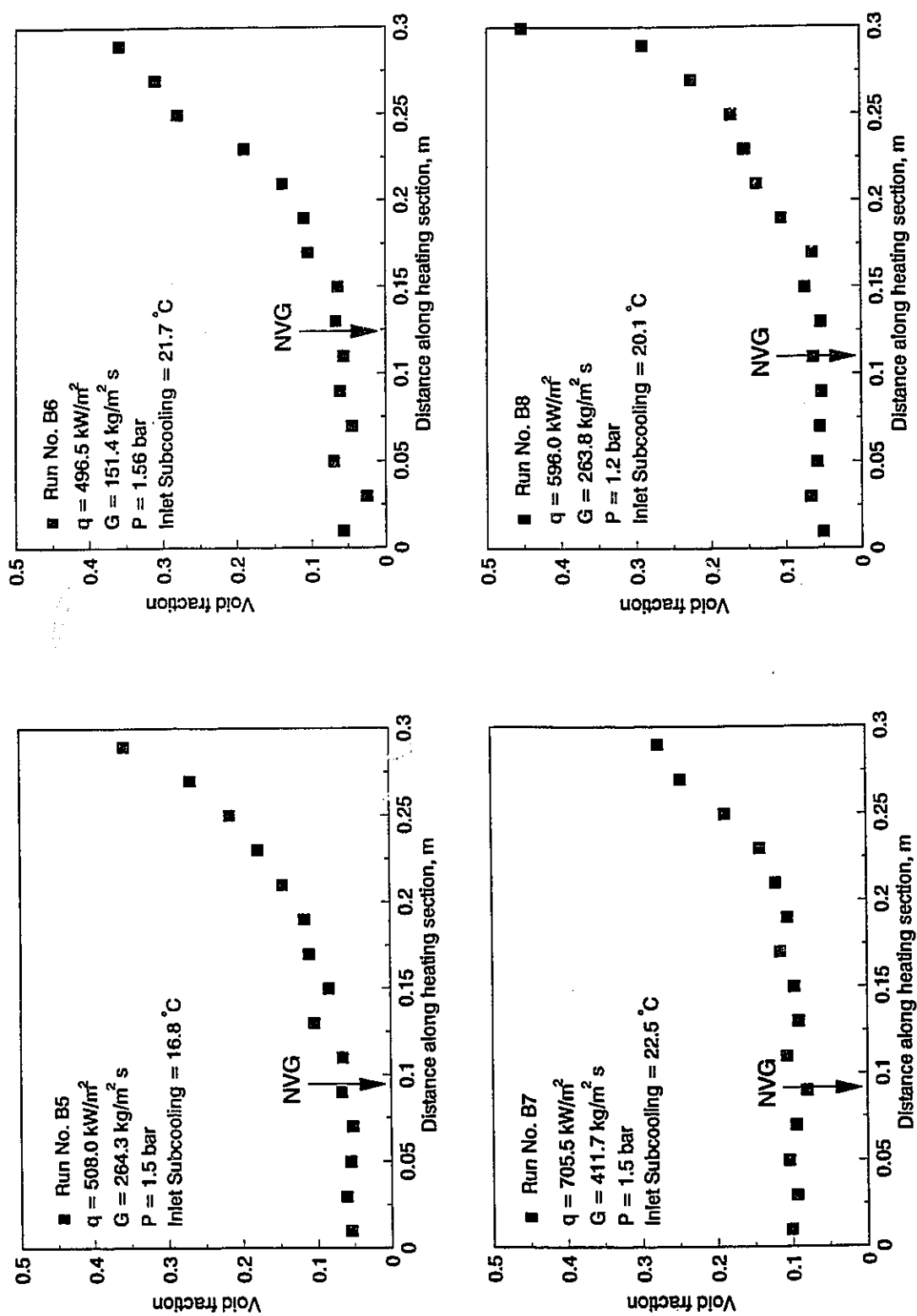


Figure 5.2b Void fraction distribution along the heating section

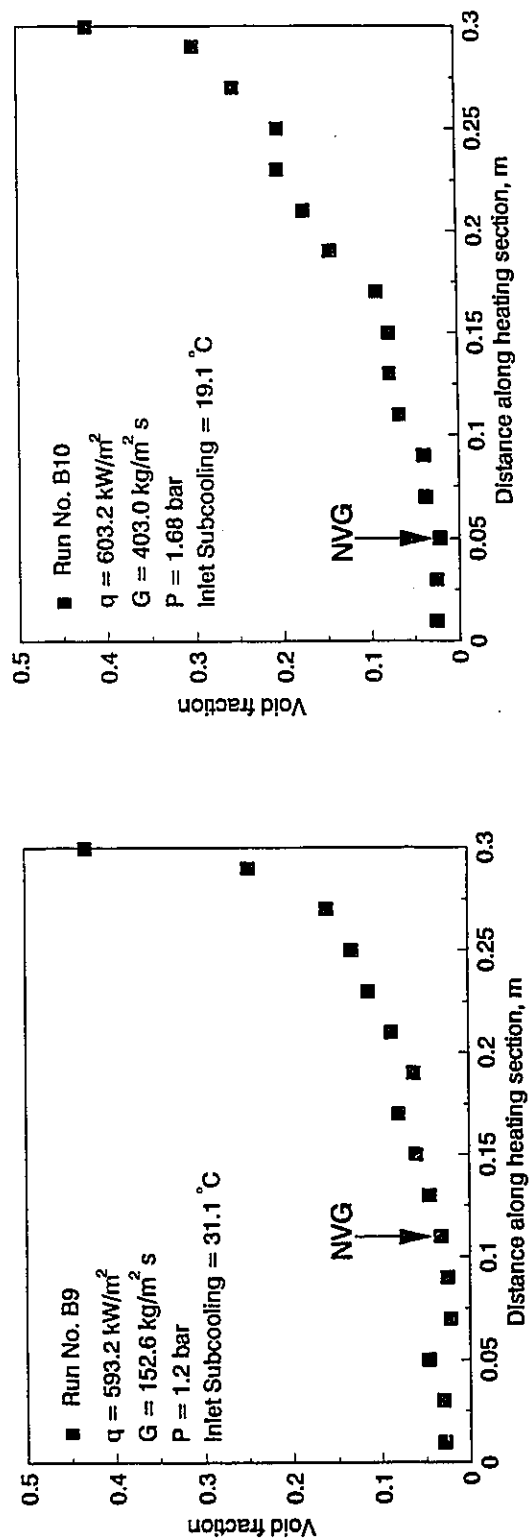


Figure 5.2c Void fraction distribution along the heating section

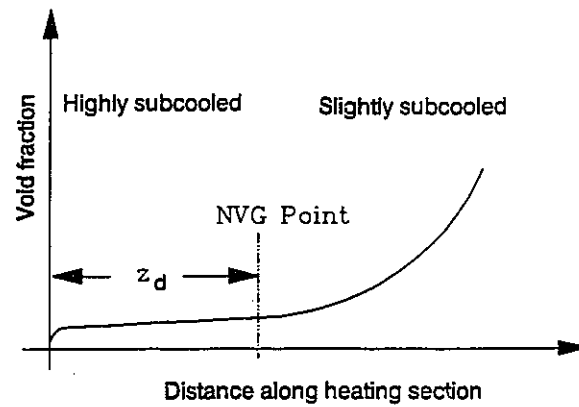


Figure 5.3a NVG point location

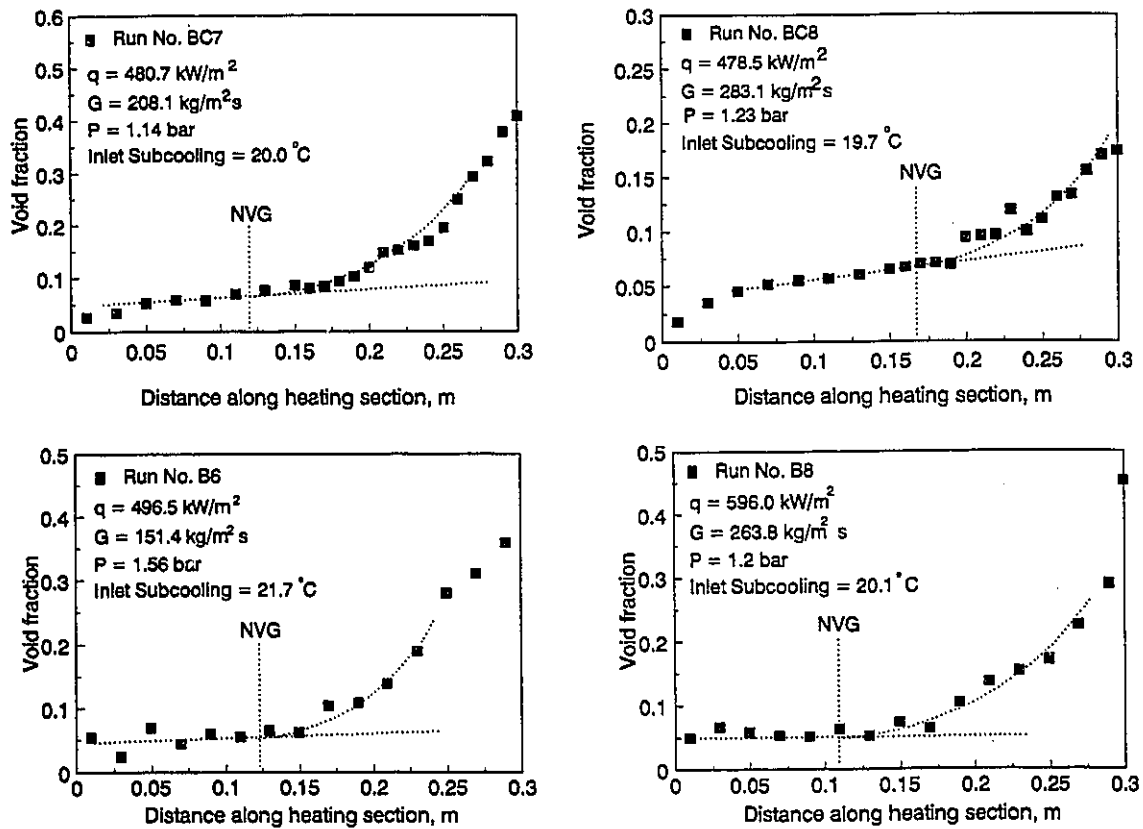


Figure 5.3b NVG point location

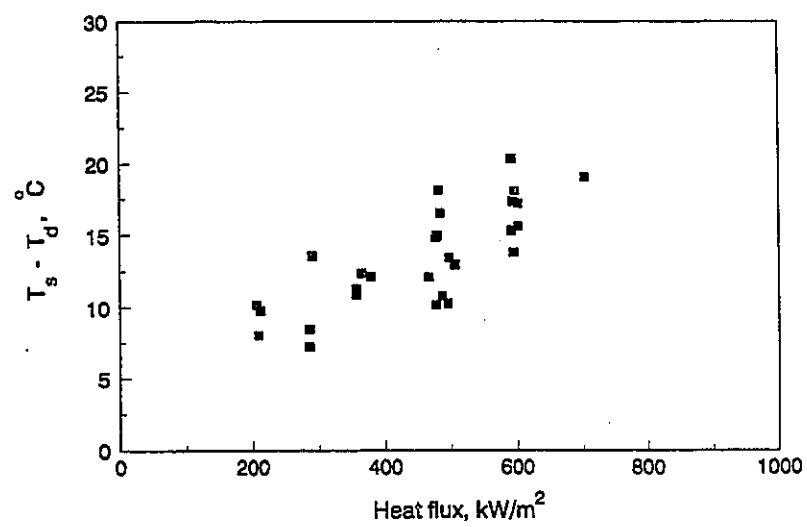


Figure 5.4 Subcooling at NVG point versus applied heat flux

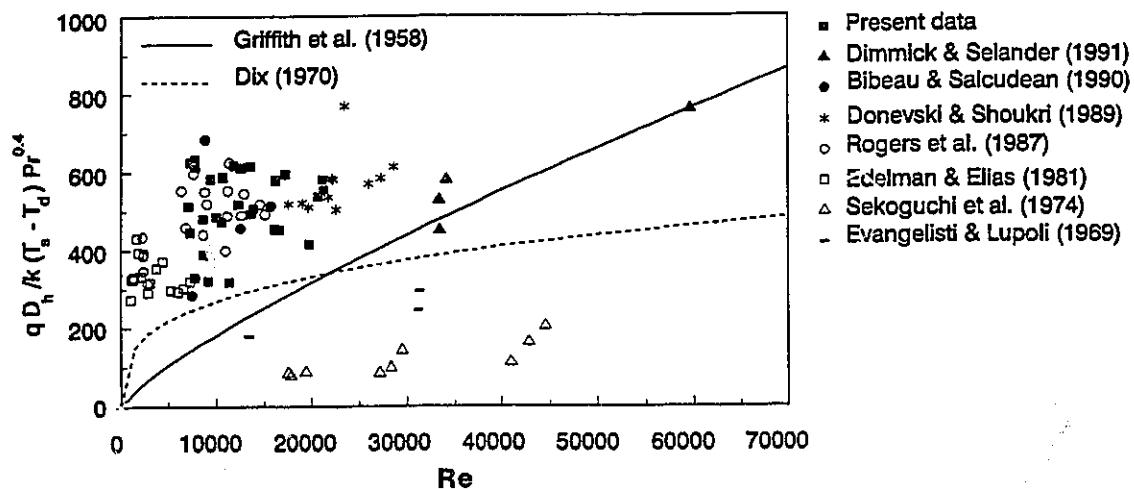


Figure 5.5a Comparison between experimental data and existing NVG models

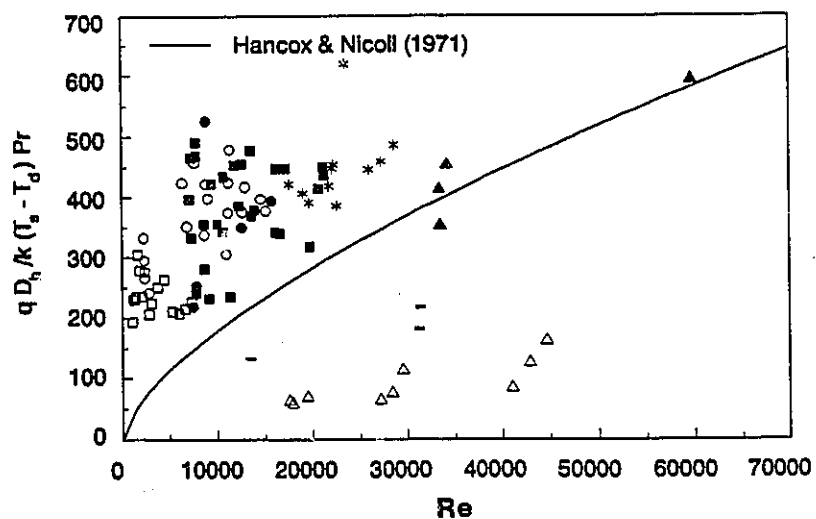


Figure 5.5b Comparison between experimental data and existing NVG models

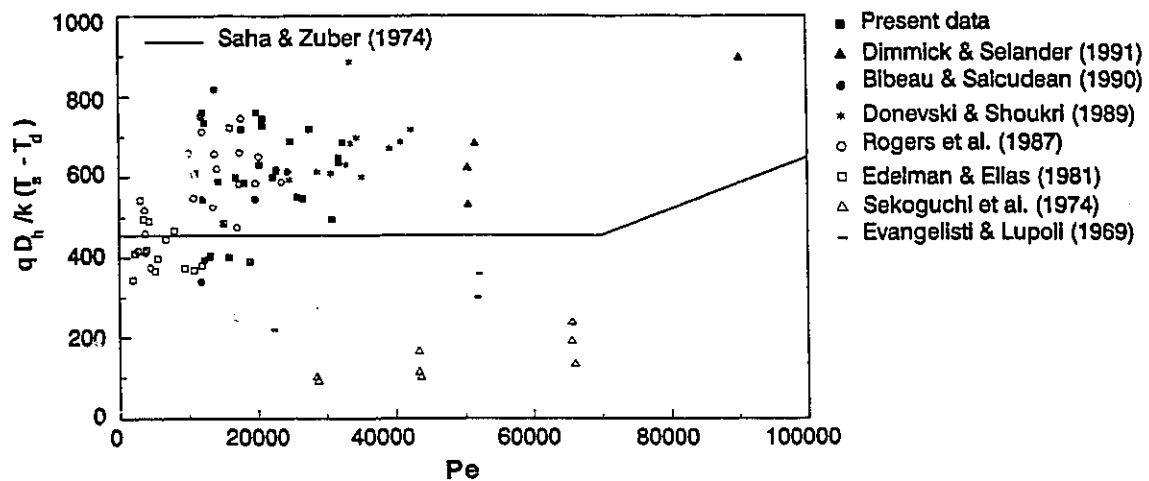


Figure 5.5c Comparison between experimental data and existing NVG models

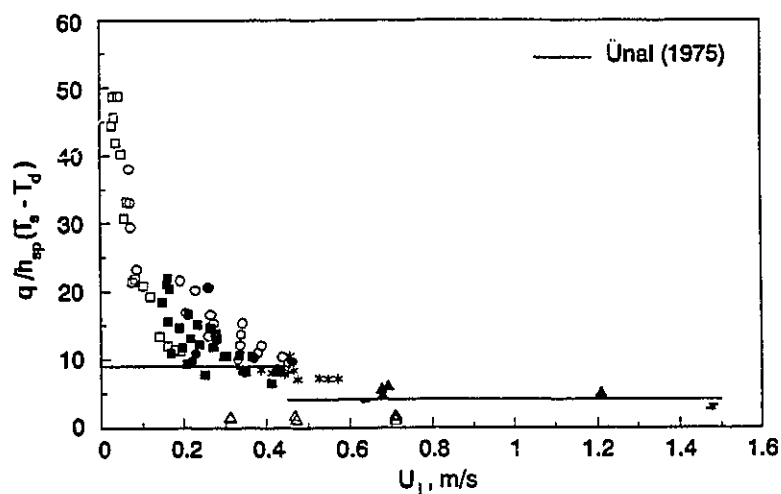


Figure 5.5d Comparison between experimental data and existing NVG models

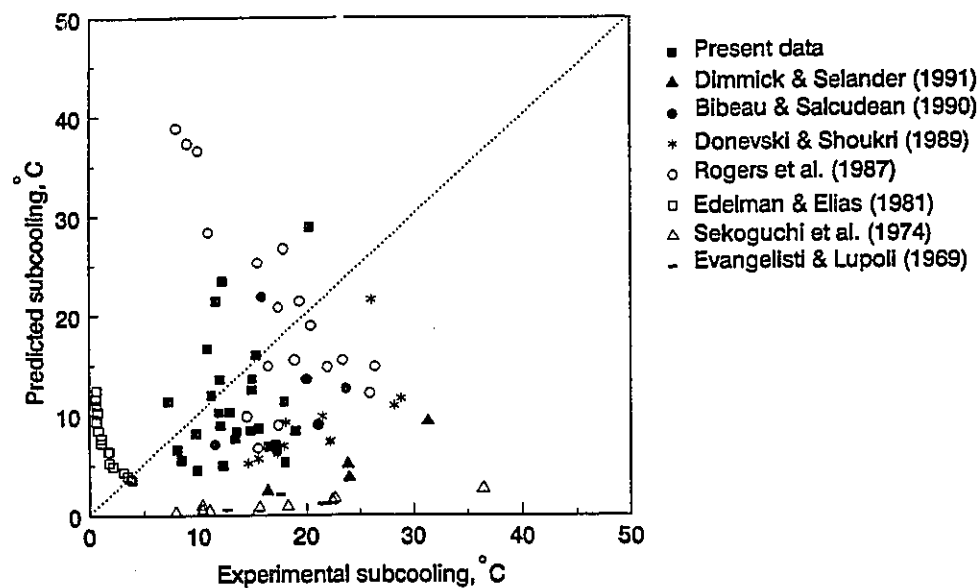


Figure 5.5e Comparison between experimental data and NVG model of Yang and Weisman (1991)

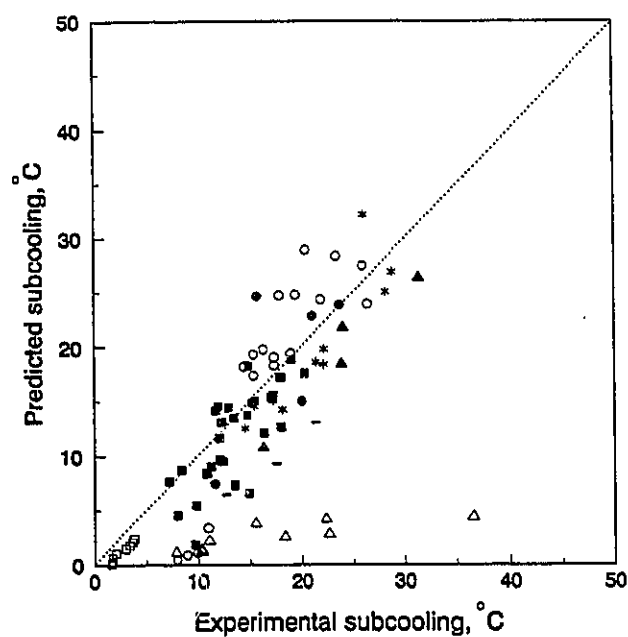


Figure 5.5f Comparison between experimental data and NVG model of Levy (1967)

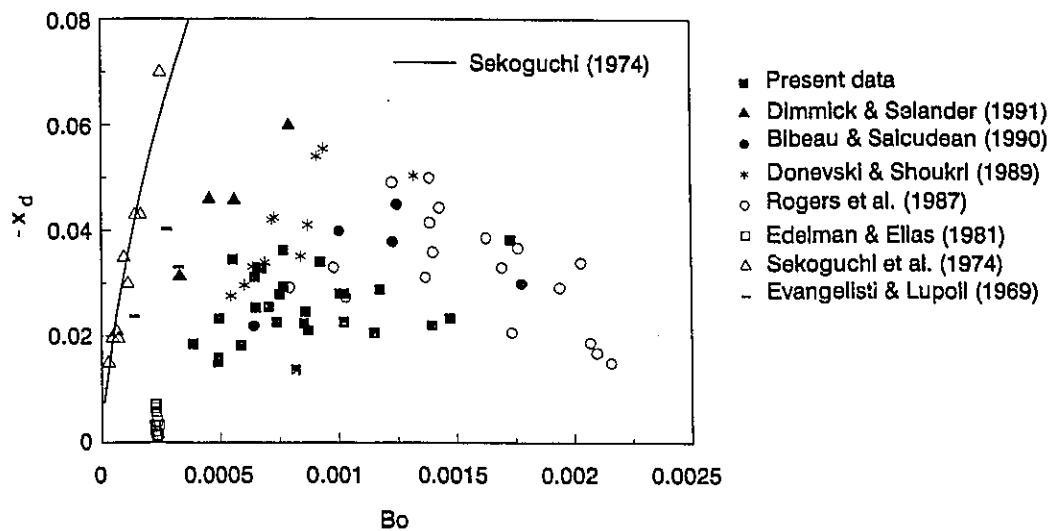


Figure 5.5g Comparison between experimental data and NVG model of Sekoguchi et al. (1974)

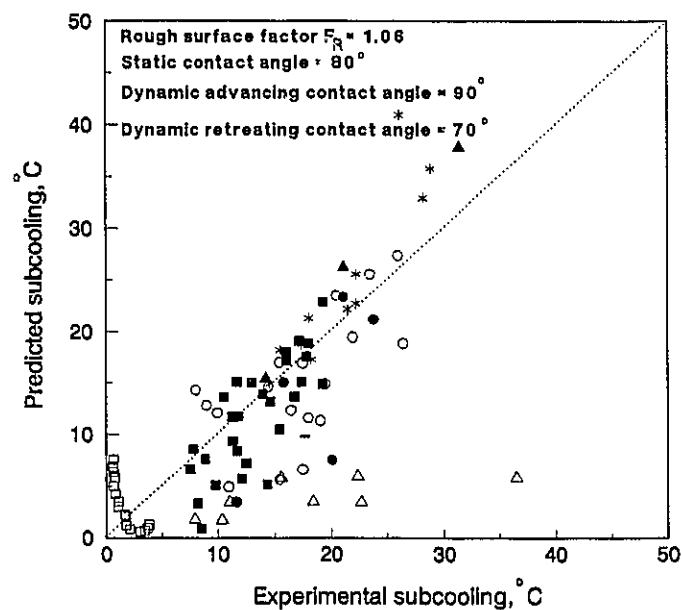


Figure 5.5h Comparison between experimental data and NVG model of Rogers et al. (1987)

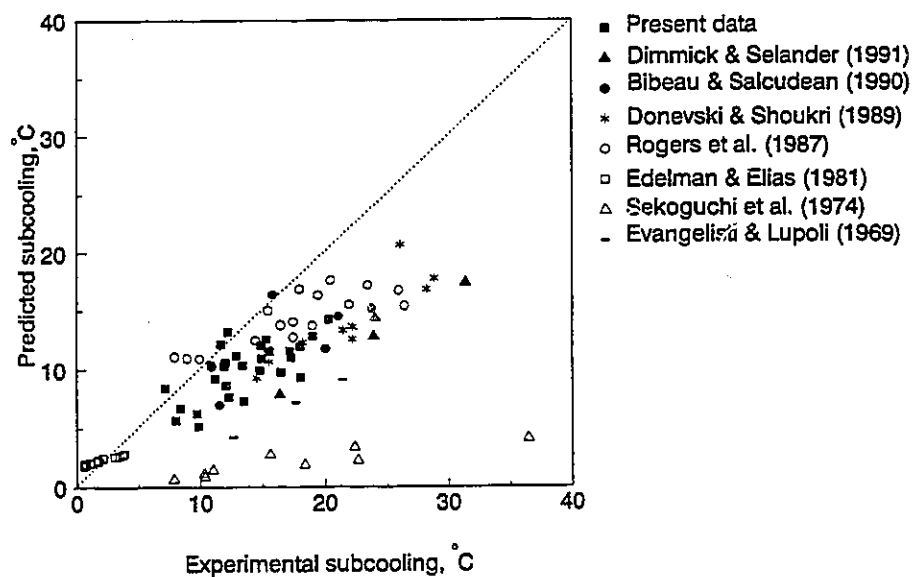


Figure 5.5i Comparison between experimental data and NVG model of Serizawa (1979)

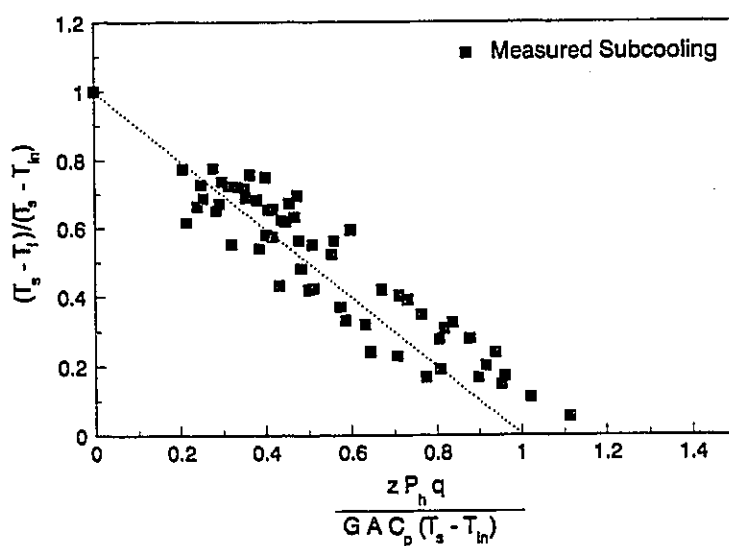


Figure 5.6 Liquid subcooling along heated section

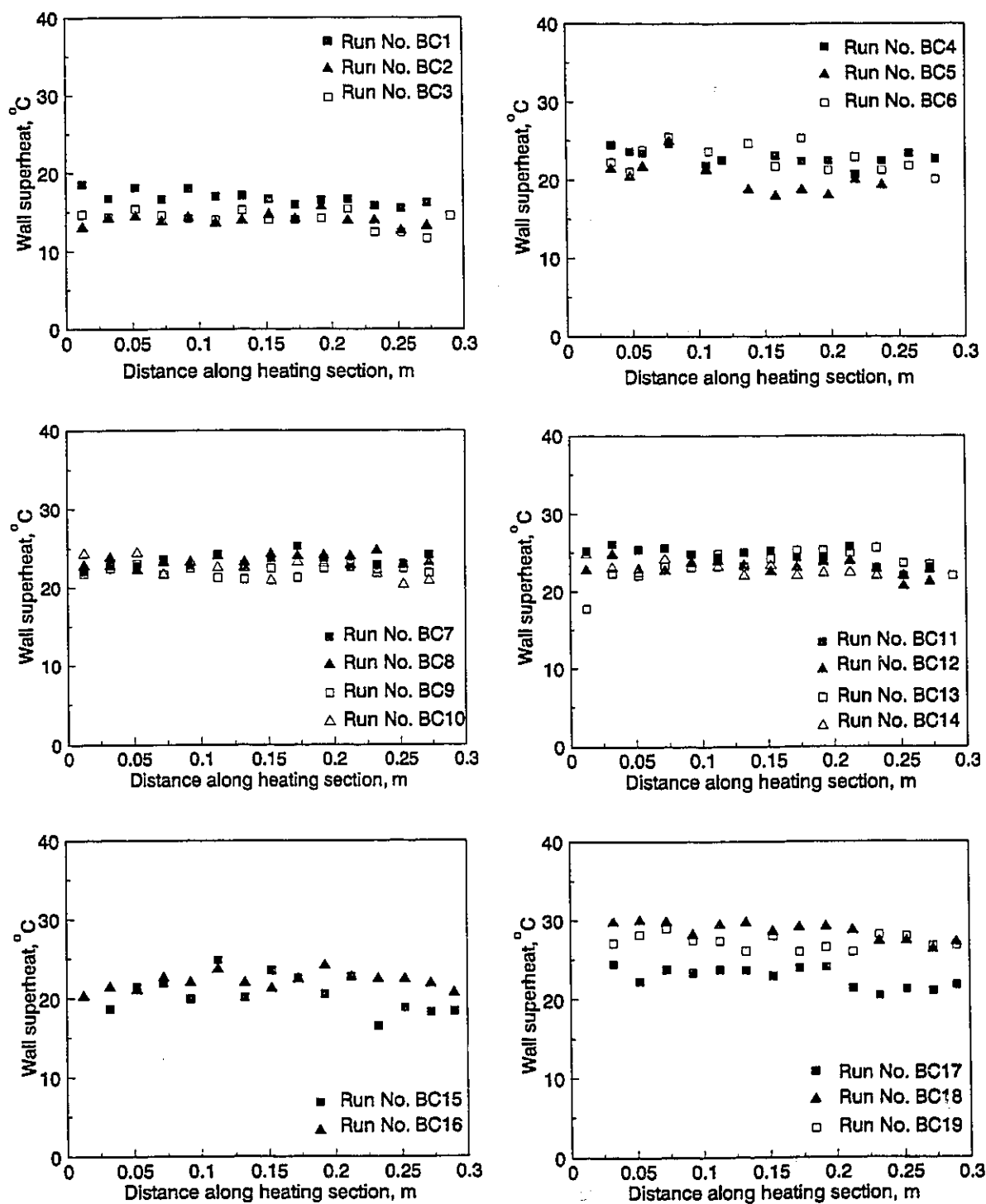


Figure 5.7 Inner wall superheat along heating section

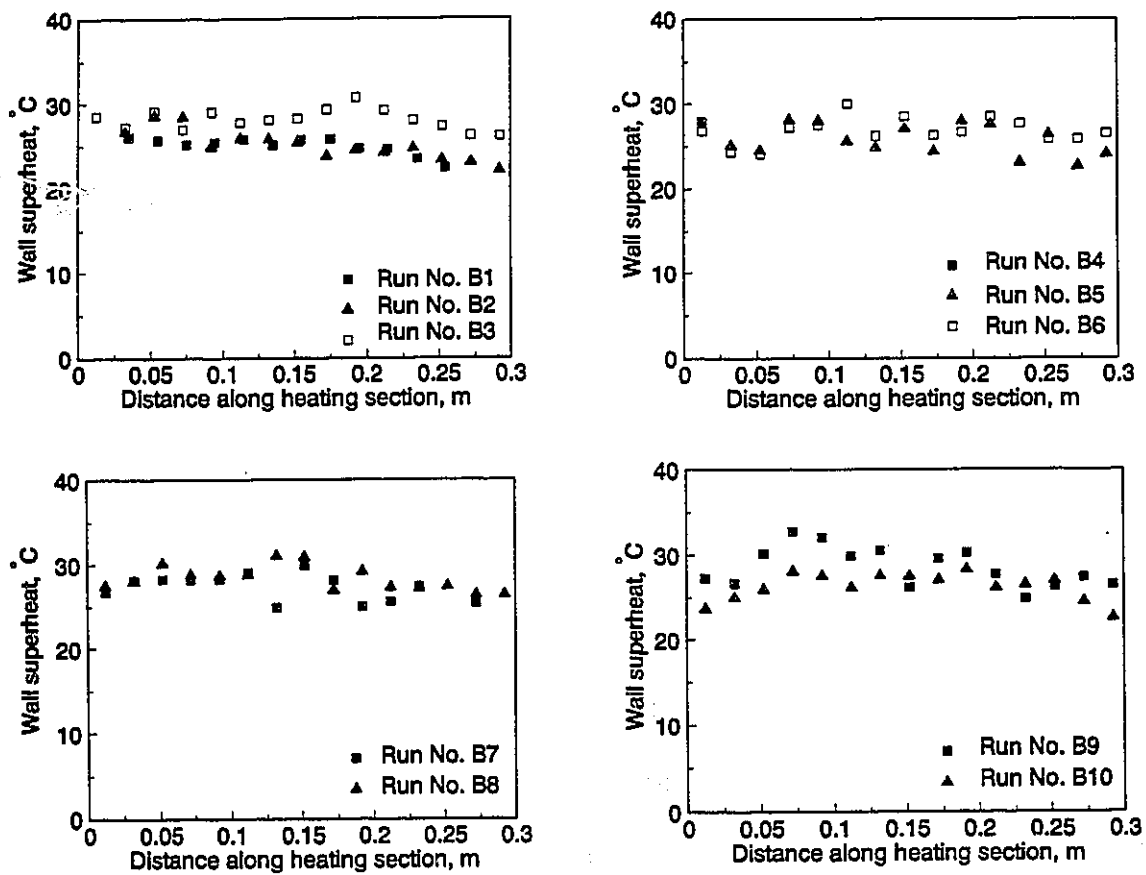


Figure 5.8 Inner wall superheat along heating section

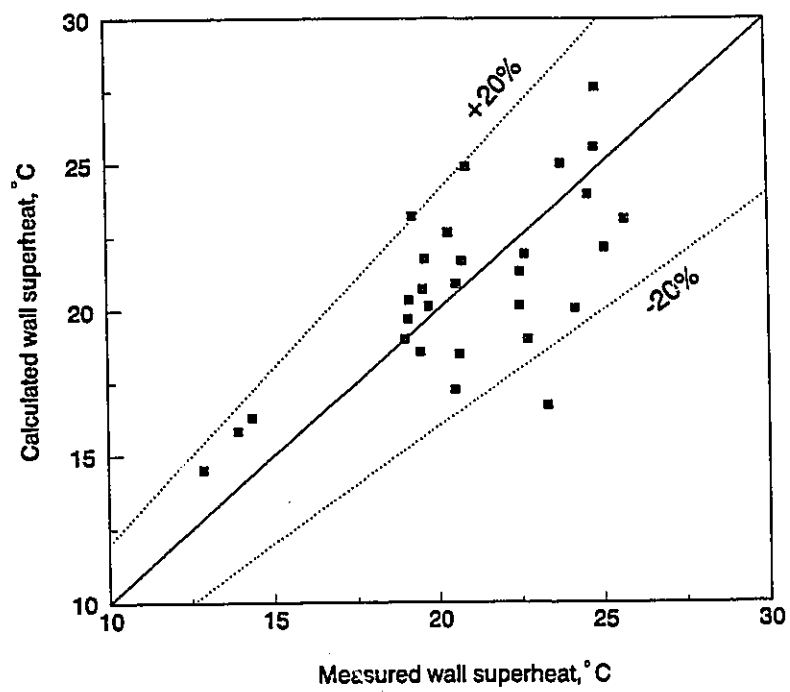
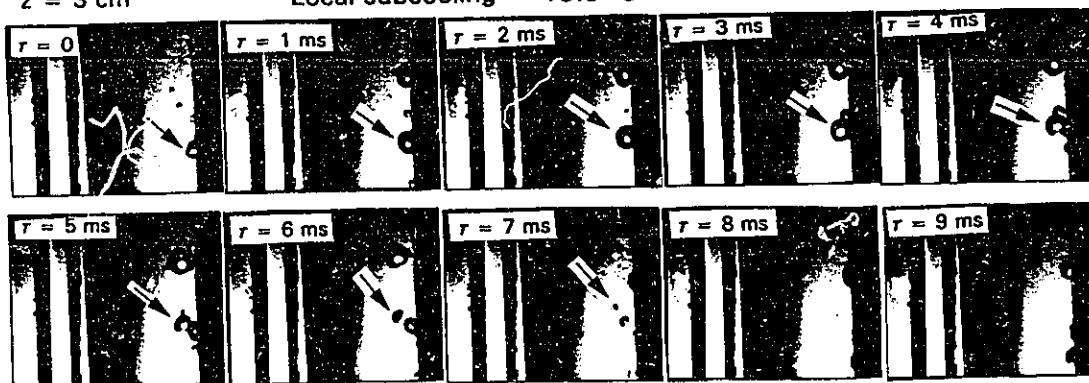


Figure 5.9 Comparison between measured wall superheat and Shah's model (1983)

Before the NVG point

$z = 3 \text{ cm}$

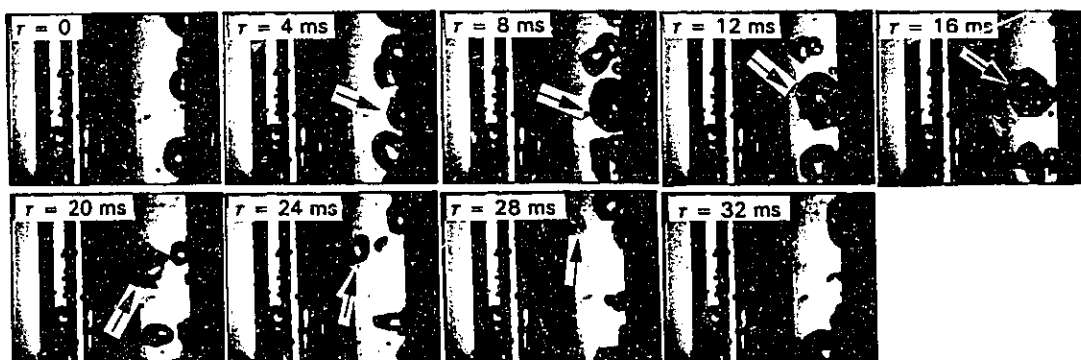
Local subcooling = 13.9°C



Near the NVG point

$z = 19 \text{ cm}$

Local subcooling = 6.6°C



After the NVG point

$z = 25 \text{ cm}$

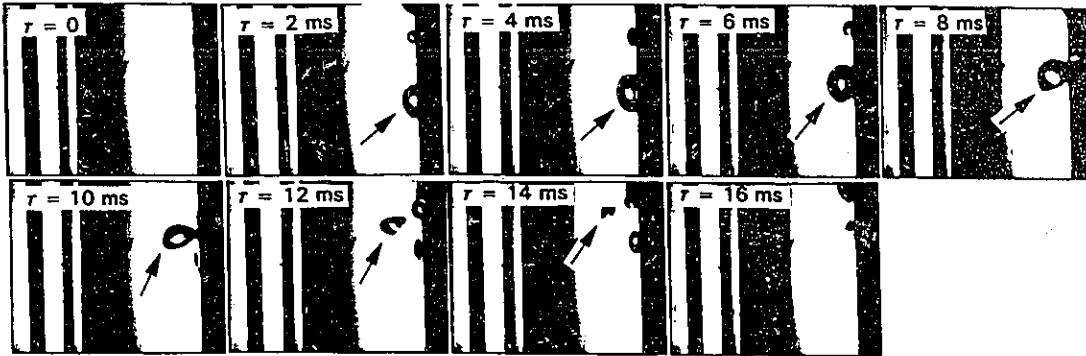
Local subcooling = 3.4°C



Figure 5.10 Bubble growth-collapse cycle before, near and after the NVG point for run no. B1 ($q = 286.7 \text{ kW/m}^2$, $G = 156.2 \text{ kg/m}^2 \text{ s}$, inlet subcooling = 14.9°C and $Z_d = 17.5 \text{ cm}$)

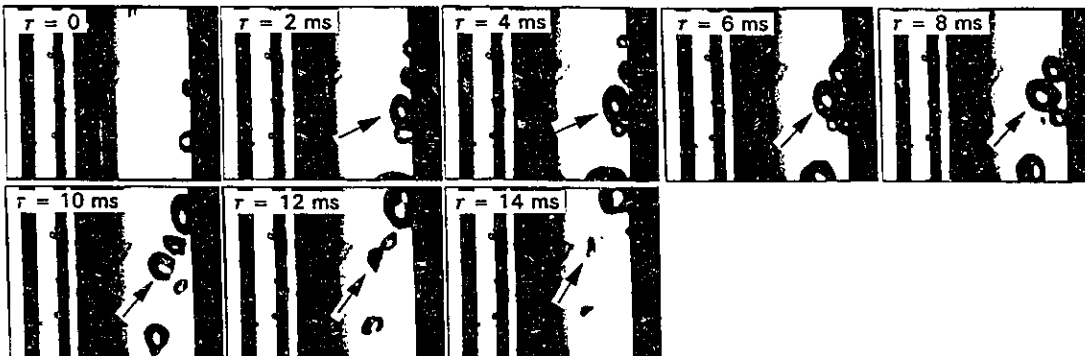
Before the NVG point
 $z = 1 \text{ cm}$

Local subcooling = 11.6°C



Near the NVG point
 $z = 9 \text{ cm}$

Local subcooling = 9.4°C



After the NVG point
 $z = 25 \text{ cm}$

Local subcooling = 5.0°C

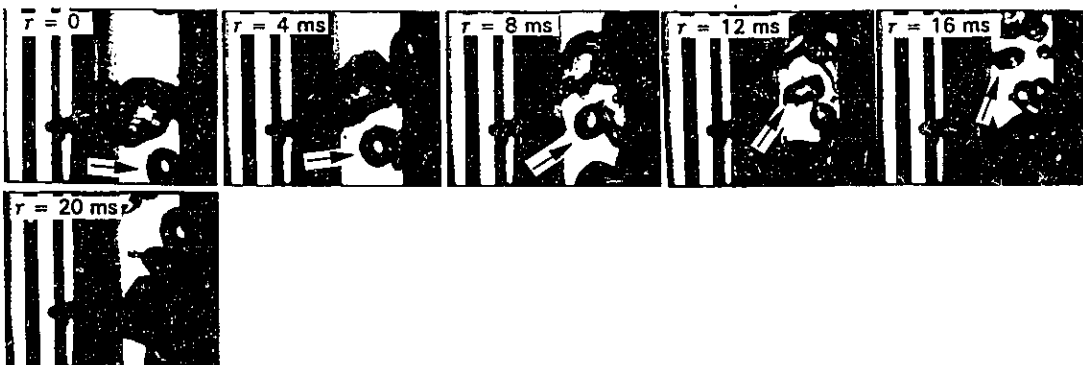


Figure 5.11 Bubble growth-collapse cycle before, near and after the NVG point for run no. B2
 $(q = 286.5 \text{ kW/m}^2, G = 258.2 \text{ kg/m}^2 \text{ s, inlet subcooling} = 11.6^\circ\text{C and } Z_d = 12.5 \text{ cm})$

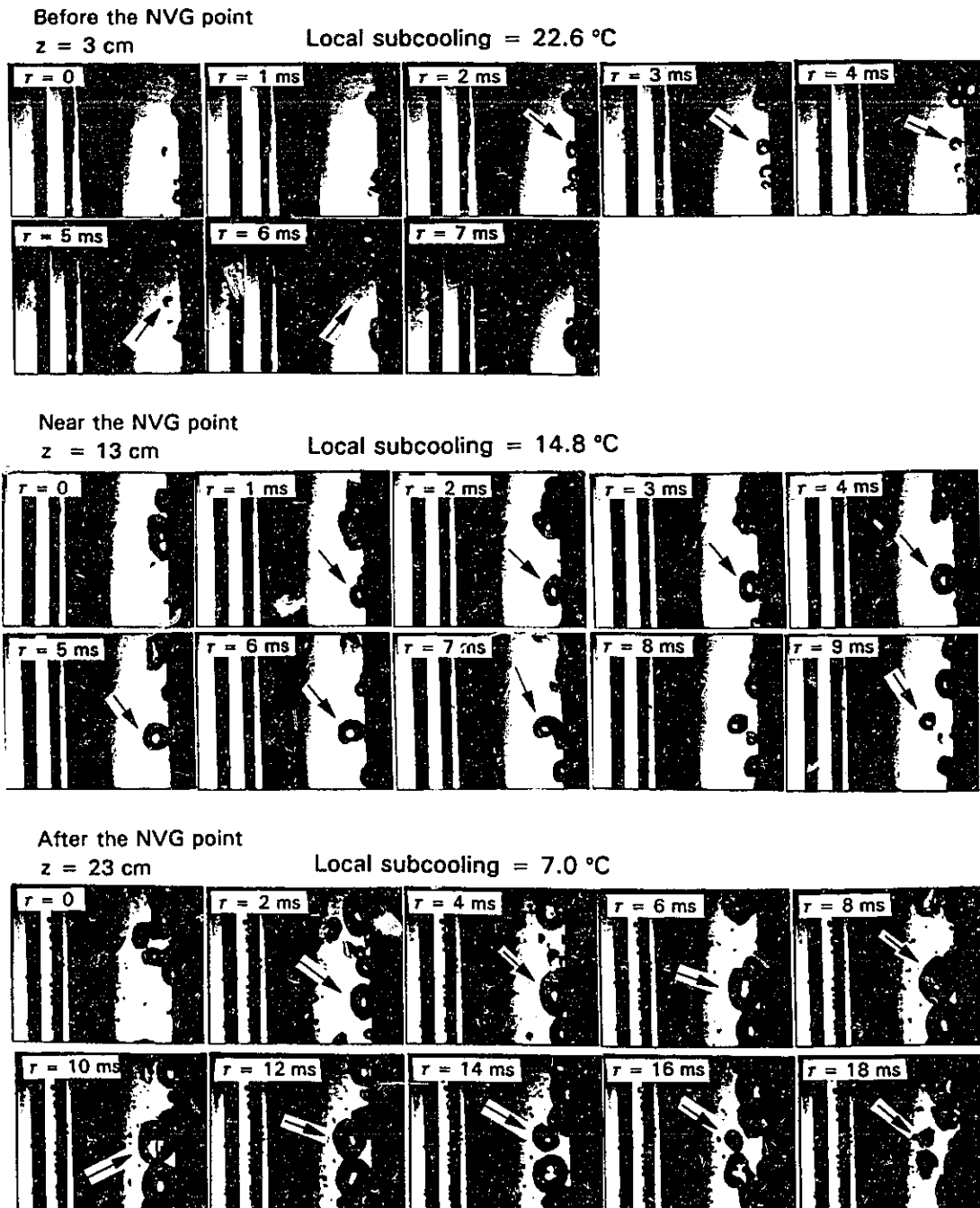
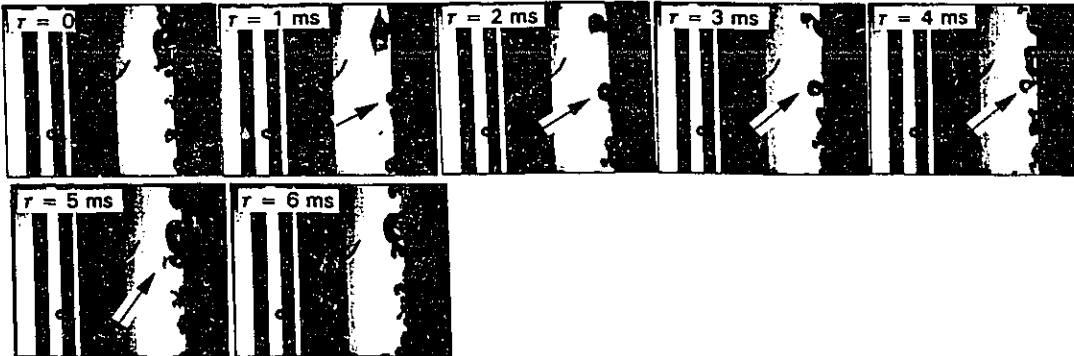


Figure 5.12 Bubble growth-collapse cycle before, near and after the NVG point for run no. B4
 ($q = 478.4 \text{ kW/m}^2$, $G = 152.5 \text{ kg/m}^2 \text{ s}$, inlet subcooling = 24.7°C and $Z_d = 17.0 \text{ cm}$)

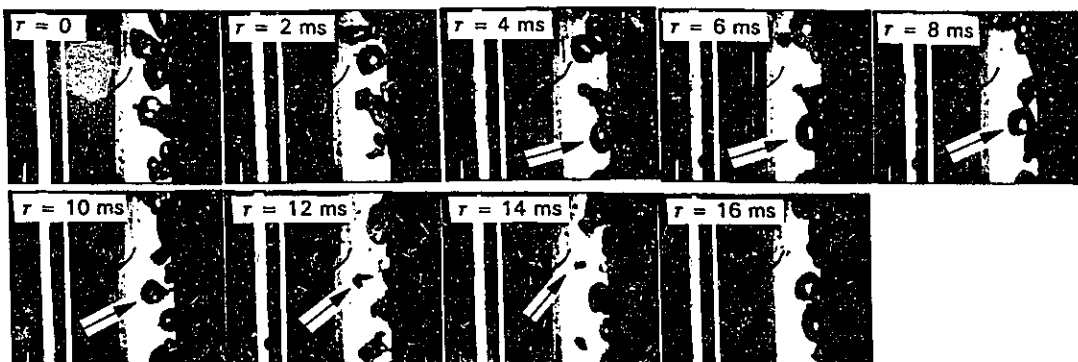
Before the NVG point
 $z = 7 \text{ cm}$

Local subcooling = 17.0°C



Near the NVG point
 $z = 13 \text{ cm}$

Local subcooling = 13.6°C



After the NVG point
 $z = 17 \text{ cm}$

Local subcooling = 11.4°C

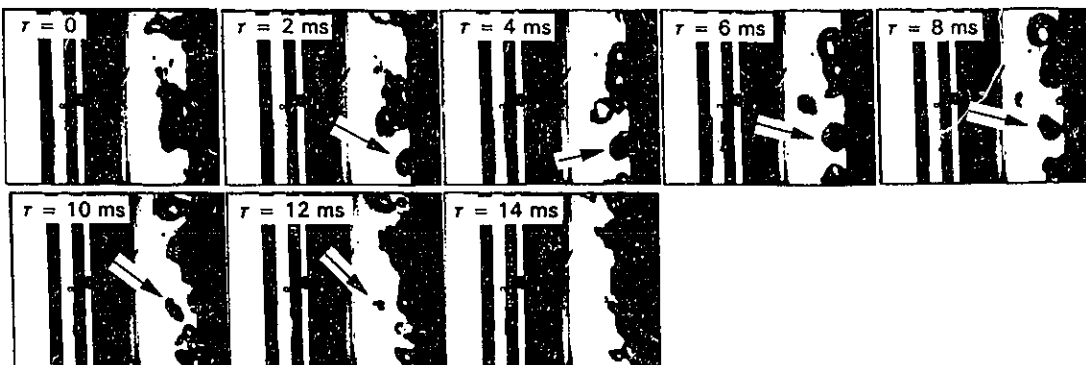


Figure 5.13 Bubble growth-collapse cycle before, near and after the NVG point for run no. B8
 $(q = 596.0 \text{ kW/m}^2, G = 263.8 \text{ kg/m}^2 \text{ s, inlet subcooling} = 21.1^\circ\text{C and } Z_d = 11.0 \text{ cm})$

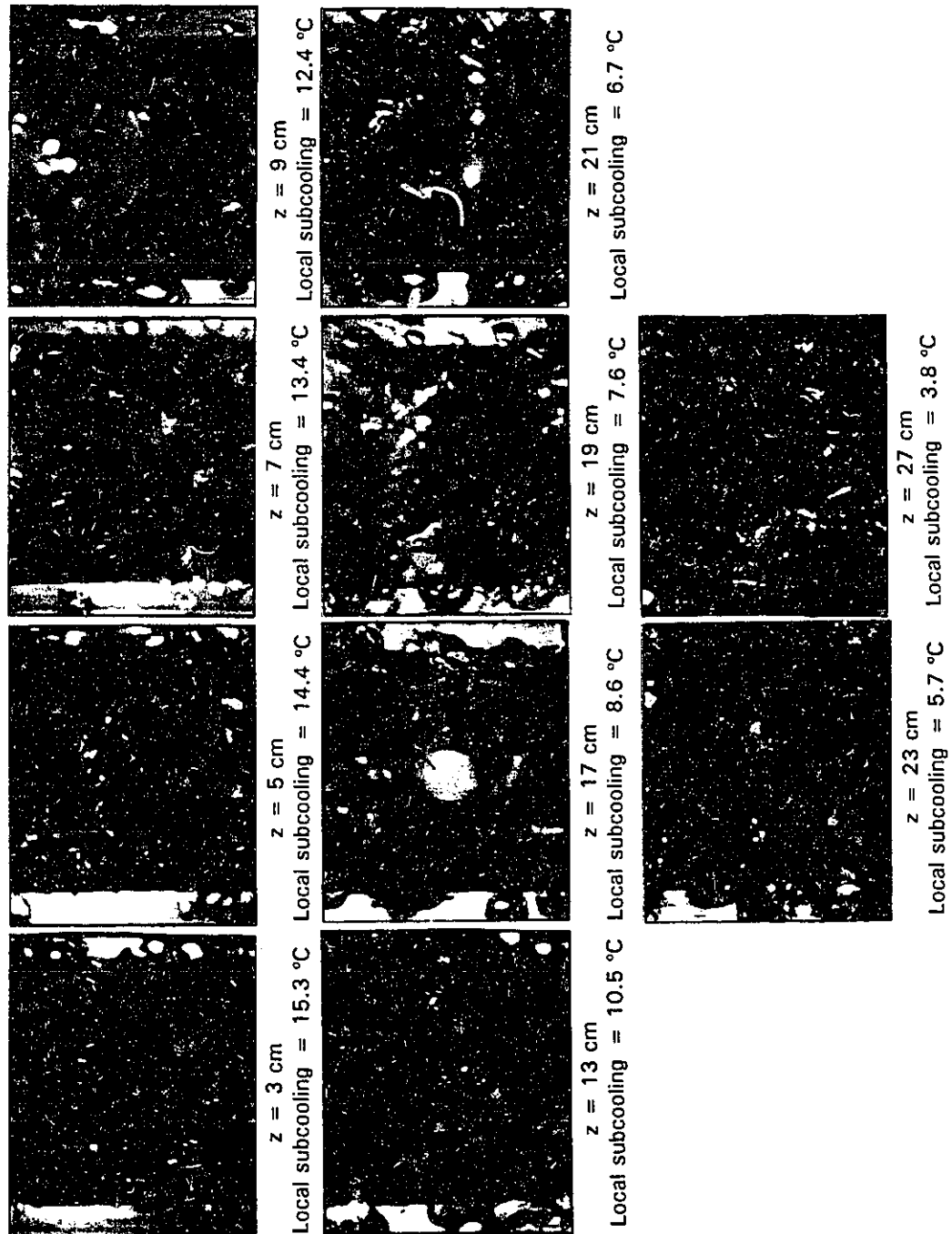


Figure 5.14 Bubble Behaviour along subcooled flow boiling region for run no. B3
($q = 487.9 \text{ kW/m}^2$, $G = 252.8 \text{ kg/m}^2 \text{ s}$, inlet subcooling = 16.6°C and $Z_d = 10.0 \text{ cm}$)

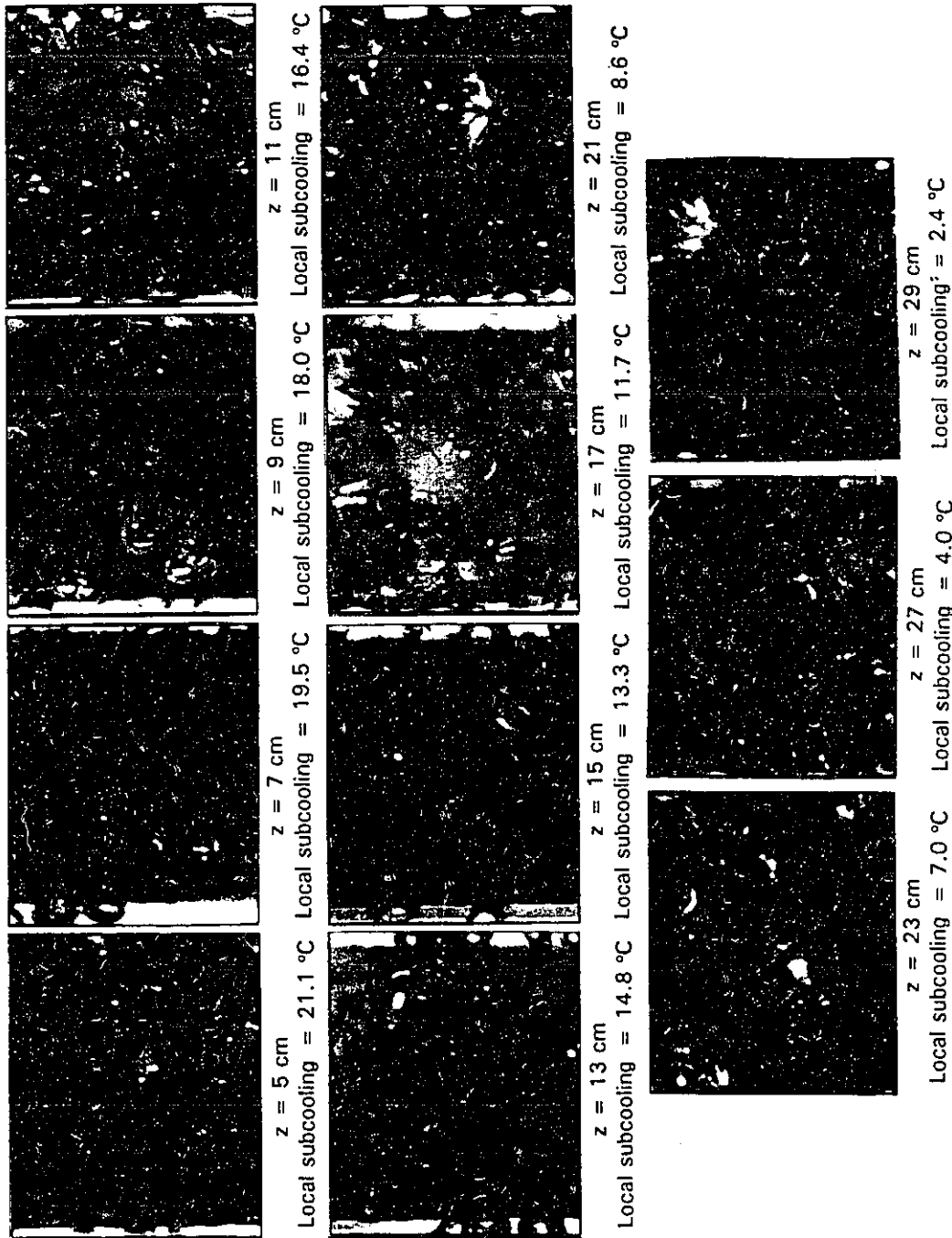


Figure 5.15 Bubble Behaviour along subcooled flow boiling region for run no. B4
($q = 478.4 \text{ kW/m}^2$, $G = 152.5 \text{ kg/m}^2 \text{ s}$, inlet subcooling = 24.7°C and $Z_d = 17.0 \text{ cm}$)

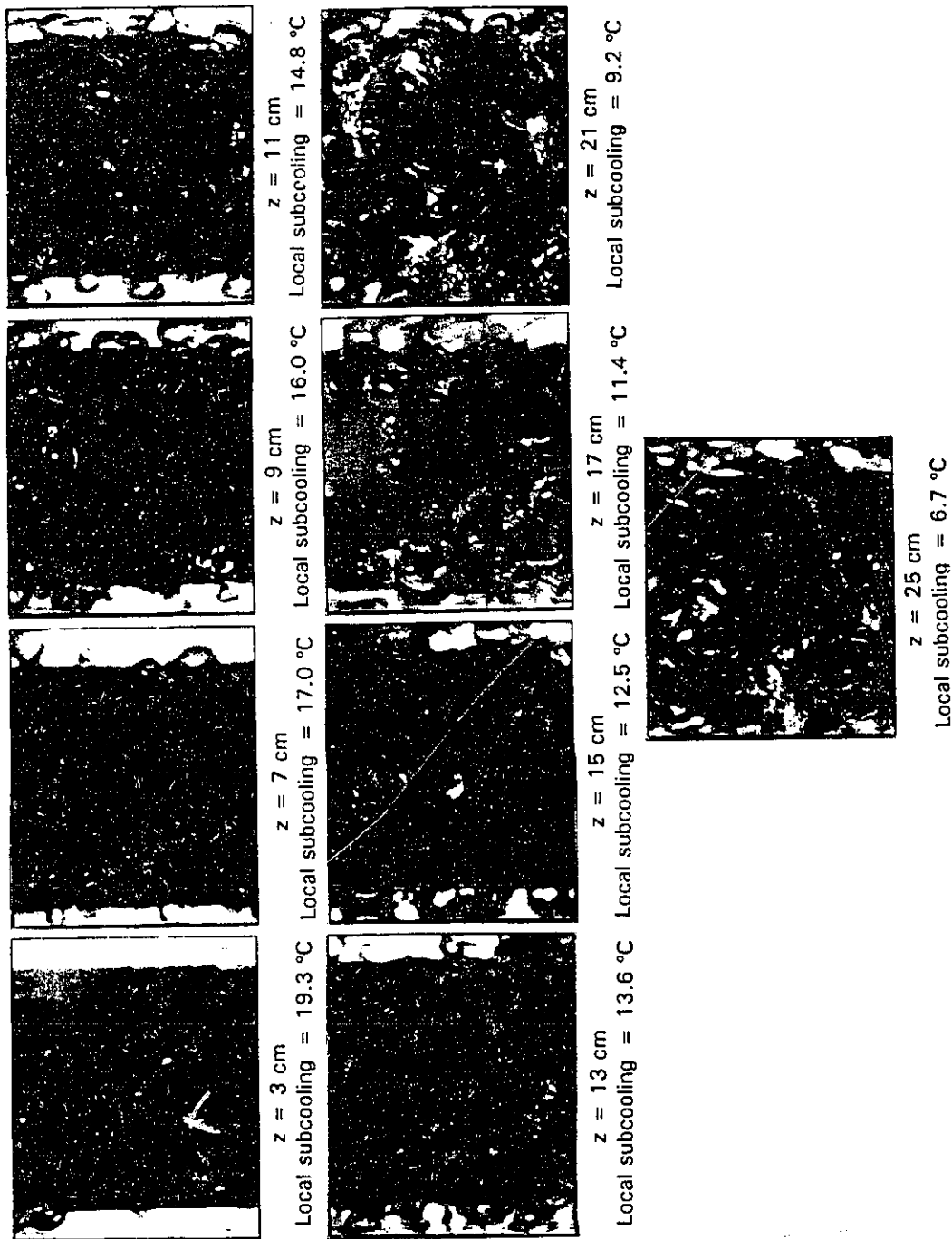


Figure 5.16 Bubble Behaviour along subcooled flow boiling region for run no. B8
 $(q = 596.0 \text{ kW/m}^2, G = 263.8 \text{ kg/m}^2 \text{ s, inlet subcooling} = 20.1^\circ\text{C and } Z_d = 11.0 \text{ cm})$

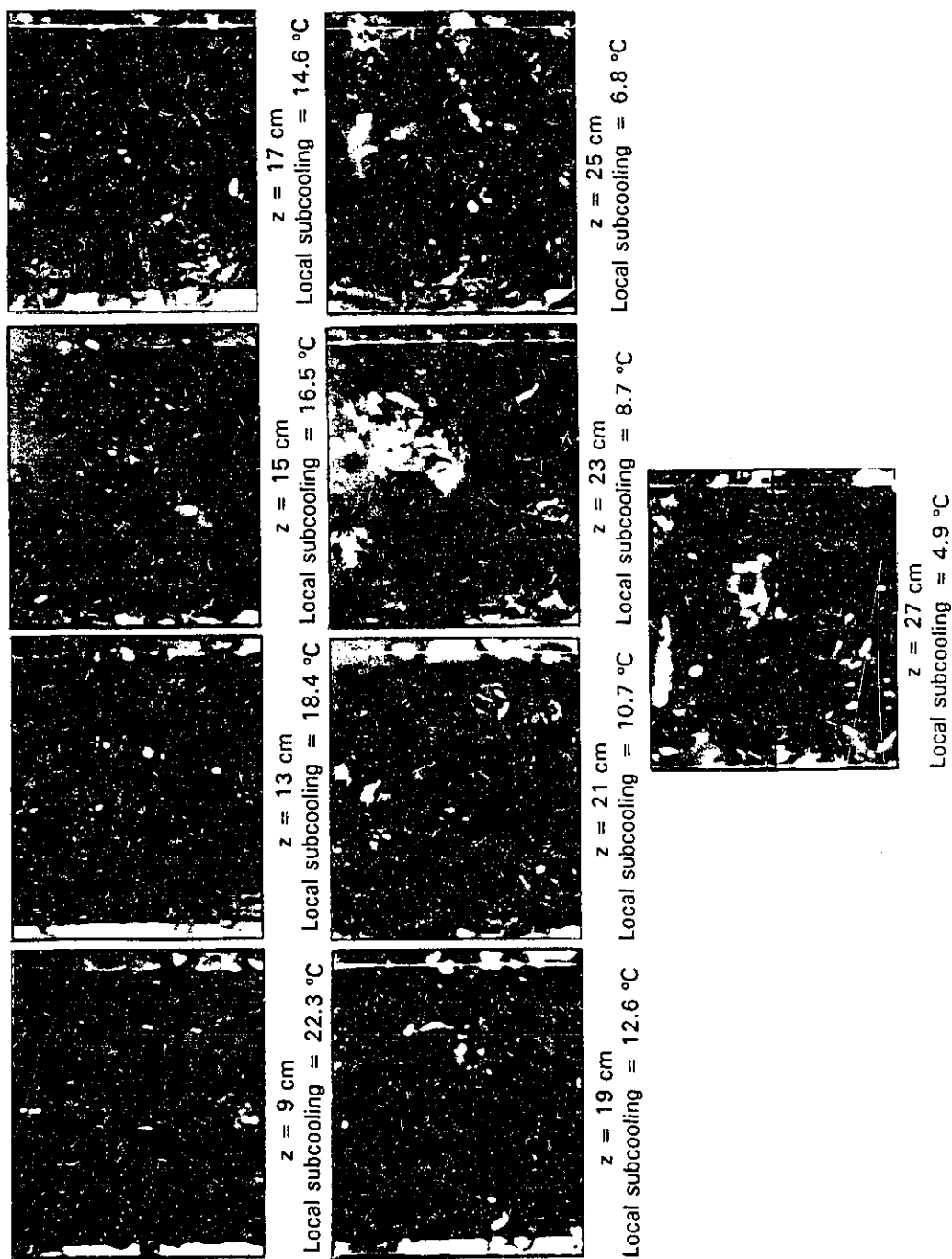


Figure 5.17 Bubble Behaviour along subcooled flow boiling region for run no. B9
 ($q = 593.2 \text{ kW/m}^2$, $G = 152.6 \text{ kg/m}^2 \text{ s}$, inlet subcooling = 31.2°C and $Z_d = 11.0 \text{ cm}$)

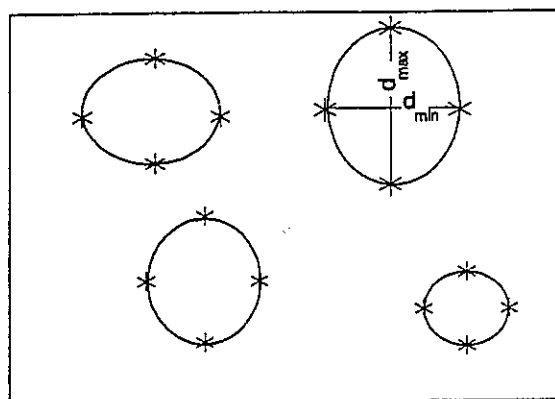


Figure 5.18 Bubble size measurement

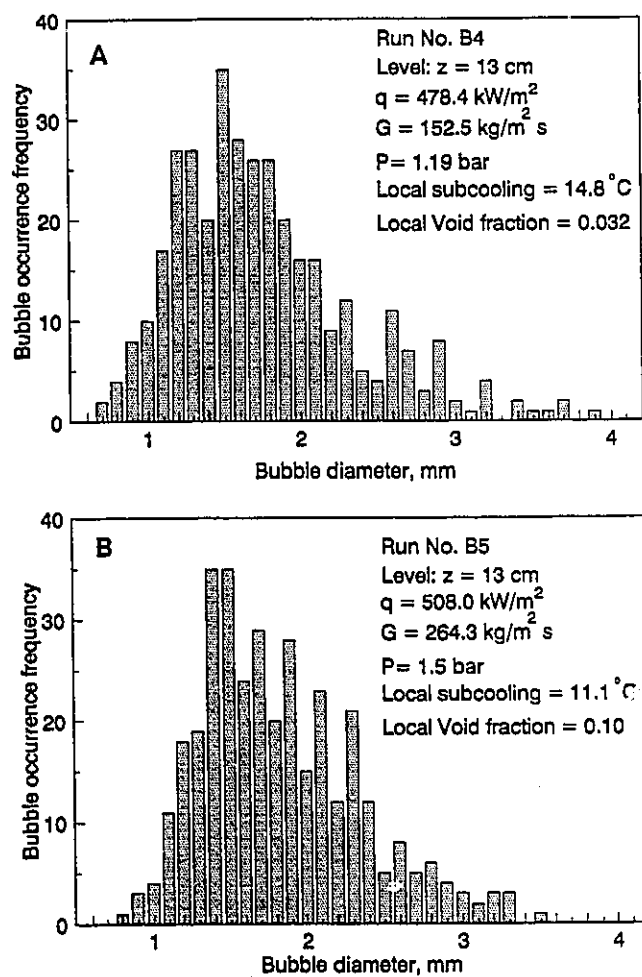
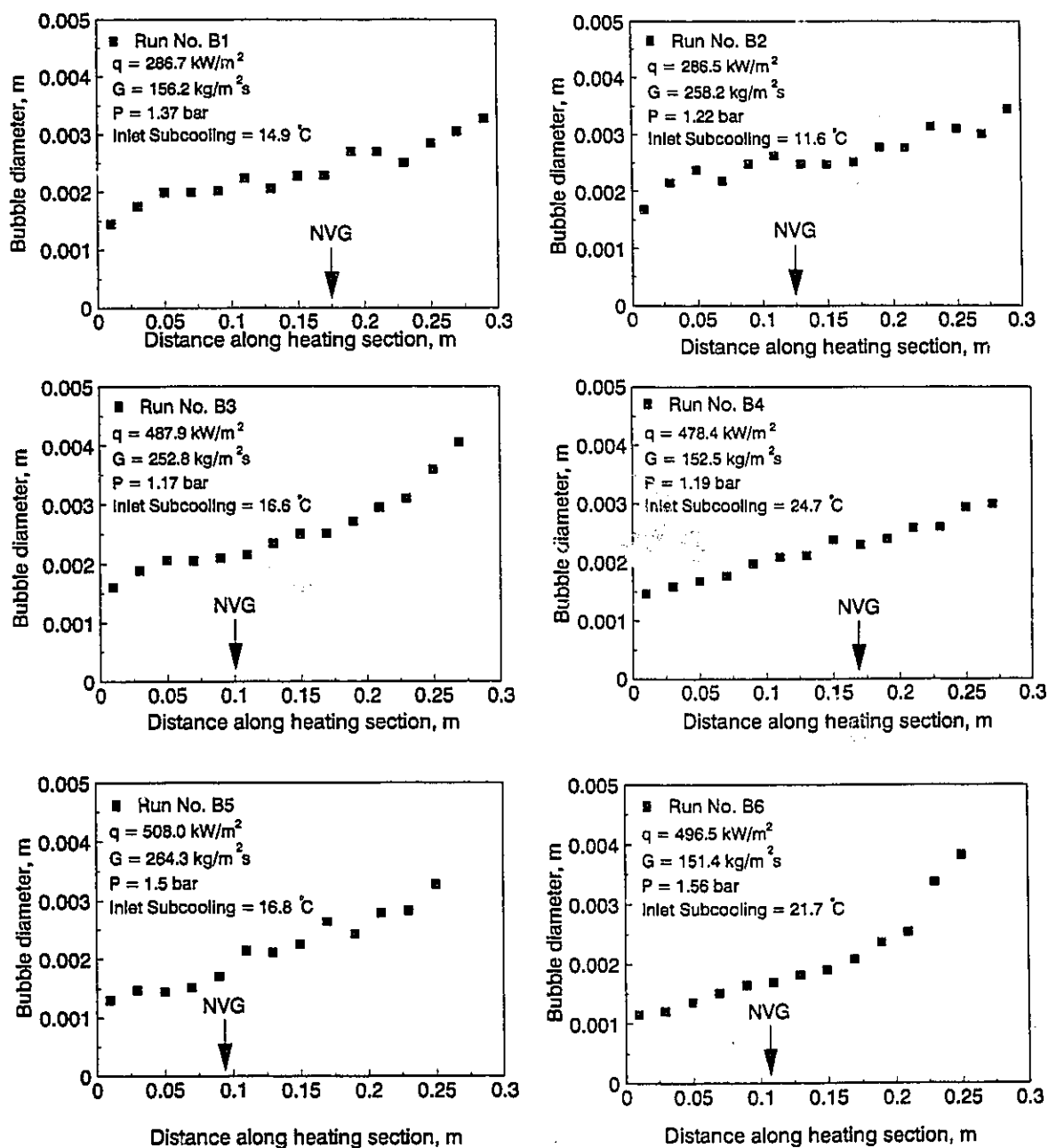
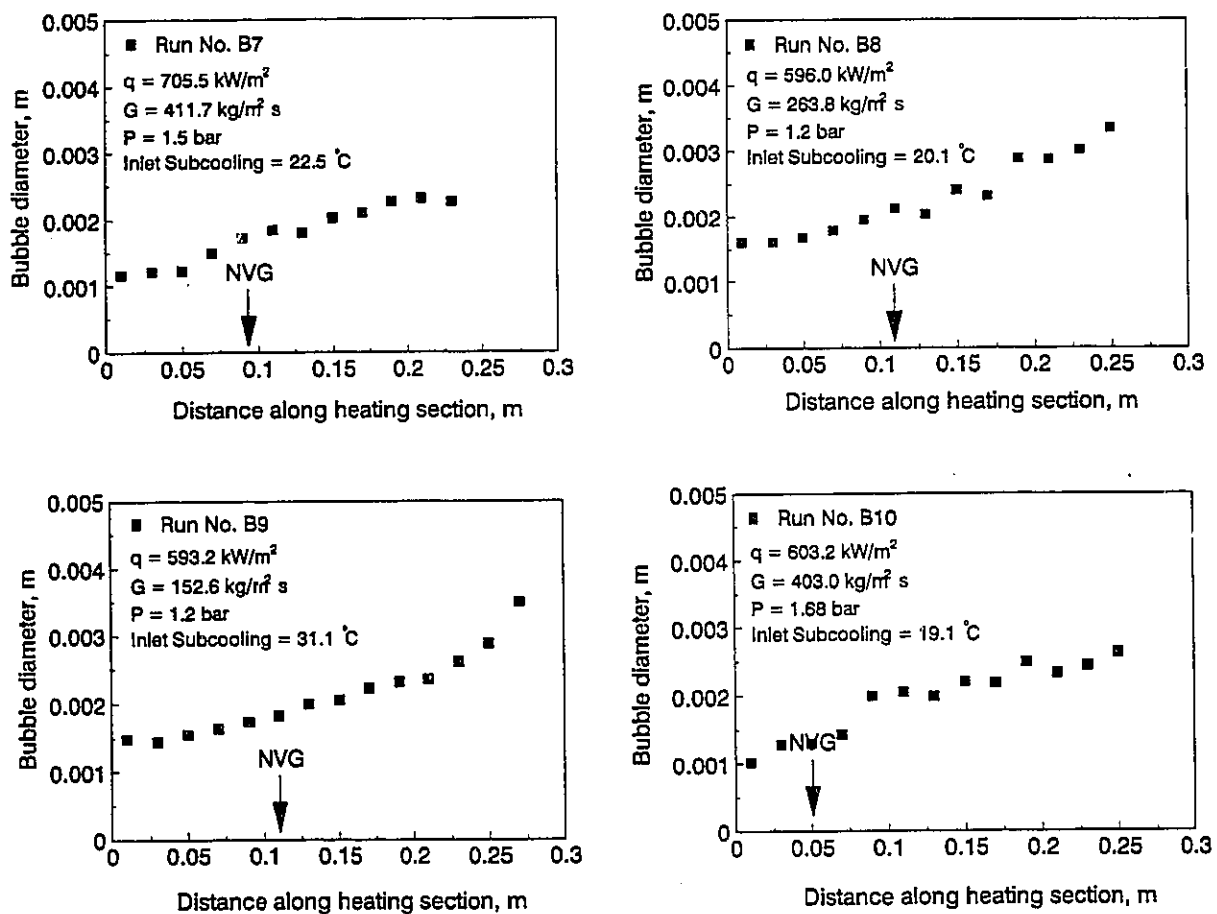


Figure 5.19 Typical histogram of bubble occurrence frequency versus individual Sauter bubble diameter



**Figure 5.20a Measured mean Sauter bubble diameter
along heating section**



**Figure 5.20b Measured mean sauter bubble diameter
along heating section**

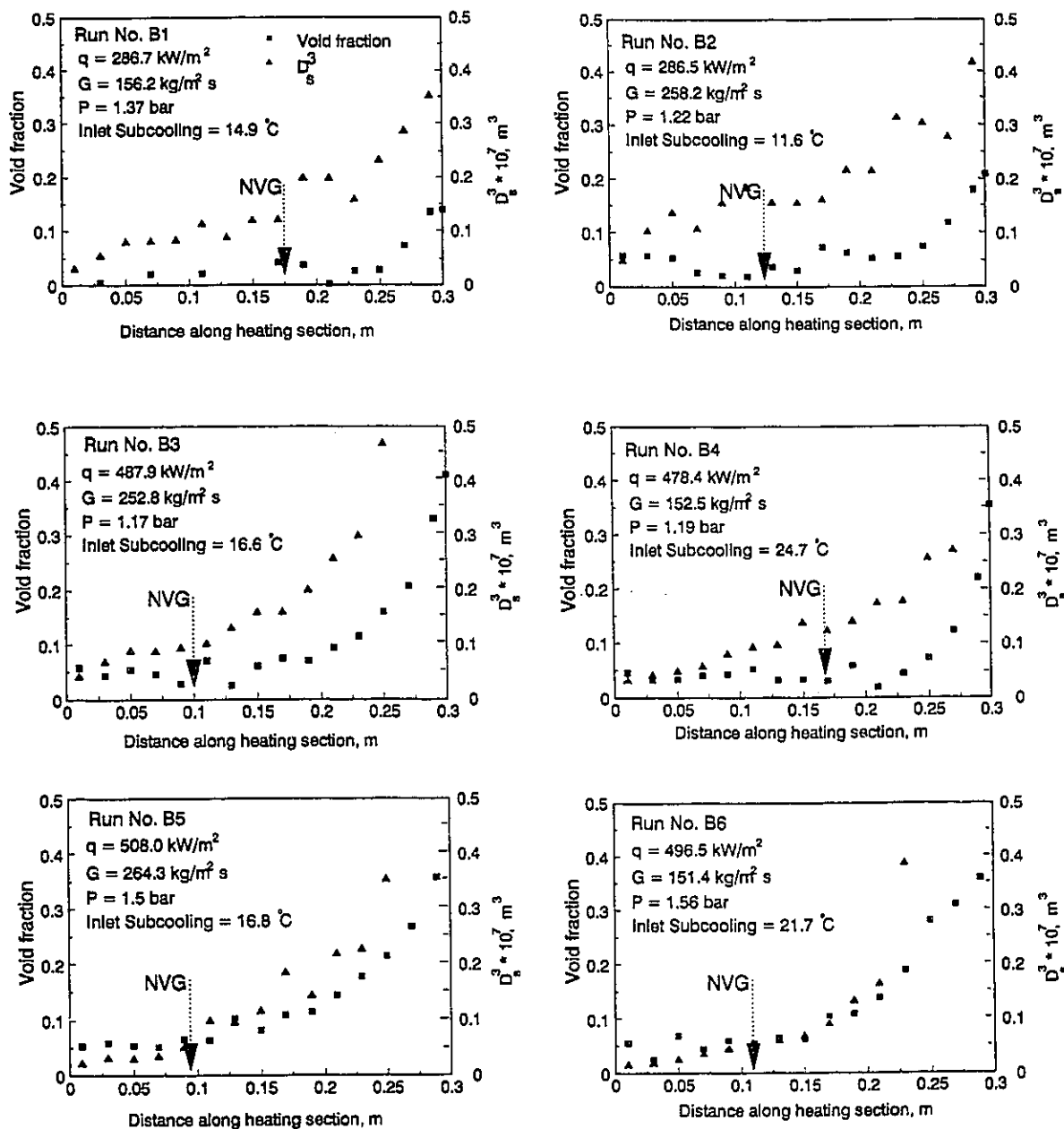


Figure 5.21a Relation between bubble size and void fraction along heated section

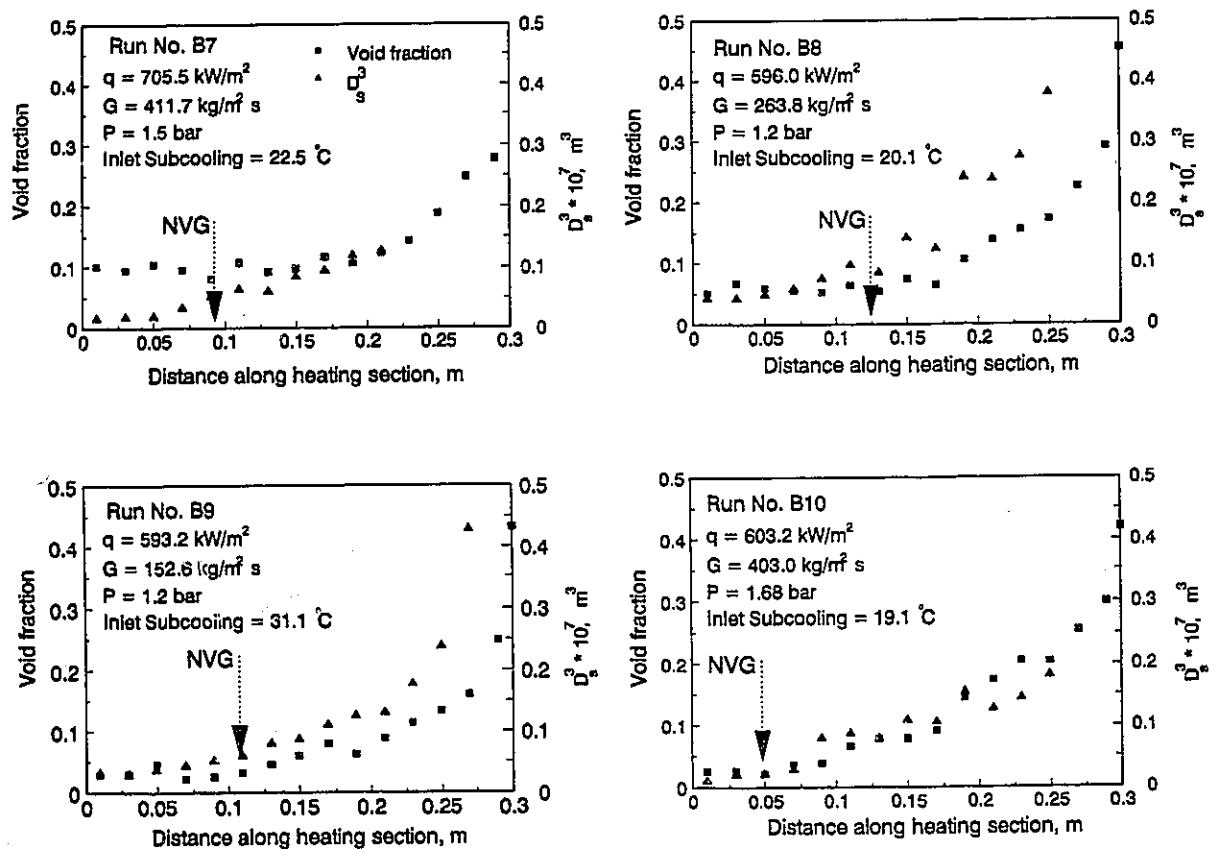


Figure 5.2 1b Relation between bubble size and void fraction along heated section

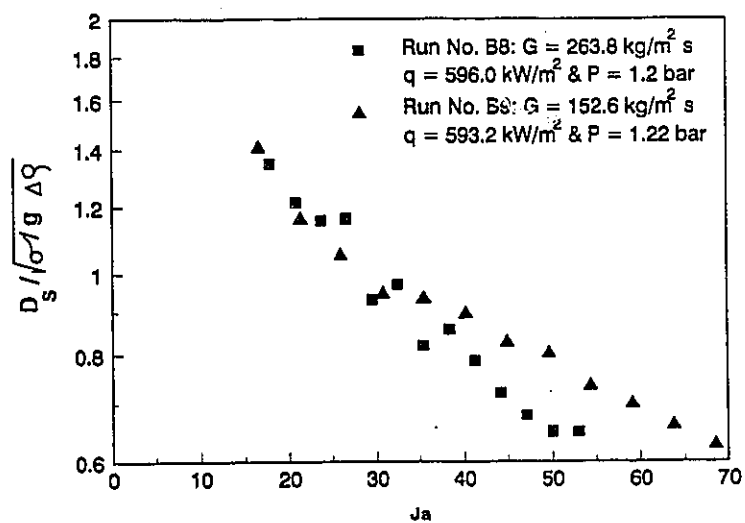
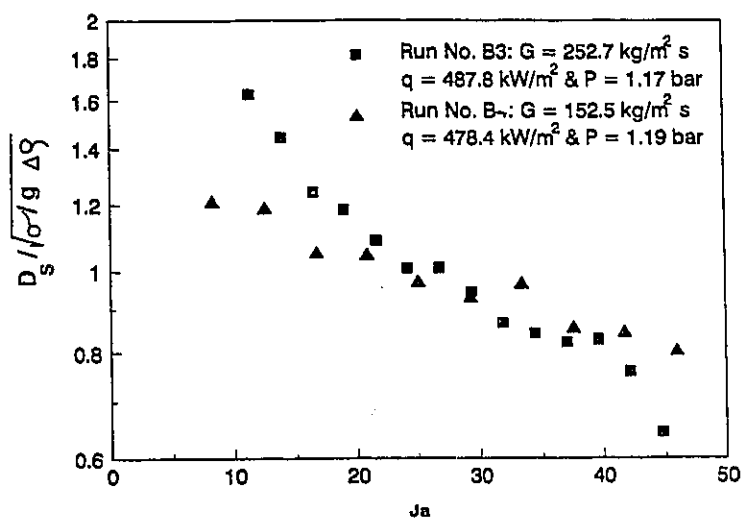


Figure 5.22 Effect of mass flux on bubble size

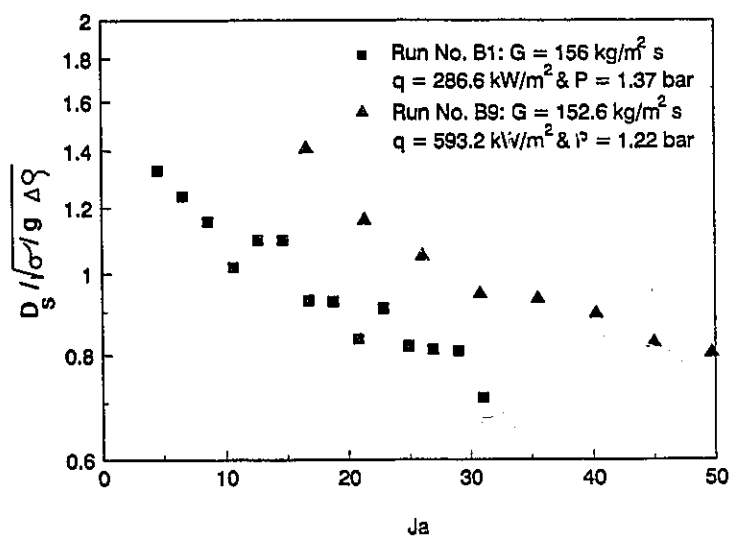
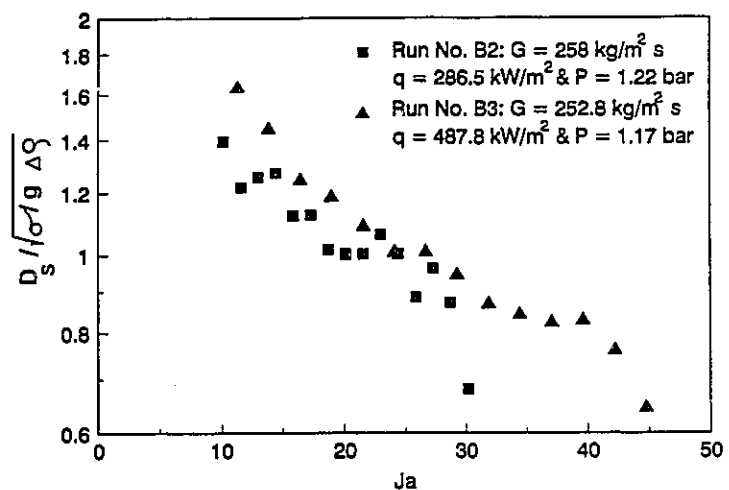


Figure 5.23 Effect of applied heat flux on bubble size

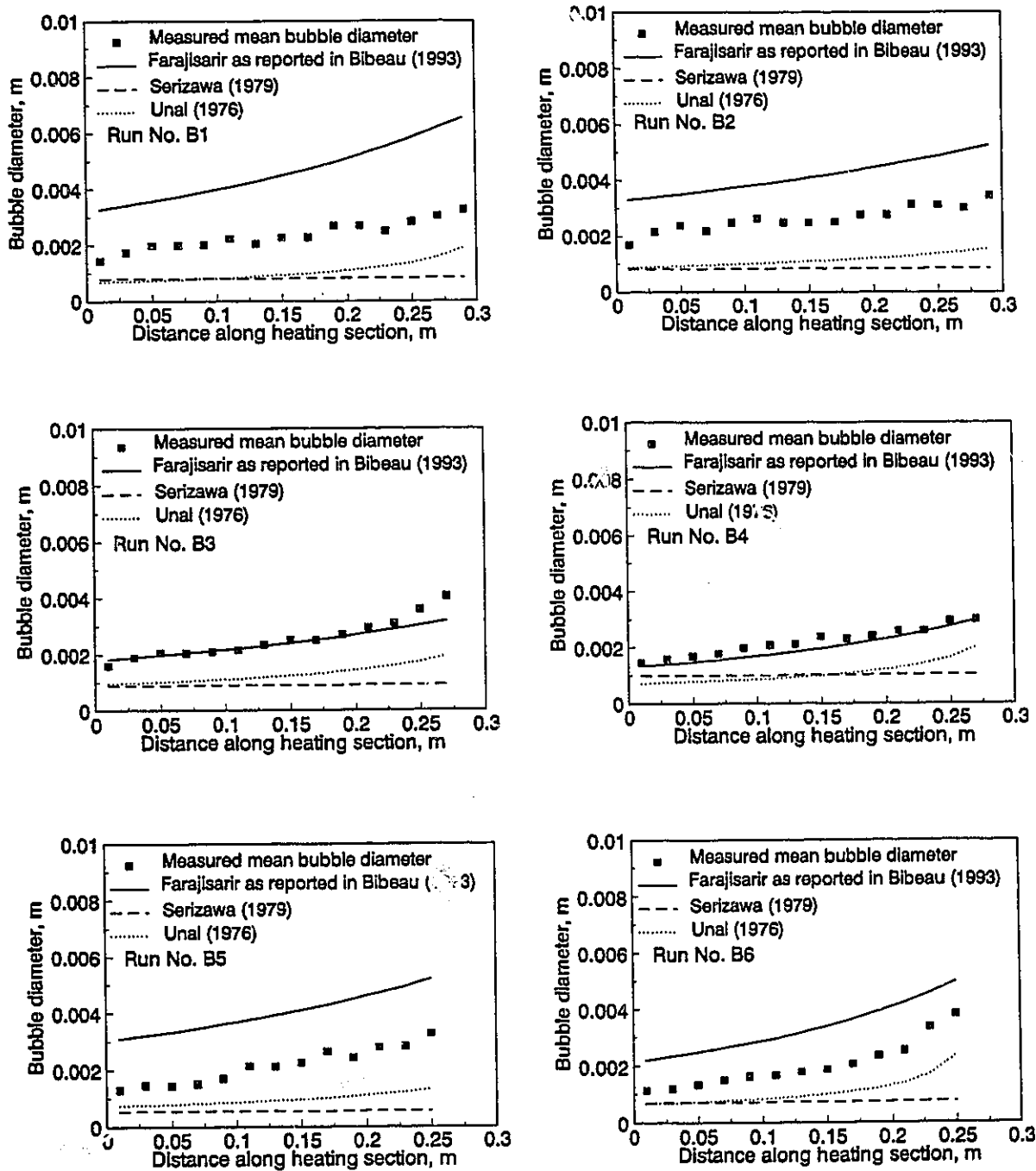


Figure 5.24a Comparison between measured mean bubble diameter and existing models of maximum and detachment bubble diameter

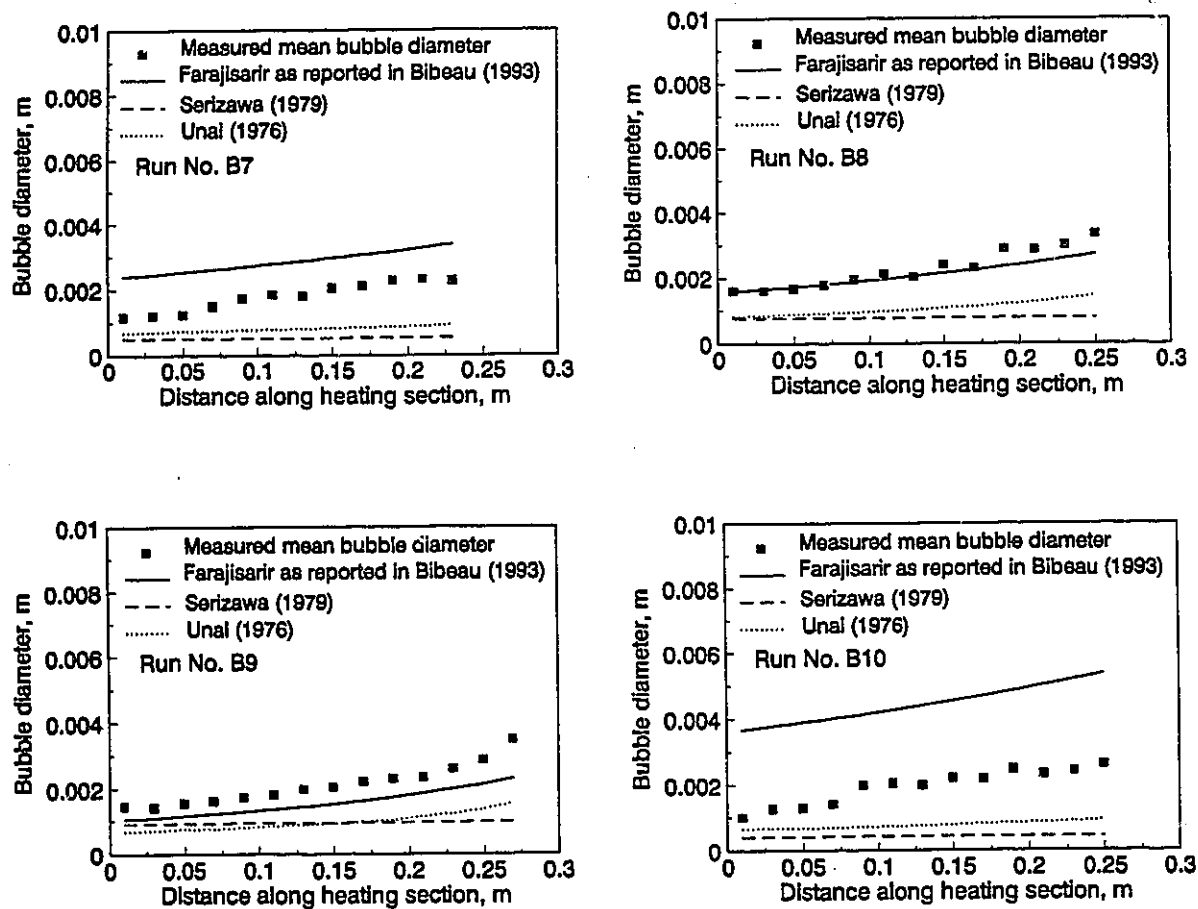
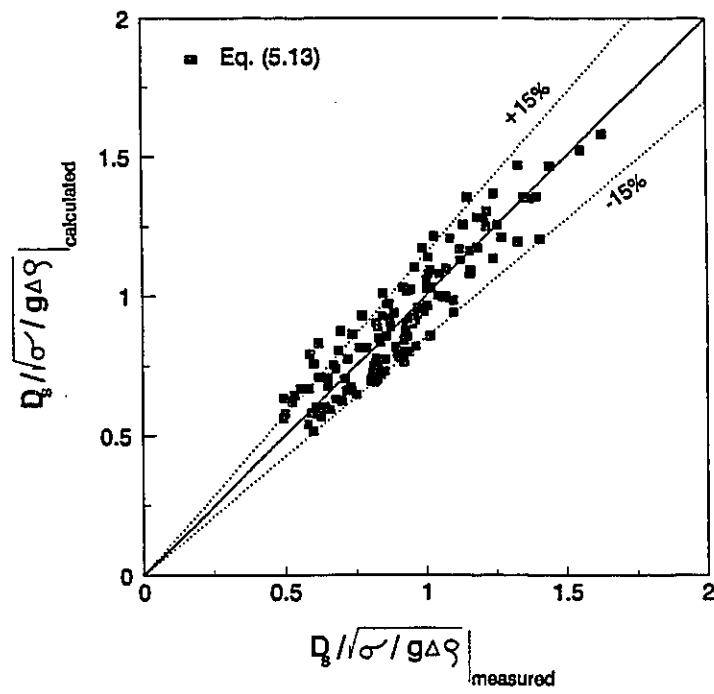


Figure 5.24b Comparison between measured mean bubble diameter and existing models of maximum and detachment bubble diameter



**Figure 5.25 Comparison between proposed correlation
and measured mean bubble diameter**

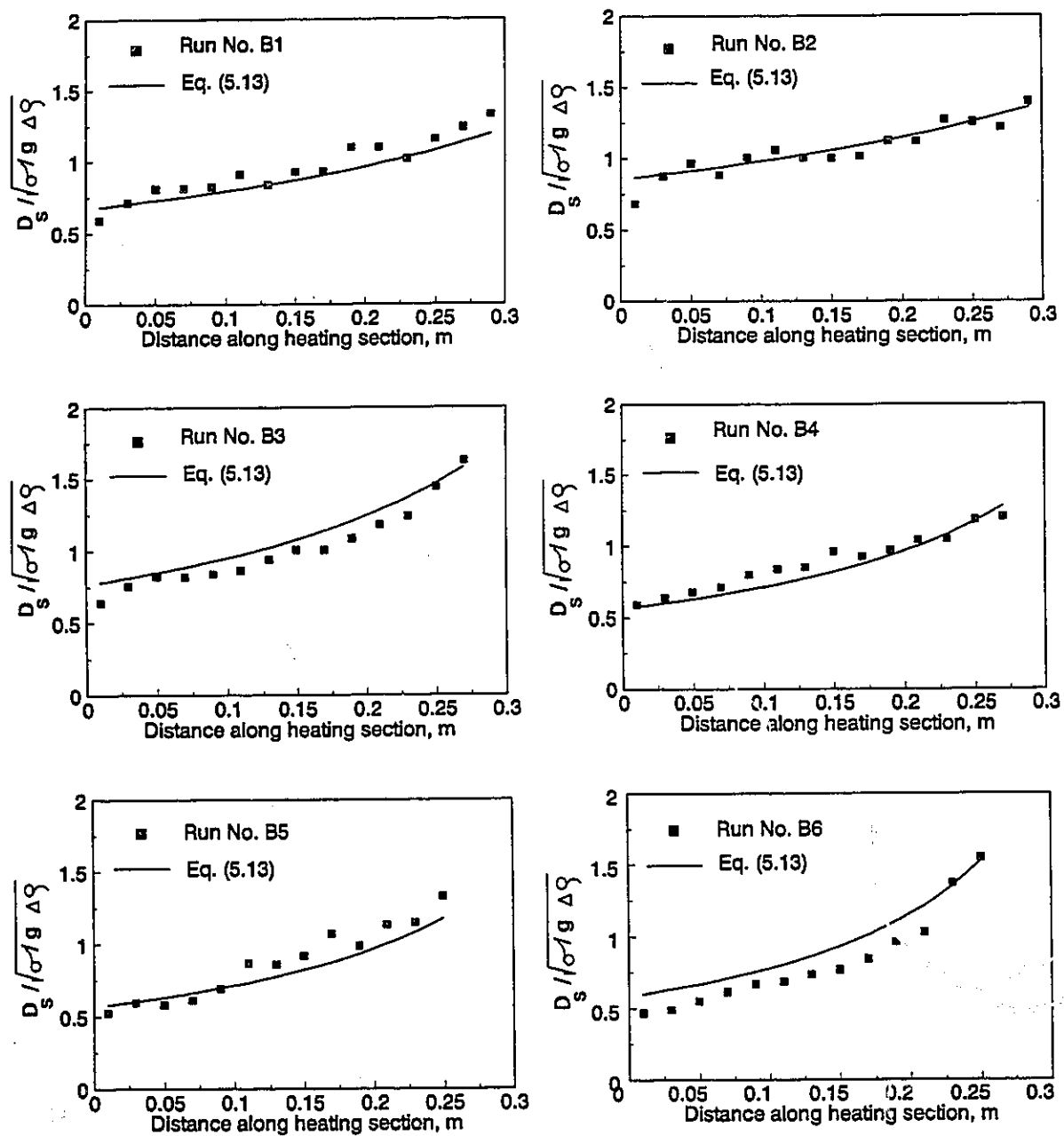
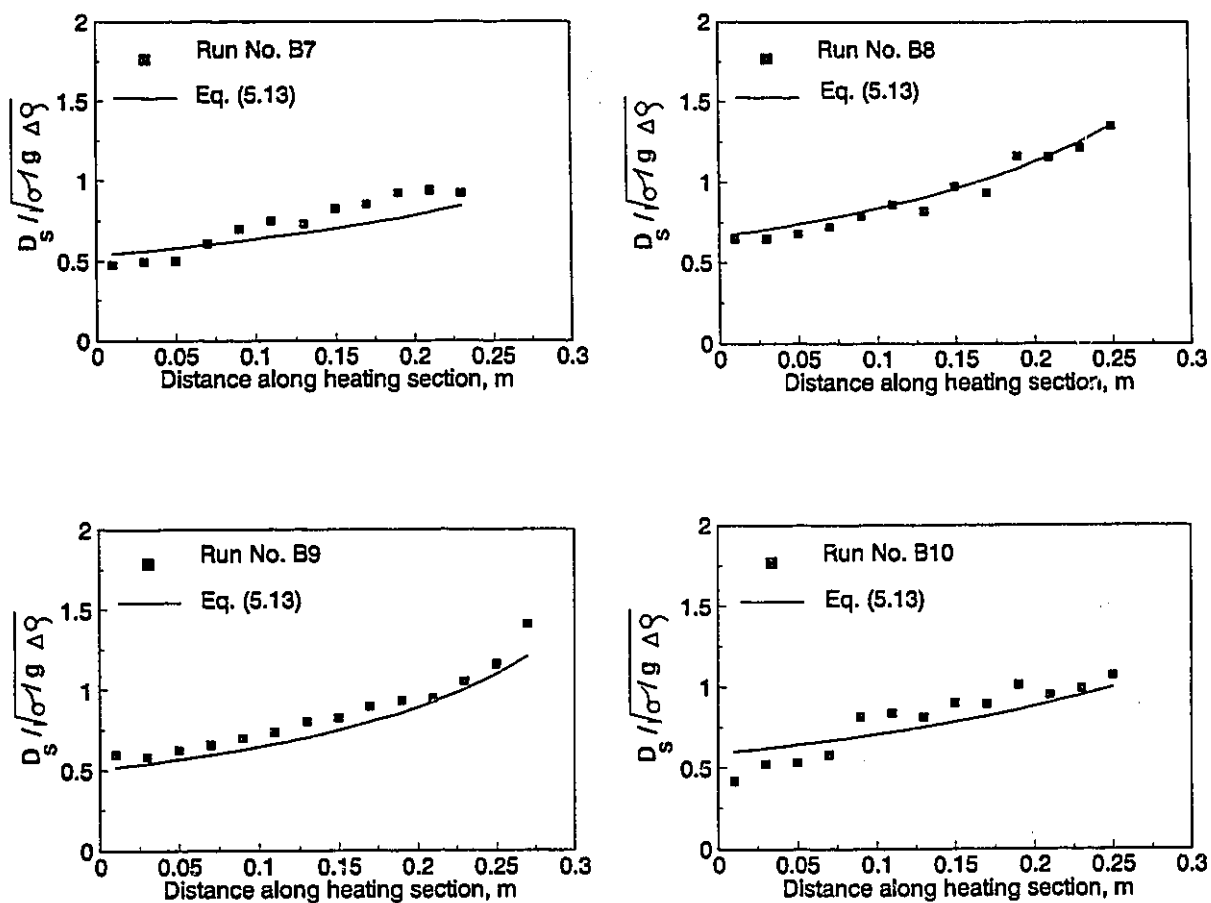


Figure 5.26a Comparison between proposed correlation and measured mean bubble diameter



**Figure 5.26b Comparison between proposed correlation and
measured mean bubble diameter**

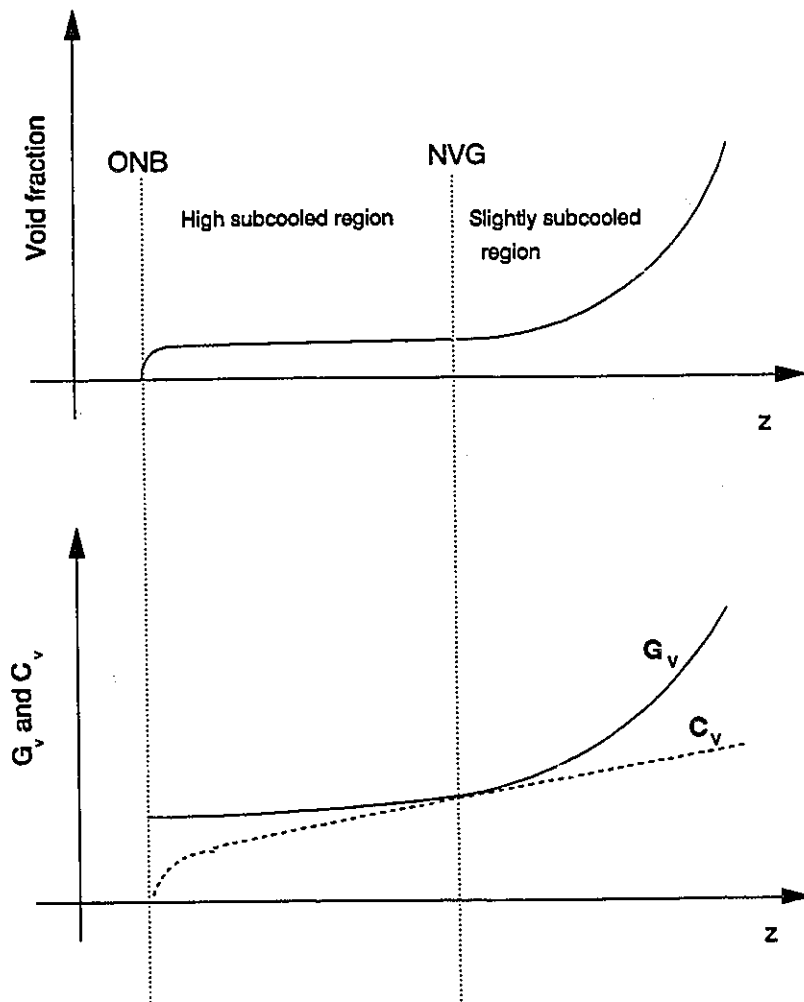
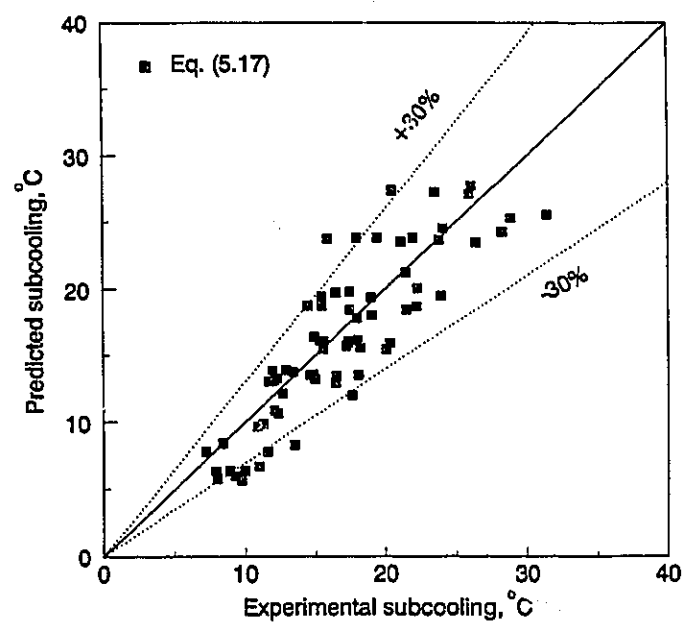


Figure 5.27 Speculated vapour generation and condensation functions



**Figure 5.28 Comparison between the proposed NVG model
and experimental data**

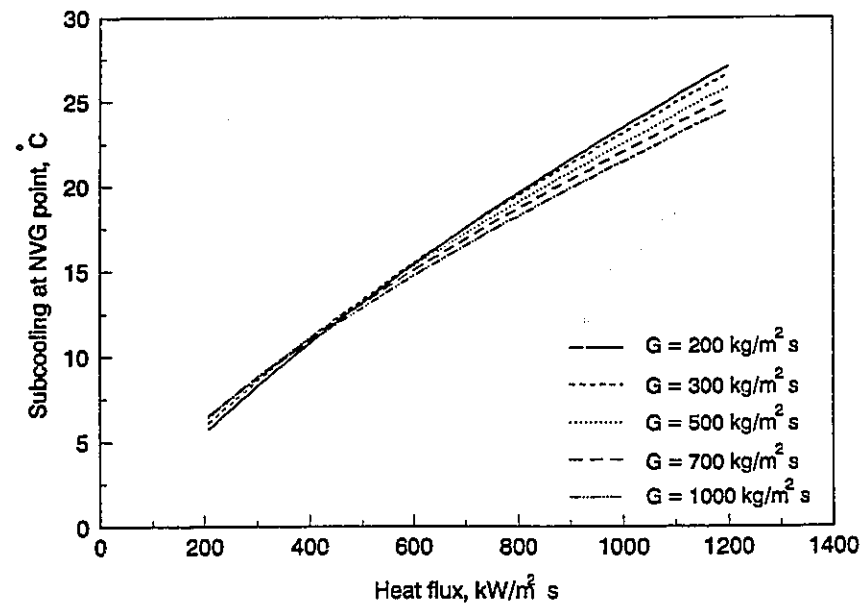


Figure 5.29a Effect of heat flux on the subcooling at the NVG point

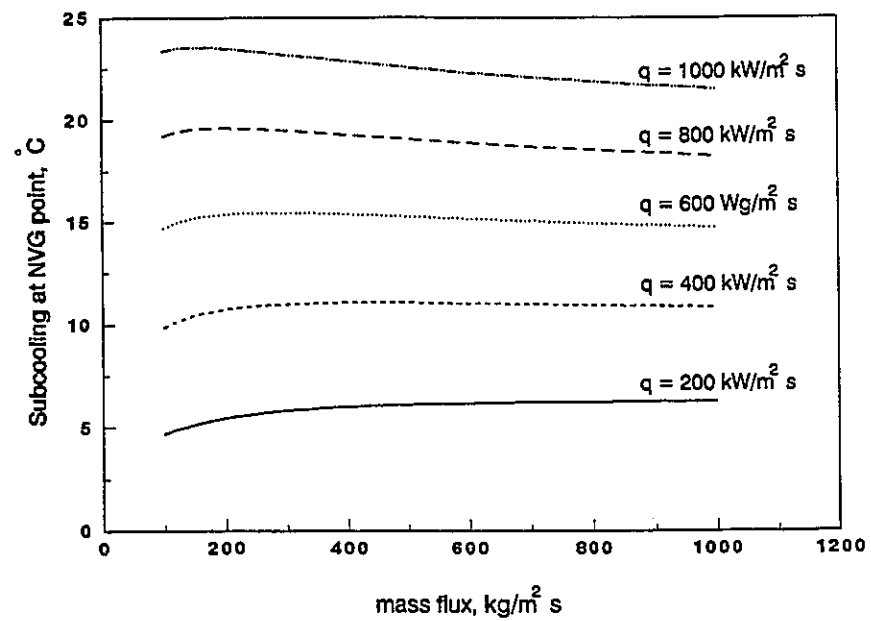


Figure 5.29b Effect of mass flux on the subcooling at the NVG point

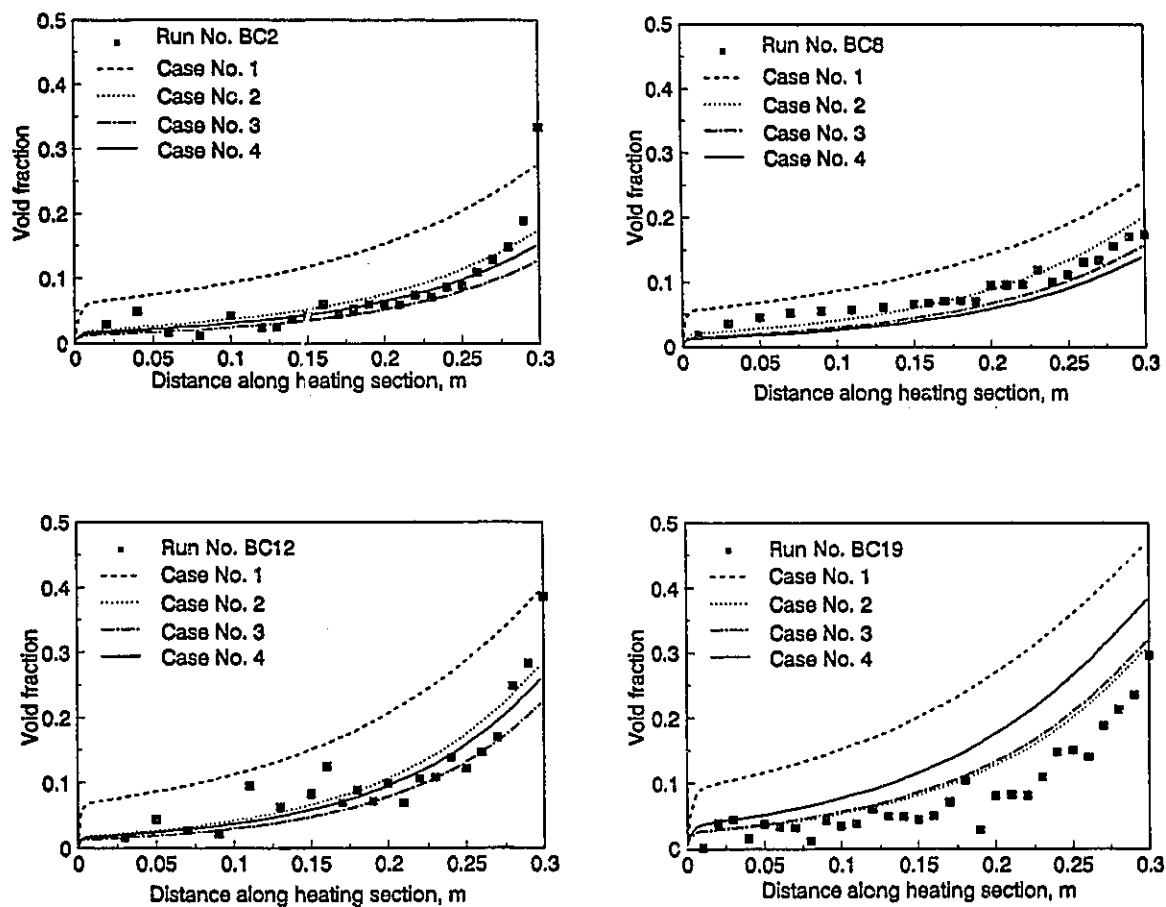


Figure 5.30 Effect of imposing the NVG point on the predicted void fraction profile

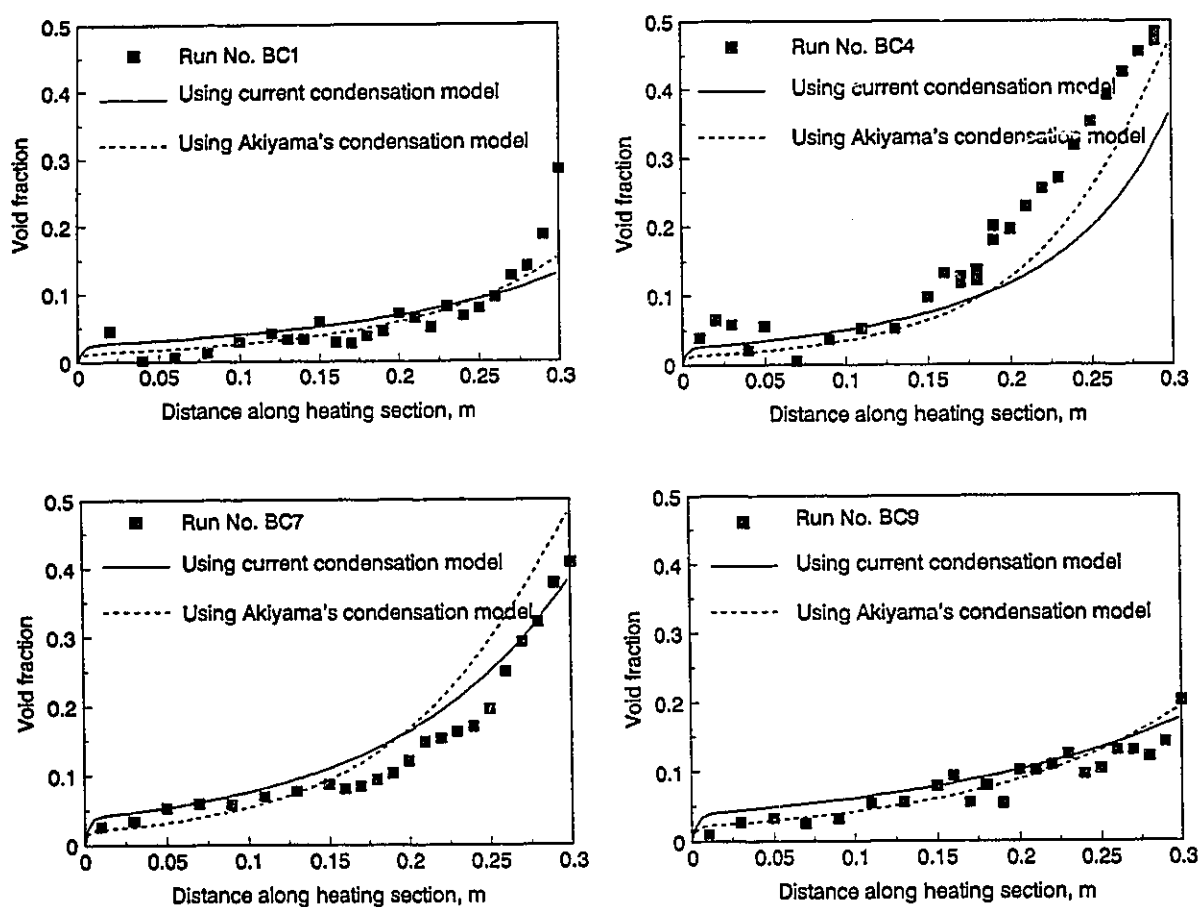


Figure 5.3 1a Effects of various bubble condensation models on the predicted void fraction profile

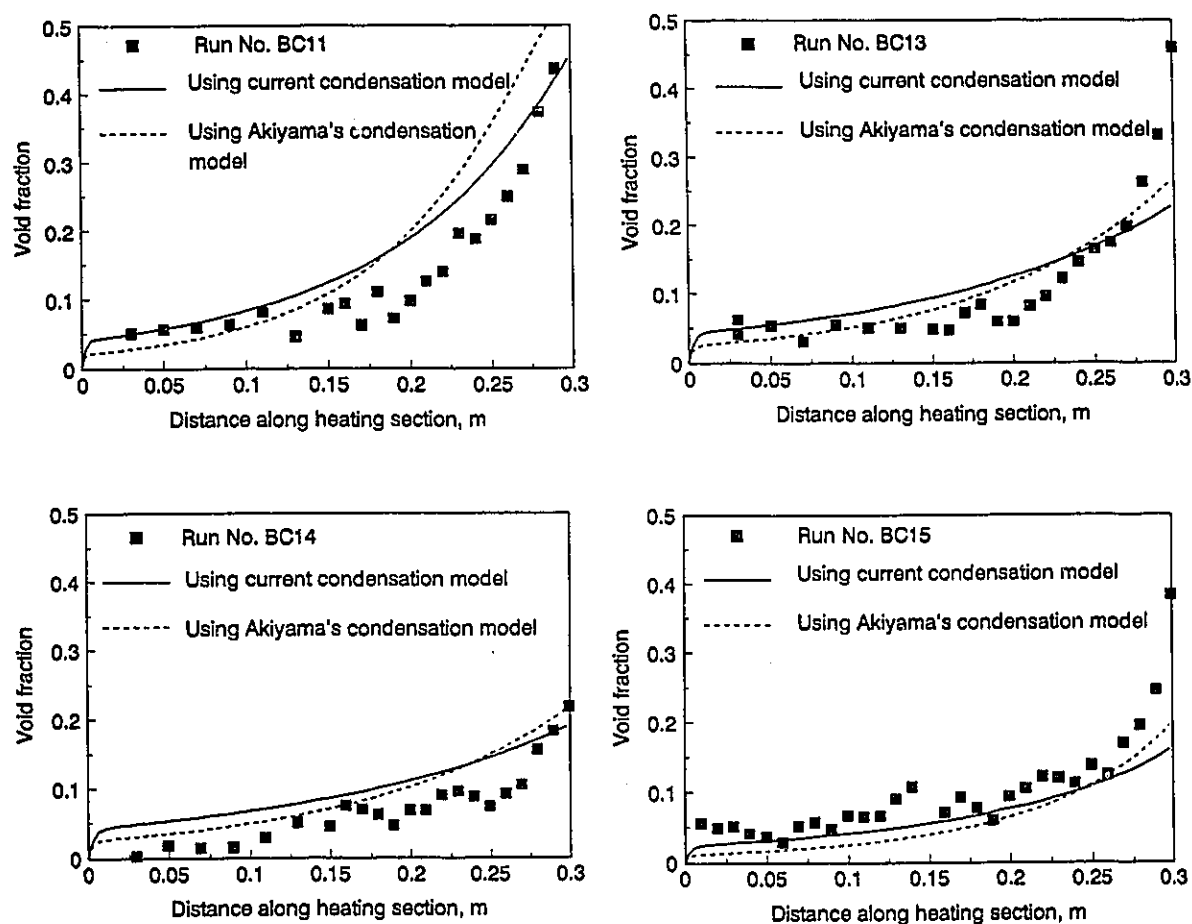


Figure 5.3 1b Effects of various bubble condensation models on the predicted void fraction profile

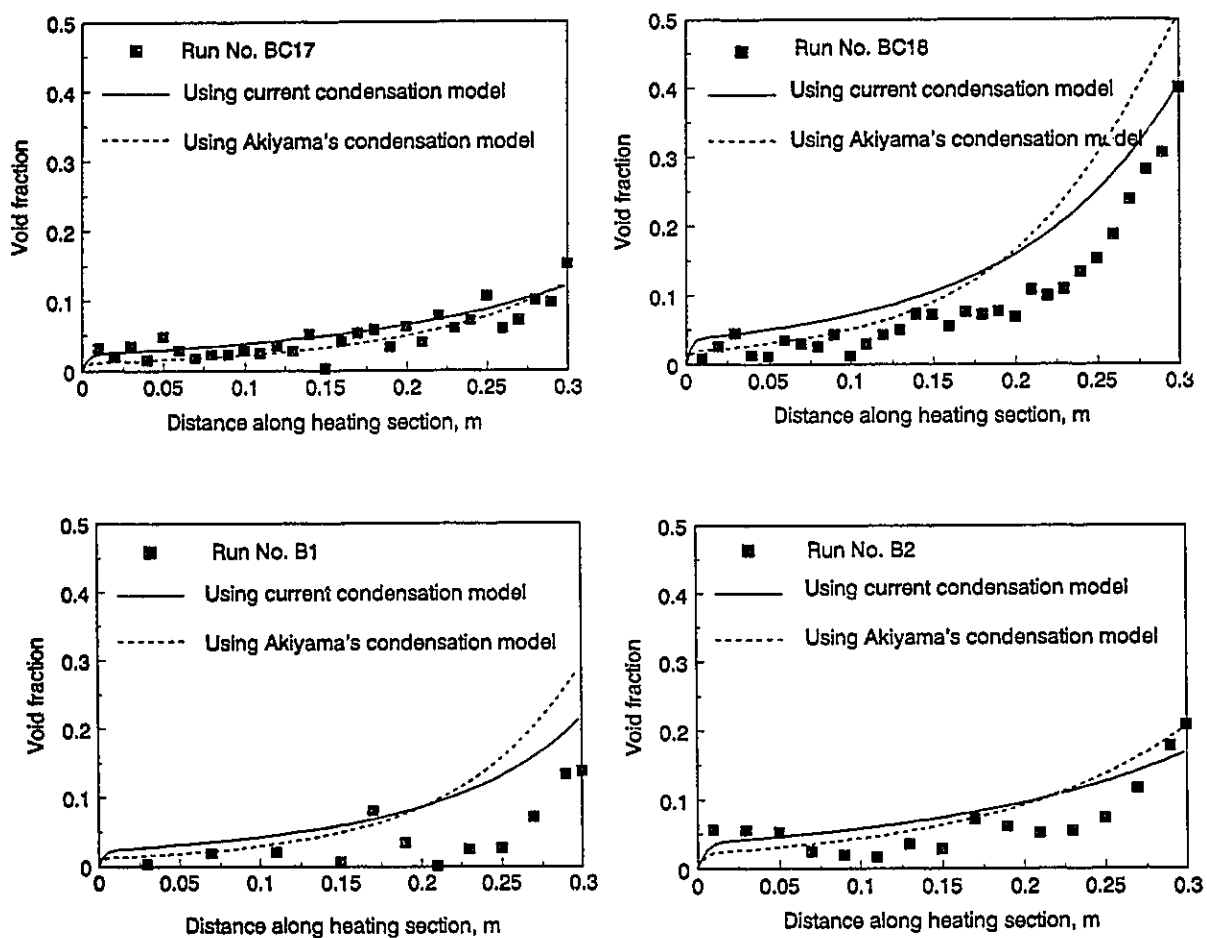


Figure 5.3 1c Effects of various bubble condensation models on the predicted void fraction profile

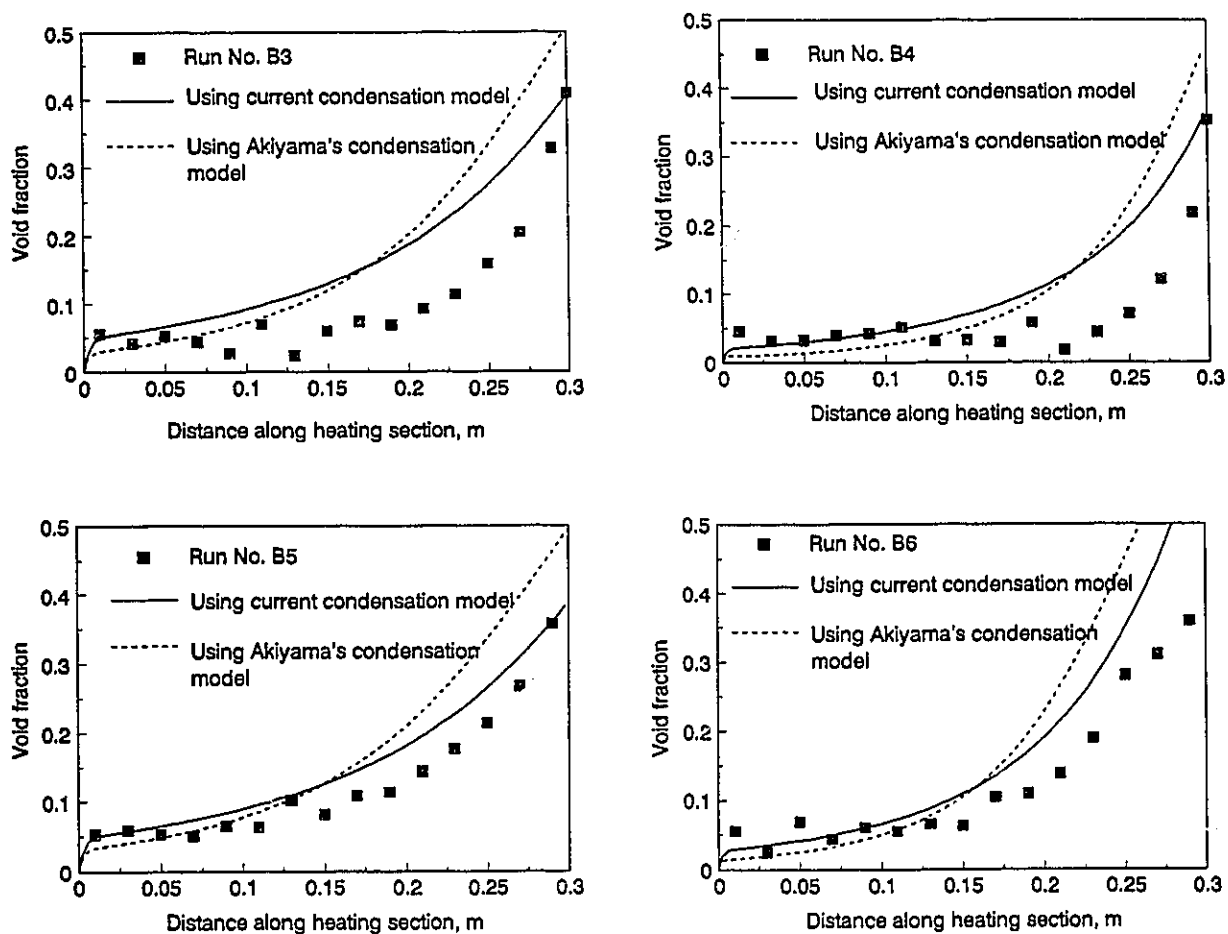


Figure 5.31d Effects of various bubble condensation models on the predicted void fraction profile

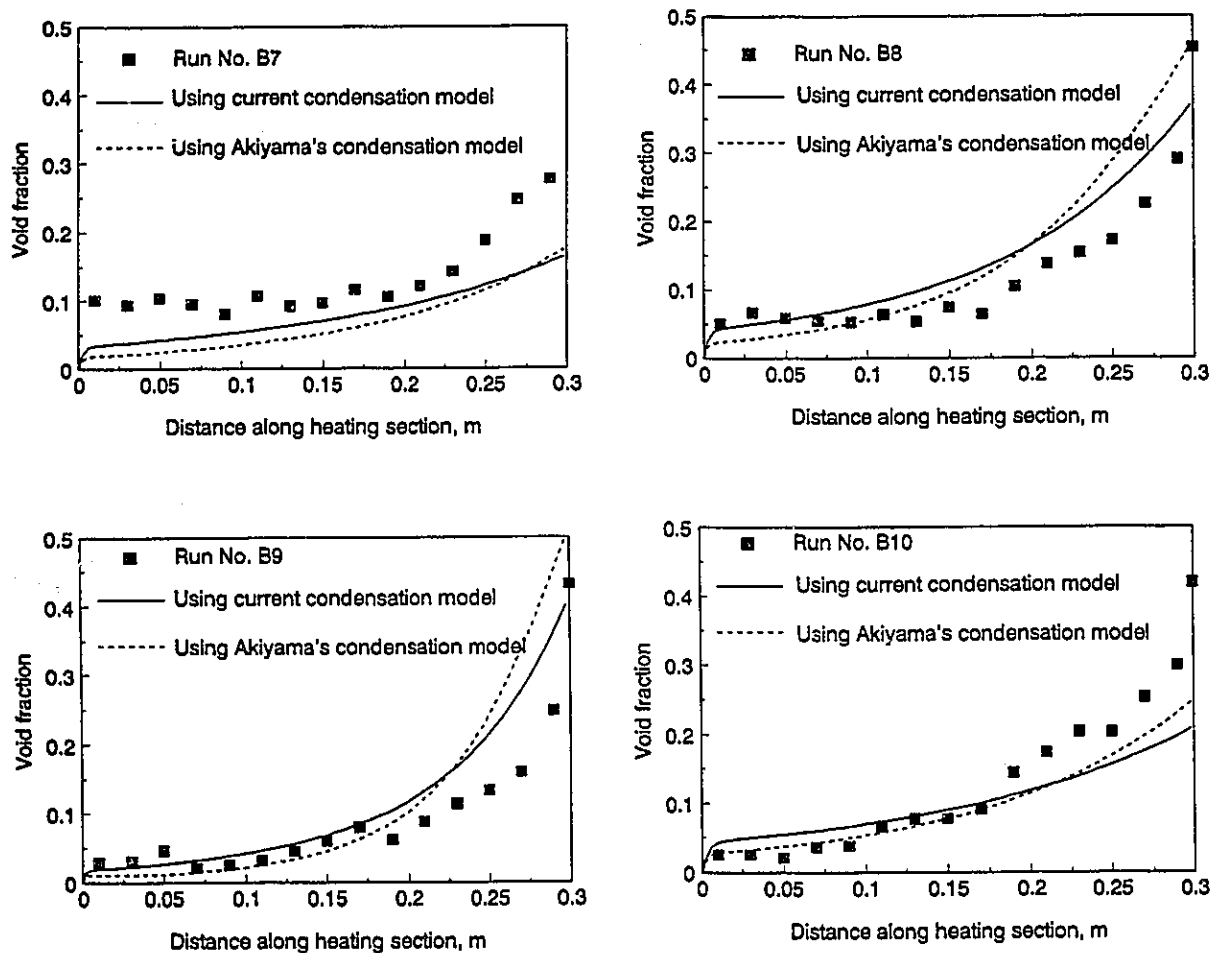


Figure 5.31e Effects of various bubble condensation models on the predicted void fraction profile

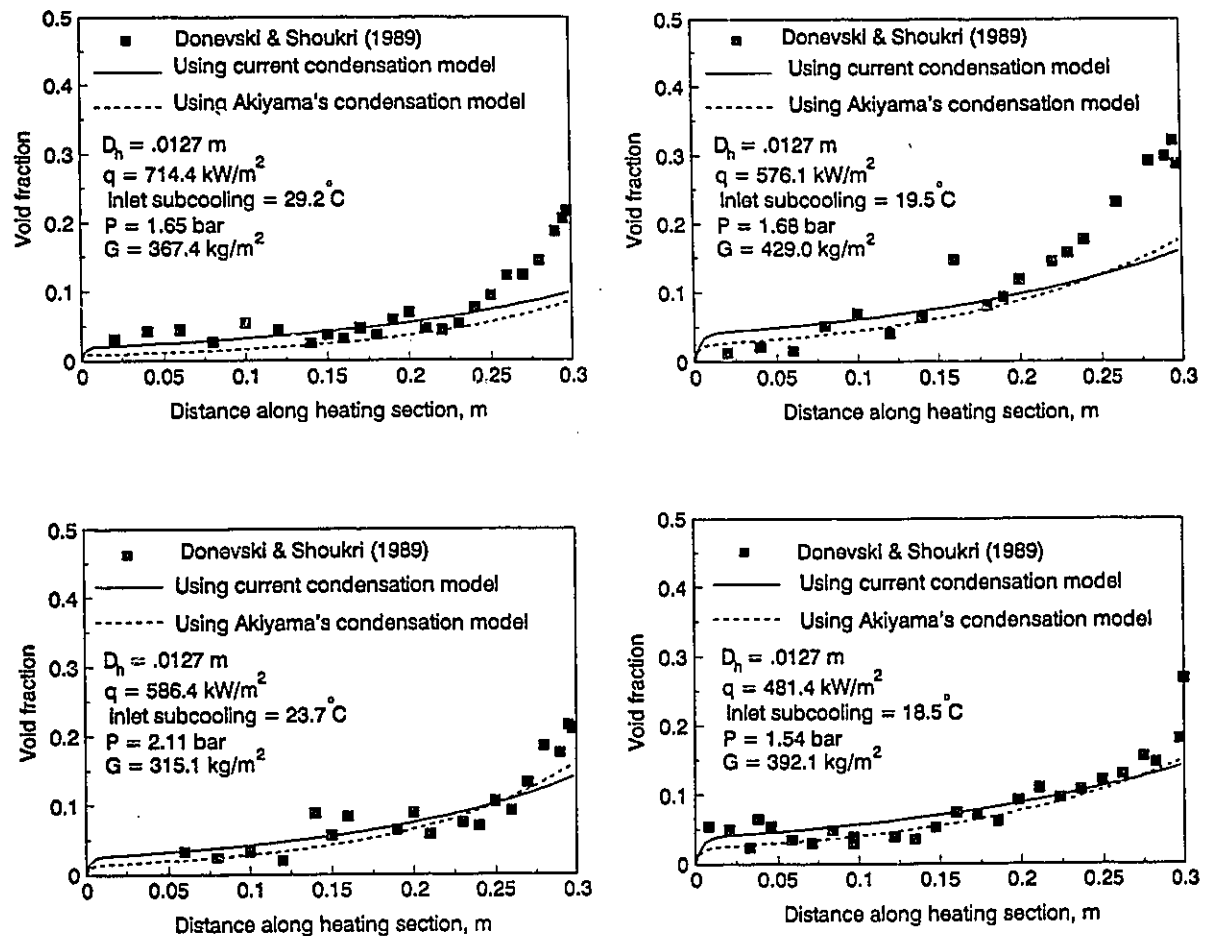


Figure 5.32 Effects of various bubble condensation models on the predicted void fraction profile

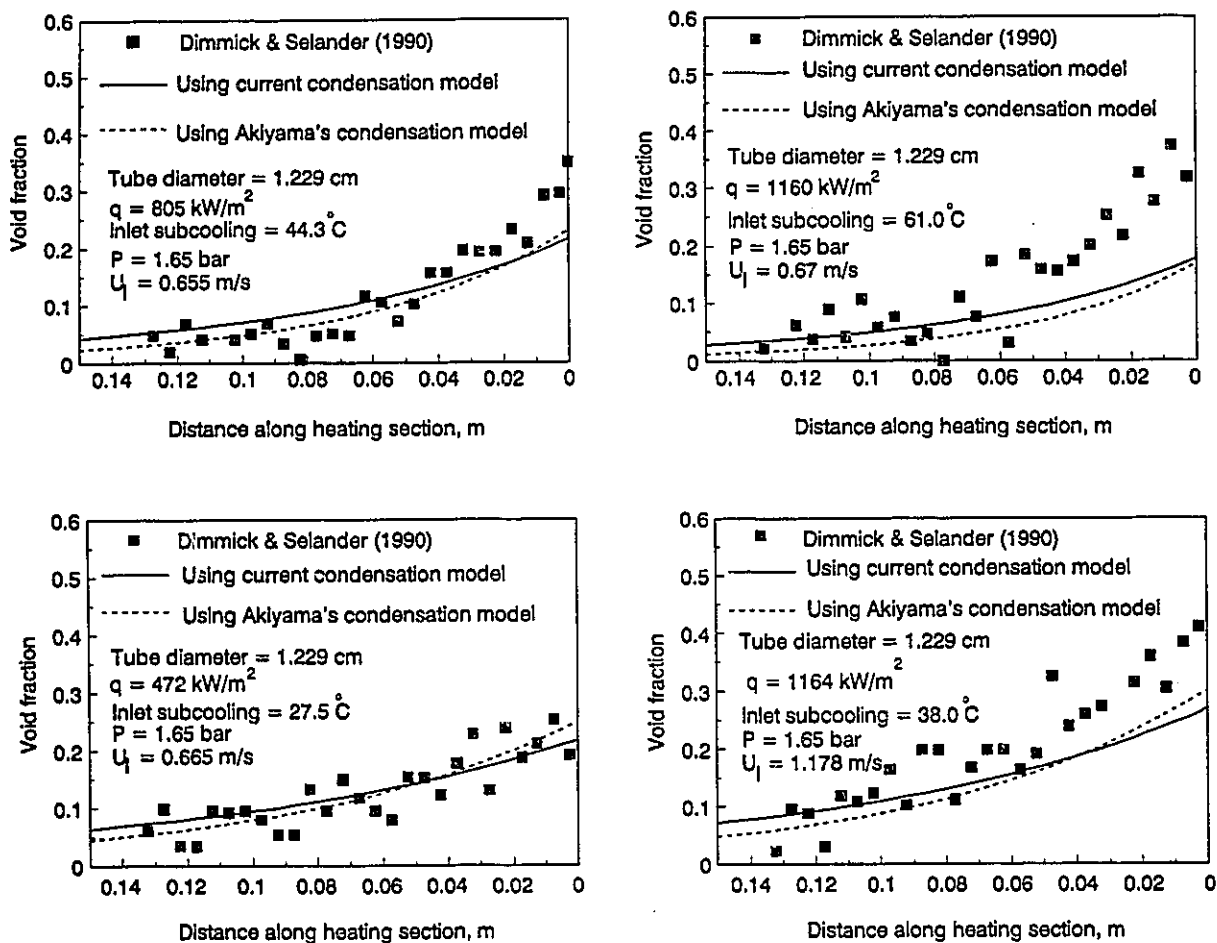


Figure 5.33 Effects of various bubble condensation models on the predicted void fraction profile

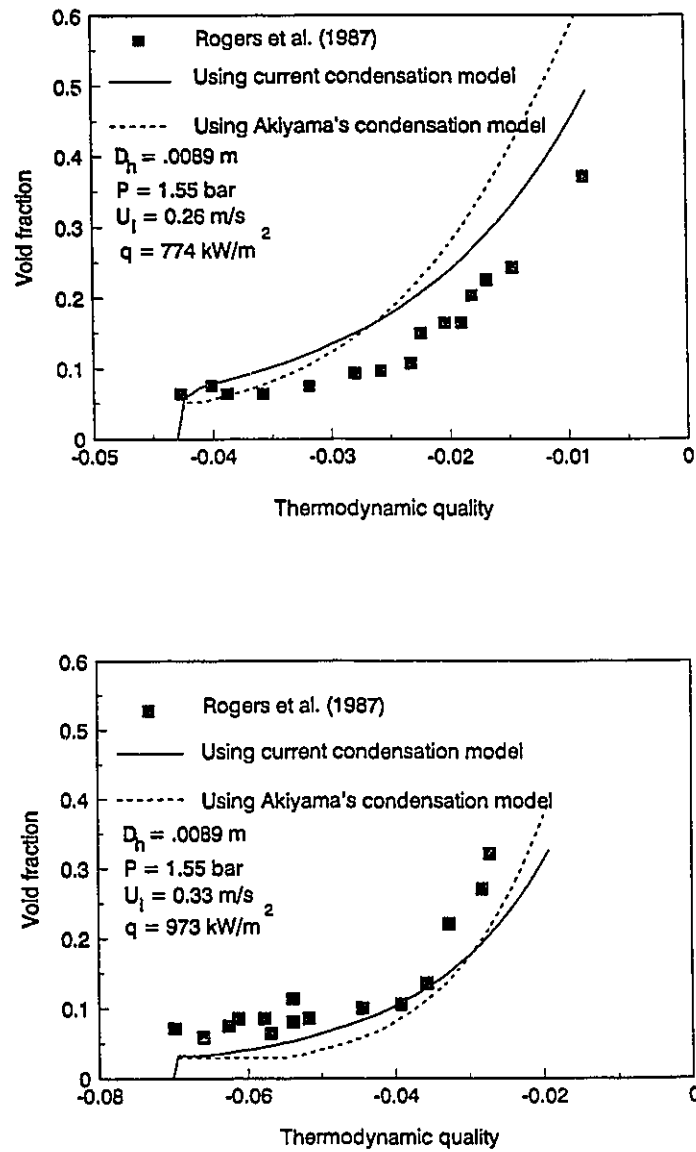


Figure 5.34 Effects of various bubble condensation models on the predicted void fraction profile

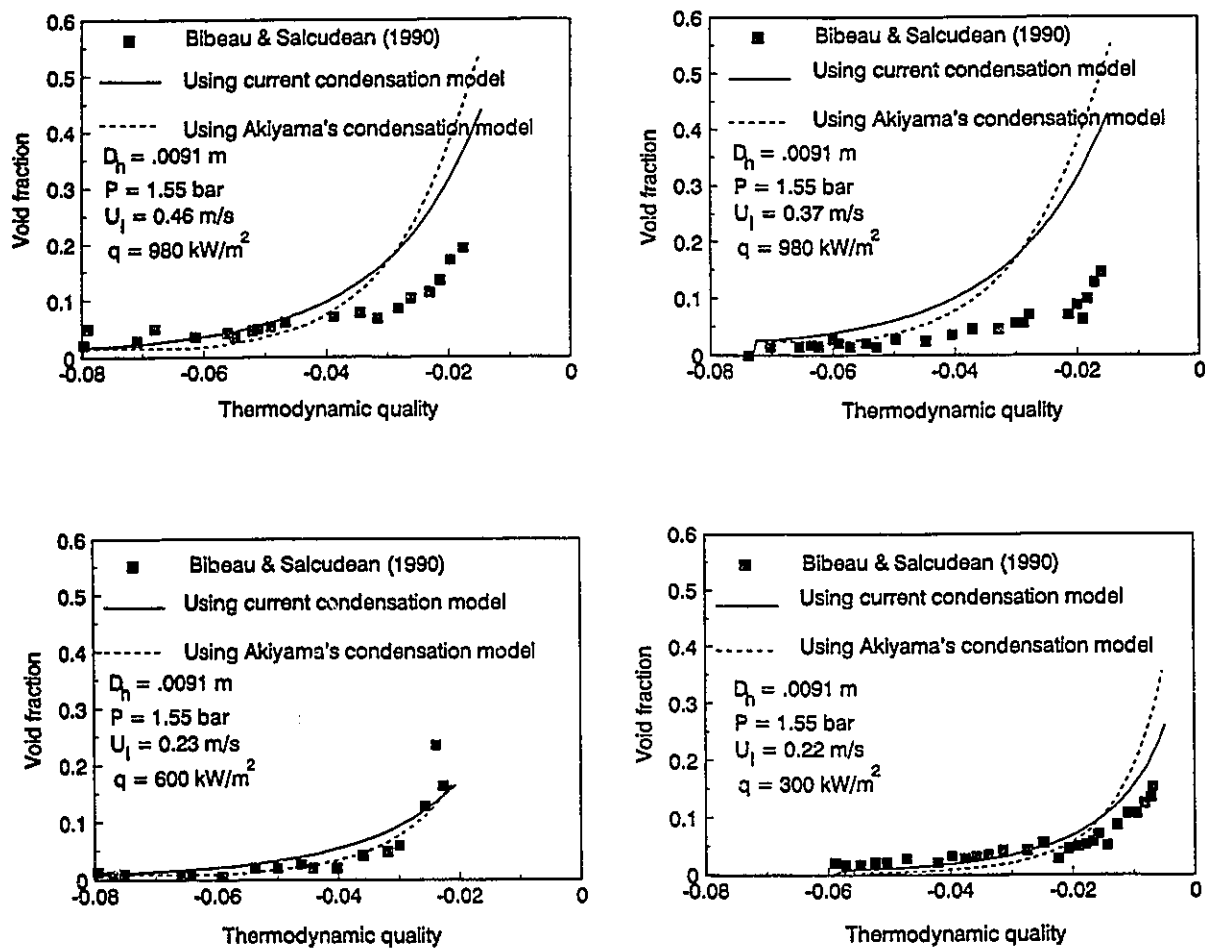


Figure 5.35 Effects of various bubble condensation models on the predicted void fraction profile

CHAPTER 6

CONCLUSIONS AND RECOMMENDATIONS

6.1 Summary and Conclusions

For subcooled water-steam condensing bubbly flows in vertical annular channels at low pressure and low mass flux, experimental data on the axial distribution of the area-averaged void fraction, interfacial area concentration, bubble relative velocity and interfacial heat transfer coefficient were obtained for various levels of mass flux, inlet void fraction and inlet subcooling. A two-fluid model for axial void fraction profile was introduced. The contributions to knowledge of the current investigation of this flow regime are:

- 1- Experimental data on interfacial area concentration in one-component subcooled water-steam flow as a function of void fraction, local subcooling and mass flux were obtained. The data were obtained by measuring bubble surface area and volume distributions using high speed photographic and digital image processing techniques and void fraction distributions were obtained using a

gamma densitometer. The present data were compared with available correlations, developed on the basis of adiabatic gas-liquid flows. It was shown that available correlations were unable to predict the data accurately. Based on the present data, a new correlation was proposed. The proposed correlation showed that the interfacial area concentration is a strong function of void fraction, a weak function of mass flux and is independent of local subcooling.

2- Experimental data on bubble relative velocity were obtained using high speed photographic and digital image processing techniques. The measured bubble relative velocity falls in the range of 0.2-0.4 m/s. The bubble relative velocity data were compared with the prediction of available models. The model of Zuber-Findlay (1965) for drift flux is recommended to estimate bubble relative velocity.

3- Experimental data on bubble condensation in low pressure cocurrent upward subcooled liquid-vapour bubbly flow were obtained. Digital image processing techniques were used to obtain the rate of bubble condensation in terms of bubble size, local subcooling, void fraction and bubble rise velocity. The data was used to develop a new empirical correlation for the interfacial condensation Nusselt number as a function of bubble Reynolds number, void fraction and Jakob number. The proposed correlation for interfacial heat transfer coefficient is also compared with those available in the literature, which were mostly developed on the basis of single bubble condensation.

4- The applicability of the proposed correlations of interfacial area

concentration, interfacial heat transfer coefficient and bubble rise velocity as closure relationships in two-phase flow numerical codes was examined by incorporating them in a two-fluid model to predict axial void fraction profiles in condensing bubbly flows. The comparison between the predictions of the model and the present data as well as data from the literature showed good agreement. Effects of mass flux, inlet subcooling and inlet void fraction on axial void fraction were examined.

For subcooled flow boiling in vertical annular channels, measurements, including local void fraction, subcooling, heating surface temperature and mean bubble diameter profiles, bubble behaviour, and physical mechanisms of the NVG phenomenon were carried out. A two-fluid model was introduced and different closure relationships were examined. The contributions to knowledge of the current study in this flow regime are:

- 1- Experimental data on void fraction, wall superheat and liquid subcooling profiles along the subcooled flow boiling region were generated at various levels of mass flux, heat flux and inlet subcooling.
- 2- A high speed video system was used to visualize the subcooled flow boiling phenomenon before, near, and after the NVG point. The high speed photographic results confirmed the fact that bubble parallel, or normal detachment, is not the reason for the NVG phenomenon.
- 3- Experimental data on mean bubble diameter distributions along the subcooled

boiling region were obtained using high speed photographic and digital image processing techniques. A correlation for mean bubble diameter, as function of the mass flux, heat flux and local subcooling, was proposed. Effects of mass and heat flux and local subcooling on mean bubble size were examined.

4- The physical mechanisms of the NVG phenomenon were investigated using the high speed photographic results. A net vapour generation model was proposed. The proposed model was based on the balance between the vapour generation and condensation rates at this point. Predictions of the model were compared with the current experimental data as well as available data from the literature. The agreement between the proposed model and the experimental data was within $\pm 30\%$.

5- A two-fluid model for void fraction profile in subcooled flow boiling along vertical channels was introduced and various closure relationships were investigated. A modified heat flux division mechanism was proposed by modifying Bowring's pumping factor (1962). The proposed two-fluid model was reasonably capable of predicting the void fraction profiles along the both regions of the subcooled flow boiling. The location of the NVG point is not required as an input in the model.

6.2 Recommendations

During the course of this study, the lack of information on specific topics has made it difficult to understand or model them. Therefore, the following subjects are recommended for further investigation:

- 1- Theoretical and experimental investigation of bubble growth-collapse cycle in subcooled flow boiling: In the theoretical investigation, the forces acting on the bubble should be simultaneously related to the growth-collapse process. From this investigation, valuable information on bubble average and maximum diameters, departure diameter, and bubble growth and collapse time can be obtained.
- 2- Effects of various parameters; subcooling, heat flux and mass flux, on active nucleation site density and bubble frequency in subcooled flow boiling: This information is useful in understanding heat flux division mechanisms at the heating surface and in simulating the void fraction profiles.
- 3- Bubble velocity before and after the NVG point: During bubble growth-collapse process, the bubble has two velocity components; in the flow direction and in the lateral direction. The information on this topic is important in modelling bubble growth-collapse cycle and in the two-fluid formulation of boiling flow.
- 4- Radial distributions of velocity, temperature and void fraction: This

information is required to estimate distribution parameters needed in area-averaged conservation equations.

5- Bubble condensation coefficient in subcooled flow boiling: The difficulty with this point is the simultaneous evaporation and condensation around the bubble. By measuring bubble growth-collapse history from nucleation until complete condensation, the condensation period of the bubble life can be used to estimate the bubble condensation coefficient.

6- Further investigation of wall heat flux division mechanisms: This is a challenging problem and solving the subcooled flow boiling relies on modelling this problem.

7- Examining various methods for measuring void fraction at the heating surface. The void fraction at the heating surface is also required in modelling the wall heat flux division.

REFERENCES

- Abdelmessih, A. H., Hooper, F. C. and Nangia, S. 1972 "Flow Effects on Bubble Growth and Collapse in Surface Boiling", *Int J. Heat and Mass Transfer*, Vol. 15, pp. 115-125.
- Ahmad, S. Y. 1970 "Axial Distribution of Bulk Temperature and Void Fraction in a Heated Channel with Inlet Subcooling", *J. Heat Transfer*, Vol. 92, pp. 595-609.
- Akita, K. and Yoshida, F. 1974 "Bubble Size, Interfacial Area, and Liquid-Phase Mass Transfer Coefficient in Bubble Columns", *Ind. Eng. Chem., Process Des. Develop.*, Vol. 13, pp. 85-91.
- Akiyama, M. 1973 "Bubble Collapse in Subcooled Boiling", *Bulletin of JSME*, Vol. 16, pp. 570-575.
- Akiyama, M. and Tachibana, F. 1974 "Motion of Vapour Bubbles in Subcooled Heated Channel", *Bulletin of the JSME*, Vol. 104, pp. 241-247.
- Banerjee, S., Scott, D.S. and Rhodes, E. 1970 "Studies on Concurrent Gas-Liquid Flow in Helically Coiled Tubes", *Can. J. Chem. Eng.*, Vol. 48, pp. 542-551.
- Beer, H., Burow, P. and Best, R. 1977 "Bubble Growth, Bubble Dynamics, and Heat Transfer in Nucleate Boiling, Viewed with a Laser Interferometer", in: *Heat Transfer in Boiling*, ed. E. Hahne and U. Grigull, Hemisphere Publishing corporation, Ch. 2, pp. 21-52.
- Bergles, A. E. and Rohsenow, W. M. 1964 "The Determination of Forced-Convection Surface-Boiling Heat Transfer", *J. Heat Transfer*, pp. 365-371.

Bibeau, E. L. 1993 "Void Growth in Subcooled Flow Boiling for Circular and Finned Geometries for Low Values of Pressure and Velocity", Ph. D. Thesis, The University of British Columbia.

Bibeau, E. L. and Salcudean, M. 1990 "The Effect of Flow Direction on Void Growth at Low Velocities and Low Pressure", *Int. Comm. Heat Mass Transfer*, Vol. 17, pp. 19-25.

Bjorge, R. W., Hall, G. R. and Rohsenow, W. 1982 "Correlation of Forced Convection Boiling Heat Transfer Data", *Int. J. Heat Mass Transfer*, Vol. 25, pp. 753-757.

Bowring, R. W. 1962 "Physical Model Based on Bubble Detachment and Calculation of Steam Voidage in the Subcooled Region of a Heated Channel", HPR-10, Institute for Atomenergi, Halden.

Brucker, G. G. and Sparrow, E. M. 1977 "Direct Contact Condensation of Steam Bubbles in Water at High Pressure", *Int. J. Heat and Mass Transfer*, Vol. 20, pp. 371-381.

Bucher, B. and Nordmann, D. 1976 "Investigations of Subcooled Boiling Problems", in *Two-Phase Transport and Reactor Safety*, ed. Veziroglu, T. N. and Kakaç, S., Vol. I, Hemisphere Pub. Corp., Washington, pp. 31-49.

Burden, R. L., Faires, J. D. and Reynolds, A. C. 1981 "Numerical Analysis", PWS Publishers, Boston, Ch. 5, pp. 180-258.

Chan, A.M.C. and Banerjee, S. 1981 "Design Aspects of Gamma Densitometers for Void Fraction Measurements in Small Scale Two-Phase Flow", *Nuclear Instrumentation and Methods*, Vol. 190, pp.135-148.

Chatoorgoon, V. 1992 "A generation-condensation void fraction transport model for low pressure", in: *Two-Phase Flow and Energy Exchange System*, ed. M.S. Sohel and T.J. Rabes, ASME, HTD Vol. 220.

Chatoorgoon, V., Dimmick, G. R., and Carver, M. B. 1993 "Modelling of Low Pressure Subcooled Boiling Instability Experiments", in: *Instability in Two-Phase Flow Systems*, ed. J. H. Kim, HTD-Vol. 260, pp. 41-51.

Chatoorgoon, V., Dimmick, G. R., Carver, M. B., Selander, W. N. and Shoukri, M. 1992 "Application of generation and condensation models to predict subcooled boiling void at low pressure", *Nuclear Technology*, 98, pp. 366-378.

Chen, Y. M. and Mayinger, F. 1992 "Measurement of Heat Transfer at Phase

Interface of Condensing Bubble", *Int. J. Multiphase Flow*, Vol. 18, pp. 877-890.

Chisholm, D. 1973 "Pressure Gradients due to Friction During the Flow of Evaporating Two-Phase Mixtures in Smooth Tubes and Channels", *Int. J. Heat Mass Transfer*, Vol. 16, pp. 347-358.

Cole, R. 1979 "Boiling nucleation", in: *Boiling Phenomena*, ed. S. Van Stralen and R. Cole, Hemisphere Publishing Corporation, Vol. 1, Ch. 5 & 6.

Collier, J. G. 1972 "Convective Boiling and Condensation", Chapter 10, 2nd ed., McGraw-Hill, New York.

Cooper, M. G., Mori, K. and Stone, C. R. 1983 "Behaviour of Vapour Bubbles Growing at a Wall with Forced Flow", *Int. J. Heat and Mass Transfer*, Vol. 26, pp. 1489-1507.

Cooper, M. G. and Lloyd, A. J. P. 1969 "The Microlayer in Nucleate Pool Boiling", *Int. J. Heat and Mass Transfer*, Vol. 12, pp. 895-913.

Davis, E. J. and Anderson, G. H. 1966 "The Inception of Nucleate Boiling in Forced Convection Flow", *A.I.Ch.E. Journal*, Vol. 12, pp. 774-780.

DeJesus, J.M. and Kawaji, M. 1990 "Investigation of Interfacial Area and Void Fraction in Upward, Concurrent Gas-Liquid Flow", *Can. J. Chem. Eng.* Vol. 68, pp. 904-912.

Dimić, M. 1977 "Collapse of One-Component Vapour Bubble with Translatory Motion", *Int J. Heat and Mass Transfer*, Vol. 20, pp. 1325-1332.

Dimmick, G. R. and Selander, W. N. 1990 "A Dynamic Model for Predicting Subcooled Void: Experimental Results and Model Development" EURO THERM Seminar # 16, Pisa, Italy.

Dix, G. E. 1970 "Vapour Void Fraction for Forced Convection with Subcooled Boiling at Low Flow Rates", General Electric Report No. NEDO-10491.

Donevski, B. and Shoukri, M. 1989 "Experimental Study of Subcooled Flow Boiling and Condensation in Annular Channel", McMaster University, Dept. Mech. Eng., Thermofluids Report No. ME/89/TF/R1.

Evangelisti, R. and Lupoli, P. 1969 "The Void Fraction in an Annular Channel at Atmospheric Pressure", *Int. J. Heat Mass Transfer*, Vol. 12, pp. 699-711.

Edelman, Z. and Elias, E. 1981 "Void Fraction Distribution in Low Flow Rate Subcooled Boiling", Heat Transfer Division, ASME, Winter Annual Meeting.

Firstenberg, A. and Neal, L. G. 1966 "Kinetic Studies of Heterogenous Water Reactors", STL 372 38.

Florschuetz, I. W. and Chao, B. T. 1965 "On the Mechanics of Bubble Collapse", J. Heat Transfer, pp. 209-220.

Forster, K. and Greif, R. 1959 "Heat Transfer to a Boiling Liquid: Mechanism and Correlations", J. Heat Transfer, Vol. 81, pp. 43-53.

Fukuma, M., Muroyama, K. and Yasunishi, A. 1987 "Specific Gas-Liquid Interfacial Mass Transfer Coefficient in a Slurry Bubble Column", J. Chem. Eng. Japan, Vol. 20, pp. 321-324.

Griffith, P., Clark, J. A. and Rohsenow, W. M. 1958 "Void Volumes in Subcooled Boiling", ASME Paper 58-HT-19, U.S. National Heat Transfer Conf., Chicago.

Gungor, K. and Winterton, R. 1986 "A General Correlation for Flow Boiling in Tubes and Annuli", Int. J. Heat Mass Transfer, Vol. 29, No. 3, pp. 351-358.

Gunther, F. C. 1951 "Photographic Study of Surface-Boiling Heat Transfer to Water with Forced Convection", Transaction of ASME, pp. 115-123.

Hancox, W. T. and Nicoll, W. B. 1971 "A General Technique for the Prediction of Void Distributions in Non-Steady Two-Phase Forced Convection", Int. J. Heat Mass Transfer, Vol. 14, pp. 1377-1394.

Hewitt, H. C. and Parker, J. D. 1968 "Bubble Growth and Collapse in Liquid Nitrogen", J. Heat Transfer, pp. 22-26.

Hori, Y. and Toda, S. 1991 "Condensation Rate of Vapour Bubble in Subcooled Flow in a Vertical Tube", Proceeding of The International Conference on Multiphase Flow '91-Tsukuba, Japan, pp. 161-164.

Hudgson, A., 1968 "Forced Convection Subcooled Boiling Heat Transfer with Water in an Electrically Heated Tube at 100-550 lb/in²", Trans. Inst. Chem. Engrs, Vol. 46, pp. T25-T31.

Hsu, Y. Y. 1962 "On the Size of Range of Active Nucleation Cavities on a Heating Surface", J. heat Transfer, Vol. 84, pp 207.

- Isenberg, J. and Sideman, S. 1970 "Direct Contact Heat Transfer with Change of Phase: Bubble Condensation in Immiscible Liquid", *Int. J. Heat and Mass Transfer*, Vol. 13, pp. 997-1011.
- Ishii, M. and Mishima, K. 1984 "Two-Fluid Model and Hydrodynamic Constitutive Relations", *Nuclear Engineering and Design*, Vol. 82, pp. 107-126.
- Ishii, M. and Mishima, K. 1980 "Study of Two-Fluid Model and Interfacial Area", NUREG/CR-1873, ANL-80-111, U.S. Nuclear Regulatory Commission.
- Jain, P. K., Nourmohammadi, K., Roy, R. P. 1980 "A Study of Forced Convective Subcooled Boiling in Heated Annular Channels", *Nuclear Engineering and Design*, Vol. 60, pp. 401-411.
- Jepsen, J.C. 1970 "Mass Transfer in Two-Phase Flow in Horizontal Pipelines", *AIChE J.* Vol. 16, pp. 705-711.
- Kasturi, G. and Stepanek, J.B. 1974 "Two-Phase Flow -III. Interfacial Area in Concurrent Gas-Liquid Flow", *Chem. Eng. Sci.*, Vol. 29, pp. 713-719.
- Katto, Y. 1986 "Forced-Convection in Uniformly Heated Channels", *Handbook of Heat and Mass Transfer*, Ed. N. P. Cheremisinoff, Gulf Pub. Co. Houston, pp. 303-325.
- Kelly, J. and Kazimi, M. S. 1982 "Interfacial Exchange Relations for Two-Fluid Vapour-Liquid Flow: A Simplified Regime-Map Approach", *Nuclear Science and Engineering*, Vol. 81, pp. 305-318.
- Kocamustafaogullari, G., Huang, W.D., and He, T. 1992 "Measurement and Modelling of Interfacial Area Concentration", *ANS Proceedings, National Heat Transfer Conference*, San Diego, California, Vol. 6, pp. 53-62.
- Koffman, L. D. and Plesset, M. S. 1983 "Experimental Observations of the Microlayer in Vapour Bubble Growth on a heated Solid", *J. Heat Transfer*, Vol. 105, pp. 625-632.
- Koumoutsos, N., Moissis, R. and Spyridonos, A. 1968 "A Study of Bubble Departure in Forced-Convection Boiling", *J. Heat Transfer*, pp. 223-230.
- Kroeger, P. G. and Zuber, N. 1968 "An Analysis of the Effects of Various Parameters on the Average Void Fraction in subcooled Boiling", *Int. J. Heat Mass Transfer*, Vol 11, pp. 211-233.
- Lahey, R. T. 1978 "A Mechanistic Subcooled Boiling Model", *Sixth Int. Heat*

Transfer Conf., Toronto, Vol. I, pp. 293-297.

Lahey, R. T. and Moody, F. J. 1977 "The Thermal Hydraulic of a Boiling Water Nuclear Reactor", American Nuclear Society, pp. 211-226.

Lai, J. C. and Farouk, B. 1992 "Numerical Simulation of Subcooled and Low Quality Forced convective Boiling Flows", ANS Proceedings, National Heat Transfer Conference, Vol. 6, pp. 12-20.

Landau, J., Boyle, J., Gomma, H.G. and Al Taweel, A.M. 1977 "Comparison of Methods for Measuring Interfacial Area in Gas-Liquid Dispersions", Can. J. Chem. Eng., Vol. 55, pp. 13-18.

Larsen, P. S. and Tong, L. S. 1969 "Void Fraction in Subcooled Boiling", J. Heat Transfer, Vol. 91, pp. 471-476.

Lee, S. C., Dorra, H. and Bankoff, S. G. 1992 "A Critical Review of Predictive Models for the Onset of Significant Void in Forced Convection Subcooled Boiling" HTD-Vol 217, Fundamentals of Subcooled Flow Boiling, ASME, pp. 33-39.

Lee, S. C. and Bankoff, S. G. 1992 "Prediction of the Onset of Significant Void in Downflow Subcooled Nucleate Boiling" HTD-Vol 197, Two-Phase Flow and Heat Transfer, ASME, pp. 93-100.

Levenspiel, O. 1959 "Collapse of Steam Bubbles in Water", Industrial and Engineering Chemistry, Vol. 51.

Levy, S. 1967 "Forced Convection Subcooled Boiling: Prediction of Vapour Volumetric Fraction", Int. J. Heat Mass Transfer Vol. 10, pp 951-965.

Maitra, D. and Subba Raju, K. 1975 "Vapour Void Fraction in Subcooled Flow Boiling", Nuclear Engineering and Design, Vol. 32, pp. 20-28.

Maroti, L. 1977 "Axial Distribution of Void Fraction in Subcooled Boiling", Nuclear Technology, Vol. 34, pp. 8-17.

Martin, R. 1972 "Measurement of the Local Void Fraction of High Pressure in a Heating Channel", Nuclear Science and Engineering, Vol. 48, pp. 125-138.

Mayinger, F. and Bucher, B. 1977 "Subcooled Boiling", in Two-Phase Flows and Heat Transfer, ed. Kakaç, S. and Veziroglu, T. N., Vol. II, Hemisphere Pub. Corp., Washington, pp. 581-621.

Meister, G. 1979 "Vapour Bubble Growth and Recondensation in Subcooled Boiling Flow", Nuclear Engineering and Design, Vol. 54, pp. 97-114.

Michel, H. and Bartsch, G. 1983 "A Statistical Microscopical Method for the Calculation of the Heat Transfer at Subcooled Flow-Boiling with Low Void Fraction and Low Pressure", Advances in Two-Phase Flow and Heat Transfer, ed. Kakaç, S. and Ishii, M., Vol. 1, pp. 321-337.

Mikic, B. B. and Rohsenow, W. M. 1969 "Bubble Growth Rates in Non-Uniform Temperature Field", Progress in Heat and Mass transfer II, pp. 283-293.

Moalem, D. and Sideman, S. 1973 "The Effect of Motion on Bubble Collapse", Int. J. Heat and Mass Transfer, Vol. 16, pp. 2321-2329.

Moles, F. and Shaw, J. 1972 "Boiling Heat Transfer to Subcooled Liquids under Conditions of Forced Convection", Trans. Inst. Chem. Engrs, Vol. 50, pp. 76-83.

Mosher, D. 1989 "Digital Image Processing of Two Phase Flow", Thermo-Fluids Research Report No. ME/89/TF/R2, McMaster University, Ont., Canada.

Okhotsimskii, A. D. 1988 "The Thermal Regime of Vapour Bubble Collapse at Different Jacob Numbers", Int. J. Heat and Mass Transfer, Vol. 31, pp. 1569-1576.

Plesset, M. S. and Zwick, S. 1952 "A Non-Steady Heat Diffusion Problem with Spherical Symmetry", J. Applied Physics, Vol. 23, pp. 95-98.

Rayleigh, 1917 "On the Pressure Developed in a Liquid During Collapse of a Spherical Cavity", Philosophy Magazine, Vol. 34, pp. 94-98.

Rogers, J. T. and Li, J. 1992 "Prediction of the Onset of Significant Void in Flow Boiling of Water", HTD-Vol. 217, Fundamentals of Subcooled Flow Boiling, ASME, pp. 41-52.

Rogers, J. T., Salcudean, M., Abdullah, Z., McLeod, D. and Poirier, D. 1987 "The Onset of Significant Void in up-Flow Boiling of Water at Low Pressure and Low Velocities", Int. J. Heat Mass Transfer, Vol. 30, No. 11, pp. 2247-2260.

Rouhani, S. Z. 1968 "Calculation of Steam Volume Fraction in Subcooled Boiling", J. Heat Transfer, Vol. 90, pp. 158-164.

Rouhani, S. Z. and Axelsson, E. 1970 "Calculation of Void Volume Fraction in the Subcooled and Quality Boiling Regions", Int. J. Heat Mass Transfer, Vol.

13, pp. 383-393.

Ruckenstein, E. and Davis, E. J. 1971 "The Effect of Bubble Translation on Vapour Bubble Growth in a Superheated Liquid", *Int. J. Heat and Mass Transfer*, Vol. 14, pp. 939-952.

Ruckenstein, E. and Constantinescu, D. 1969 "Mass or Heat Transfer with a Change in Interfacial Area-I", *Int. J. Heat and Mass Transfer*, Vol. 12, pp. 1249-1255.

Ruckenstein, E. 1967 "Mass Transfer between a Single Drop and a Continuous Phase", *Int. J. Heat and Mass Transfer*, Vol. 10, pp. 1785-1792.

Ruckenstein, E. 1959 "On Heat Transfer between Vapour Bubbles in Motion and The Boiling Liquid from which They Are Generated", *Chemical Engineering Science*, Vol. 10, pp. 22-30.

Saha, P. and Zuber, N. 1974 "Point of Net Vapour Generation and Vapour Void Fraction in Subcooled Boiling", *Proceeding of Fifth Int. Heat Transfer Conf.*, Tokyo, Vol. IV, pp. 175-179.

Sekoguchi, K., Nishikawa, K., Nakasatomi, M., Hirata, N. and Higuchi, H. 1974 "Flow Boiling in Subcooled and Low Quality Regions-- Heat Transfer and Local Void Fraction", *Proceedings of Fifth Int. Heat Transfer Conf.*, B4.8, pp. 180-184.

Sekoguchi, K., Tanaka, O., Esaki, S. and Imasaka, T. 1980 "Prediction of Void Fraction in Subcooled and Low Quality Boiling Regions", *Bulletin of the JSME*, Vol. 23, pp. 1475-1482.

Serizawa, A. 1979 "A Study of Forced Convection Subcooled Flow Boiling", *Two-Phase Momentum, Heat and Mass Transfer in Chemical Processes and Energy Engineering Systems*, ed. Drust, F., Tsiklauri, G. V. and Afgan, N. H., Vol. I, pp. 231-242.

Shah, M. M. 1983 "General Prediction of Heat Transfer during Subcooled Boiling in Annuli", *Heat Transfer Engineering*, Vol. 4, No. 1, pp 24-31.

Shah, M. M. 1977 "A General Correlation for Heat Transfer During Subcooled Boiling in Pipes and Annuli", *ASHRAE Trans.*, Vol. 83, Pt. 1, pp 202-217.

Smith, S. L. 1969-70 "Void Fraction in Two-Phase Flow: A Correlation Based upon an Equal Velocity Head Model", *Proceeding Inst. Mech. Eng.*, Vol. 184, pp. 647-664.

Shilimkan, R.V. and Stepanek, J.B. 1977 "Interfacial Area in Concurrent Gas-Liquid Flow in Tubes of Various Size", Chem. Eng. Sci., Vol. 32, pp. 149-154.

Shoukri, M., Judd, R.L., Donevski, B. and Dimmick, G.R. 1991 "Experiments on Subcooled Flow Boiling and Condensation in Vertical Annular Channels", in: Phase-Interface Phenomena in Multiphase Flow, Ed. Hewitt, G.F., Mayinger, F. and Riznic, J.R., Hemisphere Pub. Corp., pp. 413-422.

Simpson, H. C., Beggs, G. C. and Isikan, O. M. 1986 "Collapse of Steam Bubble in Sub-Cooled Water", Proceedings of the Eighth International Heat Transfer Conference, San Francisco, CA., USA, Vol. 4, pp. 1919-1924.

Snell, V. G., Takáts, F. and Szivós, K. 1992 "The SLOWPOKE Licensing Model", Nuclear Engineering and Design, Vol. 137, pp. 191-198.

Sridhar, T. and Potter, O.E. 1978 "Interfacial Area Measurements in Gas-Liquid Agitated Vessels", Chem. Eng. Sci., Vol. 33, pp. 1347-1353.

Stangl, G. and Mayinger, F. 1990 "Void Fraction Measurement in Subcooled Forced Convection Boiling with Refrigerant 12", Experimental Heat Transfer, Vol. 3, pp. 323-340.

Staub, F. W. 1968 The "Void Fraction in Subcooled Boiling-- Predicting of the Initial Point of Net Vapour Generation", J Heat Transfer Vol. 90, pp 151-157.

Staub, F. W. and Walmet, G. E. 1970 "The Void Fraction and Pressure Drop in Subcooled Flow Boiling", Fourth Int. Heat Transfer Conf., Paris, B4.11, pp. 1-16.

Tabei, K., Hasatani, M. and Kuroda, M. 1989 "Effective Gas-Liquid Interfacial Area in a Mobile-Bed Contactor", Int. Chem. Eng., Vol. 29, pp. 679-688.

Theofanous, T. G., Biasi, L., Isbin, H. S. and Fauske, H. K. 1970 "Nonequilibrium Bubble Collapse: A Theoretical Study", Chemical Engineering Progress Symposium Series, No. 102, Vol. 66, pp. 37-47.

Thom, J. R. S., Walker, W. W., Fallon, T. A. and Reising, G. F. 1965-66 "Boiling in Subcooled Water during Flow up Heated Tubes or Annuli", Proceeding of Inst. of Mech. Eng., Paper No. 6, pp. 226-246.

Toda, S. and Hori, Y. 1989 "Dynamic Relationships between Void and Temperature Distributions in Subcooled Bulk Flow in a Vertical Tube", NURETH-4, Karlsruhe.

Tomida, T., Yusa, F. and Okazaki, T. 1978 "Effective Interfacial Area and Liquid-Side Mass Transfer Coefficient in the Upward Two-Phase Flow of Gas-Liquid Mixtures", Chem. Eng. J., Vol. 16, pp. 81-88.

Tsung-Chang, G. and Bankoff, S. G. 1990 "On the Mechanism of Forced-Convection Subcooled Nucleate Boiling", J. Heat Transfer, Vol. 112, pp. 213-217.

Ünal, H. C. 1977 "Void Fraction and Incipient Point of Boiling During the Subcooled Nucleate Flow Boiling", Int. J. Heat Mass Transfer, Vol. 20, pp. 409-419.

Ünal, H. C. 1976 "Maximum Bubble Diameter, Maximum Bubble-Growth Time and Bubble-Growth Rate During the Subcooled Nucleate Flow Boiling of Water up to 17.7 MN/m^2 ", Int. J. Heat Mass Transfer, Vol. 19, pp. 643-649.

Ünal, H. C. 1975 "Determination of the initial point of Net Vapour Generation in Flow Boiling System" Int. J. Heat Mass Transfer, Vol. 18, pp. 1095-1099.

Van Stralen, S. J. D., Sohal, M. S., Cole, R. and Sluyter, W. M. 1975 "Bubble Growth Rates in Pure and Binary Systems: Combined Effect of Relaxation and Evaporation Microlayers", Int. J. Heat and Mass Transfer, Vol. 18, pp. 453-467.

Van Stralen, S. J. D. 1979 "The Evaporation Microlayer in Pure System", in: Boiling Phenomena, ed. S. Van Stralen and R. Cole, Hemisphere Publishing Corporation, Vol. 2, Ch. 14.

Voutsinos, C. M. and Judd, R. L. 1975 "Laser Interferometric Investigation of the Microlayer Evaporation Phenomenon", J. Heat Transfer, pp. 88-92.

Wallis, G. B. 1974 "The Terminal Speed of Single Drops or Bubbles in an Infinite Medium", Int. J. Multiphase Flow, Vol. 1, pp. 491.

Winterton, R. H. S. 1984 "Flow Boiling: Prediction of Bubble Departure", Int. J. Heat Mass Transfer, Vol. 27, pp. 1422-1424.

Wittke, D. D. and Chao, B. T. 1967 "Collapse of Vapour Bubble with Translatory Motion", J. Heat Transfer, pp. 17-24.

Yamazaki, Y. and Ymaguchi, K. 1976 "Void Fraction Correlation for Boiling and Non-Boiling Vertical Two-Phase Flows in Tubes", Journal of Nuclear Science and Technology, Vol. 13, pp. 701-707.

Yang, J. Y. and Weisman, J. 1991 "A Phenomenological Model of Subcooled Flow Boiling in the Detached Bubble Region", *Int. J. Multiphase Flow*, Vol. 17, pp. 77-94.

Yasunishi, A., Fukuma, M. and Muroyama, K. 1986 "Measurement of Behaviour of Gas Holdup in a Slurry Bubble Column by a Dual Electroresistivity Probe Method", *J. Chem. Eng. Japan*, Vol. 19, pp. 444-449.

Zeng, L. Z., Klausner, J. F. and Mei, R. 1993a "A Unified Model for the Prediction of Bubble Detachment Diameters in Boiling Systems-I. Pool Boiling", *Int. J. Heat and Mass Transfer*, Vol. 36, pp. 2261-2270.

Zeng, L. Z., Klausner, J. F. and Bernhard, D. M. and Mei, R. 1993b "A Unified Model for the Prediction of Bubble Detachment Diameters in Boiling Systems-II. Flow Boiling", *Int. J. Heat and Mass Transfer*, Vol. 36, pp. 2271-2279.

Zijl, W., Ramakers, F. J. M. and Van Stralen, S. J. D. 1979 "Global Numerical Solutions of Growth and Departure of Vapour Bubble at a Horizontal Superheated Wall in a Pure Liquid and Binary Mixture", *Int. J. Heat and Mass Transfer*, Vol. 22, pp. 401-420.

Zuber, N. 1961 "The Dynamic of Vapour Bubbles in Nonuniform Temperature Fields", *Int. J. Heat and Mass Transfer*, Vol. 2, pp. 83-98.

Zuber, N. and Findlay, J. 1965 "Average Volumetric Concentration in Two-Phase Flow System", *J. Heat Transfer*, Vol. 87, pp. 453-462.

Zuber, N. and Staub, F. W. and Bijwaard, G. 1966 "Vapour Void Fraction in Subcooled Boiling Systems", *Proceedings of the Third Int. Heat Transfer Conf.*, Chicago, Vol. 5. pp. 24-38.

APPENDIX A

HEAT BALANCE ACROSS TEST SECTION

A heat balance was performed across the test section to check the accuracy of the wall heat flux calculation, temperature measurement, and heat losses from the test section. The applied heat flux along the heating section was assumed uniform and calculated from the input electric DC power as follows:

$$q = \frac{I}{P_h} \frac{V}{Z_h} \quad (\text{A.1})$$

where I is the current through the heater, V is the voltage drop across the heater, P_h is the heater perimeter, and Z_h is the heater length. This value was compared to the heat flux q_w calculated from the heat balance across the test section,

$$q_w = \frac{G A C_p (T_{out} - T_{in})}{P_h Z_h} \quad (\text{A.2})$$

where T_{in} and T_{out} are the water temperature at test section inlet and outlet respectively. The comparison is shown in Figure A.1. As shown in the figure, the heat flux calculated from the heat balance across the test section is 5% less than that calculated from the electric input power. This difference is attributed to the heat losses by convection outside the test section.

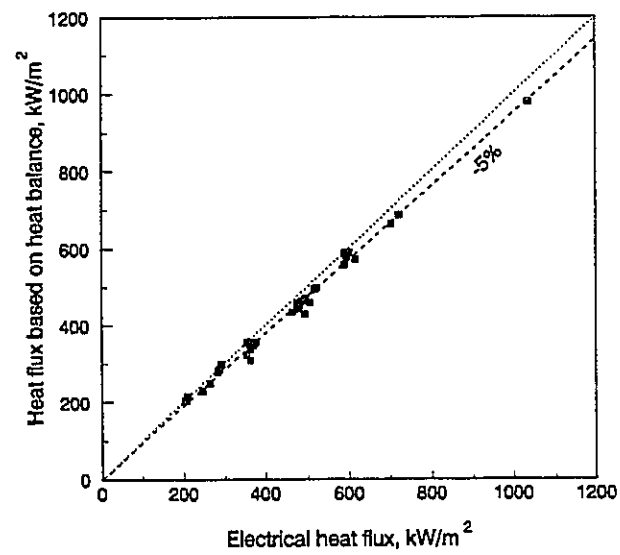


Figure A.1 Comparison between heat flux calculated from heat balance across the test section and that calculated from input electrical power

APPENDIX B

UNCERTAINTY ANALYSIS

The uncertainty of calculated results was estimated from error propagation equation,

$$\zeta(\phi) = \frac{\epsilon(\phi)}{\phi} = \left(\left(\frac{\partial \phi}{\partial x_1} \frac{\epsilon(x_1)}{\phi} \right)^2 + \left(\frac{\partial \phi}{\partial x_2} \frac{\epsilon(x_2)}{\phi} \right)^2 + \dots + \left(\frac{\partial \phi}{\partial x_n} \frac{\epsilon(x_n)}{\phi} \right)^2 \right)^{1/2} \quad (\text{B.1})$$

where:

ϕ computed results

$\zeta(\phi)$ percentage uncertainty in the result ϕ

$\epsilon(\phi)$ absolute uncertainty in the result ϕ

$\epsilon(x_n)$ absolute uncertainty in the result x_n

x_n n^{th} variable

Table B.1 contains uncertainties in measured quantities in boiling and condensation regions.

An example of uncertainty calculation for computed quantities at the three centimetre level, Run no. C5, in the condensing region is listed in Table B.2. For Run no. B5, and at twenty one centimetre level, the uncertainty for

computed quantities in the subcooled flow boiling region are listed in Table B.3. As discussed in Chapter 5, the location of the NVG point is not sharply defined. As shown in Figure B.1, the NVG phenomenon falls in a range rather than at a point. It was found for the experiment conditions listed in Tables 3.1 and 3.3, the maximum uncertainty in the NVG point location is ± 2 cm. Following the above procedure, the uncertainty in the liquid subcooling at the NVG point, calculated from Equation 5.1, falls in the range $\pm 5\%$ - $\pm 15\%$.

Table B.1 Uncertainty in Measured Quantities

Quantity	Absolute uncertainty	Percentage uncertainty
Temperature	$\pm 0.2\text{ }^{\circ}\text{C}$	
Void fraction		± 4.0
Voltage drop		± 1.0
Mass flux		± 2.0
Length (from monitor screen)		
- in condensing region	$\pm 0.1\text{mm}$	
- in boiling region	$\pm 0.05\text{mm}$	
Heat flux		± 5.0

Table B.2 Uncertainty for Quantities Computed in Condensing Region

Quantity	Value	Percentage uncertainty
Void fraction	0.1	± 4.0
Mass flux	413.9 kg/m ² s	± 2.0
Subcooling	9.5 °C	± 3.0
Mean bubble volume		± 5.0
Mean bubble surface area		± 3.3
Mean Sauter bubble diameter	5.6 mm	± 6.0
Liquid velocity	0.484 m/s	± 2.1
Bubble absolute velocity	0.72 m/s	± 0.5
Bubble relative velocity	0.24 m/s	± 4.5
Interfacial area concentration	100 m ² /m ³	± 7.2
Interfacial heat transfer coefficient	7788 W/m ² K	± 9.0
Condensation Nusselt number	64.00	± 11.0
Bubble Reynolds number		± 7.5

Table B.3 Uncertainty for Quantities Computed in Boiling region

Quantity	Value	Percentage uncertainty
Void fraction	0.145	± 4.0
Mass flux	264.3 kg/m ² s	± 2.0
Heat flux	508 kW/m ²	± 5.0
Subcooling	7.25 °C	± 6.0
Z_d	0.09 m	± 22.0
$T_s - T_d$	13 °C	7.5
Mean bubble volume		± 5.3
Mean bubble surface area		± 3.5
Mean Sauter bubble diameter	2.8 mm	± 6.4

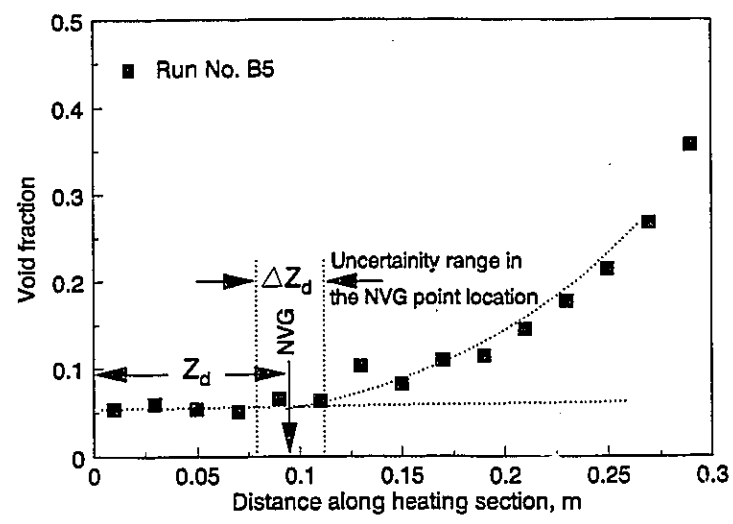


Figure B.1 Uncertainty in the NVG point location